Beam-Gas Imaging at the LHCb Experiment

George Rufus Coombs

Submitted in fulfilment of the requirements for the degree of
Doctor of Philosophy

School of Physics and Astronomy

College of Science and Engineering
University of Glasgow

January 2021

Abstract

This thesis presents a new absolute luminosity calibration measurement at the LHCb experiment for pp collsions at $\sqrt{s} = 13$ TeV measured via the beam-gas imaging (BGI) technique with data acquired in the 2016 luminosity calibration session. The measured reference cross-sections under these conditions for the *Track* and *Vertex* counters are $\sigma_{Track} = 65.82 \pm 1.14$ mb and $\sigma_{Vertex} = 60.00 \pm 0.98$ mb, respectively.

The principle of the BGI technique is set out and the BGI measurements from 2016 are presented alongside beam imaging results from a broader set of run 2 calibration data. The procedure for determining the vertex position resolution from collision data via the split vertex method, a crucial element of a precise BGI measurement, is described and measurements of this resolution are reported. With a precise knowledge of the detector resolution it is possible to accurately measure the LHC beam profiles and parameters on a bunch-by-bunch level from their interactions with gas molecules in the LHCb beam pipe and with each other. This allows for a precise evaluation of the overlap integral, a quantity that is directly proportional to the luminosity produced at a collider.

The circulating bunch populations are measured by LHC instrumentation and the results relevant for the calibration measurement are presented. Ghost charge results measured via the BGI technique are reported, including the first such measurements made with the VELO subdetector in its open position and with the first xenon beams circulating in the LHC. The utility of the LHCb measurement as a cross-check on measurements from LHC instrumentation is demonstrated and a novel timing technique making use of the LHCb Outer Tracker is set out. The additional timing information from this subdetector permits the first LHCb measurement of the longitudinal LHC beam profile with a time granularity less than 25 ns.

The luminosity calibration cross-section results are then reported and the full range of systematic uncertainties affecting this measurement are evaluated. The reference cross-section for the *Track* counter, used for the luminosity determination in LHCb physics data, is determined to a precision of 1.73%.

Two additional studies that make use of beam-gas interactions at LHCb are also included. The first is a collaborative effort in which a cross-calibration of all existing bunch profile measurement techniques at the LHC was performed. The second looks at possible dynamic vacuum effects due to the movement of the VELO subdetector and relies on a novel vertexing approach making use of the LHCb experiment's downstream tracking stations. This approach demonstrates a statistically significant pressure increase within the VELO volume due to its movement, at 2.6 standard deviations.

Acknowledgements

Too many people to mention here have helped me or offered advice throughout my time as a PhD student, however, most of all I need to thank my team of supervisors both at the University of Glasgow and at CERN. This thesis would not have been possible without their assistance, advice and close collaboration. In particular both Professors Paul Soler and Lars Eklund at Glasgow have supported me throughout my PhD with matters both academic and administrative and have remained in close contact with me throughout my work on this thesis. I also need to thank Paul specially for giving me the opportunity that I've had in pursuing this thesis.

In addition, I need to acknowledge the CERN doctoral programme which funded my three years of work at CERN and without which my PhD would not have been possible. I am equally indebted to Dr Massimiliano Ferro-Luzzi who was my CERN supervisor and who has always been available to provide advice and guidance throughout my time in Geneva. A special thank you has to go to Rosen Matev who took over my direct supervision at CERN part way through the project and has provided invaluable advice on a broad range of topics as well as three years of productive and enjoyable discussion. I also need to thank Colin Barschel whose previous work on this topic I have built upon and who was good enough to show me the ins and outs of a specialised and unique analysis technique.

With reference to the work presented in Chapter 5 of this thesis I would like to thank Tom Hadavizadeh for his work on the LHCb online measurements and also those members of the CERN Beam Instrumentation group who contributed to this project, in particular Dr Reyes Alemany-Fernández who led the cross-calibration effort.

In addition I need to thank my family and friends who have helped make this time both enjoyable and rewarding. Most of all I would very much like to thank Sarah who has offered nothing but support throughout the duration of this work and with whom I am looking forward to spending the foreseeable future.

Preface

The work reported in this thesis is the result of my own research carried out at CERN within the Luminosity Group of LHCb. It has not been submitted for any other degree at the University of Glasgow or at any other institution. Since the work carried out is collaborative in nature, the list below highlights all the original work carried out by the author.

Chapter 1 is an introduction to the thesis topic and goals followed by a literature review carried out by the author discussing the LHC accelerator, the LHCb detector, the SMOG system included in LHCb for luminosity measurements and how luminosity measurements are carried out at a hadron collider such as the LHC.

Chapter 2 describes work carried out by the author on beam-gas imaging (BGI) luminosity measurements undertaken at LHCb during LHC run 2. The idea behind the beam-gas imaging method was developed by Dr Massimiliano Ferro-Luzzi, Dr Plamen Hopchev and Dr Colin Barschel. The author participated in all the luminosity calibration runs from 2016-2018 as a member of the LHCb luminosity group and carried out the analysis presented in this chapter in its entirety, under the supervision of Dr Ferro-Luzzi and Rosen Matev.

Chapter 3 describes the work carried out by the author on the measurement of LHC bunch populations and ghost charge corrections that affect the luminosity measurements. The bunch population measurements are provided by the LHC beam instrumentation group and their analysis was carried out in its entirety by the author. All LHCb measurements presented in this chapter were performed by the author.

Chapter 4 describes the measurement of per-bunch interaction rates at LHCb and their combination with the measurements carried out in chapters 2 and 3 to obtain the reference cross-section required for a luminosity calibration at LHCb in run 2. The systematic uncertainties that affect this calibration measurement are also discussed. This work was carried out by the author in its entirety.

Chapter 5 was a collaborative measurement and calibration of the LHC beam profile monitors carried out by the author with colleagues from the beam instrumentation team of the LHC and other LHC experiments. The calibration programme was coordinated by Dr Reyes Alemany-Fernández in the context of the LHC Luminosity Calibration and Monitoring working group, the online measurements at LHCb were carried out by Dr Thomas Hadavizadeh and the author performed the BGI offline measurements and the comparison with the online measurements and the reference measurements from the LHC wire scanners.

Chapter 6 is a measurement carried out by the author of dynamic vacuum effects in the LHCb VELO system using a novel vertexing approach. The author actively participated in the measurements that were carried out in 2016 and 2017 by the LHCb experiment and carried out the analysis of the data presented in this chapter.

Tomorrow still blind
advances slowly.
Sight and light
race towards each other,
and from their embrace
is born the day,
eyes open
tall as a foal.
- *John Berger*

Table of Contents

Chapter 1

Introduction and Overview

1.1 Introduction

Luminosity is one of the most important performance parameters for any collider experiment. It provides the relation between the number of observed interactions for a given process and the cross-section of that process. Precision cross-section measurements form an integral part of the LHCb physics programme and thus a precise luminosity measurement is a priority for the experiment. For several absolute cross-section measurements using run 2 data, the uncertainty on the luminosity calibration is currently the limiting systematic uncertainty [1]. These cross-section measurements allow LHCb to test the predictions of the Standard Model of particle physics and to place constraints on parton distribution functions (PDF) in the forward region covered by the experiment. These PDF measurements are especially interesting as theoretical predictions of PDFs depend on the pseudorapidity η of the final state. Most of the pseudorapidity range covered by the LHCb experiment, $2 < \eta < 5$ is not accessible to the general purpose experiments at the LHC, with their coverage overlapping only in the range $2 < \eta < 2.5$.

At lepton colliders such as LEP, previously installed in the tunnel now housing the LHC, luminosity could be measured to a precision of around 0.05% by making use of precise theoretical calculations of the cross-section for electron-positron elastic scattering [2]. In the hadronic environment at the LHC, however, there is no equivalent precisely known cross-section that it is experimentally feasible to make use of, and the best precision can be achieved via a direct luminosity measurement. Here an effective process is defined for a particular detector response, e.g. at least one reconstructed track, and this is used as a luminosity counter. The cross-section of this process is then measured by making a precise measurement of the luminosity under controlled conditions and counting the number of events observed in the detector corresponding to the given effective process.

Two techniques are in use at LHCb for the purpose of luminosity measurement in collider mode. These are the van der Meer scan (vdM) method and the Beam-Gas Imaging (BGI) technique [3, 4, 5, 6, 7]. The vdM approach is used across the LHC experiments and will be described in Sec. 1.6. The focus of this thesis will be on the BGI technique and its application in run 2 for luminosity calibration at LHCb as well as for a variety of other beam imaging measurements. For data acquired during run 1 of the LHC a record precision of 1.16 % was achieved by the LHCb experiment on its luminosity calibration. This was achieved by combining results from these two measurement techniques with largely uncorrelated systematic uncertainties [5]. The run 2 conditions necessitate a new measurement largely due to the increase in beam energy to 6.5 TeV per beam and presents new challenges due to the changed beam conditions. A new measurement is also made necessary by changes in the detector over time whether due to changes to reconstruction algorithms, recalibration of subdetectors or radiation exposure of detector hardware. However, only a preliminary BGI measurement has been performed during run 2 to date, with an uncertainty of 3.9 % [8]. This thesis presents an updated luminosity calibration using the BGI technique for p-p collision data recorded at $\sqrt{s} = 13$ TeV.

The present chapter will describe the LHC accelerator complex and the LHCb detector in detail before moving on to explain the concepts underlying direct luminosity measurements at a bunched beam hadron collider such as the LHC. The principle of the BGI technique and its application for the run 2 LHCb luminosity calibration will be presented in chapter 2. In chapter 3 the measurement of bunch populations at the LHC will be discussed as well as the LHCb programme of ghost charge measurements throughout run 2. In chapter 4 the results of chapters 2 and 3 will be used together to provide a direct measurement of the calibration cross-section for the LHCb run 2 dataset. Alongside this, chapters 5 and 6 present the results of studies making use of beam-gas interactions for further beam measurements. In chapter 5 the LHCb contribution to an LHC-wide programme of cross-calibration of emittance measuring devices is presented with transverse beam-size measurements from the BGI method compared to those from LHC instrumentation. In chapter 6 a study of dynamic vacuum effects is presented with the goal of using beam-gas interaction rates to determine if the proximity to the beams of LHCb's VELO subdetector contributes to the degradation of the beam vacuum around the LHCb interaction point via beam-induced surface bombardment phenomena.

1.2 The LHC Accelerator

The Large Hadron Collider (LHC) is a bunched-beam hadron collider located in a tunnel of length 26.7 km at the laboratories of the European Organisation for Nuclear Research (CERN) in Geneva [9]. The accelerator is composed of eight arcs each containing 154 dipoles or bending magnets and eight straight sections where so called insertions are located. These insertions include interaction points where the four major particle physics experiments (ALICE, ATLAS, CMS and LHCb) are located as well as equipment necessary for the running of the accelerator such as the accelerating RF cavities, the collimation system or the beam instrumentation (some of which is described in Sec. 3.1). A schematic picture of this arrangement can be seen in Fig. 1.1.

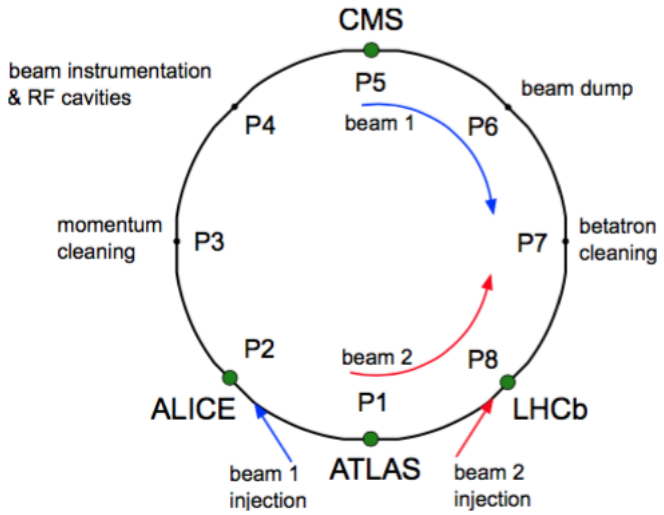

Figure 1.1: A schematic diagram of the LHC showing the experiment or instrumentation located at each point on the ring. There are 8 points labelled P1 through P8 and the directions of the two counter-circulating proton beams are also shown [7].

The LHC has a design energy of 7 TeV per beam but the highest achieved beam energy to date is 6.5 TeV giving a centre-of-mass (c.o.m.) energy available in collisions of $\sqrt{s}$ = 13 TeV. Its RF cavities operate at a frequency of approximately 400 MHz and serve both to accelerate the beams during the machine ramp and to define the longitudinal structure of the beams, with charges confined to buckets with a period of 2.5 ns. There are 35640 such RF buckets across the whole ring which are divided up into 3564 25 ns bunch slots. Each bunch slot thus spans ten RF buckets and is identified at LHCb by a number known as a bunch crossing identifier (BCID).

Before protons arrive in the LHC they first pass through the injection chain that can be seen in Fig. 1.2. They are produced from hydrogen by a duoplasmatron source [10] before undergoing a first acceleration up to 50 MeV in the LINAC2 linear accelerator. From here

they enter the PS booster which further accelerates them to 1.4 GeV before injection into the Proton Synchrotron (PS). In the PS the particles are further accelerated up to 26 GeV before being transferred into the Super Proton Synchrotron (SPS) and finally injected into the LHC at an energy of 450 GeV. The particle beams are then 'ramped' up to their collision energy before being brought into collision at each of the interaction points (IPs). This acceleration is induced by the electric field of the RF cavities while the current in LHC dipoles is increased to keep the higher momentum particles within the ring. Data-taking at each of the experiments starts once the LHC has declared itself to be in 'Stable Beams'.

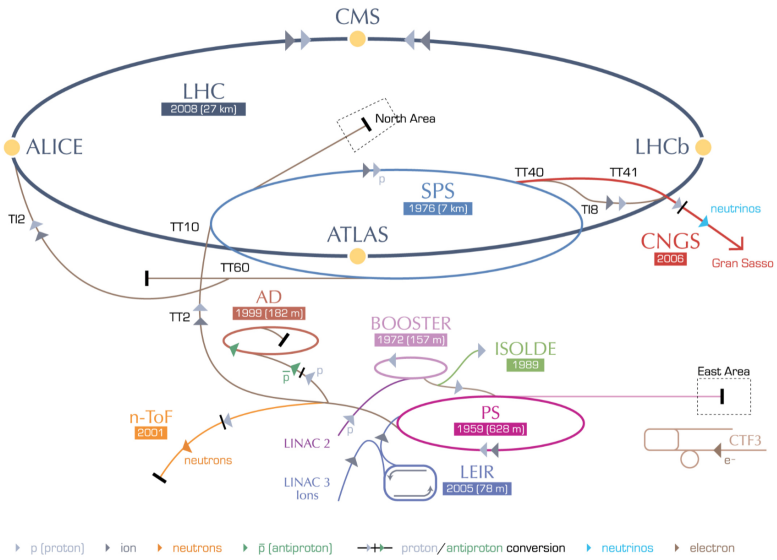

Figure 1.2: The CERN accelerator complex, including the whole LHC injection chain [11].

The first run of proton-proton collisions at the LHC started in 2009 and continued in 2010, 2011 at a c.o.m. energy of $\sqrt{s}$ = 7 TeV before reaching $\sqrt{s}$ = 8 TeV in 2012. Operations restarted after a first long shutdown in 2015, where collisions at $\sqrt{s}$ = 13 TeV were delivered during the second run of the LHC, ending in 2018. The cumulative integrated luminosity recorded by the LHCb detector throughout these two periods can be seen in Fig. 1.3. A series of new record peak luminosities were achieved at the LHC in run 2 by increasing the strength of the focusing magnets at IPs 1 and 5 and thus reducing the value of the β function below its design value. Improvements in machine availability and an increase in the fraction of time spent in stable beams (to over 50%) allowed all four experiments to record more data and meet or exceed their integrated luminosity goals [12].

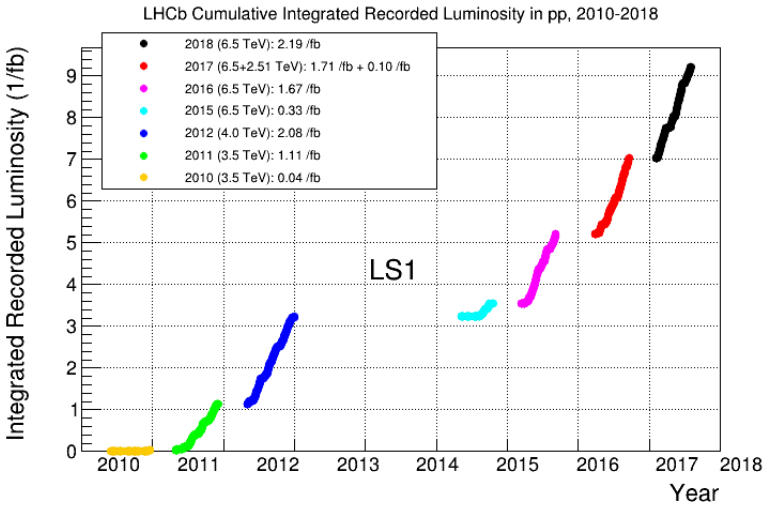

Figure 1.3: The cumulative integrated luminosity recorded by the LHCb detector throughout runs 1 and 2 of the LHC.

1.3 The LHCb Experiment

The LHCb experiment is one of four large particle physics experiments situated around the LHC ring located at IP 8, see Fig. 1.1. It was designed primarily to make measurements of the physics of heavy flavour phenomena such as CP violation or the rare decays of charm and beauty hadrons. The detector has an asymmetric geometry, being designed to make measurements exclusively in the forward region, and covers a range of $1.8 < \eta < 4.9$ in pseudorapidity[1] or an angle of 15 to 300 mrad. The geometry and positions of its various subdetectors can be seen in Fig. 1.4 and the detector is fully described in [13].

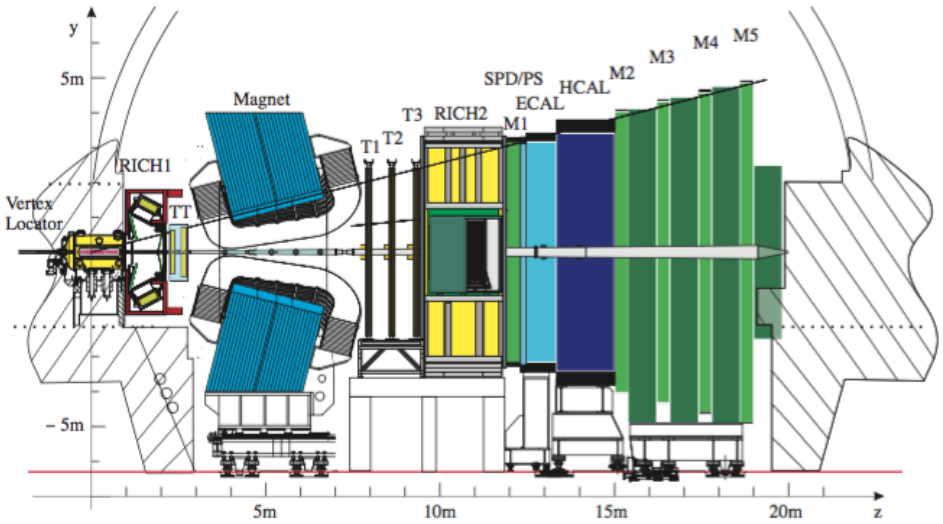

Figure 1.4: A vertical cross-section through the LHCb detector, taken from [13].

[1]The pseudorapidity η is related to the polar angle θ between the particle trajectory and the beam direction by $\eta \equiv -\ln\left[\tan\left(\frac{\theta}{2}\right)\right]$.

The data recorded by the LHCb detector is divided into numbered fills and runs. A fill is the entire period of collisions from the start of injection until the LHC beam is dumped. These typically last on the order of 12 hours during normal physics data-taking although a record fill length of almost 38 hours was recorded during 2016 [14]. At LHCb these fills are then further subdivided into runs which can last up to one hour. After one hour the automatic run control will stop the current run and increment the run number by one. This can also be done manually by the shift team in the LHCb control room.

1.3.1 The Vertex Locator and Tracking Stations

The Beam-Gas Imaging analysis makes extensive use of LHCb's tracking system which consists of the Vertex Locator (VELO), the Tracker Turicensis (TT) and the tracking stations,T1-3, indicated in Fig. 1.4. These components are used to measure the trajectories of particles passing through the detector: matching 'hits' in individual tracking sensors to form 'tracks'. The tracks that are observed in a given event are then combined to identify interaction vertices.

The LHCb Vertex Locator (VELO) surrounds the collision region and is designed to reconstruct primary and secondary interaction vertices from b and c hadron decays. The VELO makes use of silicon microstrip sensors grouped into 42 modules each containing one radial or R-sensor and one azimuthal or ϕ-sensor (see Fig. 1.5). These modules are grouped into two detector halves which are retractable and kept away from the beams until they are stable to avoid damaging the detector. After the declaration of stable beams the sensors are then moved in to within 7 mm of the collision point. These two halves are also shielded by a thin aluminium 'RF foil' to avoid any Radio Frequency pick up from the charged particle beams. This foil also serves to separate the VELO vacuum of $\sim 10^{-6}$ mbar from the beam vacuum of $\sim 10^{-9}$ mbar. There are also four R-sensors placed upstream of the detector which form the Pile-Up system (PU) used as part of the Level-0 hardware trigger [13].

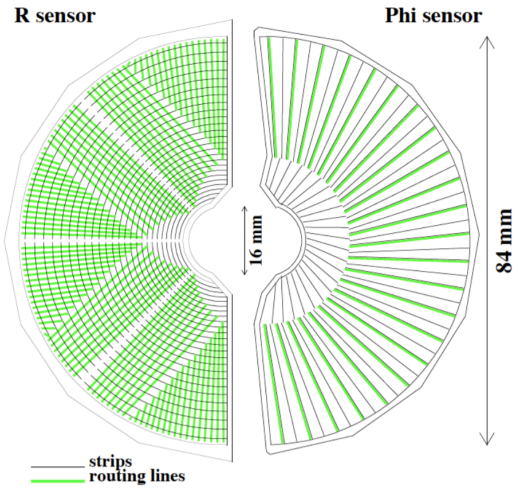

Figure 1.5: A schematic view of the R and ϕ sensors that makes up the VELO [15].

The VELO is designed to cover the forward region with an angular acceptance in the range 15-390 mrad allowing it to cover the pseudorapidity range of interest. In order for tracks to be within this acceptance they must cross at least three of the subdetector's sensor modules. This small angle acceptance is ideally suited for the reconstruction of beam-gas interactions where a very high momentum proton from the LHC beam collides with a thermal gas molecule, essentially at rest. The VELO transverse scale has a known precision of 0.05% due to the difference between the temperature at which it was manufactured and the temperature at which it is operated.

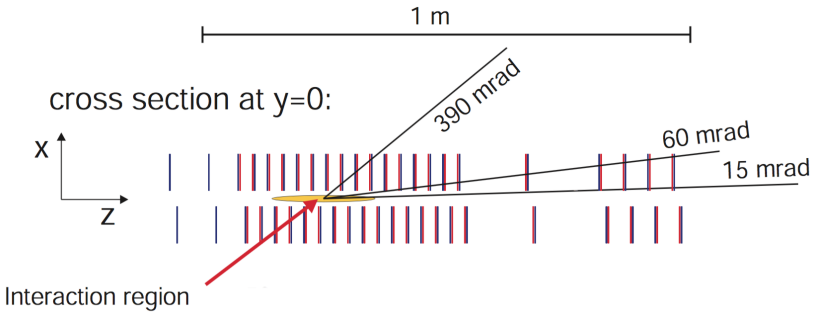

Figure 1.6: A cross-sectional view of the VELO sensor positions showing tracks at the extremes of the detector acceptance. The blue (red) lines depict the R (ϕ) sensors [16].

Tracks from the VELO that continue and make hits in the tracking stations (TT, T1-3 on Fig. 1.4) are classified as 'Long' tracks (see Fig. 1.7). These tracks that then pass through the LHCb magnet (with an integrated field of 4 T·m) can be assigned a momentum with a resolution of $\Delta p/p$ = 0.4-0.6%. The TT and the inner parts of tracking stations T1-3 (IT) use silicon microstrip sensors while the outer region of the tracking stations (OT) makes use of gaseous straw-tube detectors. The TT and IT are together known as the silicon tracker system (ST) and are composed of sensors with a pitch of about 200 μm arranged into four

detector layers per station. The first and last stations in each layer are arranged vertically while intermediate layers are rotated by 5° in alternate directions. The OT stations each contain just under 100 modules with each module made up of two staggered layers of drift tubes.

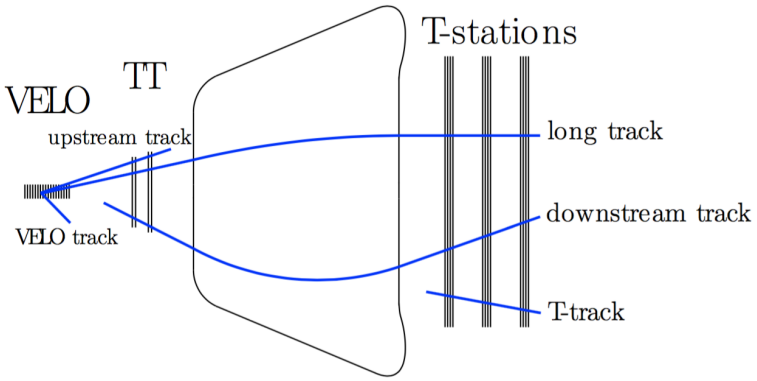

Figure 1.7: A diagram showing the different types of track defined at LHCb, with the magnetic field region indicated between the TT and T stations [17].

1.3.2 The Ring Imaging Cherenkov Detectors

The two Ring Imaging Cherenkov detectors, RICH1 and RICH2, are designed to provide particle identification, allowing different hadronic species to be distinguished. Protons, kaons and pions can be differentiated as their masses can be determined when the Cherenkov information is combined with the momentum measurement provided by the the LHCb tracking system (see Sec. 1.3.1). Two detectors are necessary to cover the full momentum range of interest at LHCb with RICH1 primarily covering the range 1-60 GeV/c and RICH2 the range 15-100 GeV/c. These detectors work by capturing the radiation emitted by decay products as they pass through a transparent material with a velocity greater than the phase velocity of light in that medium. The angle at which the radiation is emitted, θ can be related to the speed of the particle, $\beta = v/c$, and the refractive index of the material, n, as in Eq. 1.1.

$$\cos\theta = \frac{1}{\beta n} \tag{1.1}$$

The emitted light is redirected onto a set of Hybrid Photon Detectors (HPDs) and focused into a ring by an array of spherical and planar mirrors. The Cherenkov angle, and thus the speed, can be determined from the radius of this ring. The identity of the particles is then determined by comparing the likelihood of a given ring to have been produced by a given particle species.

RICH1 contains a decafluorobutane (C_4F_{10}) radiator with a refractive index of n = 1.0014 and originally contained an aerogel radiator with a larger refractive index designed to im-

prove performance for low momentum tracks. This was removed in run 2 as the PID efficiency was found to benefit from the reduction in material and the higher than design pile-up led to a higher density of photons within RICH1 and thus a reduced effectiveness of the aerogel for the identification of low momentum hadrons [19]. In RICH2 the radiator is a tetrafluoromethane gas (CF_4) with a refractive index of n = 1.0005

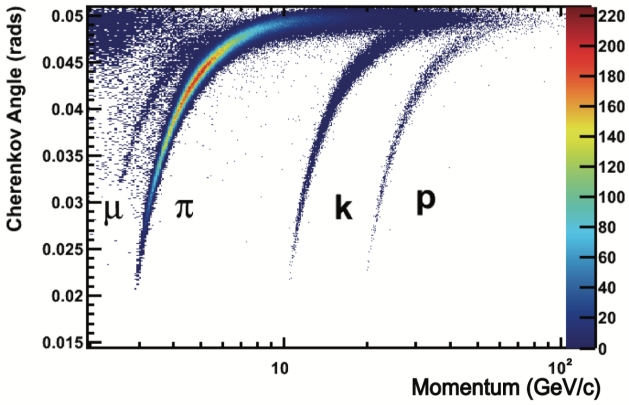

Figure 1.8: The reconstructed Cherenkov angle in RICH1 as a function of track momentum. Different bands corresponding to different particle species can be clearly observed [18].

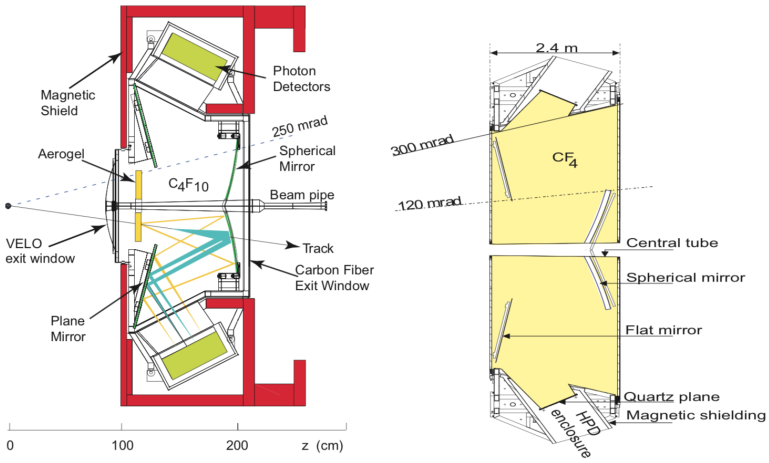

Figure 1.9: A schematic view of RICH1 (left) seen from the side and RICH2 (right) seen from above. Note that the Aerogel shown here was removed from RICH1 in run 2. Taken from Ref. [13].

1.3.3 The Calorimeters

The LHCb calorimetry system is designed to measure the energy deposited by particles in the detector. This is especially important for the detection of neutral particles which are not seen by the tracking stations. It also makes up an integral part of the LHCb trigger approach, being used to provide a fast (within 4 μs) measurement of high transverse energy deposits in

the detector. The system has four components: the scintillator pad detector (SPD), the preshower detector (PS), an electromagnetic calorimeter (ECAL) and a hadronic calorimeter (HCAL). All four components work on a similar principle with particles passing through the calorimeter generating scintillator light that is then transported along wavelength shifting optical fibres to be detected by photomultiplier tubes (PMT) outside the detector's acceptance. The quantity of collected light can be related to the energy deposited by the particle in the scintillator.

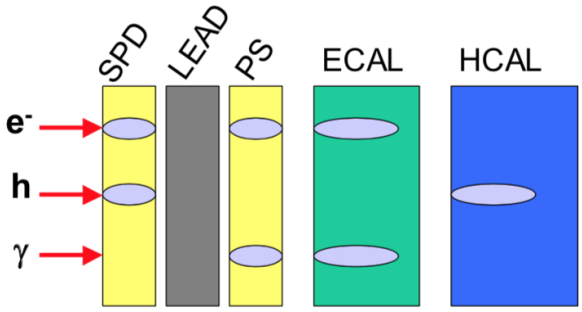

Figure 1.10: A schematic view of the layout of the different components of the LHCb calorimeter system. The response from each system to an electron (e^-), a charged hadron (h) and a photon (γ) is shown [20].

The SPD serves to differentiate charged and neutral particles as the former will deposit energy in the scintillator while the latter will not. It is separated from the PS by a thin (12 mm) layer of lead. This induces showering of electromagnetically interacting particles (electrons and photons), the energy from which can then be observed in the PS. The ECAL will absorb the full remaining energy deposit from electromagnetic particles while the HCAL will detect the energy deposited by hadrons such as protons, neutrons, pions and kaons.

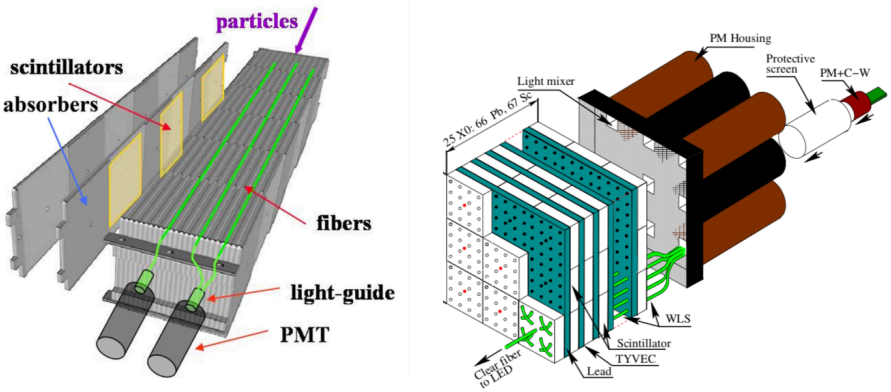

Figure 1.11: Diagrams showing the structure of modules from the LHCb HCAL (left) and ECAL (right). Taken from Ref. [13].

The SPD and PS are similar in construction being composed of polystyrene scintillators containing wavelength shifting dopants. The scintillating pads of each have a light proof coating and contain optical fibre loops designed to collect the scintillation light and transport it to the PMTs. The ECAL is composed of 66 alternating layers of scintillator and lead. It has a total depth of 42 cm which is equivalent to 25 radiation lengths. The scintillating pads are arranged in cells whose segmentation varies with proximity to the beam-pipe as shown in Fig. 1.12. The light from these cells is collected by fibres running throughout the whole structure of the ECAL and collected by PMTs located at its end. In the HCAL, however, the scintillating pads are arranged such that they are parallel to the incident particles and are separated by iron tiles of width 1 cm. The emitted light is again collected by fibres running throughout the structure and captured by PMTs at the rear of the subdetector.

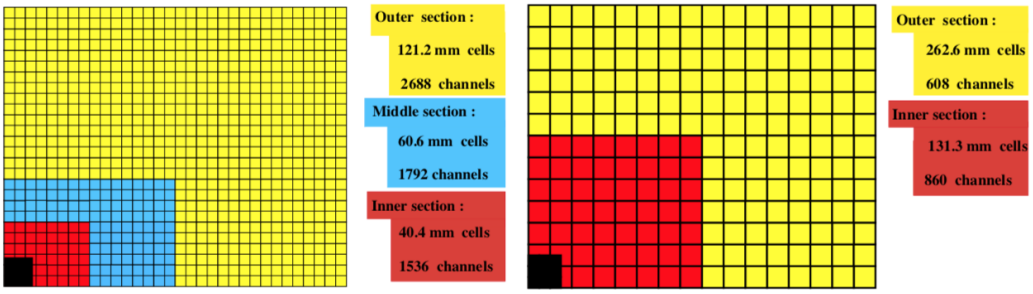

Figure 1.12: A front view of the cells in one quarter of the ECAL (left) and HCAL (right). The SPD and PS have a similar structure to the ECAL but the dimensions given are those for the latter. Taken from Ref. [13].

1.3.4 The Muon System

The Muon System is primarily designed to observe and identify muons from heavy flavour decays at the LHCb IP. It also serves as an essential part of the LHCb trigger system, providing fast muon p_T measurements that can be used to select interesting events. The subdetector itself is composed of five rectangular stations, with the first (M1) located before the calorimeters and the rest (M2-M4) located to their rear (see Fig. 1.13).The muon subdetector is positioned almost entirely after the other LHCb subdetectors as muons are highly penetrating particles with a relatively long lifetime (2.2 μs) and a low cross-section to interact with the detector material. These later stations are alternated with 80 cm thick sheets of iron that help to further isolate the muons by stopping any other stray particle species.

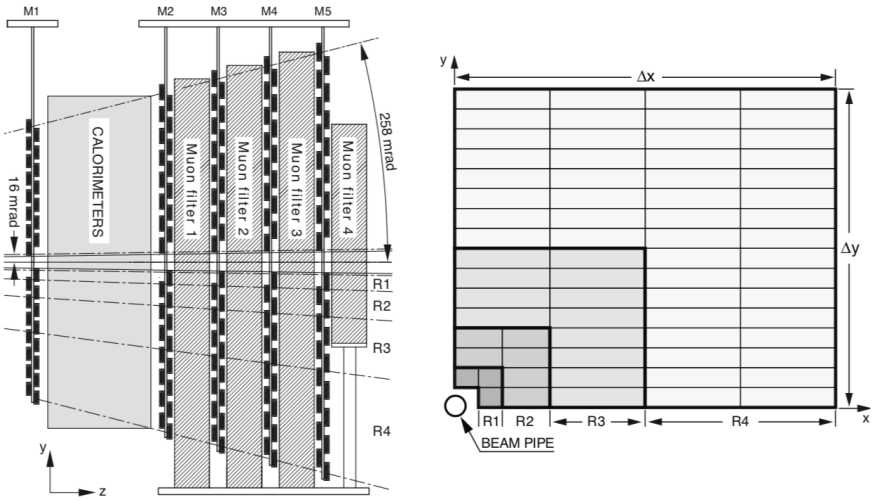

Figure 1.13: A cross-sectional view of the LHCb muon subdetector (left) and the muon system regions [13].

Each station is divided into four regions R1-R4 located further out from the beam pipe with ascending number as shown in Fig. 1.13. Each region is divided up into channels with a higher density of channels in the inner regions such that the integrated particle flux is roughly equal between the regions. The detectors themselves are, for the most part, Multi Wire Proportional Chambers containing a mixture of carbon dioxide, argon and tetrafluoromethane gases. The one exception to this is the inner region of the very first subdetector station (M1). This region is instrumented with triple gas electron multiplier detectors. This technology was chosen for this particular region as it is required to be especially radiation hard in order to remain operational for the full life of the detector as the particle flux here is particularly high [22].

1.3.5 The LHCb Trigger Chain

The experiment's trigger system is a set of algorithms designed to classify events as either interesting or uninteresting for the physics analyses conducted at the experiment. This is necessary in order to reduce the extremely high rate of events that are produced by the LHC to a more manageable level. Constraints on the maximum useable event rate are imposed by the detector readout electronics as well as the available computing resources. Individual trigger classification algorithms are commonly referred to as 'lines' such that the trigger is said to consist of a set of trigger lines.

The LHCb trigger consists of two main components. A hardware or 'Level 0' (L0) trigger that uses thresholds in the transverse energy/momentum deposited in the muon system and calorimeters to select interesting bunch crossings. A software or 'High-Level' trigger (HLT) then selects events from these crossings based on a real-time partial event reconstruction. In

run 2 this software trigger was split into two parts with a first stage (HLT1) running using a set of real-time reconstruction algorithms and a second asynchronous stage (HLT2) making use of a disk buffer to perform more complex offline selections [17]. As shown in Fig. 1.14 the selection at Level 0 reduces the rate from the full 40 MHz crossing rate down to 1 MHz and selection algorithms in HLT1 reduce this further to 110 kHz of events saved to the disk buffer. The detector then undergoes an online alignment and calibration and the events are reprocessed asynchronously in HLT2 where the full event reconstruction takes place without the time constraints imposed by real-time processing. The HLT2 selections reduce the event rate by a further order of magnitude and the output is written to disk for offline analysis

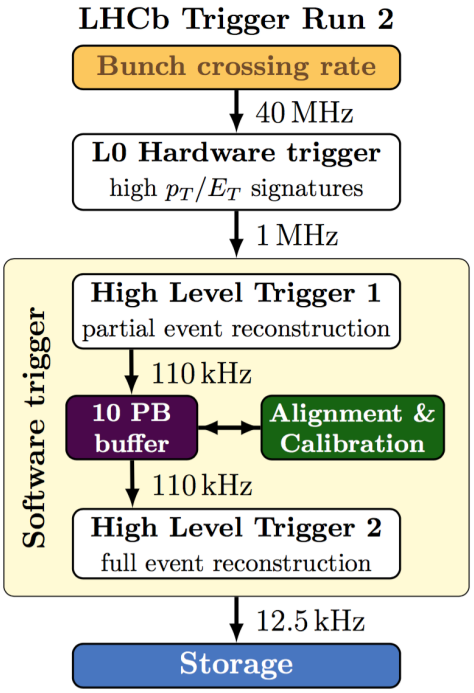

Figure 1.14: An overview of the LHCb trigger system in Run 2 [17].

The BGI analysis makes use of dedicated trigger lines to trigger beam-gas events. At L0, crossings are selected based on minimum energy deposits in the calorimeters and hits in the rearmost VELO sensors (PU), for beams 1 and 2 respectively. Beam 1 here is the beam moving towards the the LHCb magnet at the collision point (i.e. from left to right in Fig. 1.4) while beam 2 is moving away from the magnet at the collision point (i.e. from right to left in Fig. 1.4). Beam-gas interaction vertices are then reconstructed in HLT1 and classified according to their longitudinal position and track multiplicity.

The BGI analysis also makes use of dedicated triggers on non-colliding bunch crossings. Accounting for these different types of crossing leads to the definition of four bunch crossing types. Beam-beam crossings, bb, are crossings where both of the intersecting bunch slots are nominally filled as part of the LHC filling scheme. Beam-empty, be, and empty-beam, eb,

crossings are those where only the bunch in beam 1 or beam 2 respectively is filled. Empty-empty, ee, crossings are those where both of the bunches are nominally empty. These are also assigned integer keys by the LHCb DAQ with the values 0, 1, 2 and 3 corresponding to bunch crossing types ee, be, eb and bb. Random triggers including all crossing types are used as part of the interaction rate analysis while triggers specifically on crossings where one or both of the bunch slots are nominally empty are used in the ghost charge analysis (see Sec. 3.2).

1.4 SMOG and the LHC Vacuum System

In order to achieve the required long beam lifetimes (on the order of tens of hours) and to minimise background in the particle detectors from interactions between the circulating proton beams and residual gas the entire LHC beam pipe is pumped to ultra high vacuum (UHV) conditions at a nominal pressure of 1×10^{-9} mbar. The initial pump down is achieved with turbomolecular pumps distributed around the ring but can be maintained after pump down using only the cryopumping provided by the large cold surface area of the superconducting magnets, used to guide and control the charged particle beam, which are immersed in liquid helium at a temperature of 1.9 K. Additional external pumping is available to compensate for any excessive helium leaks and the full system is described in detail in [23]. The sections of the beam pipe surrounding LHCb are also coated with a layer of TiZrV non-evaporable getter (NEG) [24] and sputter ion pumps are located both within the VELO volume and at each end of the beam pipe. The NEG acts as a distributed pump, providing low outgassing and lowering the rate of desorption which can be caused by the interaction of the high intensity particle beam with the beam pipe walls. The ion pumps are required to pump any residual gases unaffected by the chemical getters. Due to the long active lifetime of the detector (on the order of decades) the NEG coating becomes saturated over time and loses pumping capacity. It thus needs to be baked out at regular intervals by heating the coated areas to a temperature of 200 °C for a period of 24 hours. As can be seen in Fig. 1.15 the stability of the LHCb beam vacuum has been observed to fall within acceptable limits with a pressure of less than 1×10^{-9} mbar in the absence of proton beams, rising to a maximum of 5×10^{-9} mbar just after the injection due to dynamic vacuum effects [15].

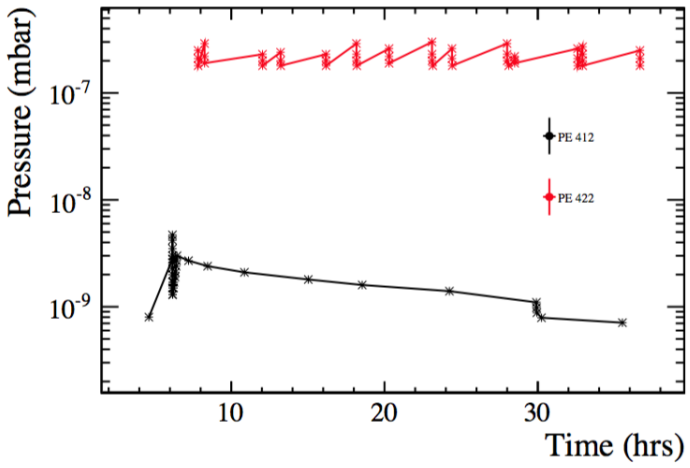

Figure 1.15: The black line in this figure shows the evolution of the pressure within the VELO over the course of one fill of the LHC as measured by a Penning gauge located within the beam volume (PE412). The pressure at gauge PE422 remains constant as it is located in the VELO vacuum tank and thus isolated from the beam vacuum. The beams were injected after 6 hours and sent to the beam dump 24 hours later [15].

In addition to the vacuum system required for normal operation as a proton-proton collider LHCb has also developed a system of gas injection known as the System for Measuring the Overlap with Gas or SMOG. This system allows the controlled injection of a limited number of gas species (currently He, Ne and Ar) to increase the pressure in the interaction region by several orders of magnitude, from $\sim 10^{-9}$ mbar to $\sim 10^{-7}$ mbar. This system was initially developed to enhance the number of beam-gas interactions in special calibration runs of the detector where such interactions are used to measure the beam profiles [7, 5] and its performance during a luminosity calibration fill in April 2012 can be seen in Fig. 1.16.

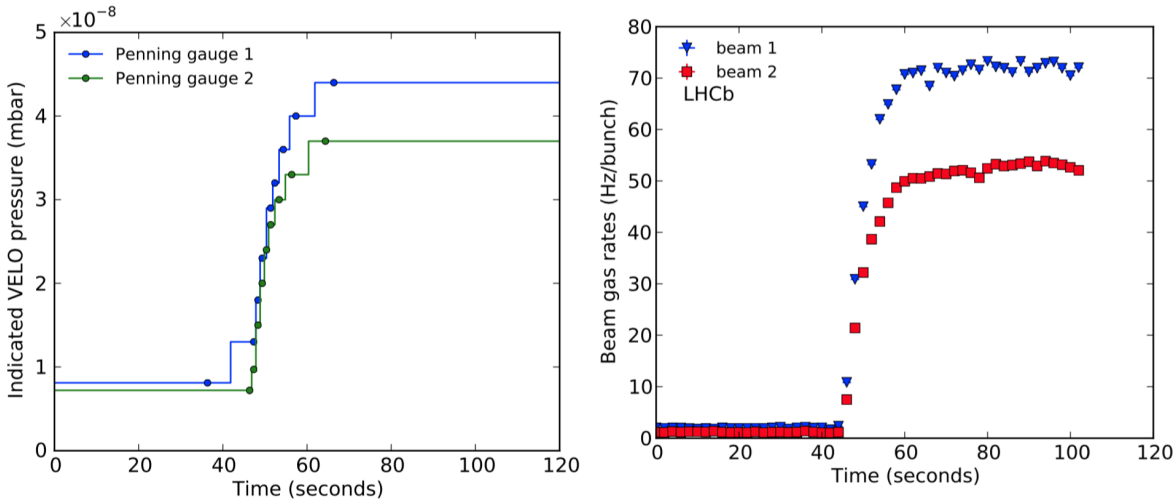

Figure 1.16: The increase in pressure in the VELO volume and in the beam-gas interaction rate after the injection of neon gas via SMOG during LHC fill no. 2520 (April 2012). The pressure values are those measured on Penning gauges PE411 and PE412 shown in Fig. 1.18 and located within 50 cm of the interaction point. The true pressure after injection is about four times that shown in the figure, after accounting for neon gauge sensitivity [7].

It has since also been repurposed for use as part of a rich programme of fixed-target physics to produce measurements that are complementary both to LHCb's flavour physics programme and to other fields such as cosmic ray physics [25, 26, 27]. The choice of gas species is limited, by a variety of operational concerns, to a select group of noble gases that will not be captured by the NEG coating near LHCb but can be effectively pumped once they reach the cold surfaces downstream and upstream of the detector. A photograph of the SMOG system hardware can be seen in Fig. 1.17 with all the major components labelled and the full schematic representation is shown in Fig. 1.18. The valves Fill and Bypass are software controlled while the valves HP and Pump are manually operated. The basic principle of operation of the system is that once the Fill valve is opened the gas is transported from the high pressure (1-4 bar) gas bottle to the pre-VELO vacuum volume via a restriction with a conductance of about 10^{-8} l/s. This limits the throughput toward the VELO to around 3×10^{-5} mbar$l$/s. The base pressure can then be controlled by varying the pumping speed of the turbopump TP301 in the pre-VELO volume (normally operating at 250 l/s). A NEG filter is also present just before the pre-VELO volume to remove any getterable impurities in the injected gas.

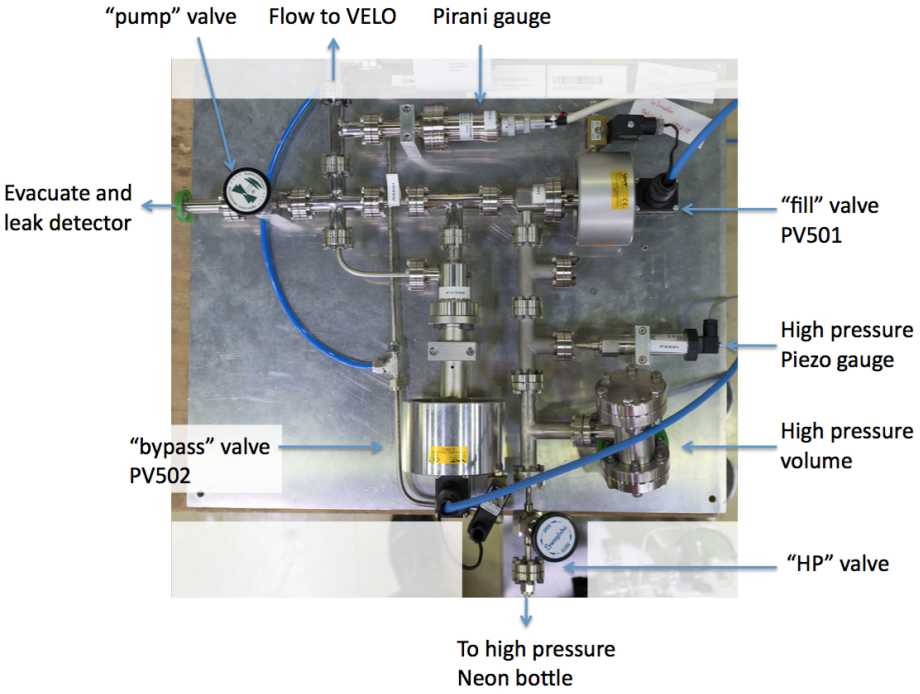

Figure 1.17: The SMOG system shown in the laboratory before installation [7].

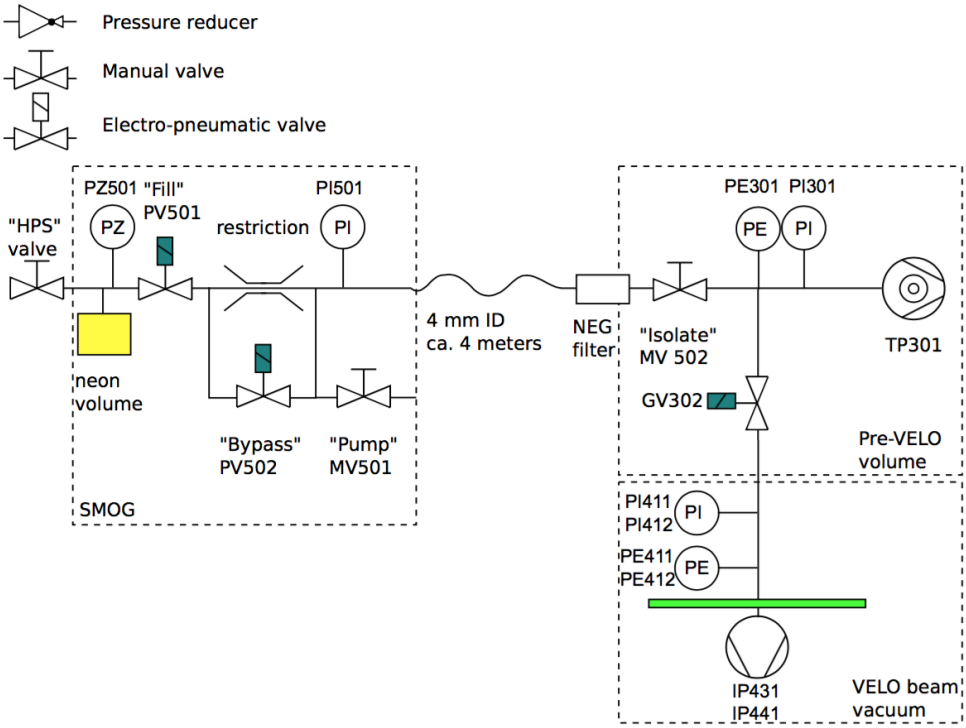

Figure 1.18: A schematic representation of the SMOG vacuum system once installed. PE represents a Penning gauge, PI a Pirani gauge, PZ a Piezo gauge, TP a turbomolecular pump and IP an ion pump [7].

1.5 Luminosity Calculation

The luminosity is one of the key quantities for any particle collider experiment, it relates the cross-section for a given physical process to the number of times it is observed. The relationship between the instantaneous luminosity, $\mathcal{L}$, and the number of observed events, n, for a process with cross-section σ_n is given in eq. 1.2.

$$\frac{dn}{dt} = \mathcal{L}\sigma_n \tag{1.2}$$

We can also write the luminosity in terms of the beam parameters and geometries. For two individual colliding bunches of protons the luminosity per bunch pair can be expressed as in Eq. 1.3 where f_{rev} is the revolution frequency for particles in the ring, $N_{1,2}$ are the bunch intensities for each beam, K is the kinematic factor shown in Eq. 1.4 and $\mathcal{O}$ is the overlap between the two bunches, determined by the collision geometry [28].

$$\mathcal{L} = f_{rev} N_1 N_2 K \mathcal{O} \tag{1.3}$$

The revolution frequency is easily obtained from the speed of the protons ($\simeq c$) and the circumference of the ring. The bunch populations are measured directly, primarily using two pieces of LHC instrumentation: the Direct Current Current Transformer (DCCT) and the Fast Beam Current Transformer (FBCT) [42, 46]. The kinematic factor can be expressed in terms of the velocity vectors of two colliding objects as in Eq. 1.4. It simplifies as shown for the ultra-relativistic case where $|\vec{v}_1| \approx |\vec{v}_2| \approx c$, with ϕ the half-angle between the two vectors [30]. At the very small crossing angles at which the LHC operates, $\mathcal{O}(100\mu\text{rad})$, the further approximation $\cos^2\phi \approx 1$ can be made and thus a value of $K \approx 2c$ used.

$$K = \sqrt{(\vec{v}_1 - \vec{v}_2)^2 - (\vec{v}_1 \times \vec{v}_2)^2/c^2} \approx 2c\cos^2\phi \tag{1.4}$$

The overlap $\mathcal{O}$ can be expressed as a 4D integral in space and time over the density distributions of the two colliding bunches, $\rho_{1,2}$, as in Eq. 1.5

$$\mathcal{O} = \int\int\int\int_{-\infty}^{\infty} \rho_1(x,y,z,t)\rho_2(x,y,z,t)dxdydzdt \tag{1.5}$$

Analytic solutions to this integral can be found in a variety of simplified cases [28, 31, 32]. For example, in the simple case of two beams of equal size with symmetric Gaussian shaped transverse distributions with standard deviation σ, colliding without a crossing angle, Eq. 1.6 can be used:

$$\mathcal{O} = \frac{1}{4\pi\sigma^2} \tag{1.6}$$

Transverse Beam Size

The variable σ in Eq. 1.6 is the transverse beam size and is often defined as in Eq. 1.7 as a function of two other variables: the transverse β function and the transverse beam emittance.

$$\sigma = \sqrt{\beta\epsilon} \tag{1.7}$$

The value of the transverse β function is determined by the strength of the focusing quadrupole magnets at each point around the accelerator while ϵ is the emittance: a value that is defined by the spread of the particles making up the beam in position-momentum phase space. The value of β changes as a function of the position around the LHC ring but for the purposes of luminosity calculation only the value at the interaction point, β^*, is of interest. The emittance is an inherent property of the beam and generally remains relatively stable during normal operation of the accelerator.

These parameters are derived from the solution to the Hill's equation (Eq. 1.8), a second order differential equation that is the equation of motion for a pseudo-harmonic oscillator in which the spring constant, k, depends on the position of the oscillator [33].

$$x''(s) - k(s)x(s) = 0 \tag{1.8}$$

This equation can be found to describe the transverse motion of charged particles travelling through the multipolar magnetic field around an accelerator ring where the particle's position is described by the Frenet-Serret coordinate system, as shown in Fig. 1.19 [34]. Here, the

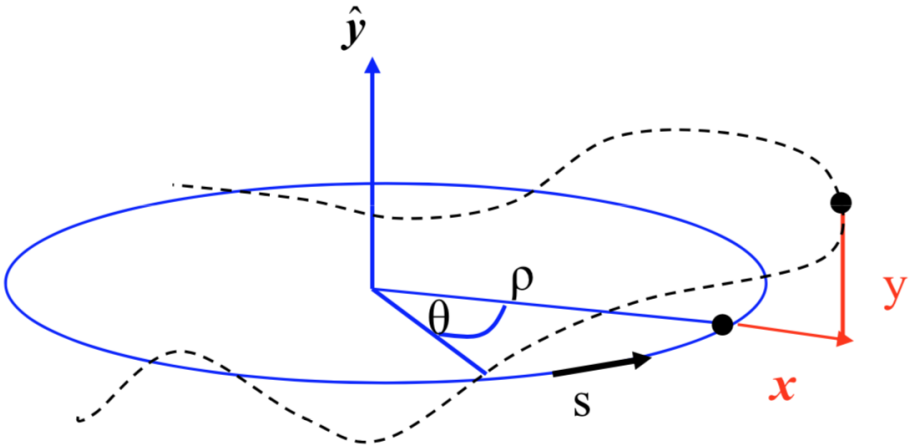

Figure 1.19: The Frenet-Serret coordinate system describes a particle's oscillations around a circular trajectory.

individual particles that collectively make up the stored beam are oscillating around some

ideal trajectory with a radius of curvature, ρ. This trajectory is defined by the dipolar field of the bending magnets while the particle oscillates within the quadrupolar field of the focusing magnets. An oscillating particle at position s along the closed orbit trajectory thus has transverse displacements from the ideal orbit x and y.

In this coordinate system the solution to the Hill's equation for the transverse coordinate x as a function of s can be shown to be:

$$x(s) = A\sqrt{\beta(s)}\sin(\phi(s) + \phi_0) \tag{1.9}$$

The particles in the beam thus undergo what are known as betatron oscillations with some constant amplitude factor, A, an amplitude modulation function, $\beta(s)$ and a phase advance along the particle trajectory, $\phi(s)$, that can be shifted by some arbitrary phase, ϕ_0. The values of A and β therefore define the envelope of these oscillations at any point around the ring and thus the transverse size of the beam. The constant A can further be expressed in terms of $x(s)$ and $x'(s)$ as in Eq. 1.10:

$$A^2 = \gamma(s)x^2(s) + 2\alpha(s)x(s)x'(s) + \beta(s)x'^2(s) \tag{1.10}$$

This expression for A leads to a parametric representation of an ellipse in the transverse phase space (x, x'), as shown in Fig. 1.20. The parameters α, β, γ in this expression are commonly referred to as the Twiss parameters and are related as in Eq. 1.11:

$$\alpha(s) = -\frac{\beta'(s)}{2}, \gamma(s) = \frac{1+\alpha(s)^2}{\beta(s)} \tag{1.11}$$

The constant on the left hand side of Eq. 1.10 is defined as the emittance, such that $\epsilon \equiv A^2$ and thus $\epsilon =$ Ellipse Area$/\pi$. According to Liouville's theorem, the emittance is a constant of the motion assuming the particles feel only conservative forces and undergo no energy dissipation [35]. This theorem does not hold during the acceleration of the beams which leads to a decrease in the transverse size of the beams. In order to account for this effect a quantity known as the normalised emittance is defined as in Eq. 1.12 where β_{rel} and γ_{rel} are the relativistic quantities[2] (as opposed to the similarly denoted Twiss parameters).

$$\epsilon_N \equiv \beta_{rel}\gamma_{rel}\epsilon \tag{1.12}$$

This normalised quantity should thus remain constant with acceleration even as the beam size shrinks. In reality, however, a variety of other non-conservative forces act on particle beams at the LHC and due to effects such as synchrotron radiation, intra-beam scattering or electromagnetic noise the normalised emittance is observed to increase throughout the

[2]For a particle travelling at velocity v these are defined as: $\beta_{rel} \equiv \frac{v}{c}$ and $\gamma_{rel} \equiv (1-\beta_{rel}^2)^{-1/2}$.

beams' lifetimes [36]. This is commonly referred to as blow-up of the beams.

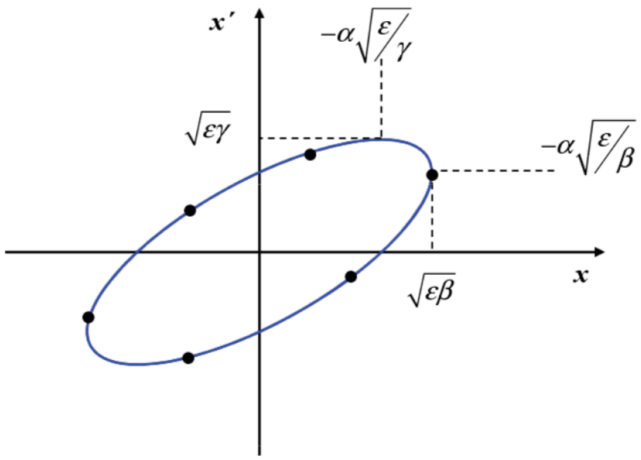

Figure 1.20: The ellipse in (x, x') phase space described by Eq. 1.10.

Geometric Reduction Factors

Various aspects of the collision geometry can reduce the luminosity produced by two colliding beams. If we add a crossing angle in the x-z plane we need to introduce a reduction factor S as defined in Eq. 1.13 while any offset in a transverse dimension x between the beams will add a reduction factor T as defined in Eq. 1.14 [28, 29]. Here ϕ is the crossing angle between the beams and Δx is the offset in x.

$$S = \frac{1}{\sqrt{1 + \frac{\sigma_z^2}{\sigma_x^2}\left(\tan\frac{\phi}{2}\right)^2}} \tag{1.13}$$

$$T = \exp\left(-\frac{\Delta x^2}{\sigma_x^2}\right) \tag{1.14}$$

If we have a situation where beams collide at an angle and with a relative offset between them the total reduction factor is the product of the independent reduction factors S and T with an additional factor W defined in Eqs. 1.15 and 1.16. This cross-term arises from the three-dimensional Gaussian distributions of the bunches and its full derivation is given in Ref. [28].

$$W = e^{\frac{B^2}{A}} \tag{1.15}$$

Where:

$$A = \frac{\sin^2\frac{\phi}{2}}{\sigma_x^2} + \frac{\cos^2\frac{\phi}{2}}{\sigma_z^2} \text{ and } B = \frac{\Delta x \sin\frac{\phi}{2}}{2\sigma_x^2} \tag{1.16}$$

Therefore if the luminosity produced by two beams colliding head-on is given by $\mathcal{L}_0$ then the luminosity produced by the same two beams colliding with a crossing angle ϕ and a

transverse offset in x of Δx is given by Eq. 1.17.

$$\mathcal{L} = \mathcal{L}_0 TSW \tag{1.17}$$

Another effect that needs consideration is the 'Hourglass Effect' that arises from the parabolic shape of the β function around the IP. Although it is conventional to use the value β^* for calculating beam sizes at the IP the β function actually follows a parabolic shape in z with a minimum of β^* as described in Eq. 1.18

$$\beta(z) = \beta^* + \frac{z^2}{\beta^*} \tag{1.18}$$

This means that the transverse beam size will increase with the square of the longitudinal displacement along the length of the colliding bunches which will cause a proportional reduction in the luminosity produced. However, for the bunches colliding at LHCb with lengths of $\sim$10 cm and with a value of $\beta^* = 24$ m (as used during the luminosity calibration session) this effect on the size of the luminous region is well below the per mille level and entirely negligible.

1.6 Luminosity Measurement

1.6.1 Luminosity Counters

The absolute value of the luminosity can either be determined directly, from knowledge of the beam parameters and geometries, or indirectly, from measuring the production rate of a process with a very well known cross-section. Past colliders have been able to make accurate indirect measurements of the luminosity using precise theoretical knowledge of cross-sections such as that of Bhabha scattering ($e^+e^- \to e^+e^-$) at lepton colliders, which is known to a precision of 0.05% [2]. At the LHC, however, there is no equivalent process for which such a measurement is practicable.

Instead at LHCb luminosity counters are defined based on some detector response and an effective cross-section is measured for this counter. For example, these counters could count the number of events where at least one track is reconstructed by the tracking systems or where a certain amount of energy is deposited in the detector's calorimeters. The counter cross-section is then measured precisely in a period of dedicated collisions by directly measuring the luminosity for that dataset and counting the number of events observed for that particular counter. The rate of that counter is measured for all subsequent collision data such that the luminosity can be determined precisely and consistently across the full LHCb

dataset. Further details of the definition of these counters and how their rates are measured at LHCb will be given in Sec. 4.1.

A precise direct measurement of the luminosity is then required in order to achieve a precise measurement of this effective cross-section. Two different techniques are used to achieve this at LHCb, each using a different approach to measuring the overlap integral defined in Eq. 1.5. The van der Meer scan method (vdM) is used at all four LHC experiments and measures the overlap by scanning the beams across each other in each transverse dimension and measuring interaction rates. It will be described briefly below in Sec. 1.6.2. The BGI method measures the bunch profiles by reconstructing the interactions between the protons in the circulating bunches and residual gas in the LHC beam-pipe. This technique is the main subject of this thesis and the measurement procedure and results for run 2 of the LHC will be described in detail in Chapter 2.

For the measurement of bunch intensities a range of LHC instrumentation is employed. These are described in Chapter 3 along with relevant corrections and associated uncertainties.

1.6.2 The van der Meer Scan Method

First introduced by S. van der Meer at the Intersecting Storage Rings collider at CERN the vdM method relies on the principle that the overlap can be expressed in terms of experimentally observable rates rather than the bunch density functions [3]. This method was later extended for use at bunched beam colliders [37], starting with the Super Proton-Antiproton Synchrotron, and is now the main method used by all of the LHC experiments for their luminosity determination.

Experimentally it consists of moving the colliding beams across each other in the transverse plane and measuring the rates observed at different positions (see Fig. 1.21). The observed interaction rate, R, is proportional to the instantaneous luminosity and will also depend on the two orthogonal transverse separations of the beams Δx and Δy. The average number of visible interactions per bunch crossing μ (see Eq. 1.19) can be obtained from the observed interaction rate and knowledge of the LHC revolution frequency f_{rev}.

$$\mu = \frac{R}{f_{rev}} \tag{1.19}$$

Assuming the bunch density distributions can be factorised in x and y it is only necessary to measure μ as a function of Δx (at a fixed Δy separation) and as a function of Δy (at a fixed Δx separation). In this case the overlap has the form shown in Eq. 1.20, where x_0 and y_0 are

fixed separations along each axis.

$$\mathcal{O} = \frac{\mu(\Delta x_0, \Delta y_0)}{\int \mu(\Delta x, \Delta y_0) d\Delta x \int \mu(\Delta x_0, \Delta y) d\Delta y} \tag{1.20}$$

The values of x_0 and y_0 are generally chosen such that the beams are as close as possible to head on, i.e. with no transverse displacement or crossing angle between the two beams in either axis. Experimentally this position is found by maximising the instantaneous luminosity (or the observed interaction rate). This technique relies on precise knowledge of the beam displacements Δx and Δy and thus requires an accurate calibration of the absolute length scale (LSC), this procedure can introduce corrections on the percent level. Non-reproducibilities have also been observed between repeated scans and these are assigned as a further systematic uncertainty. The other major correction to these measurements arises from the beam-beam force which can induce a change in β^* and a deflection of the beams as they are displaced. This occurs as the magnitude of the electromagnetic force of one beam acting on the other changes as the beams move relative to each other. In addition, the assumption that the x and y profiles of the beams are independent was shown not to hold to the necessary precision in run 1 [5].

The full details of these vdM measurements will not be described in this thesis, however, a full set of vdM scans was conducted in each LHCb luminosity calibration session during run 2 and the results from these measurements serve as an important cross-check on results obtained using the BGI technique.

1.7 Summary

In this introduction, a motivation for an updated BGI luminosity calibration for LHCb run 2 data has been given as well as a summary of what will be presented in the following chapters of this thesis. The LHC accelerator complex, including its injector chain and operational parameters, has been described. The LHCb experiment has also been presented with detailed descriptions given of all relevant subdetectors. The vacuum conditions at the LHC and the particularities of the LHCb setup in this respect have been described. Finally the underlying theory of luminosity at bunched beam colliders has been developed and experimental techniques widely used for its measurement presented.

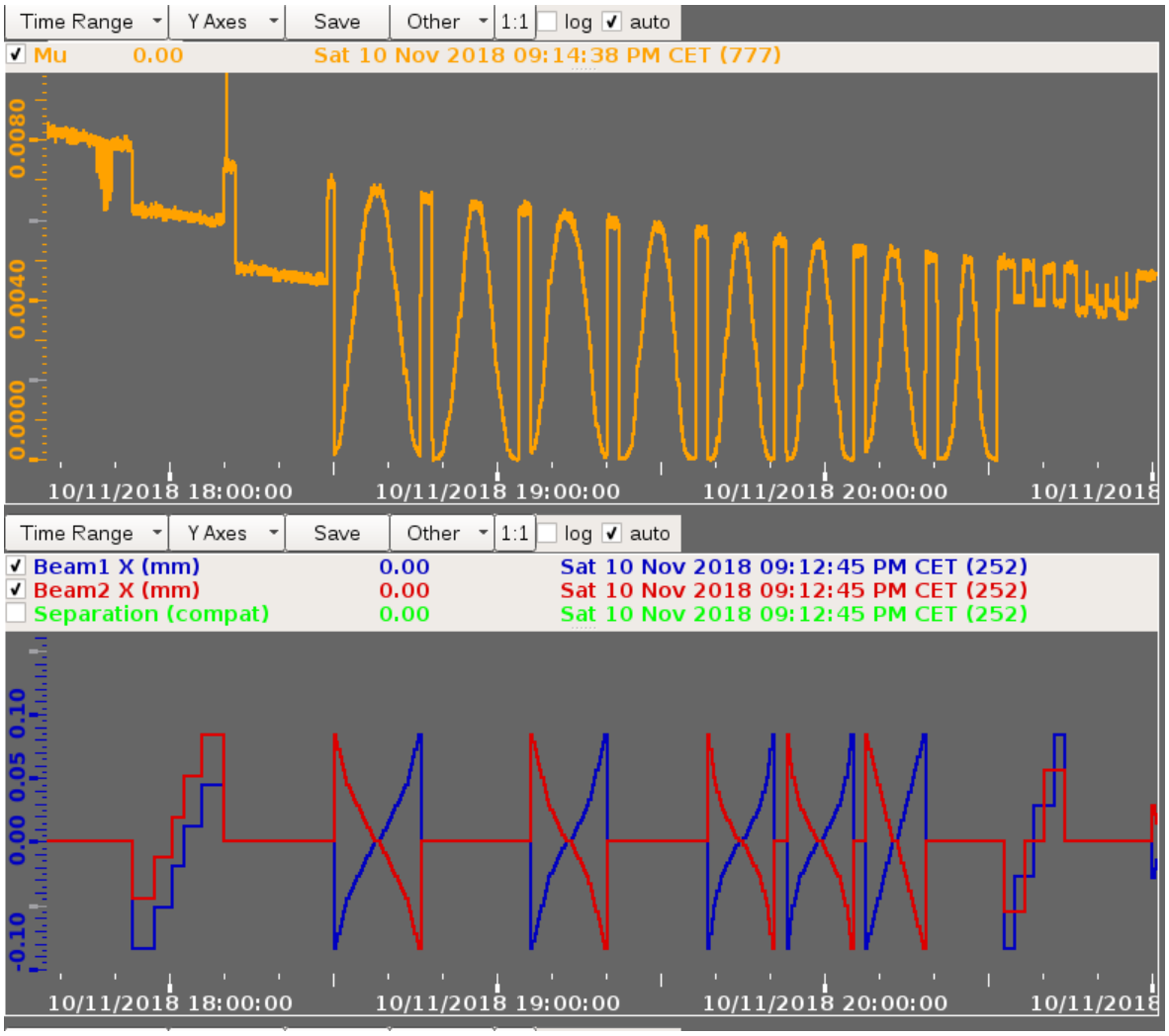

Figure 1.21: A view of the Experimental Control System [38] panel showing the changing value of the interaction rate μ (top) and the beam movement (below) during a vdM scan session that took place during LHC fill 7435 in November 2018. The beam 1 (2) displacement relative to the centre of the IP (in mm) is shown in blue (red). The interaction rate is seen to reach a maximum when the two beams have equal displacement and approaches zero as their separation increases. The online interaction rate shown in the control panel is based on the number of events triggering the L0CALO line of the level 0 trigger. This trigger line requires at least 2 hits in the SPD detector and at least 240 MeV of transverse energy to be deposited in the hadron calorimeter.

Chapter 2

Beam-Gas Imaging Measurements

2.1 Beam-Gas Imaging

The BGI technique is an alternative direct luminosity measurement technique to the vdM method presented in Chapter 1. It relies on the precise vertexing capability of the LHCb experiment and in particular its VELO subdetector. It is currently a unique capability of this experiment and has already been used with success for data taken during run 1 of the LHC. The use of this technique offers many advantages to the LHCb luminosity measurement programme. As the beams are not displaced during the measurement its systematic errors are largely uncorrelated with those of the vdM approach allowing for a more precise measurement of the luminosity, as demonstrated in run 1 of the LHC [5]. In particular the BGI approach does not require correction for beam-beam and other beam steering effects. From an operational standpoint it also allows LHCb to take data parasitically during the vdM scans of other experiments without disrupting their measurements by moving the beams at IP8.

However, the BGI measurement is affected by some factors that are unimportant for the vdM measurement. The value of the β function at the IP during a BGI measurement needs to be much larger than during nominal physics operation. This is because the BGI method relies on a precise and accurate position measurement of the reconstructed primary vertex. This measurement is made by the VELO and would be too greatly affected by the detector's spatial resolution if the colliding beams were as small as during physics production. It is also important to precisely measure the crossing angle as its effect on the luminosity produced by colliding beams can easily reach 20%. Furthermore as beam-gas interactions are measured over a significant longitudinal range it is not possible to completely exclude interactions taking place away from the IP and thus collisions of so called "satellite" bunches may be erroneously included in the BGI measurement if not properly accounted for. These are collisions between time displaced charges captured in the adjacent RF bucket to the charge

making up the filled bunch and take place at positions centred around points $\pm$37.5 cm from the IP. They can be measured using LHC instrumentation and their treatment is described in Sec. 3.2.

It is also necessary to precisely determine the fit shape required to best describe the profile of the charged particle bunches within the LHC. A simple Gaussian model has been found to be insufficient to achieve the necessary precision in the past and instead a double Gaussian shape has been preferred. It has also been necessary in the past to introduce a factorisability parameter to account for non-linear correlations in the transverse beam distributions. These issues are also relevant to the vdM analysis and results from one approach can be used to inform the other.

Thus the BGI technique is a complementary approach to the vdM method and each has its own experimental challenges that introduce systematic uncertainties that need to be understood and controlled. The uncorrelated nature of these uncertainties allows one approach to constrain the measurement of the other. In run 2 of the LHC the BGI technique also formed an integral part of the vdM luminosity measurements at LHCb as it was used to directly measure the beam positions during scans. This provided an important cross-check on the Length Scale Calibration and the beam drift measurements provided by LHC instrumentation.

2.2 Calibration Fills and Data Taking Conditions

Throughout the course of run 2 of the LHC a series of luminosity calibration sessions took place, at least one per year, with calibration measurements being conducted at each of the LHC IPs. These measurements were performed in dedicated fills with a special machine setup including a filling scheme and optical configuration designed to suit the needs of each experiment and use of the SMOG gas injection system to degrade the vacuum conditions for BGI measurements at IP8. The focusing setup was such that the transverse beta function at IP8, β^*, was always set at the larger value of 24 m (as opposed to the value of $\beta^* = 3$ m generally used during physics data taking). The vdM scans were usually conducted in the same fill for the two high luminosity experiments, ATLAS at IP1 and CMS at IP5, and in a separate fill for the two lower luminosity experiments, ALICE at IP 2 and LHCb at IP8. This separation makes optimising the filling scheme for each experiment simpler. BGI data taking generally took place at LHCb during both sets of calibration fills. During these fills LHCb was also operated in a special configuration with a dedicated set of trigger selections (described in Sec. 2.3).

A complete list of calibration fills with data currently available to be used for the BGI analysis is provided in Table 2.1. These were all used for the calibration of data from proton beam collisions at $\sqrt{s} = 13$ TeV. Further calibration sessions took place for determining the

luminosity with ion beams and at lower energies, however, in these cases the beam conditions were not suitable for a BGI measurement and only the vdM technique was used. In general the luminosity calibration analysis focuses on the fill from each year during which the LHCb van der Meer (VDM) scans took place as these contain the most colliding bunches in LHCb and making use of both methods in the same fill allows us to compare beam properties and cross-validate the two measurements. The other fills can also be analysed for a calibration using the BGI method and in order to make the ghost charge measurements used by the other experiments in their VDM analyses (see Chapter 3).

One fill from October 2016 was also analysed as part of an LHC Machine Development (MD) study focused on the cross-calibration of the various pieces of LHC instrumentation used for beam-size measurements (described in full in Chapter 5). This fill contained bunches with a large range of different emittances and is therefore also of special interest for the study of resolution effects as the importance of the resolution varies with beam size.

Period	Fill	β^*	Beam 1 (2) bunches	Colliding in LHCb	Remarks
Jun 2015	3850	24 m	39 (39)	15	Early Measurements
Aug 2015	4266	24 m	44 (44)	6	VDM for ATLAS, CMS
Aug 2015	4269	24 m	51 (51)	16	VDM for LHCb, ALICE, CMS, ATLAS
May 2016	4937	24 m	55 (51)	16	VDM for LHCb, ALICE, CMS, ATLAS, FBCT Problems
May 2016	4945	24 m	56 (52)	8	VDM for CMS, ATLAS
May 2016	4954	24 m	56 (52)	8	VDM for CMS
Oct 2016	5456	24 m	10 (10)	6	Emittance MD
Jul 2017	6012	24 m	57 (56)	24	VDM for LHCb, ALICE, Emittance Instabilities in LHCb bunches
Jul 2017	6016	24 m	52 (52)	8	VDM for CMS, ATLAS, LHCb DAQ issues
Jun 2018	6864	24 m	70 (70)	22	VDM for LHCb, ALICE
Jun 2018	6868	24 m	140 (128)	19	VDM for CMS, ATLAS

Table 2.1: Conditions during $\sqrt{s}$ = 13 TeV $p-p$ calibration fills used for the BGI analysis.

The gas species used for the SMOG injection varied over the course of run 2. Neon gas is preferred for the purposes of the BGI measurement as its larger atomic mass means the resultant beam-gas interactions have a higher track multiplicity and this in turn leads to a better vertex position resolution. However, helium gas was also injected in some years primarily so that data taking for fixed target cosmic ray studies could take place concurrently with the calibration measurement [39]. Fills throughout 2015 and 2017 made use of neon gas injection

while fills in 2016 and 2018 made use of helium. The peak SMOG pressure at IP8 for each fill, recorded via a Penning gauge, can be seen in Fig. 2.1 below. This gauge has a different sensitivity for gases other than air and the raw readings must be multiplied by a correction factor of 4.1 for neon and 5.9 for helium [40]. All of the pressure values presented below are those after this correction has been applied. In some fills the gas injection took place multiple times with gas being pumped out part way through the fill to avoid excessive background from beam-gas interactions during the concurrent vdM scan programme. Examples of the pressure profile throughout two different calibration fills can be seen in Fig. 2.2.

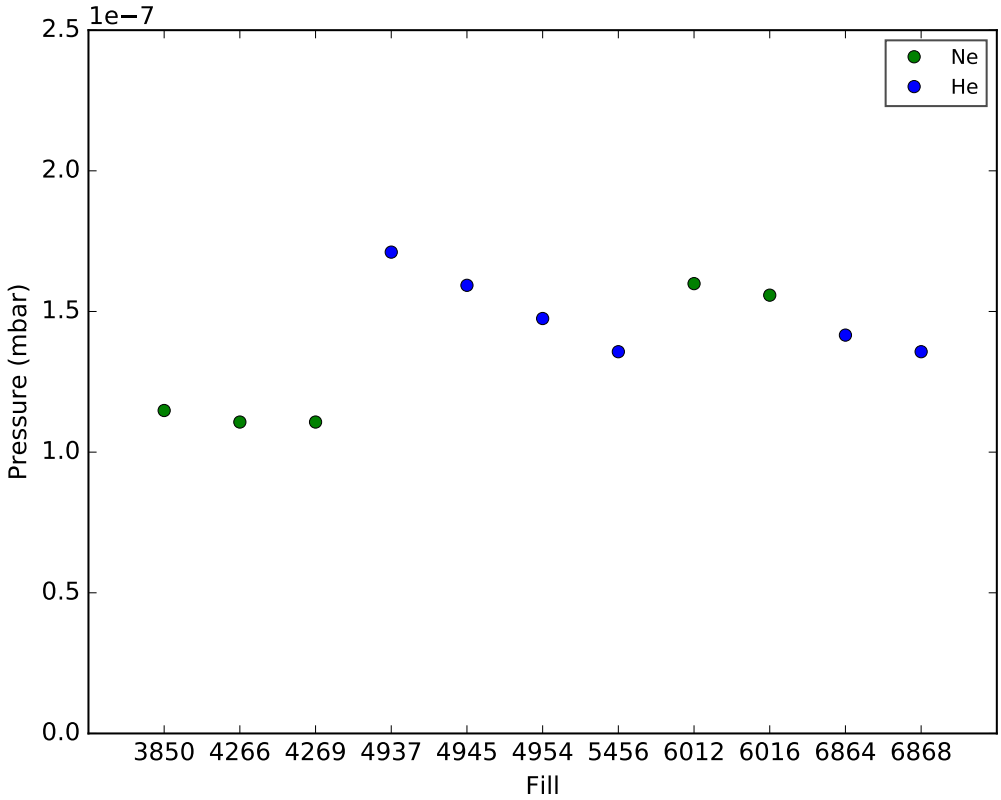

Figure 2.1: The peak pressure inside the beam pipe at IP8 throughout the gas injection period for each fill in Table 2.1 as recorded by the Penning gauge PE412 (see Fig. 1.18). The green points are those fills where neon gas was injected and the blue are those where helium was used. All values have been corrected for the sensitivity of the gauge to the relevant gas species. The peak pressure can be seen to decline slowly throughout each year as the gas bottle used as the source for the SMOG system is drained.

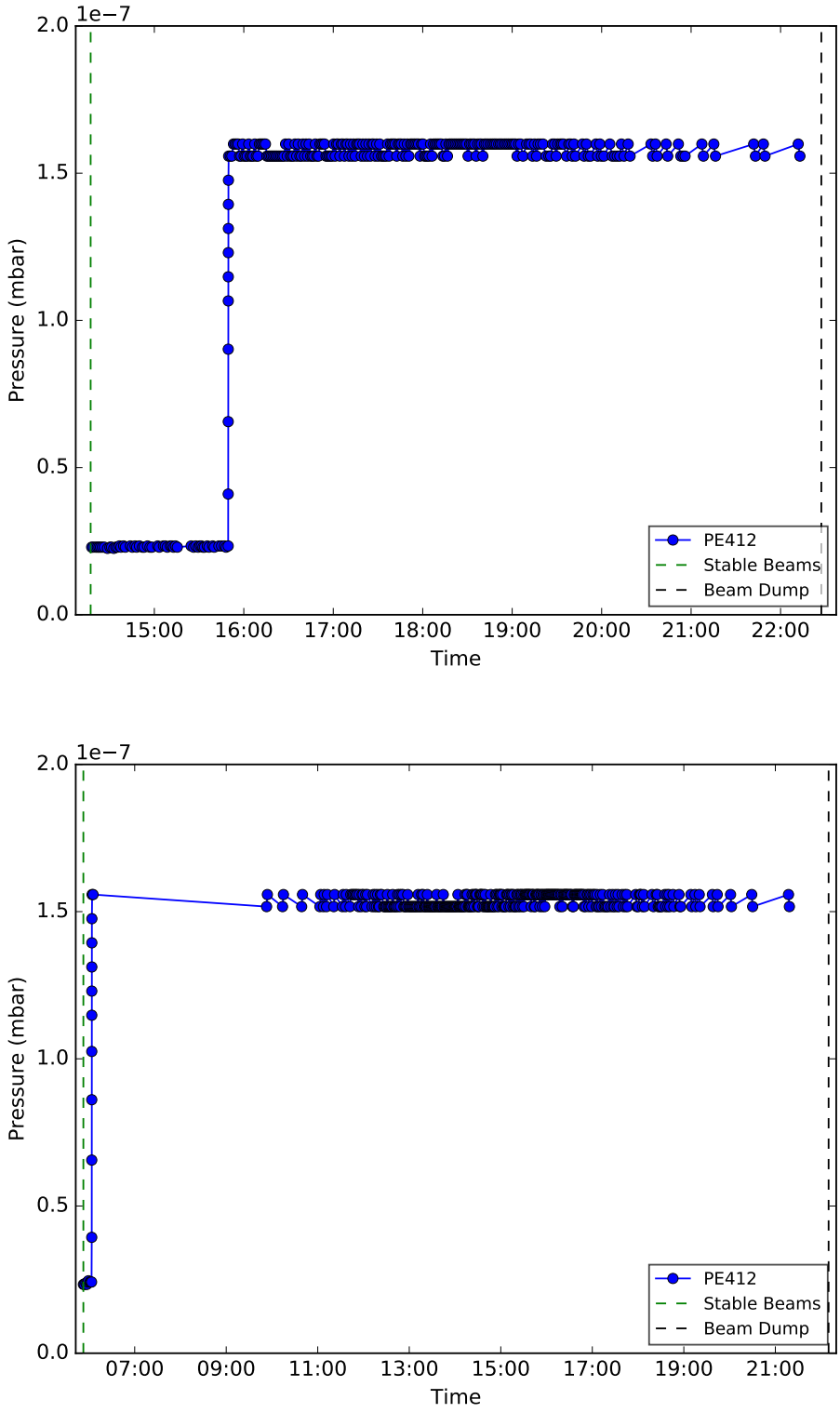

Figure 2.2: The corrected pressure values measured by the penning gauge PE412 located at IP8 during fills 6012 (top) and 6016 (bottom). Fill 6012 began with the LHCb vdM scans and so no gas was injected for the first $\sim$1.5 hours. During fill 6016, however, no scans took place at IP8 and thus the neon gas injection started shortly after the declaration of stable beams.

2.3 Trigger Configuration

As luminosity calibration measurements are performed in dedicated fills without the constraints of normal proton-proton physics data taking it is possible to optimise the trigger configuration specifically for the reconstruction and acquisition of beam-gas interactions. Throughout run 2 the LHCb trigger was operated with both a hardware and two software stages as described in Sec. 2.3. The relevant L0 trigger channels and their associated conditions are shown in Table 2.2. The selection conditions for this stage of selection were simplified in run 2. The subdetector activity thresholds were reduced with respect to run 1 and veto conditions were removed. There were also just two channels used: one for beam1-gas and another for beam2-gas. This change was made under the assumption that any beam-beam interactions will trigger at least one of these two channels.

The software selections were made in the first stage of the new High Level Trigger (HLT1) and were based on the bunch crossing types (as defined in Sec. 1.3.5), reconstructed vertex positions and vertex track multiplicities. The relevant software trigger lines and their associated selection requirements are shown in Table 2.3. The lines *BeamGasBeam1 (2)* were set to trigger beam-gas events in be and eb crossings respectively. In bb and ee crossings beam-gas vertices were selected by the lines *BeamGasNoBeam* and *BeamGasCrossingForcedReco*. Beam-beam interaction vertices were selected by the lines *BeamGasCrossingForcedRecoFullZ* and *BeamGasCrossingFullZLowNTracks*. The latter of these was only implemented for data collected after 2017 and was used to collect lower multiplicity beam-beam vertices to allow the effect of the increased multiplicity threshold to be assessed.

As in the latter part of run 1 the HLT selections were made without reference to the specific hardware trigger channel associated with the event, with each HLT line accepting events from both the L0B1gas and L0B2gas channels. The selections at this stage were also simplified with each line accepting events within the full z range except for the selection of beam gas events in bb crossing which applies a veto on the luminous region in the range $-250\text{ mm} < z < 250\text{ mm}$. An additional important change to the selection conditions in run 2 with respect to run 1 was an increase in the vertex track multiplicity threshold for beam-beam interactions in bb type crossings. This was made possible by the increase in beam energy to 6.5 TeV leading to an increase in the average vertex multiplicity and was advantageous as the primary vertex position resolution of the VELO increases with the multiplicity of the reconstructed vertex. This also allowed the prescale filter on beam-beam interactions that was present in run 1 to be removed. In some later fills a slightly altered trigger setup was used and a prescaled sample of vertices with a lower multiplicity was included in order to check that their exclusion was not producing a bias in the fitted bunch profile. Another important change for run 2 was that the vertex splitting process described in Sec. 2.5 was performed as part of the online reconstruction performed within the software trigger. This change allowed the

split vertices used for the BGI analysis to be stored along with the primary vertex from which they originate in an HLT record and eliminates the need for a separate offline reconstruction.

During these dedicated calibration fills we are able to trigger on vertices originating from both non-colliding and nominally empty bunches. In the overlap integral that is used for the BGI calibration measurement only vertices from colliding bunches are included as these are the only bunches that will produce luminosity. However, the measurement of the beam crossing angles makes use of vertices from both colliding and non-colliding bunches as this allows a much larger number of vertices to be acquired at the longitudinal extremities of the VELO. Beam-gas interaction vertices acquired in both non-colliding and nominally empty bunches are also useful for the ghost charge measurement that is part of producing an accurate description of the bunch intensities (described in further detail in Sec. 3.2).

Channels (15-16)	Logical operation	$\sum E_T$	N_{PU}	N_{SPD}
B1gas	-	-	-	>2 Hits
B2gas	-	-	>9 Hits	-

Channels (17-18)	Logical operation	$\sum E_T$	N_{PU}	N_{SPD}
B1gas	AND	>240 MeV	-	>30 Hits
B2gas	-	-	>6 Hits	-

Table 2.2: Hardware trigger (L0) channels used for the BGI analysis and their thresholds. The table above shows the channels in use in 2015-16 and the table below shows the channels for 2017-18. $\sum E_T$ is the total transverse energy deposited in the LHCb calorimeters, N_{PU} is the number of hits recorded in the pile-up sensors located at the rear of the VELO and N_{SPD} is the number of hits in the Scintillating Pad Detectors located just upstream of the LHCb magnet. In 2017 the requirements were optimised to remove spill-over (triggers in adjacent slots) for B1gas and to improve efficiency for B2gas.

Trigger Line	Prescale	Crossing Type	Longitudinal Position (mm)	Track Multiplicity
BeamGasNoBeam	1	ee	[-2000, 2000]	>9
BeamGasBeam1	1	be	[-2000, 2000]	>9
BeamGasBeam2	1	eb	[-2000, 2000]	>9
BeamGasCrossingForcedReco	1	bb	[-2000, 250] ∪[250, 2000]	>9
BeamGasCrossingFullZLowNTracks	0.25	bb	[-2000, 2000]	>9
BeamGasCrossingForcedRecoFullZ	1	bb	[-2000, 2000]	>27

Table 2.3: Software trigger (HLT1) lines used for the BGI analysis and their selection requirements. All lines also impose a constraint of $x^2 + y^2 < 4$ mm on the radial transverse vertex position and accept events from either of the beam-gas L0 channels (B1gas OR B2gas).

2.4 Event Selection

The events acquired by the LHCb trigger are reconstructed using the standard set of LHCb reconstruction algorithms within the software component of the trigger and then saved to disk ready for analysis. Each vertex has an associated track multiplicity, N_{tracks}, and each track associated with a vertex is assigned a forward or backward directionality relative to direction of travel of beam 1. Thus each vertex has an associated number of forward tracks, N_{fwd}, and backward tracks, N_{bwd}. Forward tracks are defined such that they travel downstream (towards the LHCb spectrometer) and backward tracks such that they travel upstream (away from the LHCb spectrometer) as shown in Fig. 2.3.

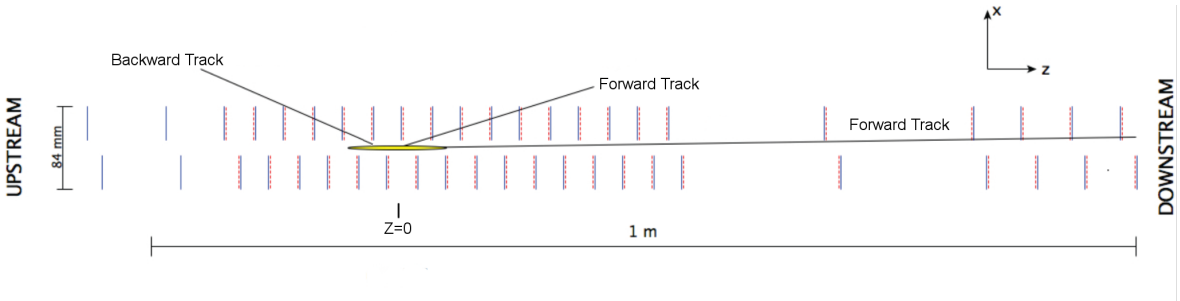

Figure 2.3: The two track directionalities defined as part of the BGI analysis shown on a schematic view of the VELO subdetector. The forward tracks travel in the downstream direction with respect to the LHCb magnet and the backward tracks travel in the upstream direction.

The acceptance for forward tracks falls off to zero at a longitudinal position of approximately $z = 600$ mm. Backward tracks are reconstructed using only VELO information and

their acceptance approaches zero for longitudinal positions of less than z =-100 mm. The longitudinal vertex distribution before further selection is shown for all bunch crossing types in Fig. 2.4. The acceptance limits for each track directionality can be clearly seen as a sharp drop in the number of reconstructed vertices from both be and eb crossings. A large peak is clearly visible in the luminous region for bb crossings due to the large number of beam-beam interactions while there is a sharp drop in the number of selected beam-gas vertices in these crossings at $z = -250$ mm and $z = 250$ mm due to the veto in the *BeamGasCrossingForcedReco* trigger line. The longitudinal distribution of vertices from non-colliding bunches is shown in two dimensions in Fig. 2.5 and for both colliding and non-colliding bunches in three dimensions in Fig. 2.6.

An unambiguous discrimination between beam-gas and beam-beam interaction vertices is an essential part of the BGI analysis as this permits independent measurements of the single beam and luminous region profiles for each beam. This is achieved by selection according to the following criteria:

- The radial position of a selected vertex is required to be within 2 mm of the beam axis ($\sqrt{x^2 + y^2} < 2$ mm) to exclude so-called material interactions between the beam protons and the detector material (most notably the VELO RF foil).
- The vertex longitudinal position must fall within the range $-1000 \leq z \leq 500$ mm for beam1-gas interactions and $0 \leq z \leq 1000$ mm for beam2-gas interactions.
- No beam-gas vertices are accepted in bb crossings within the longitudinal range $-250 < z < 250$ mm as they cannot be reliably differentiated from beam-beam interactions.
- A selected beam-gas vertex must have a multiplicity of at least 10 tracks and a selected beam-beam vertex must have a multiplicity of at least 28 tracks: $N_{tracks,bg} \geq 10$, $N_{tracks,bb} \geq 28$.
- A forward/backward track asymmetry check is then used to separate beam1-gas vertices from beam2-gas vertices where their longitudinal selection regions and acceptances overlap: $-100 \leq z \leq 600$ mm. In this overlap region beam1-gas vertices are required to have zero backward tracks: $N_{bwd} = 0$ and beam2-gas vertices are required to have zero forward tracks: $N_{fwd} = 0$.

These selection criteria are largely unchanged from those used in the run 1 BGI calibration measurement [5], with the exception of the higher track multiplicity cut imposed on beam-beam vertices introduced due to the increased collision energy in run 2 of $\sqrt{s} = 13$ TeV.

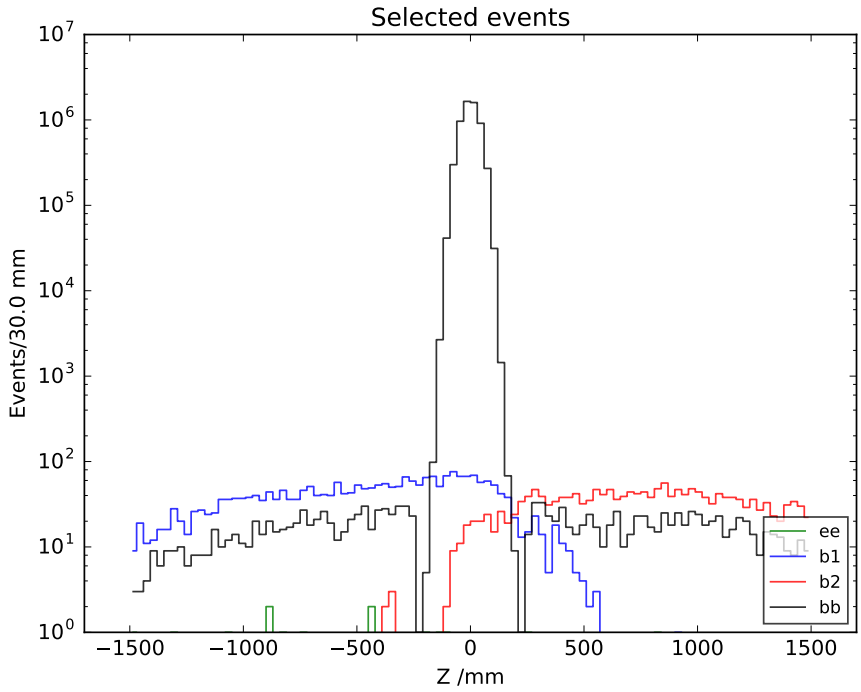

Figure 2.4: The distribution of selected vertex z positions by bunch crossing type during run 174612 of fill 4937 on a log scale and in bins of 30 mm. For the vertices selected in bb crossings the large central peak is made up of beam-beam interactions while the vertices with longitudinal positions of $|z| > 250$ mm are identified as beam-gas vertices.

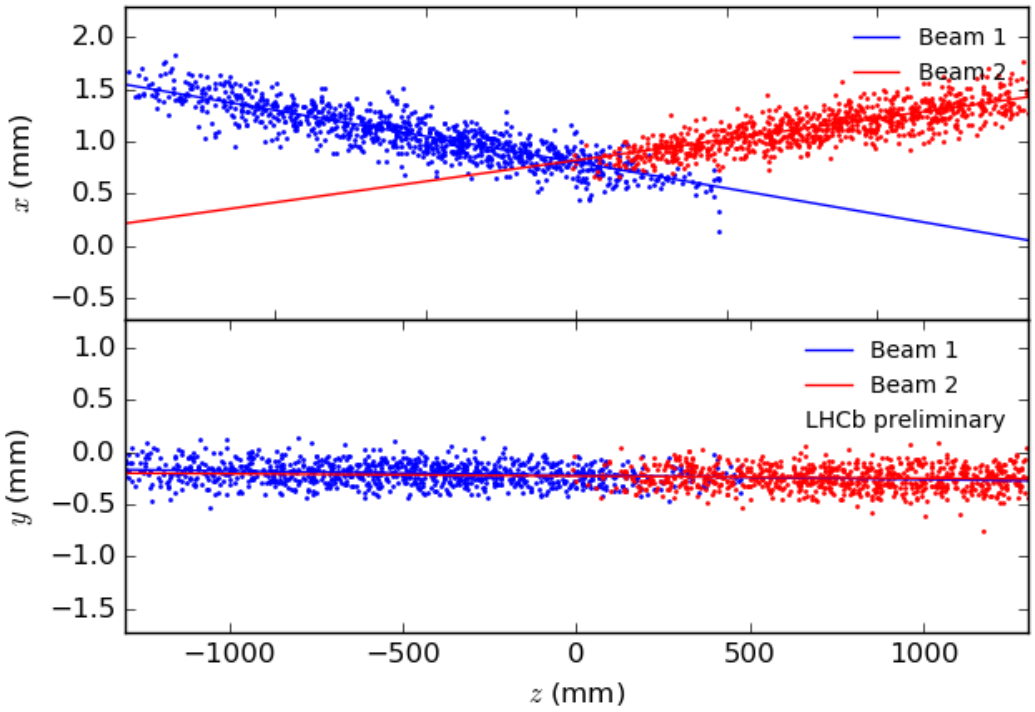

Figure 2.5: A two-dimensional view of the selected vertices from run 174625 of fill 4937. Beam 1 vertices are shown in blue and beam 2 in red. The lines are a linear fit of the individual beam slopes and the crossing angle between beams in x is clearly visible.

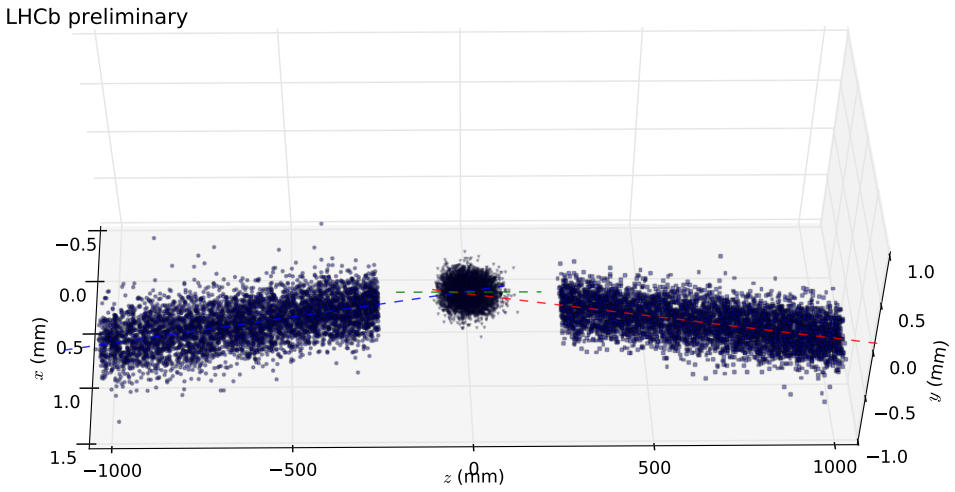

Figure 2.6: A three-dimensional view of the selected vertices from all colliding bunch pairs in run 174625 of fill 4937. Beam-gas vertices are shown in blue and beam-beam in black. The red dotted lines are a fit of the individual beam slopes and the crossing angle between beams is clearly visible. The empty areas between the beam spot and the single beam distributions are due to the veto on beam-gas vertices in the region $-250 < z < 250$ mm that is enforced at trigger level in order to clearly distinguish beam-gas from beam-beam interactions.

2.5 Vertex Resolution Determination

Useful beam profile measurements can only be achieved by making an accurate measurement of beam-gas and beam-beam vertex positions. The determination of the vertex position resolution is essential for achieving this as the observed beam profile is the convolution of the true beam profile with the detector resolution. The resolution used for the BGI analysis is defined as the standard deviation of the distance from the true vertex position and its measured position. Thus a smaller resolution implies a more accurate vertex position measurement. However, as we cannot know the true position of the vertex we cannot directly measure the resolution using this approach. Instead we measure the residual distance between two vertices originating from the same collision. This is done by reconstructing what are known as "split" vertices. These are created by randomly splitting up the tracks making up a "primary" vertex into two groups and then reconstructing two new vertices from each group of tracks. The resolution is then determined from the residual distance between these two split vertices. This is achieved by fitting the distribution of these residuals with a Gaussian function (as shown in Fig. 2.7) and assigning the width of this distribution as the resolution.

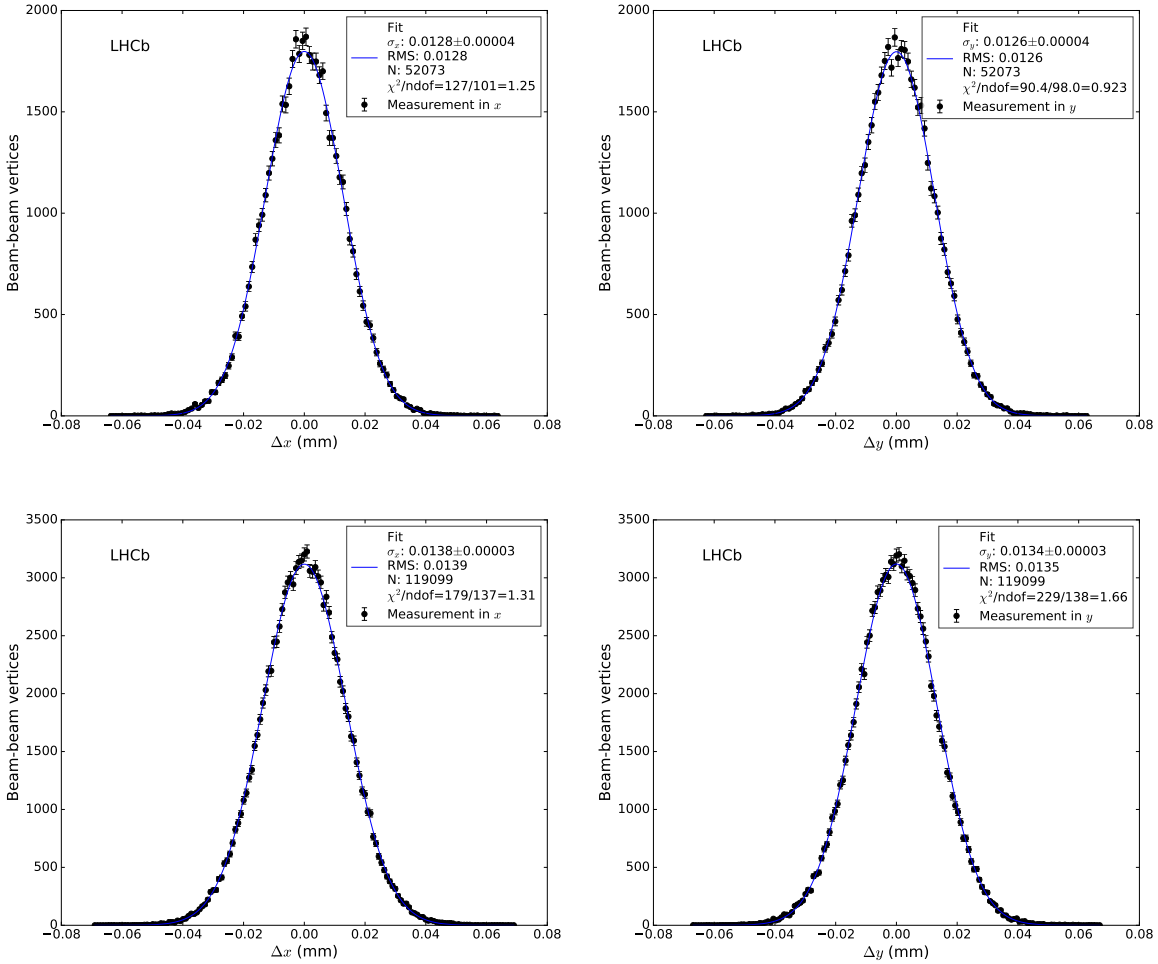

Figure 2.7: A Gaussian fit to the residuals on the x (left) and y (right) axes for all pairs of split beam-beam vertices with the given track multiplicities from fill 4937. The fit at 57 tracks per vertex is shown above and at 50 tracks per vertex below. For the final measurement these fits are performed along each axis for all possible multiplicity combinations as explained in Sec. 2.5.2. The value σ_x is the standard deviation of the fitted Gaussian, the RMS is the root mean square of the data points and N is the total number of vertices included in the plot.

This resolution function is determined from data separately for the beam-beam and beam-gas vertices and thus two separate uncertainties are assigned for each. Its value also depends on the track multiplicity of the vertex being reconstructed as well as its spatial position. Various correction factors to the resolution are also determined with the longitudinal variation of the resolution of particular importance due to the asymmetric geometry of the VELO and the longitudinal variation in acceptance for different track directionalities. The measurement of the resolution is not statistically limited.

2.5.1 Resolution Unfolding

As the measured vertex distribution is the convolution of the true beam distribution with the detector resolution it is necessary to unfold these two components in order to produce an accurate measurement of the physical beam shapes. The transverse resolution can be described by an effective resolution function $\mathcal{R}(m)$ per coordinate, with coordinates $m = x, y$. In this case each measured vertex will have an associated resolution that is determined by vertex properties such as the vertex type, position and track multiplicity. The resolution function for a sample of vertices is typically non-Gaussian but can be described, as in Eq. 2.1 as the sum of a number, K, of Gaussian functions, g_k, of width $\sigma_{res,k}$ with weights, w_k.

$$\mathcal{R}(m) = \sum_{k=1}^{K} w_k g_k(m; \sigma_{res,k}) \tag{2.1}$$

The weights are determined by the proportion of measured vertices that have a resolution within a range with average value $\sigma_{res,k}$ and are defined such that $\sum^{K} w_k = 1$. If we define $\rho(m)$ as the physical beam distribution and $M(m)$ as the measured beam distribution we can then write the convolution as in Eq. 2.2.

$$M(m) = \int_{-\infty}^{\infty} \sum_{k=1}^{K} w_k g_k(\tau) \rho(m - \tau) d\tau \tag{2.2}$$

If we then assume that the physical beam distribution for a given beam can be described by a Gaussian function, $\rho(m, \mu_{phys,m}, \sigma_{phys,m})$, with its centre at $\mu_{phys,m}$ and with a width of $\sigma_{phys,m}$, we can then make use of the fact that the convolution of a Gaussian distribution with another Gaussian distribution, $f * g$, is itself a Gaussian distribution with a width given by $\sigma_{f*g} = \sqrt{\sigma_f^2 + \sigma_g^2}$. This allows us to express the measured vertex distribution in the form given in Eq. 2.3:

$$M(m) = \sum_{k=1}^{K} w_k \rho(m; \mu_m, \sigma^*_{m,k}) \tag{2.3}$$

where $\sigma^*_{m,k} = \sqrt{\sigma^2_{res,k} + \sigma^2_{phys,m}}$ and the values of $\sigma_{res,k}$ are determined by the track multiplicity and longitudinal position of the vertex.

This same analytical approach to the resolution deconvolution is also valid when the physical beam distribution is described by a sum of Gaussian distributions rather than a single Gaussian function as above.

2.5.2 Beam-beam Resolution

The beam-beam vertices used for the resolution analysis are selected according to the same criteria as those described in Sec. 2.4. Examples of the distributions of both longitudinal positions and track multiplicities for selected beam-beam vertices are shown in Fig. 2.8 and are taken from the 2016 luminosity calibration fill no. 4937.

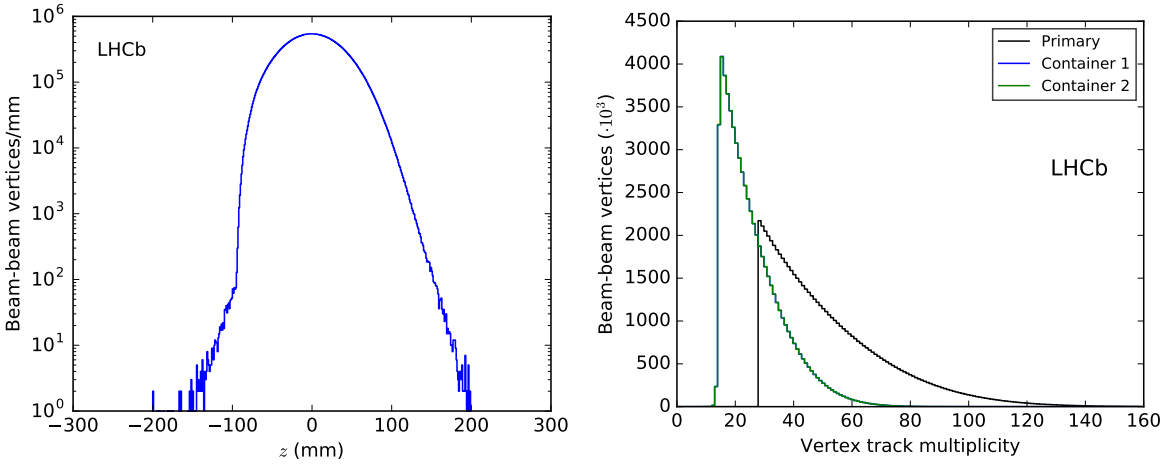

Figure 2.8: Selected beam-beam vertices used for the resolution analysis in fill 4937. On the left is shown the distribution of longitudinal positions for the selected primary vertices. The requirement for at least two forward and two backward tracks causes the steep drop at $z = -100$ mm as the VELO acceptance for backward tracks falls away sharply here. On the right is the distribution of track multiplicity for the selected primary and split vertices. The sharp cut-off for primary vertices at 28 tracks is part of the selection criteria described in Sec. 2.4.

As described in Sec. 2.5 the resolution analysis is conducted using the split vertex approach and therefore does not directly use the primary reconstructed vertex positions. Instead the tracks associated with this vertex are divided up into two sets of similar or equal size and the tracks in each of the sets are used to reconstruct a new vertex as if these tracks originated from two distinct events. If only one of these reconstruction attempts is successful the other split vertex and the associated primary vertex are not used for the analysis. In order to avoid a bias to the left or right sides of the VELO subdetector (which is constructed in two interlocking halves, see Sec. 1.3.1) the vertex splitting is done in two stages. The tracks from the primary vertex are first split according to which VELO half they passed through (left or right) and then these two sets are split randomly again. Two of each of these four sub-groups (one from each half) are then recombined and used to reconstruct each of the split vertices such that these have approximately half the track multiplicity of the primary vertex and approximately the same ratio of tracks from each detector half. The track multiplicity can vary by a small number of tracks ($\lessapprox$4 tracks) between split vertices as the original vertex may contain an odd

number of tracks (which cannot be split exactly evenly) and there is a chance of some tracks being lost in the refitting of the split vertices if they negatively affect the fit quality.

The distance, Δv, between the two split vertices with positions v_1 and v_2 can be written as in Eq. 2.4.

$$\Delta v = v_1 - v_2 \tag{2.4}$$

If these residuals are distributed following a Gaussian distribution the width of this distribution, $\sigma_{\Delta v}$ is a convolution of each individual vertex resolution, $\sigma_{v1,2}$, and therefore depends only on the number of tracks in each split vertex, $N_{Tr,1,2}$ as in Eq. 2.5. This equation will hold even in the case where $N_{Tr,1} \neq N_{Tr,2}$.

$$\sigma_{\Delta v} = \sqrt{\sigma_{v1}^2(N_{Tr,1}) + \sigma_{v1}^2(N_{Tr,2})} \tag{2.5}$$

The variation of the beam-beam resolution with the vertex track multiplicity, N_{Tr}, is measured over the full length of the luminous region. However, due to the asymmetric geometry of the VELO leading to asymmetric acceptance of forward and backward tracks there is also some dependence of the beam-beam resolution on the longitudinal position of the reconstructed vertex, even within the luminous region. These effects and the corrections made for them are described in Sec. 2.5.2.

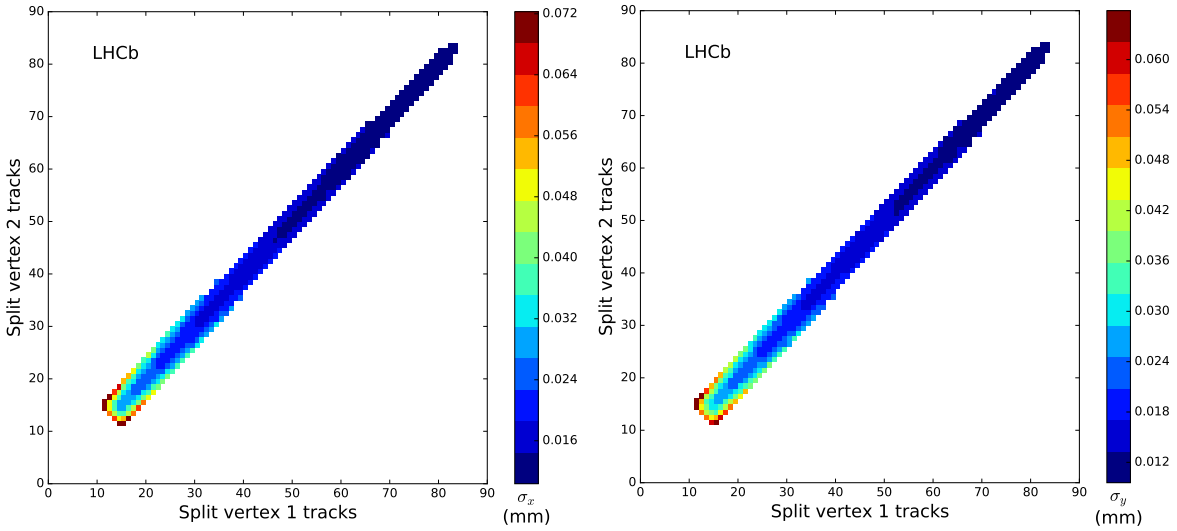

Figure 2.9: These two plots illustrate the beam-beam resolution variation across the split vertices from fill 4937. The measured resolution for split vertex pairs of the given track multiplicities is shown with a colour code. The results for x are given on the left and the results for y on the right. The width of the band is due to the variation in track multiplicity between split vertices.

The measured distances between split vertices, Δv, are assigned to bins according to the track multiplicity of each constituent split vertex ($N_{Tr,1}$, $N_{Tr,1}$). A Gaussian function is then

fitted to the combined values of Δv in each bin and the width of this fit is calculated. An example of the results of such a measurement across all split vertex multiplicity combinations is shown in Fig. 2.9 for fill 4937. Each colour coded point in the left-hand plot is the result of a fit similar to that shown in the right-hand plot.

The resolution for a split vertex with a given track multiplicity $\sigma_{res}(N_{Tr})$ can then be determined from a simultaneous least squares fit across all the fitted widths, $\sigma_{\Delta v}$ for each multiplicity combination. The χ^2 of this fit is given by Eq. 2.6 with the fit parameters $\sigma^2_{res_{vi}}(N_{Tr,vi})$ (i = 1,2) being the resolution of each split vertex for a given number of tracks and the value $\delta_{\sigma_{\Delta v}}$ being the uncertainty from the fit to the residuals.

$$\chi^2 = \frac{\left[\sqrt{\sigma^2_{res_{v1}}(N_{Tr,v1}) + \sigma^2_{res_{v2}}(N_{Tr,v2})} - \sigma_{\Delta v}\right]^2}{\delta^2_{\sigma_{\Delta v}}} \tag{2.6}$$

As the number of reconstructed split vertices with a multiplicity larger than 60 falls away very quickly to zero, see Fig. 2.8 (right), the resolution of these vertices is calculated via the parametrisation shown in Eq. 2.7. The parameters A, B and C are determined from a fit to all measured σ_{res} values at lower multiplicities.

$$\sigma_{res}(N_{Tr}) = \frac{A}{N^B_{Tr}} + C \tag{2.7}$$

The results of this parametrisation are shown in Fig. 2.10 (top) for a fill from the 2016 luminosity calibration session and the residuals between the direct measurements and the parameterisation can be seen in Figs. 2.10 (bottom) and 2.11. The direct measurements and the fit are in good agreement with no systematic bias in the measurements and statistical fluctuations are only significant at higher vertex track multiplicities where the number of available vertices drops below that required for a good Gaussian fit. The values of these resolution parameters are given for relevant run 2 fills in Table 2.4 below.

Fill	A_x (mm)	B_x	C_x (mm)	A_y (mm)	B_y	C_y (mm)
4269	0.121	0.694	0.002	0.112	0.688	0.002
4937	0.128	0.723	0.002	0.117	0.701	0.002
5456	0.131	0.724	0.003	0.120	0.704	0.002
6012	0.127	0.714	0.002	0.116	0.695	0.002
6864	0.129	0.722	0.002	0.129	0.726	0.002

Table 2.4: Results of the beam-beam resolution parameterisation given in Eq. 2.7 for run 2 LHCb luminosity calibration fills. The statistical uncertainty on these values is negligible.

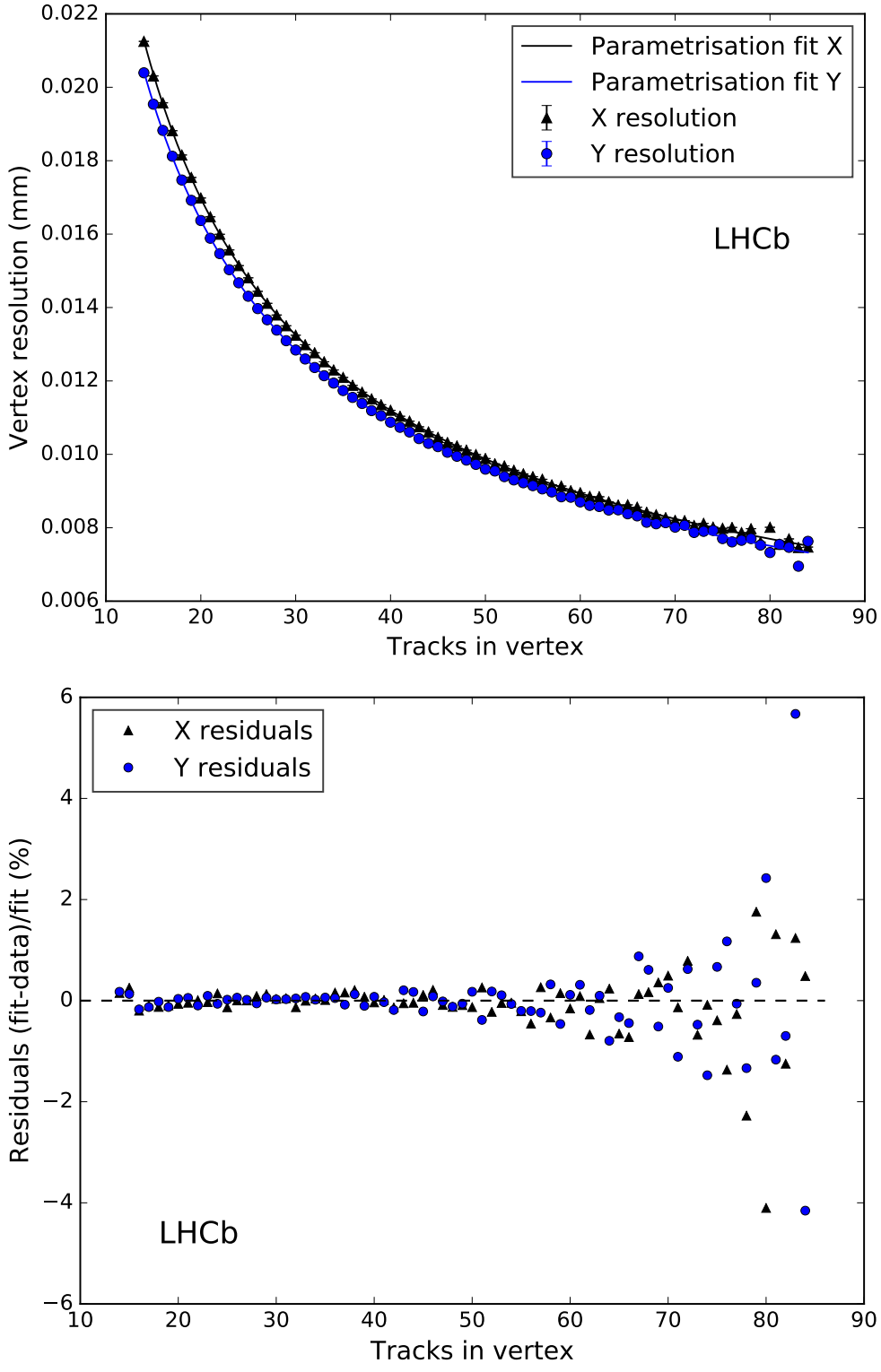

Figure 2.10: The results of the beam-beam resolution measurement as a function of track multiplicity for fill 4937. In the plot above the directly measured values are shown as points with their errors and the result of the parameterisation fit is shown as a line. The plot below confirms that both methods are in agreement, with the direct measurements starting to fluctuate beyond 1% of the fit result for vertex track multiplicities > 60 as the sample size of the measurement decreases.

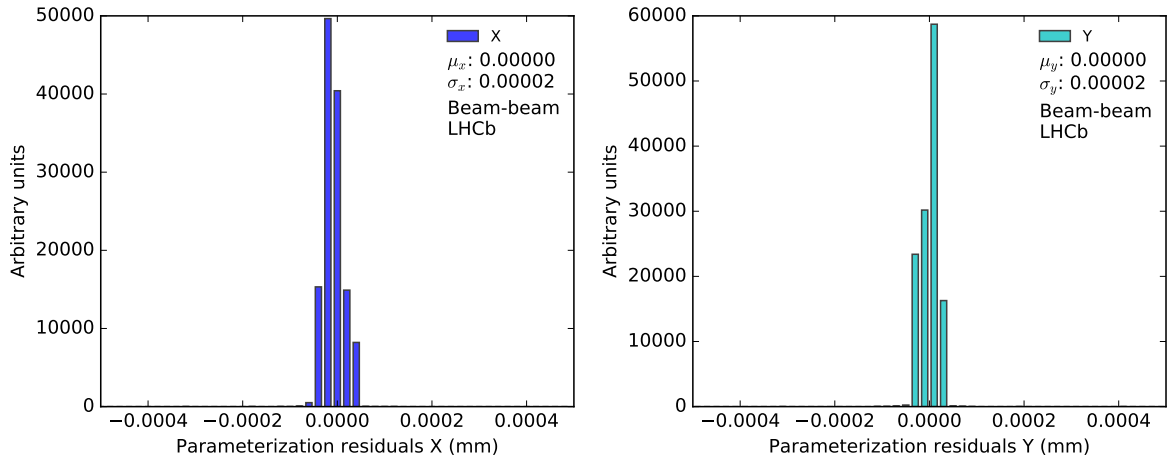

Figure 2.11: These two plots show the weighted residuals between the direct measurement of the beam-beam resolution in fill 4937 and the value from the parameterisation described above. The weighting is according to the distribution of track multiplicity shown in Fig. 2.8. The results for x are shown on the left and for y on the right. The values μ and σ for each axis are the mean and standard deviation of the distribution of residuals for that axis.

Corrections for longitudinal position dependence

Despite the small size of the beam spot the resolution is not constant for beam-beam interactions as a function of z and this longitudinal variation must be determined and accounted for in order to produce an accurate BGI measurement. This is achieved by the introduction of a correction factor, F_z, that is a function of the vertex z-position [7]. The correction factor F_z is given by the width of the distribution of ratios, ΔF, between the distance between two split vertices and their convolved resolutions at a given z-position. This ratio is defined in Eq. 2.8.

$$\Delta F = \frac{v_1 - v_2}{\sqrt{\sigma_{v1}^2(N_{Tr,1}) + \sigma_{v2}^2(N_{Tr,2})}} \tag{2.8}$$

The value of v here indicates the transverse axis x, y that is being considered and the indices $1, 2$ denote the two split vertices generated from a given primary vertex. The correction factor applied to the resolution, F_z, is the measured width of the distribution of ΔF for a given resolution parametrisation: $F_z = \sigma_{\Delta F}$. The correction is evaluated from the split vertices used for the resolution measurement with their ΔF values being binned in z bins of 20 mm across the luminous region and fitted with a Gaussian function in order to determine F_z.

The magnitude of these factors do not exceed a 4% correction with F_z values ranging from 0.98 to 1.04 for run 2 data. An example of the correction factors over the whole luminous region is shown in Fig. 2.12 for fill 4937.

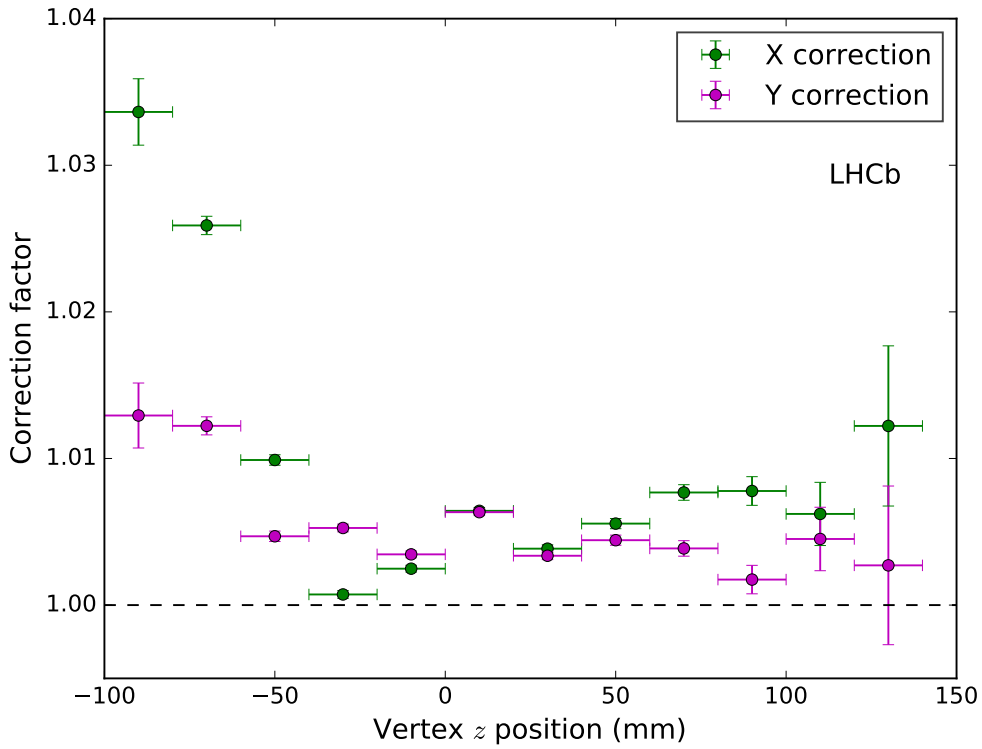

Figure 2.12: The F_z corrections to the transverse beam-beam vertex resolution over the longitudinal range of the luminous region for LHC fill no. 4937.

2.5.3 Beam-gas Resolution

The beam-gas vertex resolution is measured directly for both beams independently and separately in each fill. The principle of the measurement is similar to that in the case of beam-beam vertices described above. The principal differences are in the selection criteria used for the vertices and in the much stronger longitudinal dependence, due to the significant size of the VELO acceptance relative to the luminous region.

The beam-gas vertices used for the resolution measurement are selected according to the same criteria described in Sec. 2.4. The only exception is that in addition to making use of beam-gas events from colliding bunch pairs (bb crossings) vertices are also included from non-colliding (be and eb) crossings. As well as improving the statistical precision in outer areas of the VELO the increased number of vertices available allows a measurement of the beam-gas resolution down to z = 0 without pollution from the large number of beam-beam interactions at the collision point. Vertices in be and eb crossing types are assigned to beam 1 and beam 2 respectively.

As a result of the longitudinal variation of the beam-gas resolution, measurements of this resolution are performed separately in different sets of z bins for each of the two beams. For beam 1 the ranges [-1200, -800], [-800, -500], [-500, -250], [-250, 0] and [0, 250] mm are chosen and for beam 2 measurements are made in the ranges [0, 250], [250, 500], [500, 800] and [800, 1200] mm. The number and size of the bins is determined by the available number of events in each range and is more limited for beam 2 due to the asymmetric longitudinal acceptance of the VELO. Results are shown for these measurements in Fig. 2.13 for both beam 1 (above) and beam 2 (below) and the resolution fit parameters for each axis in each longitudinal bin are given in table 2.5 below.

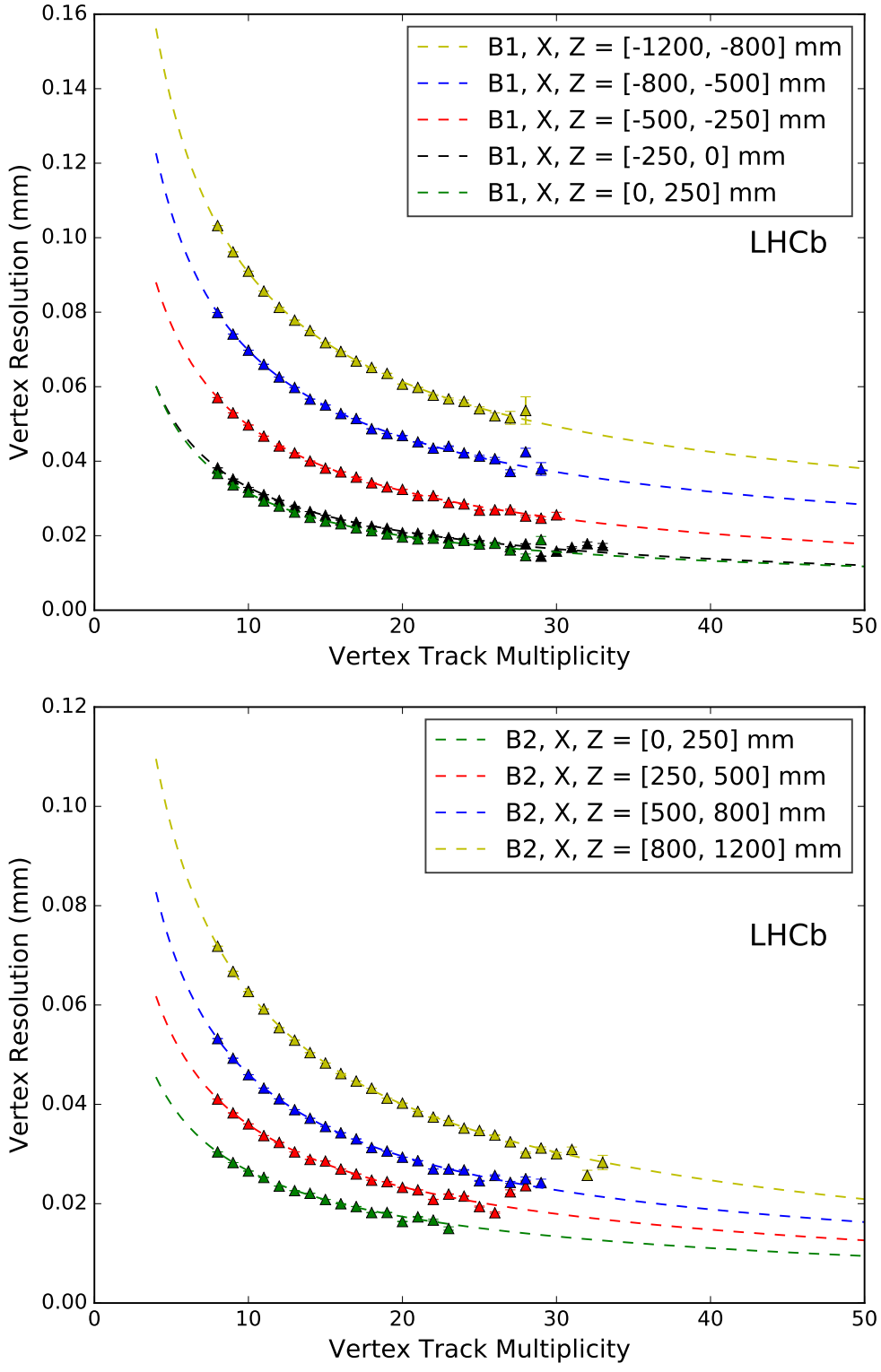

Figure 2.13: The beam-gas vertex resolution in x as a function of the vertex track multiplicity as measured in different z bins for beam 1 (top) and beam 2 (bottom). The markers show individual measurements of the resolution with their errors and the line shows the results of a fit using the parametrisation in the same z ranges. The measurements above were made during LHC calibration fill no. 6012 in 2017. The resolution value is larger further away from the collision point at the centre of the VELO and decreases with increasing multiplicity. The results are similar for the y resolution.

z range (mm)	Beam	A_x (mm)	B_x	C_x (mm)	A_y (mm)	B_x	C_x (mm)
[-1200, -800]	1	0.359	0.644	0.009	0.363	0.679	0.012
[-800, -500]	1	0.292	0.666	0.007	0.269	0.600	0.001
[-500, -250]	1	0.209	0.616	-0.001	0.203	0.604	-0.002
[-250, 0]	1	0.150	0.678	0.001	0.139	0.643	0.001
[0, 250]	1	0.166	0.778	0.004	0.139	0.681	0.001
[0, 250]	2	0.102	0.540	-0.003	0.099	0.566	-0.001
[250, 500]	2	0.140	0.545	-0.004	0.151	0.674	0.003
[500, 800]	2	0.200	0.633	-0.001	0.196	0.697	0.003
[800, 1200]	2	0.255	0.560	-0.008	0.247	0.707	0.004

Table 2.5: The values of the beam-gas resolution fit parameters, defined as in Eq. 2.7, for each z bin and each beam as measured in LHC calibration fill no. 6012.

The weighted residuals between this parameterisation and the direct measurements from fill 6012 are shown in the histograms in Fig. 2.14. The residuals are weighted by the number of vertices per track multiplicity according to the distributions shown in Fig. 2.15. Both residual distributions are centred around zero and their statistical variation of approximately 0.2 μm is small enough to be neglected.

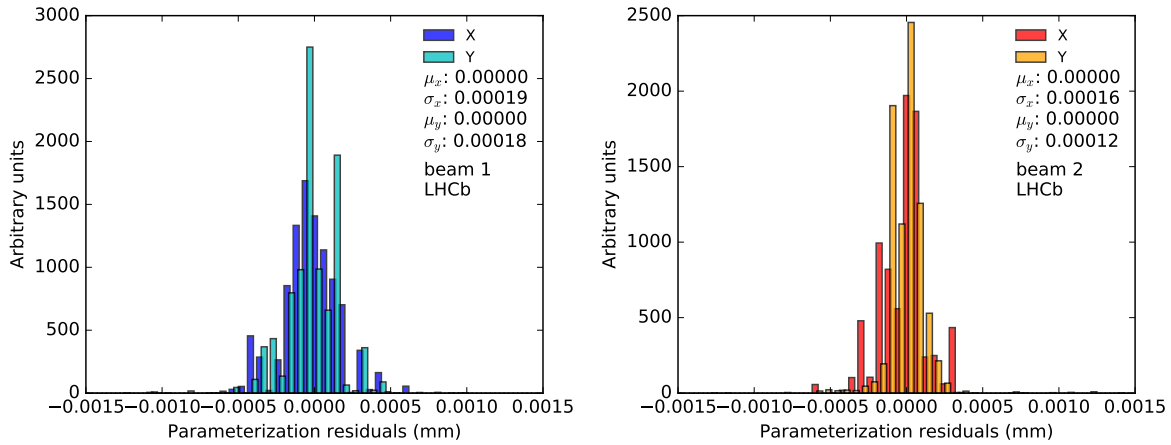

Figure 2.14: These two plots show the weighted residuals between the direct measurement of the beam-gas resolution in LHC fill no. 6012 and the value from the parameterisation described above. The results for beam 1 are shown on the left and for beam 2 on the right. The values μ and σ for each axis are the mean and standard deviation of the distribution of residuals for that axis.

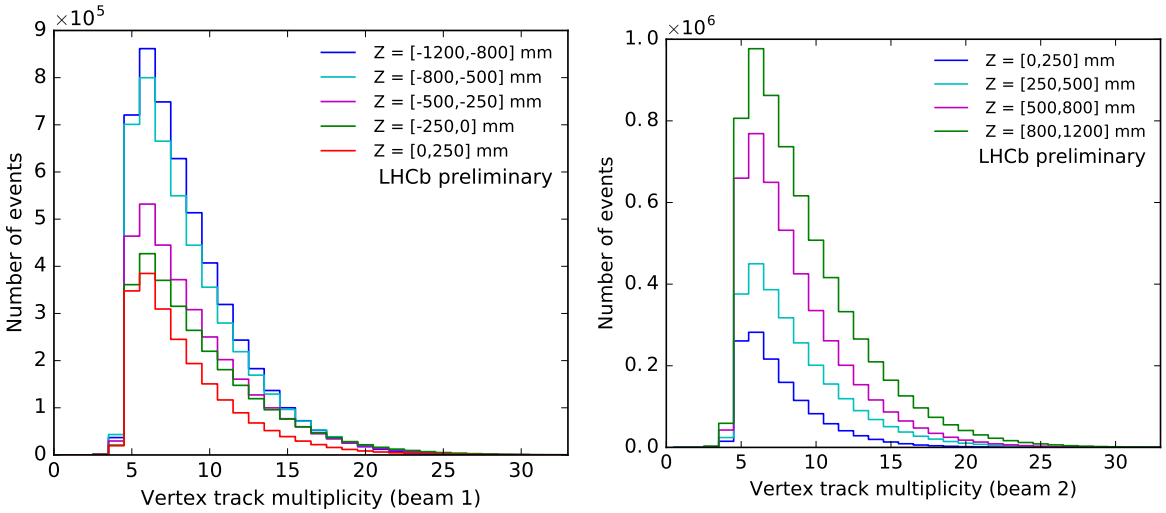

Figure 2.15: These histograms show the vertex track multiplicity distribution for the z ranges used to measure the beam-gas resolution in LHC fill no. 6012.

Beam-gas longitudinal position dependence corrections

The correction for longitudinal resolution variation is defined for beam-gas vertices in exactly the same way as for beam-beam vertices, as shown in Sec. 2.5.2, except that it is calculated per z range and per beam. Within each z range the correction factors are calculated in bins of 25 mm using Eq. 2.8. Results of this calculation are shown in Fig. 2.16 for both beam 1 and beam 2 for LHC fill no. 6012. The calculated correction factors are only applicable within a given z range.

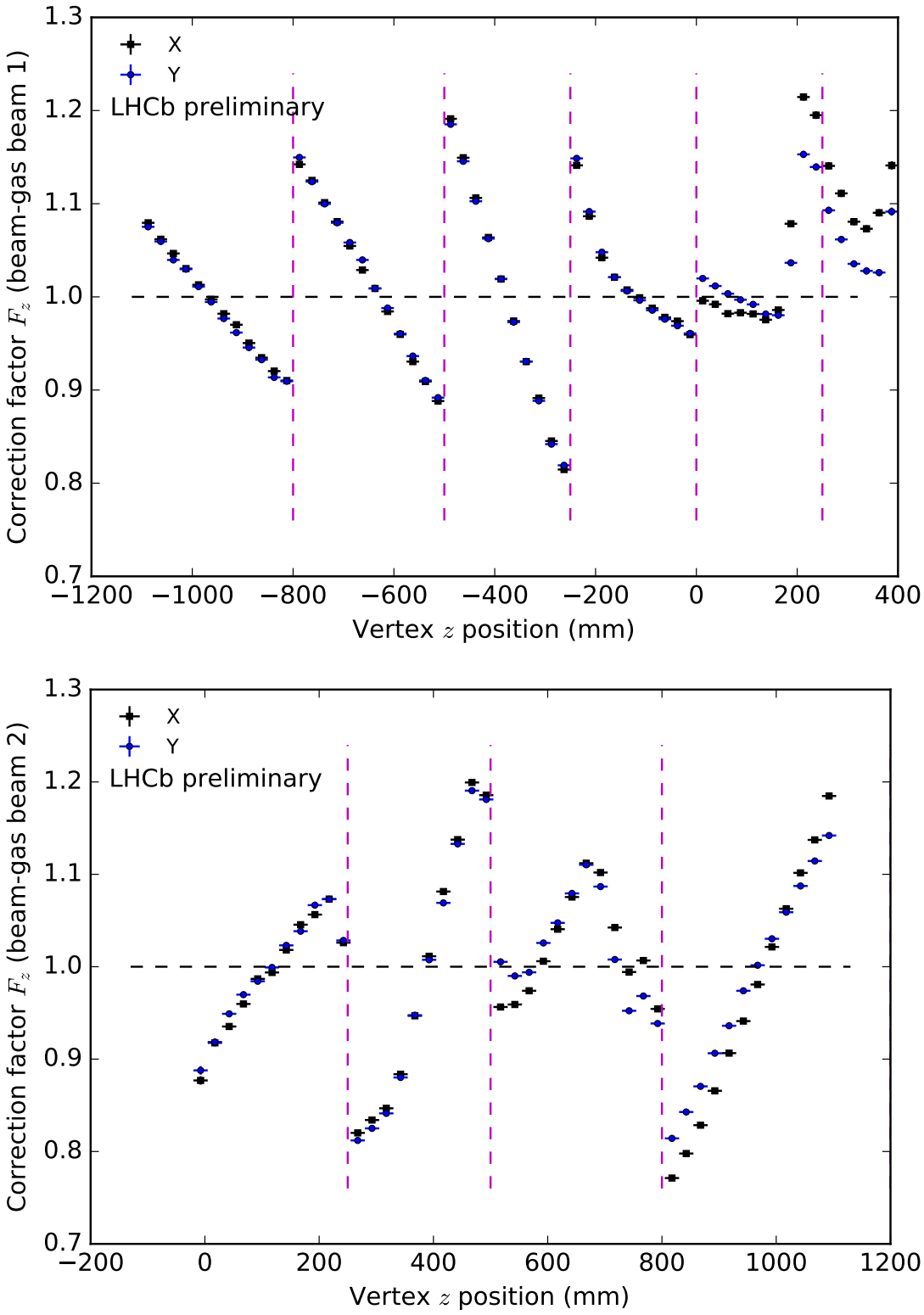

Figure 2.16: Beam-gas resolution correction factors as a function of the longitudinal position z for beam 1 (above) and beam 2 (below) for LHC fill no. 6012. The vertical dashed lines indicate the boundaries between z bins and the correction factors only apply within a given bin. The change in the shape of curves around $z = 180$ mm and 700 mm is due to the specific geometry of the VELO sensor positions.

2.6 Measuring Beam Profiles and Parameters

The overlap integral defined in Eq. 1.5 cannot be calculated without precise knowledge of the three-dimensional bunch distributions $\rho(x, y, z)$ throughout the period of measurement. This analysis makes the assumption that the longitudinal and transverse components of the bunch distributions are independent and thus that the distribution ρ is factorisable such that $\rho(x, y, z) = \rho(x, y)\rho(z)$. This factorisability is discussed later in this chapter. The longitudinal trajectory of the bunch is determined by the beam directions, the measurement of which is discussed in Sec. 2.6.1 and the bunch length measurement is discussed in Sec. 2.6.3. The transverse shape of the bunch is first measured under the assumption that the x and y coordinates are independent and factorisable and then subsequently a 2D measurement is performed to determine the magnitude of any non-factorisability. This process is described in Sec. 2.6.2.

Informed by the resolution results presented in Sec. 2.5 above, the transverse beam shape measurements are made using the distribution of the average position of the split vertices rather than the distribution of primary vertex positions. This is because the resolution assigned to the measured vertex position is determined from the analysis of split vertex positions. This is possible as the distributions of $(v_1 - v_2)/2$ (as used in the resolution) and $(v_1+v_2)/2$ (as used for the vertex position) are expected to be the same since the split vertices $v_{1,2}$ have symmetric distributions around 0 by construction.

2.6.1 Crossing Angle Measurement

The beam angles, $\alpha_{i,j}$, for beam $j = 1, 2$ and axis $i = x, y$ can be determined independently in the laboratory reference frame for each beam and each axis by directly measuring the slopes $m_{i,j}$ of each beam in the laboratory reference frame. This measurement makes use of beam-gas vertices from both colliding and non-colliding bunch pairs. The inclusion of vertices from non-colliding bunches allows this approach to cover the full z range with a good degree of precision. The measurement of the slope is done by performing a linear least-squares fit on the full set of beam-gas vertex positions for each beam projected onto each axis over a period of up to 1 hour during the fill. The resolution associated with the vertices is used to calculate the uncertainty on the fit. An example of such a measurement is shown in Fig. 2.17.

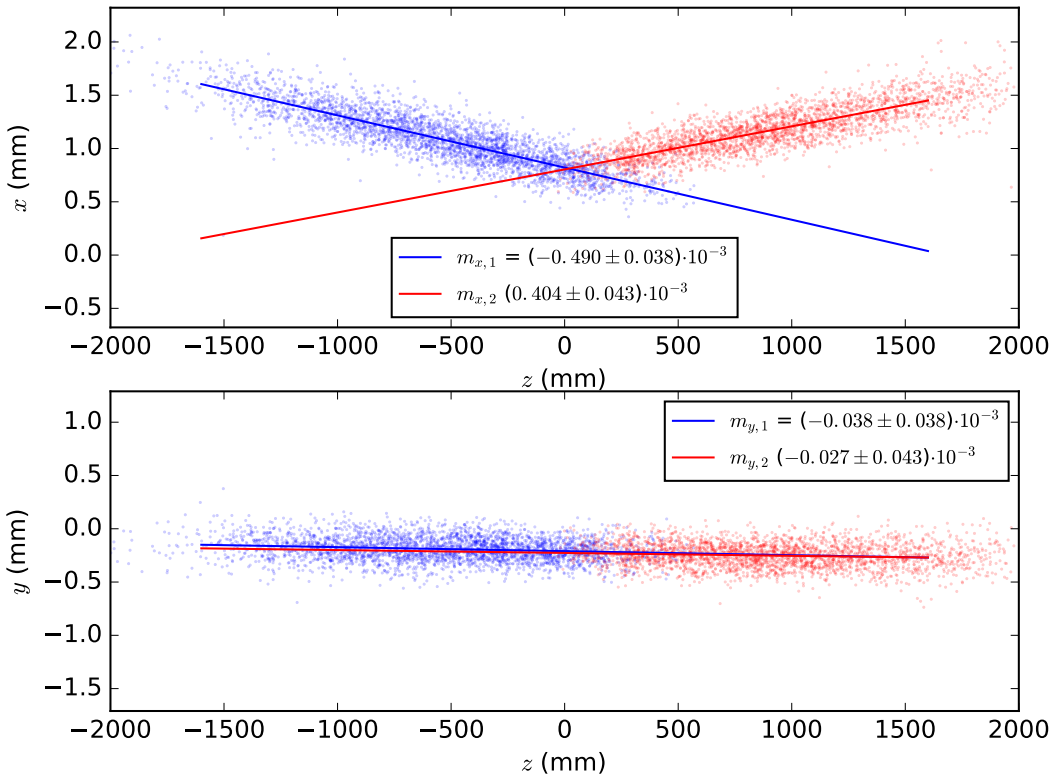

Figure 2.17: The fitted beam slopes for run 174612 of fill 4937. The crossing angle in x is clearly visible and the angle in y can be seen to be close to zero.

The beam angles can then be determined from these fitted slopes as in Eq. 2.9:

$$\alpha_{i,j} = \tan^{-1}(m_{i,j}) \tag{2.9}$$

The half crossing angle, ϕ, that is used in the luminosity calculations in Sec. 1.5 can then be defined for each axis, i, in terms of the beam angles as shown in Eq. 2.10 below:

$$\phi_i = \frac{\alpha_{i,2} - \alpha_{i,1}}{2} \tag{2.10}$$

Throughout the duration of LHC run 2 the crossing angle at IP8 was generally implemented in the x axis and the value in y was close to zero for all luminosity calibration fills. The values for fills relevant to the beam-gas imaging analysis are shown in Fig. 2.18. The value of ϕ_x was within 1% of the target angle for each calibration fill throughout the period of LHC run 2 and the absolute value of ϕ_y remained at less than 10 μrad.

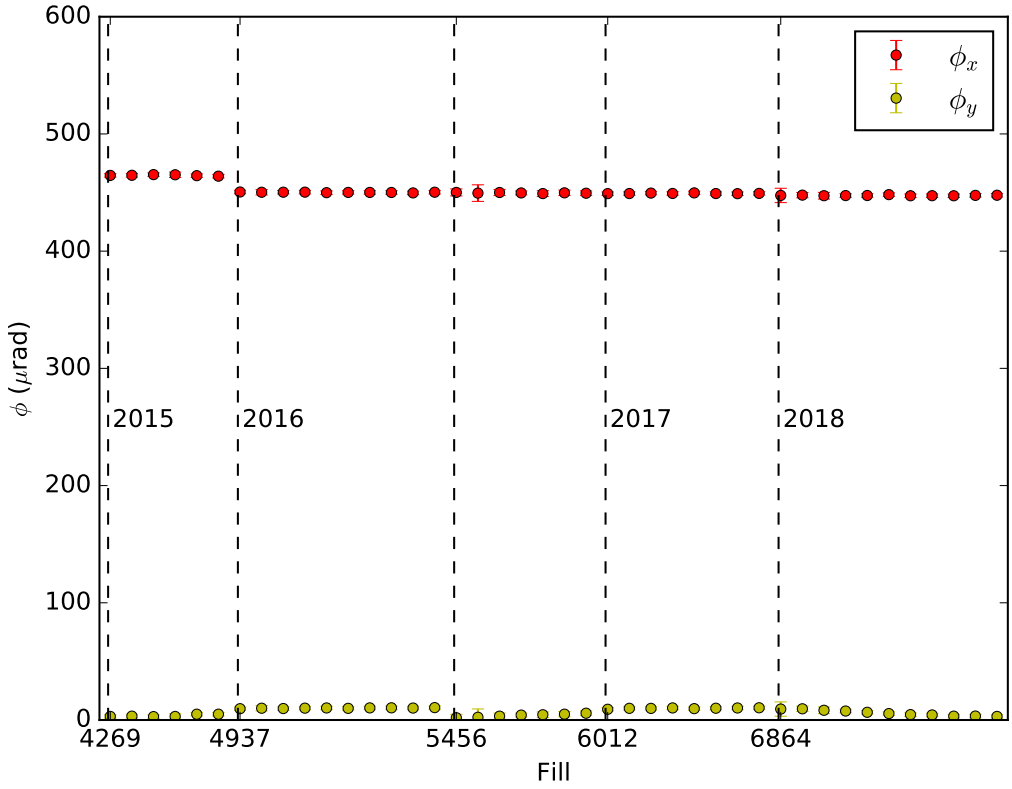

Figure 2.18: The half crossing angles ϕ_x and ϕ_y measured via beam-gas imaging for relevant fills from LHC run 2. Each point is the measured crossing angle for one LHCb run and the vertical dashed lines separate data points from different fills. The values are stable over time with a target angle in the xz plane of 460 μrad in 2015 and 450 μrad in subsequent years. The target angle was 0 μrad in the yz plane.

2.6.2 Transverse Beam Profile Measurement

The overlap between the colliding beams is determined by their individual distributions and positions so a simple measurement of the beam profiles can be performed by fitting the profile of each beam separately under the assumption that the profiles along each transverse axis are independent and that the profiles themselves have a Gaussian shape. In this case for each beam and transverse coordinate, a simultaneous fit is performed of the data in z slices corresponding to the regions used to measure the beam-gas resolution in Sec. 2.5.3 (so as to avoid mixing vertices whose resolutions are too different). First, every vertex is projected to the centre of the corresponding slice according to the measured beam angle and then the true beam width for each beam is fitted to all slices at once (taking into account the different resolution per slice). The Gaussian distribution given in Eq. 2.11 would then describe the beam profile for the coordinates $m = x, y$ in the laboratory frame.

$$g(m;\mu_m,\sigma_m) = \frac{1}{\sqrt{2\pi}\sigma_m} e^{-\frac{1}{2}\left(\frac{m-\mu_m}{\sigma_m}\right)^2} \tag{2.11}$$

Then in any given z range the vertices can be projected along the beam direction, α, onto the xy plane at a central z point z_c by using the projection given in Eq. 2.12.

$$m' = m - \alpha(z - z_c) \tag{2.12}$$

If the particles within the measured bunch are instead distributed with a double-Gaussian shape their profile will be given by Eq. 2.13.

$$\rho_m(m';\mu'_m,\sigma_{n,m},\sigma_{w,m}) = w_m g(m';\mu'_m,\sigma_{n,m}) + (1-w_m)g(m';\mu'_m,\sigma_{w,m}) \tag{2.13}$$

Here $\sigma_{n,m}$ and $\sigma_{w,m}$ are the widths of a narrow and wide component Gaussian respectively and w_m is a dimensionless weight with value between 0 and 1. The mean position μ'_m varies with longitudinal position and is related to the beam position at the centre of the longitudinal range by $\mu'_m = \mu + \alpha z_c$.

All reconstructed vertices in a selected z range are binned along each transverse axis m (x, y) and their observed distribution $M(m')$ is a convolution of the beam shape with the resolution of the LHCb detector. The relevant resolution distribution function $R(m)$ is given by the resolution distribution of all vertices from the selected sample used to construct $M(m')$.

The overlap integral in the case of this one-dimensional fully factorisable model is given in Eq. 2.14 and its calculation is discussed in Sec. 2.7.

$$\mathcal{O} = 2c \int \rho_{x1}(x')\rho_{y1}(y')\rho_{z1}(z-ct)\rho_{x2}(x')\rho_{y2}(y')\rho_{z2}(z+ct)dxdydzdt \tag{2.14}$$

An example of such single beam fits is shown using data from fill 4937 in Fig. 2.19 where this double Gaussian shape is fitted to the beam-gas vertices away from the luminous region.

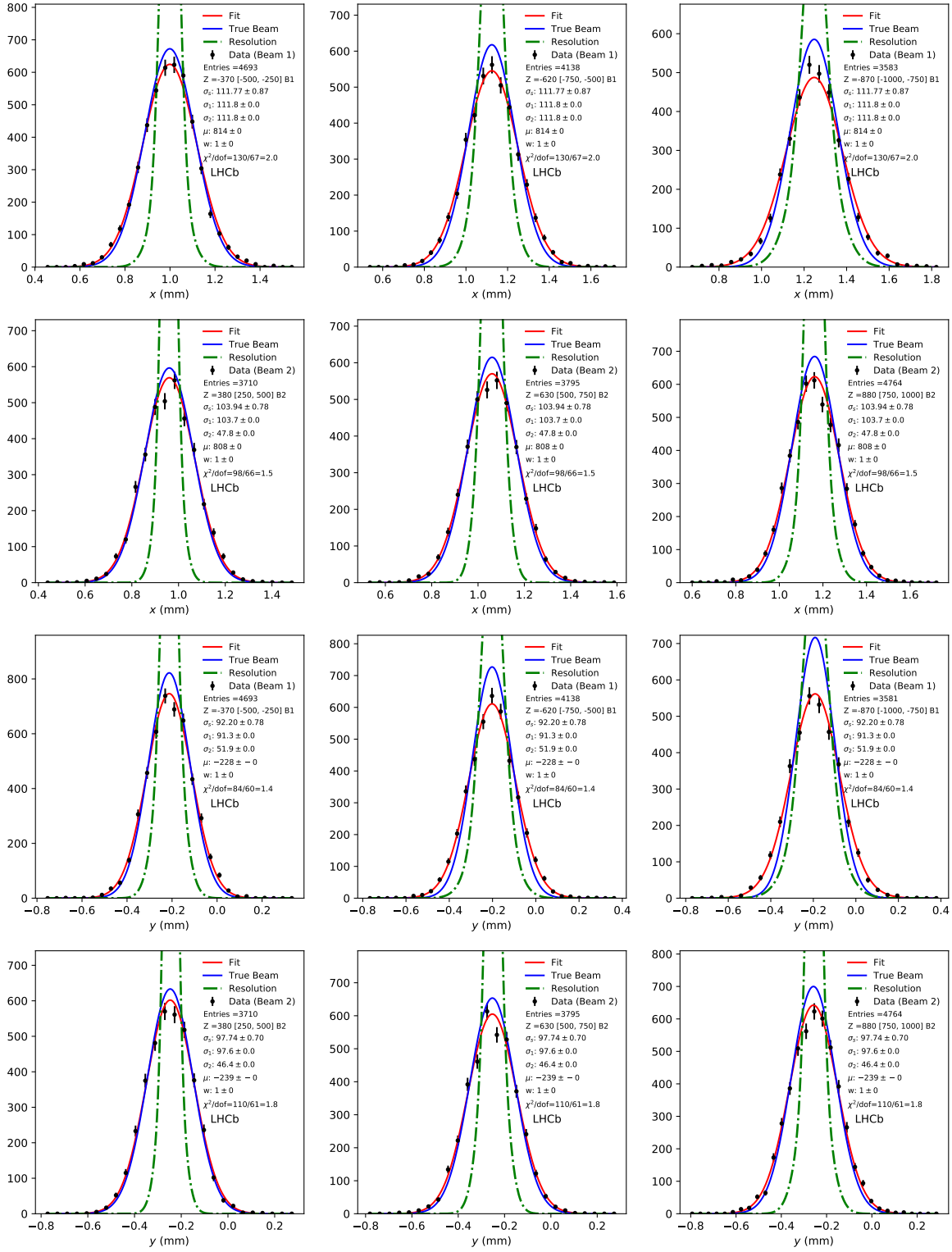

Figure 2.19: Double Gaussian fits to the single beam profiles in x and y for both beams for bunch no. 2384 in run 174635 of fill 4937. A projection is made to a point at the centre of each z slice and then the beam parameters are fitted simultaneously across all slices. The red line shows the fit to the data points, the green dashed line shows the resolution function determined in Sec. 2.5 and the blue line is the beam shape determined via the deconvolution of the resolution function from the observed shape.

Although the shape of the luminous region is fully determined by the single beam distributions ρ_1 and ρ_2, the pp collision vertices can be included in the analysis to further constrain the fit without adding any additional parameters other than the individual fit amplitudes [31]. This benefits the statistical precision of the measurement as the luminous region contains about 10 times as many vertices as the areas outside it and beam-beam vertices benefit from a smaller resolution than the beam-gas vertices.

The beam profile parameters can be measured with a global fit that combines both the single beam distribution and the luminous region distribution. This fit is performed in the x and y axes independently. Beam-gas interactions are divided into the same z slices used for the single beam fits. The luminous region is divided up into 18 z slices as the transverse profile is highly z dependent in the crossing plane. This z dependence can be induced by an asymmetry in the beam slopes (as visible in Fig. 2.17) and is also due to the z dependence of the vertex resolution.

These z slices are 10 mm wide in the very centre of the collision region ($|z| < 50$ mm) and 15 mm wide in the outer region. The longitudinal selection ranges used for the global fit in fill 4937 are shown in Fig. 2.20, as an example. The asymmetric shape of the luminous region is due to the requirement for two forward and two backward tracks for selection of a beam-beam vertex, this reduces the VELO acceptance in the negative z region where acceptance for backward tracks falls sharply. The results of such a global fit are shown in Fig. 2.21.

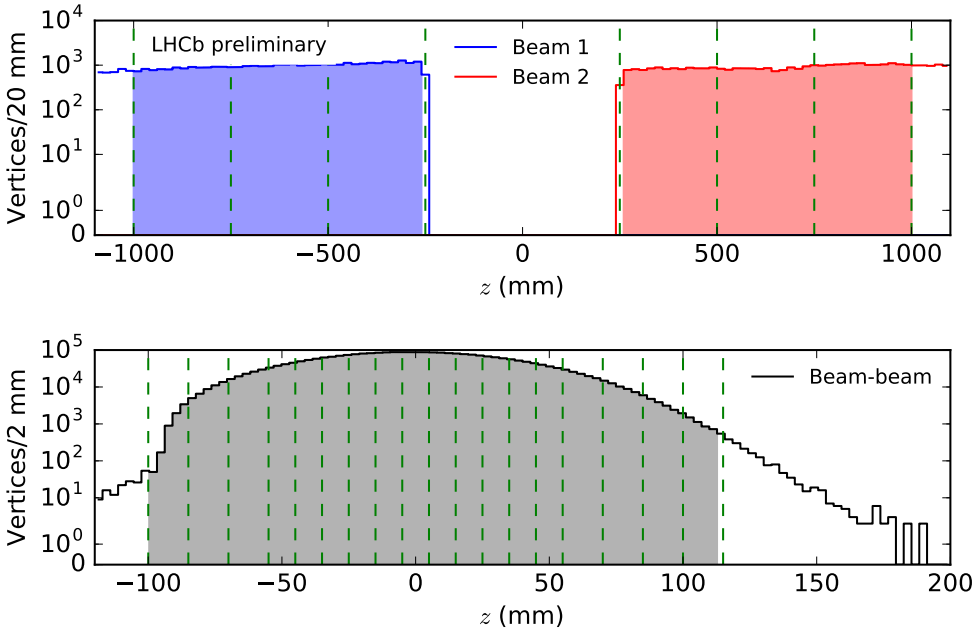

Figure 2.20: The selected z regions used for the global fit in LHC fill 4937 by assigned interaction type. Vertices both outside (above) and inside the luminous region are shown. Vertices are binned by z position with a bin width of 20 mm outside the luminous region and 2 mm inside. The asymmetry in the luminous region profile is due to the sharper decline in the acceptance for backward tracks in the negative z region relative to that for forward tracks in the positive z region.

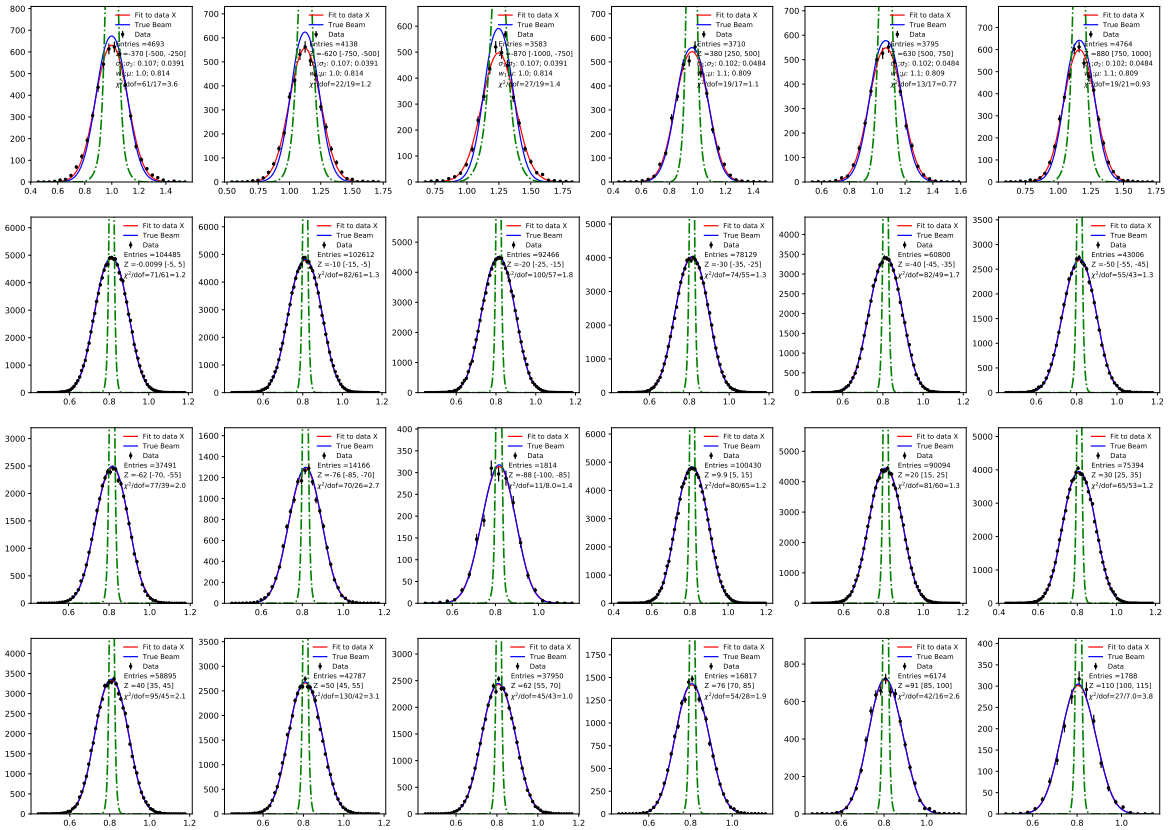

Figure 2.21: The one-dimensional global fit to the data from the same fill, run and bunch used in Fig. 2.19. Here the beam-beam vertices from the luminous region are included in addition to the beam-gas vertices and only the x results are shown. Again the red line shows the fit to the data points, the green dashed line shows the resolution function determined in Sec. 2.5 and the blue line is the beam shape determined via the deconvolution of the resolution function from the observed beam shape. The three plots in the top left show the fits to beam-gas vertices from beam 1 and the three plots in the top right show fits to beam-gas vertices from beam 2. The remaining fits are to the beam-beam vertices in individual z slices of the luminous region.

Transverse Bunch Profiles in Two Dimensions

The one-dimensional fit models described above contain the implicit assumption that the transverse bunch profiles are factorisable such that the distributions in x and y are independent from one another. In other words, that the bunch distribution in x does not vary with the position in y. Studies in run 1 showed that this is not necessarily the case for the proton bunches circulating in the LHC and thus a two-dimensional fit allowing for some correlation between these distributions is also performed [5]. The combined transverse density function, $\rho(x, y)$ is defined as the sum of four Gaussian products with a factorisable term f_j as in Eq. 2.15.

$$\begin{aligned}\rho(x,y) = &\left[f_j w_x w_y + (1-f_j)\frac{w_x+w_y}{2}\right] g_n(x')g_n(y') \\ &+ [f_j w_x(1-w_y)]g_n(x')g_w(y') \\ &+ [f_j w_y(1-w_x)]g_w(x')g_n(y') \\ &+ \left[f_j(1-w_x)(1-w_y) + (1-f_j)\left(1-\frac{w_x+w_y}{2}\right)\right] g_w(x')g_w(y')\end{aligned} \tag{2.15}$$

Here the factorisable term has been defined such that a value of $f_j = 1$ is equivalent to the fully factorisable one-dimensional model described above and a value of $f_j = 0$ causes the narrow-wide cross terms to go to zero leaving only the narrow-narrow and wide-wide Gaussian products. The Gaussian functions, $g_i(m)$, defined in Eq. 2.16, are equivalent to the narrow and wide components, ($i = n, w$), of the double Gaussian expression shown in Eq. 2.13. The transverse coordinates, ($m = x', y'$), have been transformed from their reconstructed transverse positions, (x, y), according to Eqs. 2.17 and 2.18 with the measured beam direction, α, such that all vertices are projected onto the xy plane at the longitudinal position z_c.

$$g_i(m') = g(m'; \mu_{m'}, \sigma_{i,m}) \tag{2.16}$$

where:

$$m' = m - (z - z_c)\alpha \tag{2.17}$$

and:

$$\mu_{m'} = \mu_m - z_c\alpha \tag{2.18}$$

Using this two-dimensional model the overlap integral has the form given in Eq. 2.19 with the only factorisation being in z.

$$\mathcal{O} = 2c \int \rho_1(x', y')\rho_{z1}(z - ct)\rho_2(x', y')\rho_{z2}(z + ct)dxdydzdt \tag{2.19}$$

As in the one-dimensional case every measured beam width is in fact a resolution convolved width and the true widths are determined by deconvolution with the measured resolution as described in Sec. 2.5.1. Again, as in the one-dimensional case the single beam profiles are measured first with a fit to Eq. 2.15 and using the same z regions shown in Fig. 2.20. The global fit is then performed including the same z slices from the luminous region as before. The fit parameters are the Gaussian parameters w, μ, σ_n and σ_w for both beams and both axes, a factorisable parameter f_j for each beam and one free amplitude per z slice. This leads to a complex fit with 42 parameters (18 beam parameters and 24 amplitudes). In order for this fit to converge quickly and consistently its starting values are first determined from

the one-dimensional model under the assumption that these will be reasonably close to the final results. The factorisable parameters are given a starting value of $f_j = 0.5$ and the fitted values are shown in Fig. 2.23. The spread of values shown here, with peaks towards zero and one, shows that while some significant proportion of bunch profiles are factorisable in the transverse plane the majority are not and the two-dimensional approach is necessary. The χ^2 values for all of the two-dimensional global fits performed for fill 4937 are shown in Fig. 2.22. An example of the projected two-dimensional view of the data, fit and fit pulls is shown in Fig. 2.24. Another example showing a three-dimensional view of the fitted beam shape for three different z regions along with fit values and pulls is shown in Fig. 2.25. The pulls are calculated as in Eq. 2.20:

$$\text{pulls}_{i,j} = \frac{N_{i,j} - f_{i,j}}{\sqrt{N_{i,j}}} \tag{2.20}$$

where $N_{i,j}$ is the data value for the number of vertices in bin i in x and j in y and $f_{i,j}$ is the fit prediction for this same bin.

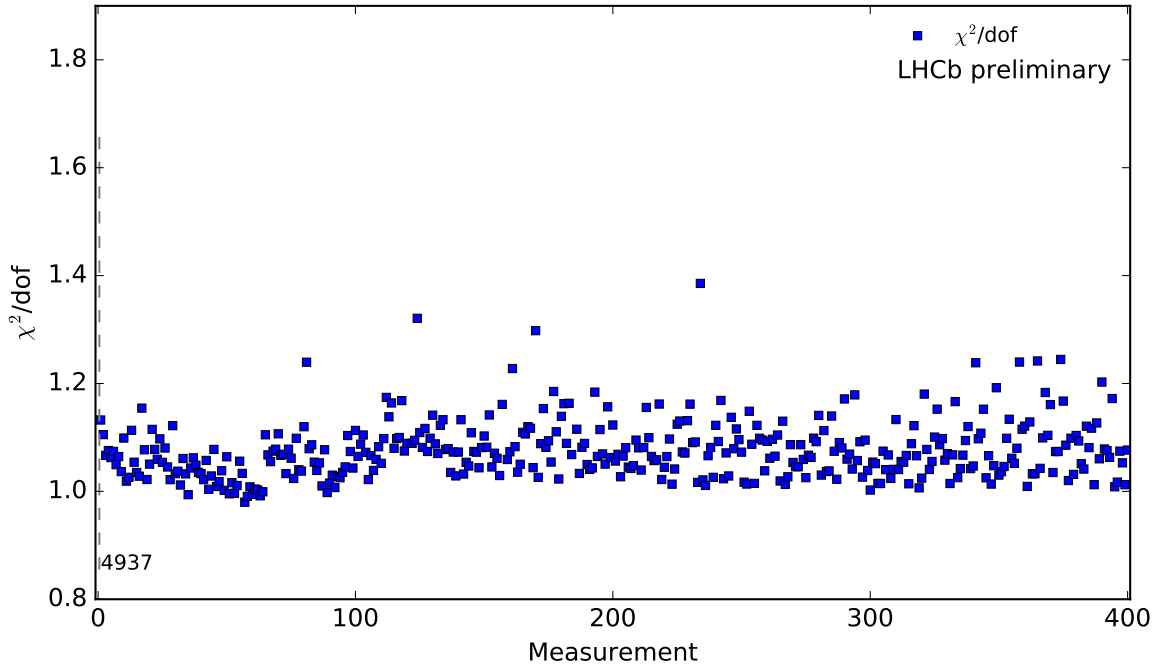

Figure 2.22: The χ^2 values per number of degrees of freedom for all 2D fits made of the transverse bunch profiles for all bunch pairs colliding at IP8 in LHC fill no. 4937. These measurements are sorted by time bin and by BCID. The measurement axis used here will be used elsewhere in this thesis. It first shows the measured value for the first 15 minute time bin for the first BCID followed by the values from the first time bin for each subsequent BCID and then repeats this sequence for each subsequent time bin.

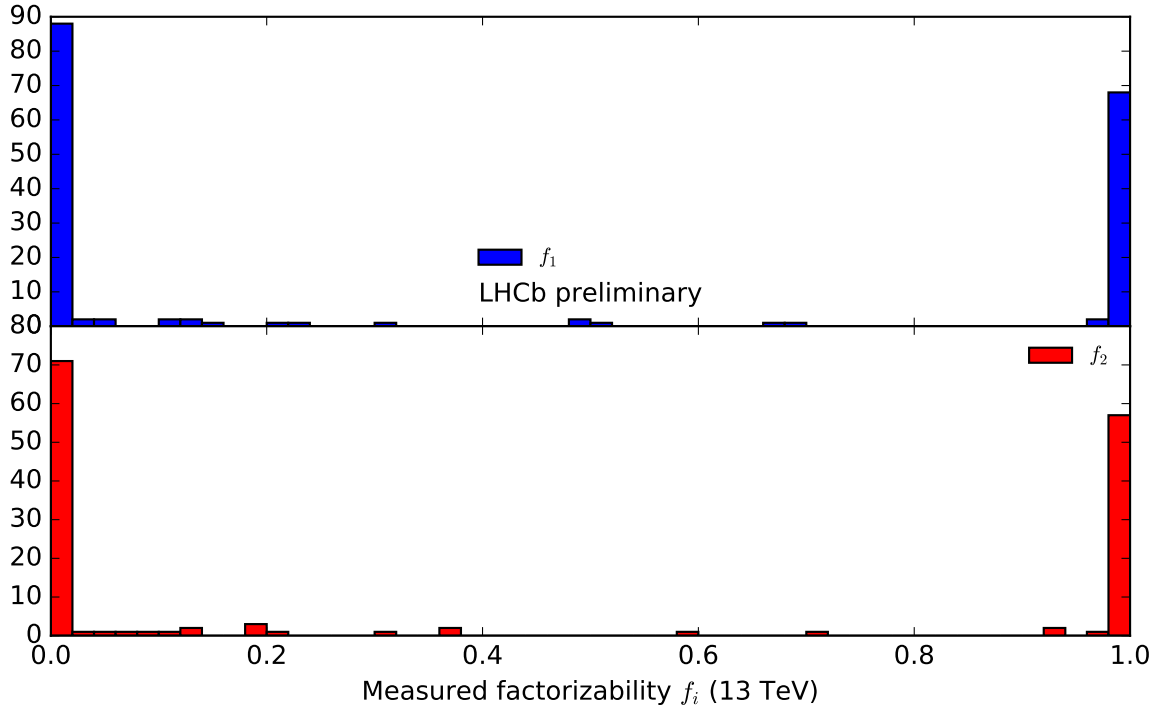

Figure 2.23: Histograms showing the factorisable parameter f_j as measured in LHC fill no. 4937.

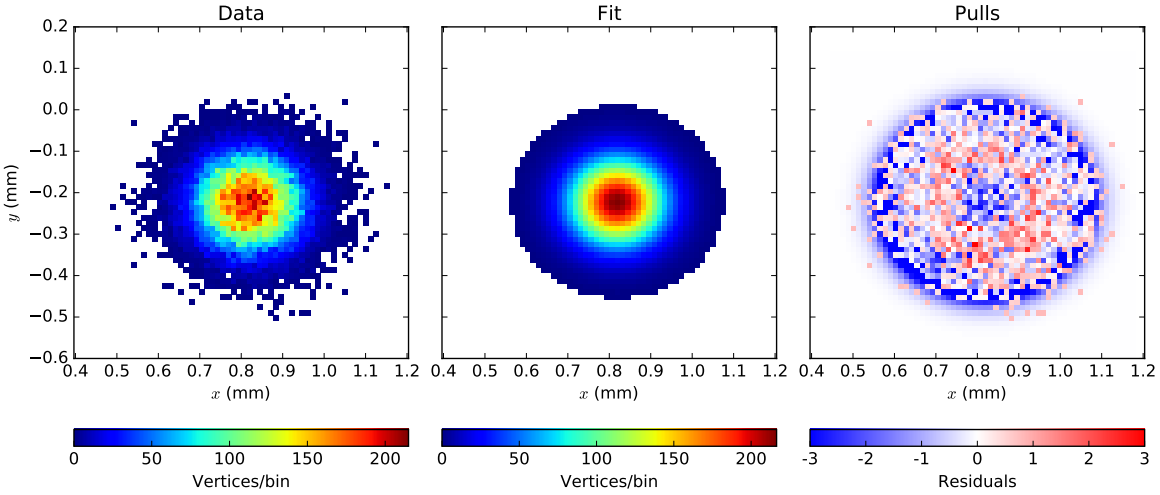

Figure 2.24: An example of the 2D global fit results in the transverse projection of one z slice of the luminous region for BCID 2384 in run 174634 of fill 4937. The left plot shows the data values for the projected transverse beam distribution and the middle plot shows the fit values. The colour code in these two plots show the number of vertices within each bin either as recorded in the data or as predicted by the fit. The right plot show the pulls between the data and fit, i.e. the residuals between each distribution in each bin normalised to the statistical uncertainty for that bin.

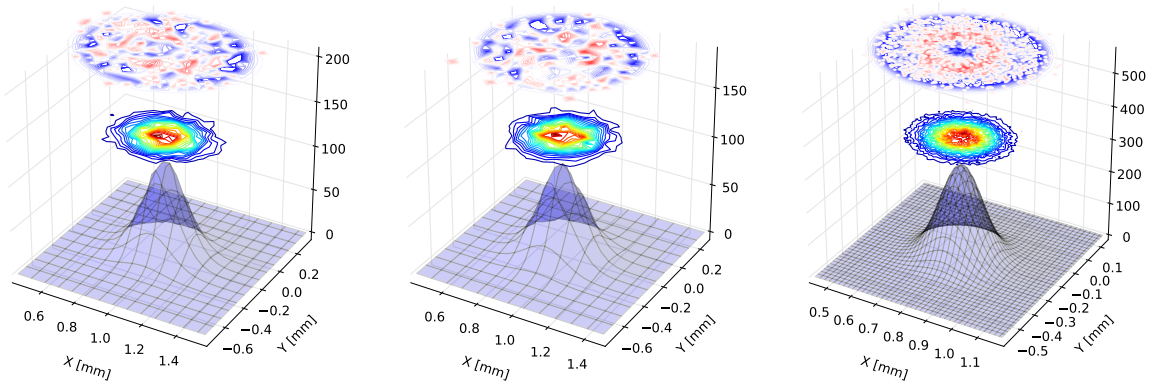

Figure 2.25: A 3D view of the 2D global fit results for BCID 2384 in run 174634 of fill 4937. From left to right examples from z slices for beam 1, beam 2 and the luminous region are shown. The 3D shape is the true beam shape after deconvolution of the resolution, the data is shown as a contour plot immediately above the fit shape and the pulls are shown on top. The colour coding is as in Fig. 2.24.

2.6.3 Measuring the Bunch Length and Crossing Point

The individual bunch lengths σ_{z1} and σ_{z2} are not directly measurable as no precise detector timing information is available at LHCb. However, the convolved bunch length $\sigma_{z1}^2 + \sigma_{z2}^2$ is related to the luminous region shape and can be measured from the longitudinal distribution of beam-beam vertices.

The crossing point Z_{RF} is determined by the LHC RF system and is shown in the context of the colliding beam geometry in Fig. 2.26. This position could be measured once during the fill when the beams have been optimised in both planes by the LHC operators and then used for all overlap integral measurements for that fill. However, this optimisation while generally done at the start of the stable beams period may be performed before the LHCb detector is switched on and in this case the luminous region cannot be measured via BGI. Therefore, the value of Z_{RF} is instead measured from the luminous region longitudinal shape and position for each colliding bunch pair.

In the case of a bunch distribution given by a three-dimensional single Gaussian the longitudinal distribution of beam-beam vertices can be written as:

$$\rho_{bb} = Ag(z) \tag{2.21}$$

with an amplitude factor A and a Gaussian distribution $g(z; \mu_{zl}, \sigma_{zl})$ with mean μ_{zl} and width σ_{zl}. This amplitude factor is proportional to the luminosity and thus the overlap integral. The mean and width of the distribution are observables and can be related back to Z_{RF} and

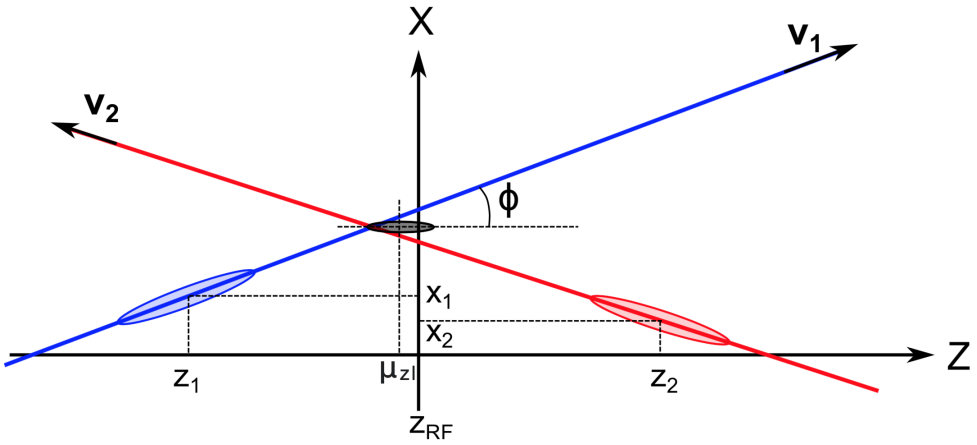

Figure 2.26: This diagram shows the colliding beam geometry in the xz plane with the two beams travelling along the directions of vectors v_1 and v_2. The value of y on this plane is constant and can be considered to be neglected. The coordinates (x_1, z_1) and (x_2, z_2) define the centre of the bunches from each beam at time t. The angle ϕ is the half crossing angle between the two beams in x. The bunches cross at time $t = 0$ at the central point Z_{RF}. In this example the two beams are at an offset with respect to each other and thus the centre of the luminous region, μ_{zl} is displaced to a point away from Z_{RF}.

$\sigma_{z1}^2 + \sigma_{z2}^2$ via the relations given in Eqs. 2.22 and 2.24 [31].

$$\mu_{zl} = Z_{RF} + \delta_{z_{l,0,m}} \tag{2.22}$$

with $m = x, y$ where:

$$\delta_{z_{l,0,m}} = -\frac{\sin 2\phi_m}{4} \frac{\sigma_{z1}^2 + \sigma_{z2}^2 - \sigma_{m1}^2 + \sigma_{m2}^2}{(\sigma_{m1}^2 + \sigma_{m2}^2)\cos^2\phi_m + (\sigma_{z1}^2 + \sigma_{z2}^2)\sin^2\phi_m} \Delta m \tag{2.23}$$

and:

$$\sigma_{zl} = \left(\frac{4\cos^2\sqrt{\phi_x^2 + \phi_y^2}}{\sigma_{z1}^2 + \sigma_{z2}^2} + \frac{4\sin^2\phi_x}{\sigma_{x1}^2 + \sigma_{x2}^2} + \frac{4\sin^2\phi_y}{\sigma_{y1}^2 + \sigma_{y2}^2} \right)^{-\frac{1}{2}} \tag{2.24}$$

In the full BGI analysis the bunch distributions are described by a double Gaussian shape rather than single Gaussian distribution and therefore the luminous region distribution ρ_{bb} has sixteen Gaussian contributions similar to the one described above in Eq. 2.21. The weighting of each these distributions is proportional to the fraction of luminosity it generates. Each of the individual Gaussian distributions that contribute are assigned a different width σ_{zl} and longitudinal offset $\delta_{z_{l,0,m}}$ whose values are determined by the single beam parameters used in Eqs. 2.23 and 2.24. The values of Z_{RF} and $\sigma_{z1}^2 + \sigma_{z2}^2$, however, are common parameters.

The longitudinal distribution of the luminous region is then described by Eq. 2.25:

$$\rho_{bb} = \sum_{i,j,k,l} A_{i,j,k,l} g_{i,j,k,l}(z) \tag{2.25}$$

where:

$$A_{i,j,k,l} = w_{i,j} w_{k,l} \mathcal{O}_{i,j,k,l} \tag{2.26}$$

In this case the indices i, j, k, l define the possible combinations of single beam distributions that make up the full luminous region distribution: $i \in \{x_{1n}, x_{1w}\}$, $j \in \{y_{1n}, y_{1w}\}$, $k \in \{x_{2n}, x_{2w}\}$, $l \in \{y_{2n}, y_{2w}\}$. The procedure for calculating the weights $w_{i,j}$, $w_{k,l}$ is as set out in Sec. 2.6.2 and the evaluation of the individual overlap integrals $\mathcal{O}_{i,j,k,l}$ will be described in Sec. 2.7.

The reconstruction efficiency of the VELO is not constant on the longitudinal axis and without correction this will distort the observed luminous region shape and affect the measurement of both Z_{RF} and $\sigma_{z1}^2 + \sigma_{z2}^2$. This variable reconstruction efficiency is evaluated with a Monte Carlo simulation and the results are shown in Fig. 2.27. The values are given as a relative efficiency with respect to the value at $z = 0$ in order to keep the fit amplitudes on a similar scale for the raw and corrected data. The Monte Carlo simulation is used to randomly generate pp interactions at a collision energy of $\sqrt{s} = 13$ TeV in the longitudinal range of the luminous region. This simulation data is then reconstructed with the usual LHCb reconstruction algorithms to evaluate the efficiency to be applied to the raw data before fitting.

The results of this measurement of the convolved bunch length are presented for fill 4937 in Fig. 2.28 and for the bunch crossing point and offsets in Figs. 2.29 and 2.30. The z position of the luminous region appears highly correlated with the offset between the beams in x for the majority of fill 4937, which is explained by the crossing angle between the beams which is implemented in the xz plane.

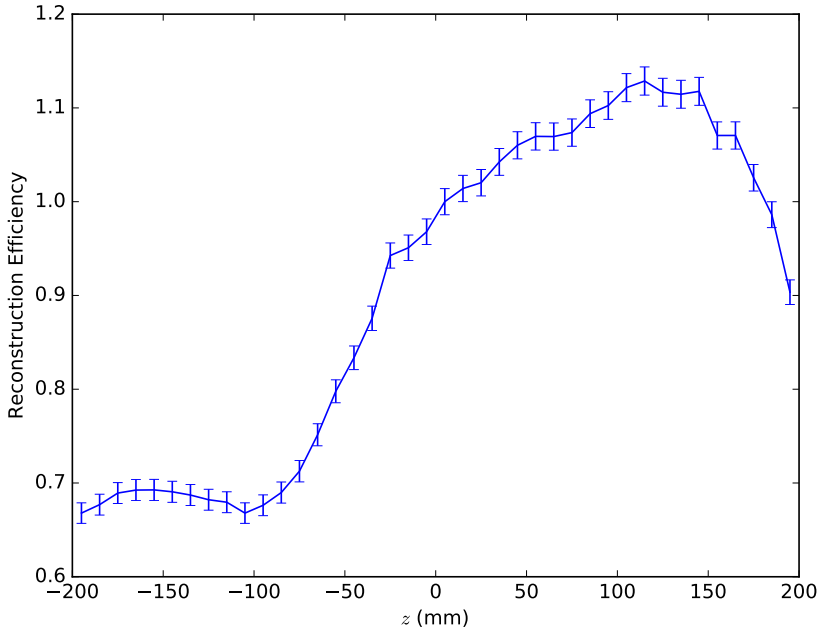

Figure 2.27: The relative vertex reconstruction efficiency as a function of z over the longitudinal range of the luminous region for pp collisions at $\sqrt{s} = 13$ TeV. The efficiency is set to 1 at a longitudinal position of $z = 0$.

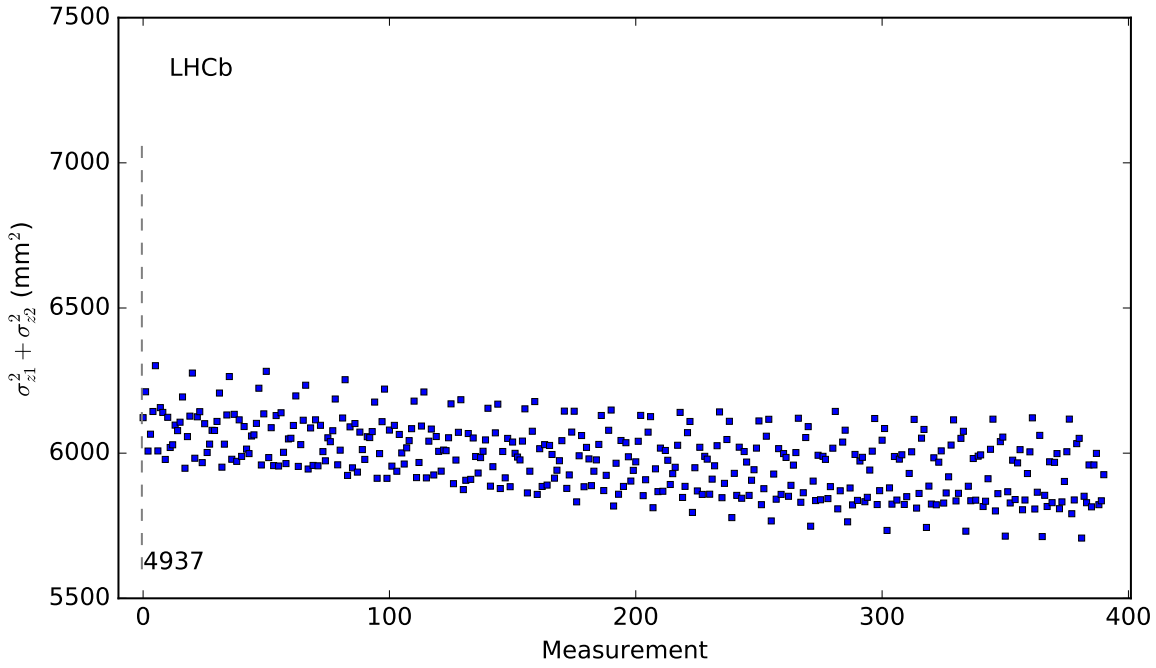

Figure 2.28: The convolved bunch length as measured by the BGI method for fill 4937. The measurements are sorted by time and by BCID.

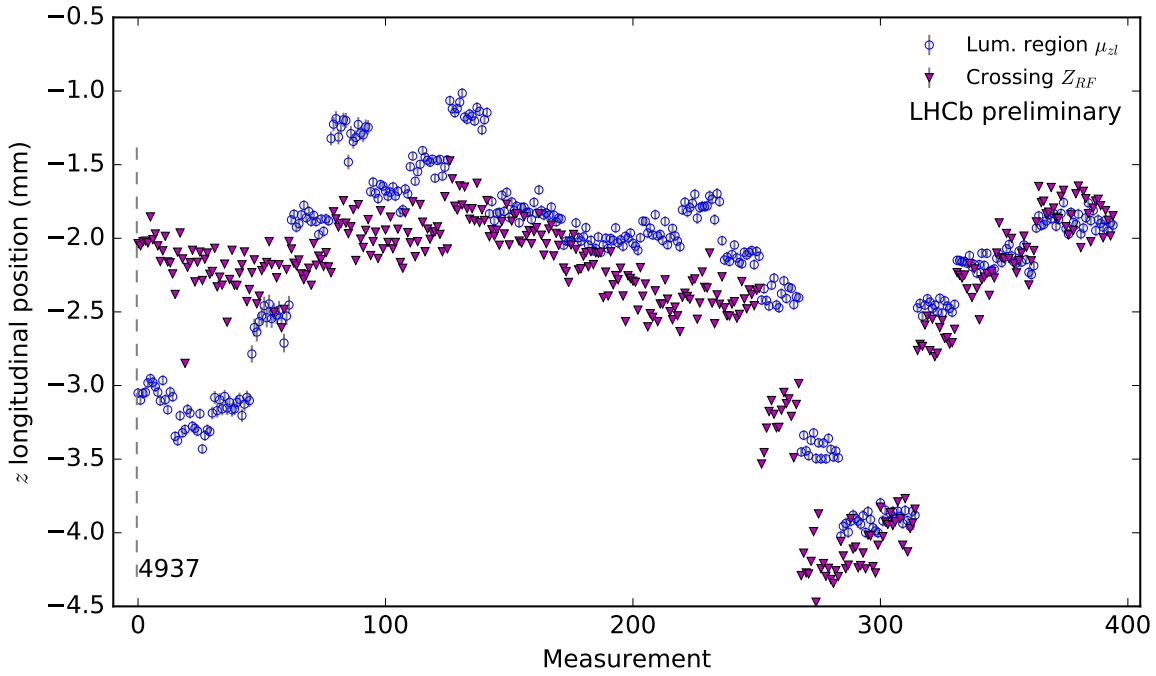

Figure 2.29: The measured positions of the bunch crossing point Z_{RF} and the luminous region centre μ_{zl} for fill 4937. The measurements are sorted by time and by BCID.

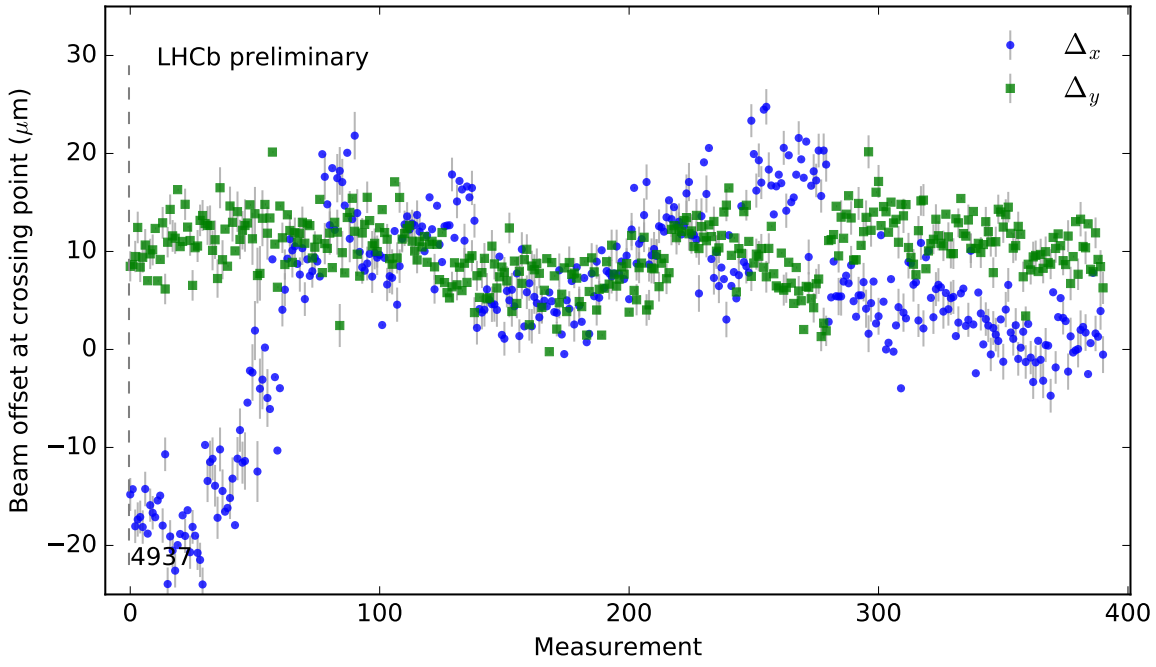

Figure 2.30: The measured transverse position of the bunch crossing point Z_{RF} throughout fill 4937. The measurements are sorted by time and by BCID.

2.6.4 Fit Corrections

The measurements of beam parameters in the sections above are made under the assumption of stationary beams and perfect alignment of the VELO subdetector. Corrections are described below for the real world accelerator conditions where beam drifts and detector misalignments are possible.

VELO Detector Alignment

The alignment of the VELO sensors is not perfect and any misalignment will have a subsequent effect on the measured luminous region position. The transverse shape and position of the luminous region is one of the constraints on the global fit used to evaluate the overlap integral. This region is measured in 18 separate z slices across the longitudinal region defined by $-100 < z < 115$ mm. Any offset in the measured transverse position of these slices can cause tensions in the global fit and affect its convergence and quality. The longitudinal variation of the transverse coordinates of the luminous region, $\mu_{ml}(z)$ (for $m = x, y$), is measured on a fill-by-fill basis. The expectation based on the fits, $\tilde{\mu}_{ml}(z)$, is also evaluated for each fill. The offset between these two positions, $\delta\mu_{ml}(z)$, is defined as in Eq. 2.27.

$$\delta\mu_{ml}(z) = \mu_{ml}(z) - \tilde{\mu}_{ml}(z) \tag{2.27}$$

An example from fill 4937 of these measurements, predictions and offsets is shown in Fig. 2.31. The measured transverse luminous region positions and the predicted values are shown for each axis above and the offset between the two for each axis is shown in the two plots below.

In order to make use of these measured offsets to correct the fit as described in Sec. 2.6.2 their values, $\delta\mu_{ml}(z)$, are added to the positions of the distributions used in Eqs. 2.13 and 2.16. The offset value used for each z slice of the luminous region is calculated by taking the average of the measured offsets over that region in z. This procedure is, therefore, able to correct for the effect of any misalignment on the measured luminous region position. This correction requires the fits of the luminous region to be performed twice: a first time in order to generate the predicted positions per BCID and a final measurement including these offset corrections which is used for the overlap measurement.

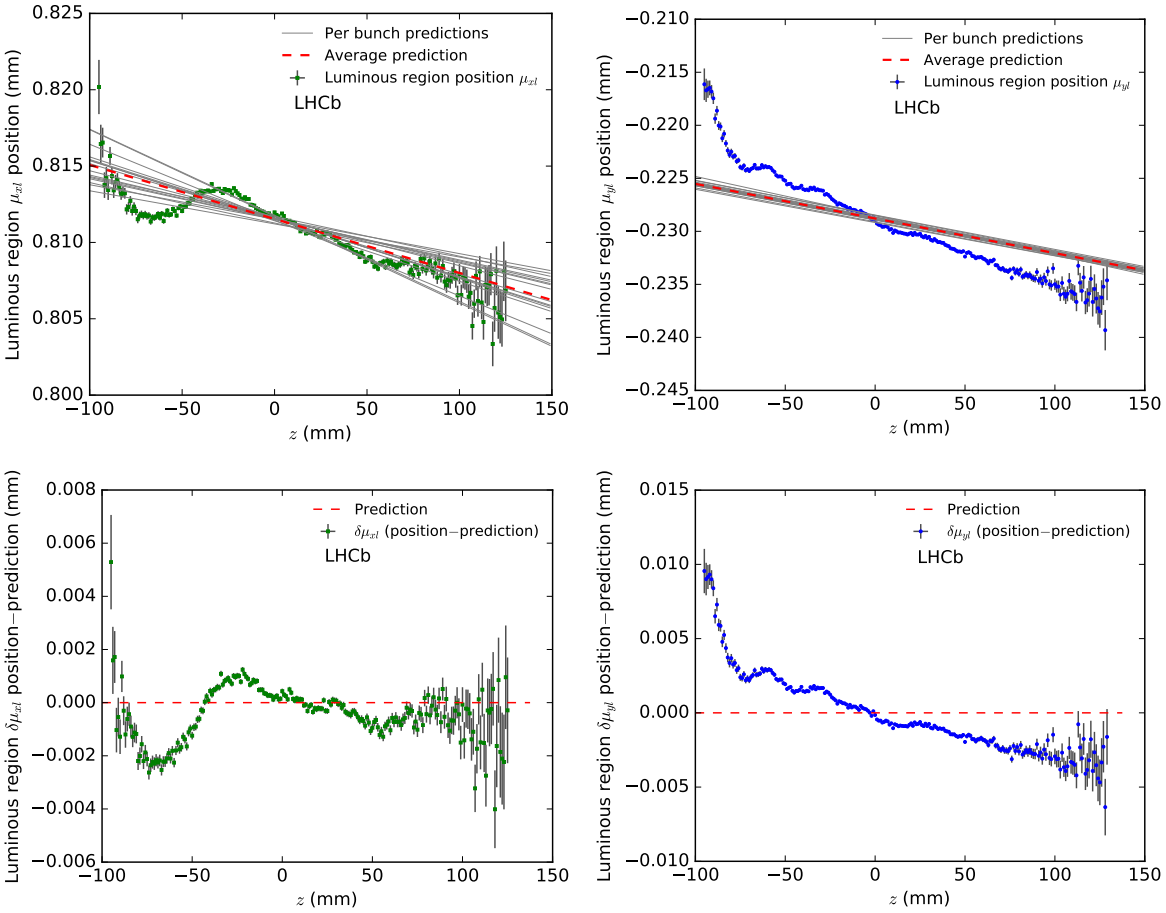

Figure 2.31: Detector alignment corrections for the VELO from fill 4937. The measured positions and predictions from the transverse fits are shown above for x (left) and y (right) with the difference between these shown below for the same axes. Each data point is a Gaussian fit of the beam-beam interaction vertices at the given z position, using vertices from all colliding bunches. The error bars shown are statistical. The solid grey lines on the top plots show the predicted positions per bunch pair. The variation in these is larger in x as the crossing angle is implemented in the xz plane.

Beam Position Drift

The positions of each beam can drift over time and fluctuations on the order of 10 μm are not out of the ordinary over the course of an LHC fill. The BGI measurements are integrated in time bins of 15 minutes and any beam drift during this time period will have an effect on the shapes and positions of the two beams. The beam positions used to evaluate the offset between beams are thus an average of the true beam positions over this integration time and the transverse shapes are a convolution of the beam shape with the both detector resolution and beam movement over the 15 minutes.

An example of a beam drift measurement is shown in Fig. 2.32 for data from fill 4937. These beam positions are measured in time bins of 30 seconds as the mean of a single Gaussian

fit to all beam-gas vertices from all bunches of the relevant beam. The broadening of the beam image due to the drifting positions of the beams is accounted for by adding the standard deviation of the measured relative beam positions to the resolution in quadrature for each 15 minute integration period. This correction has a negligible effect on the calibration measurement as the typical drift over one integration period is on the order of 1 μm or less and with $\beta^* = 24$ m beam widths are typically greater than 100 μm.

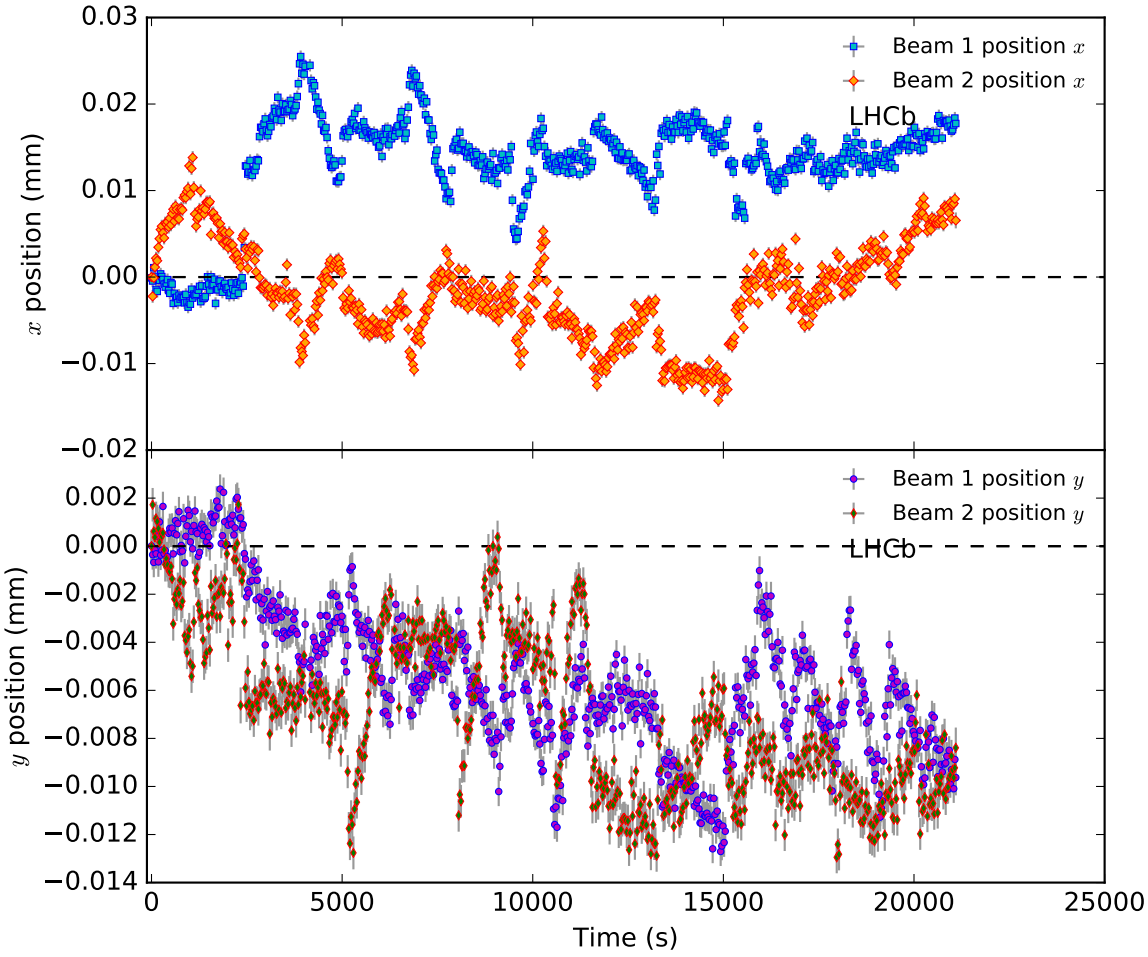

Figure 2.32: The orbit drift as measured for each beam in each axis for fill 4937. The absolute position at the start of the fill is taken as zero in order to show clearly the drift over time. Each point is measured using vertices from all bunches recorded in a 30 s interval. The error bars shown are statistical.

2.7 Overlap Integral Calculation

The beam parameters required for the evaluation of the overlap integral are measured using the methods described in Sec. 2.6. The beam-gas and beam-beam interaction vertices for each colliding bunch pair are integrated in time bins of 15 minutes. The measurement is

performed in multiples stages making use of all vertices selected according to the criteria described in Sec. 2.4.

The overlap is calculated under the assumption that the transverse distribution of the colliding bunches is a double Gaussian in form, as described in Sec. 2.6.2, with a narrow component denoted by n and a wide component denoted by w. It is also assumed that the longitudinal profile of the beam distribution is single Gaussian in form and that the the two Gaussian components of the transverse distribution are centred at the same position. In this case the distributions ρ_m (with $m = x, y$) have the form given in Eq. 2.28:

$$\rho_m(m; \mu_m, \sigma_{n,m}, \sigma_{w,m}) = w_n g(m; \mu_m, \sigma_{n,m}) + w_w g(m; \mu_m, \sigma_{w,m}) \tag{2.28}$$

Where $g(m; \mu_m, \sigma_m)$ is a normalised Gaussian function with mean μ_m and width σ_m and the weights (w_w and w_n) are defined such as to satisfy the equation $w_w + w_n = 1$. In this case the overlap integral can be written as the weighted sum of 16 components as in Eq. 2.29:

$$\mathcal{O}_d = \sum_{i,j,k,l} w_{i,j} w_{k,l} \mathcal{O}_{i,j,k,l} \tag{2.29}$$

where the indices i, j, k, l define the beam parameter combinations: $i \in \{x_{1n}, x_{1w}\}$, $j \in \{y_{1n}, y_{1w}\}$, $k \in \{x_{2n}, x_{2w}\}$, $l \in \{y_{2n}, y_{2w}\}$. The contributions from individual overlap terms, $\mathcal{O}_{i,j,k,l}$, are calculated as described in Sec. 1.5 and the fractions in this sum, $w_{i,j} w_{k,l}$, are calculated according to Eq. 2.15.

The results of these overlap calculations for run 2 are shown in Fig. 2.33 and the number of vertices and their types for each measurement are shown in Fig. 2.34 below. The value of the overlap remains relatively stable throughout fill 4937, increasing by a maximum of 7% with respect to its initial value, and is unaffected by the variations in the size of the vertex sample shown in Fig. 2.34.

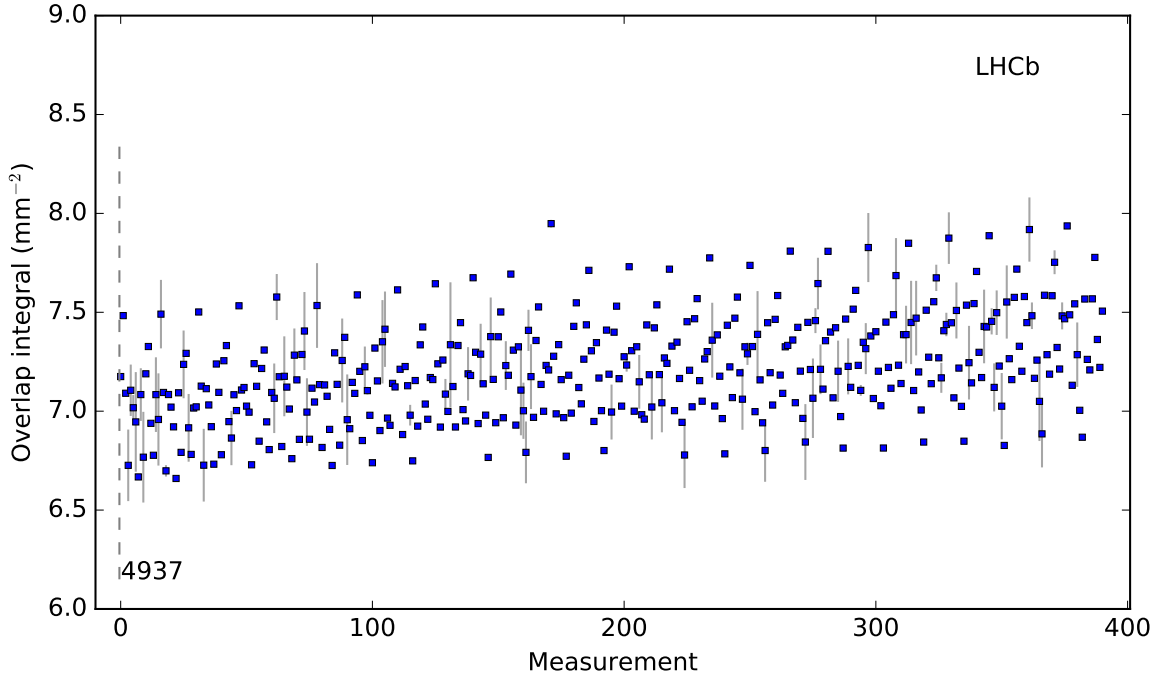

Figure 2.33: Overlap integral results calculated via beam-gas imaging.

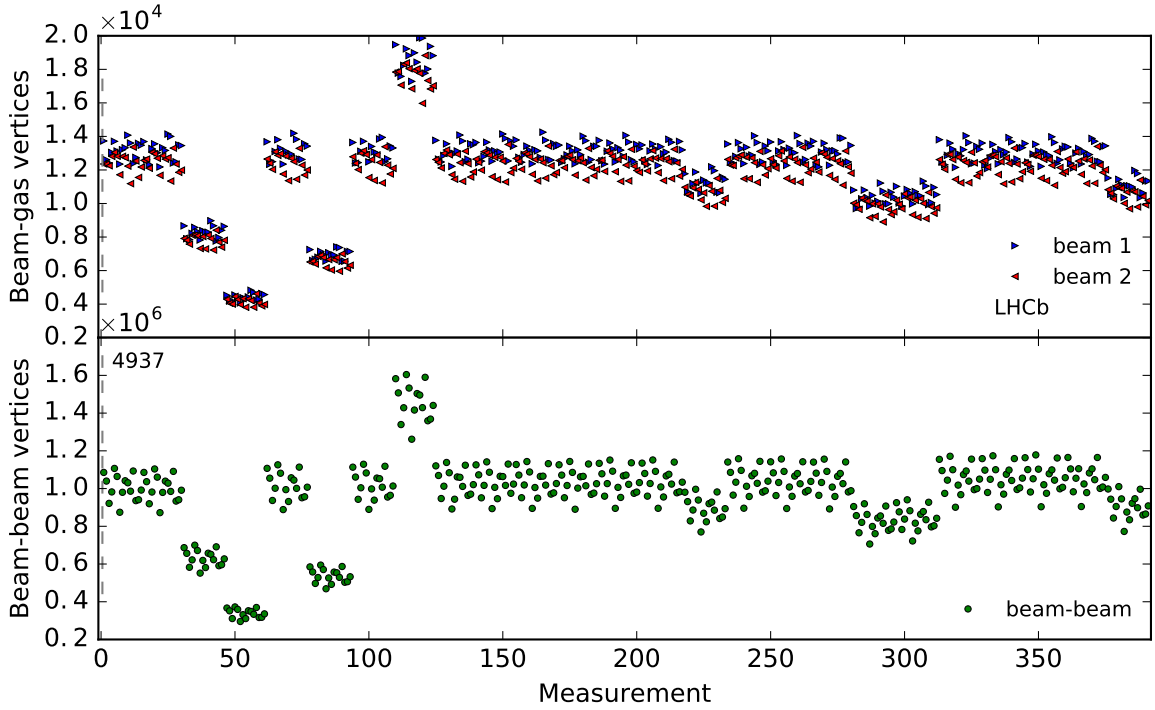

Figure 2.34: The number of vertices of each type used to make the measurements shown in Fig. 2.33.

2.8 Conclusions

In this chapter the different aspects of the Beam-Gas Imaging technique have been presented along with the results of measurements made using this approach for data collected by the LHCb experiment throughout run 2 of the LHC. The basic principle of the BGI measurement has been outlined along with the data taking, event selection and trigger setup. The method for determining the resolution of vertex position measurements via the splitting of vertices has been described and results from a selection of fills are reported. The measurement approach for the geometrical beam parameters, including the positions and relative angles of the beams, has been described in detail and the results of these measurements are given. A variety of approaches, of increasing complexity, for measuring the transverse distribution of bunches have been presented and the results of these fits to LHCb data have been ascertained. Finally the method for calculating the overlap integral necessary for a luminosity measurement is shown (bringing together the measurements of beam parameters presented earlier) and the results of this integral are reported.

Chapter 3

Bunch Population and Ghost Charge Measurements

3.1 Measurement of Bunch Populations with LHC Instrumentation

Multiple pieces of instrumentation are necessary for an accurate picture of the longitudinal distribution of charge around the LHC ring. The Fast Beam Current Transformer, or FBCT, is the standard piece of LHC instrumentation used to measure the relative populations of the bunches circulating around the LHC ring [46]. The total beam intensity is measured using a piece of LHC instrumentation known as the Direct Current Current Transformer or DCCT [41, 42]. This device measures the total charge in each beam without reference to the bunch structure. Both instruments are described in detail below.

3.1.1 The Direct Current Current Transformer

The DCCT system, designed and built at CERN, is based on the fluxgate magnetometer principle [42, 43]. This principle exploits the non-linear magnetisation curve of soft ferromagnetic materials. The transformers themselves consist of a conducting coil wrapped around a circular ferromagnetic core that is traversed by the beam whose current is to be measured. A simple example of such a setup can be seen in Fig. 3.1. As the current of the accelerated beam passes through the transformer ring a measurable current is induced in the coil of wire. However, if this coil is simply connected to a load resistor as in Fig. 3.1 then it will have a low frequency AC response determined by the inductance of the coil and the magnitude of the load resistance. In practical cases this would usually be in the range of a few kHz.

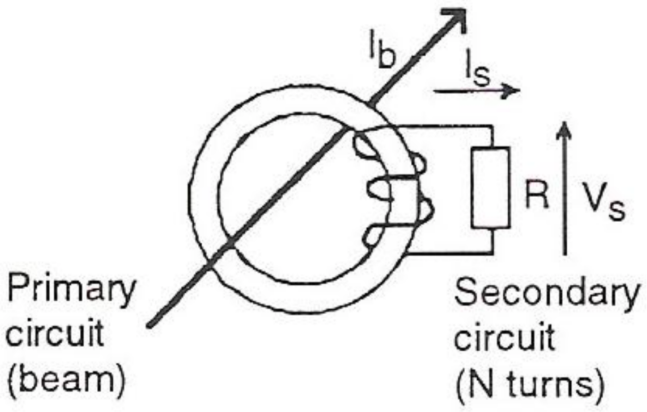

Figure 3.1: A schematic diagram showing an AC beam current transformer [43].

In order to achieve the necessary DC response, a magnetic modulator is employed and the beam passes through two separate cores with opposite windings, as shown in Fig. 3.2.

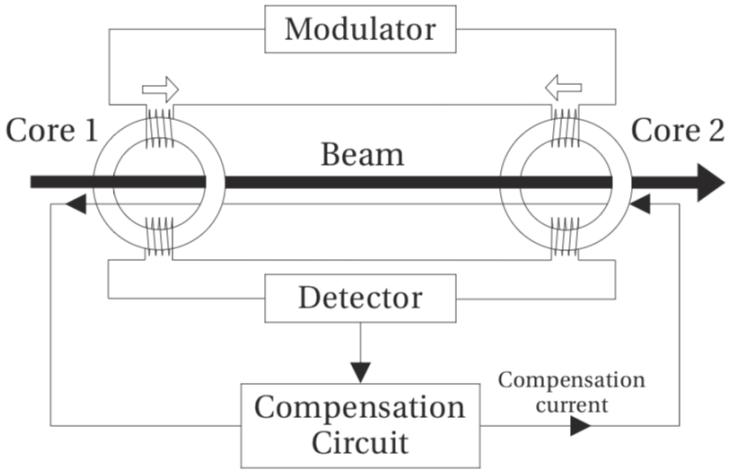

Figure 3.2: A schematic of the two-core magnetic modulator approach used for the LHC DCCT system [44].

When a core is fed a modulation current a magnetic induction, B, is created in the core material which in response creates a magnetic field, H, in the coil. There is a non-linear relationship between the induction in the core material and the field in the coil and a waveform $H(t)$ will be created in the coil. If two identical cores are wound in opposite directions and the same modulation current is applied to each then the difference between the waveforms induced in each will be zero. If, however, a beam current passes through the centre of the two coils it will induce an external field of opposite direction in each of the cores and their waveforms will no longer be symmetric. The cores can then be connected to a feedback circuit which will produce the necessary compensation current to cancel out the detected asymmetry. The magnitude of the required compensation current provides a direct measurement of

the beam current. At the LHC each DCCT system is comprised of a set of two such carefully matched cores per beam driven by a modulator operating at a frequency of 215 Hz. In order to increase the bandwidth of the system the output of this dual core system is combined with the response of a third core configured as a fast current transformer [45]. This third core is separated from the two matched cores by a layer of magnetic shielding in order to prevent modulation crosstalk.

3.1.2 The Fast Beam Current Transformer

The FBCT is designed to produce a signal proportional to the charge in a bunch slot at a response rate of 40 MHz, so as to operate synchronously with the LHC bunch spacing of 25 ns. It does this by integrating the charge observed within a fast gate. A schematic overview of one of the FBCT instruments can be seen in Fig. 3.3. The beam current is measured using a 1:40 toroid supplied by Bergoz Instrumentation [47]. The signal from this toroid is split using an RF distributor into two dynamic ranges (low and high gain) each of which can provide measurements in two bandwidths (low and high bandwidth): approximately 2 MHz for turn-by-turn measurements and about 200 MHz for bunch-by-bunch measurements.

These four measurement signals are integrated using an analog integrator ASIC and sampled using 14 bit ADCs clocked so as to operate synchronously with the beam. The FBCT has two different integrators (of the same type), that are used alternatively to integrate odd and even bunch slots respectively. The entire measurement process is driven by two Digital Acquisition Boards (DABs). Each DAB processes the two integrated signals of the same bandwidth using an FPGA. The electronics are configured such that the gain will switch from high to low at around $2.3 \times 10^{10} p$ per bunch. Proton data are thus usually taken with the low gain setting while measurements of the ion beams more typically use the high gain.

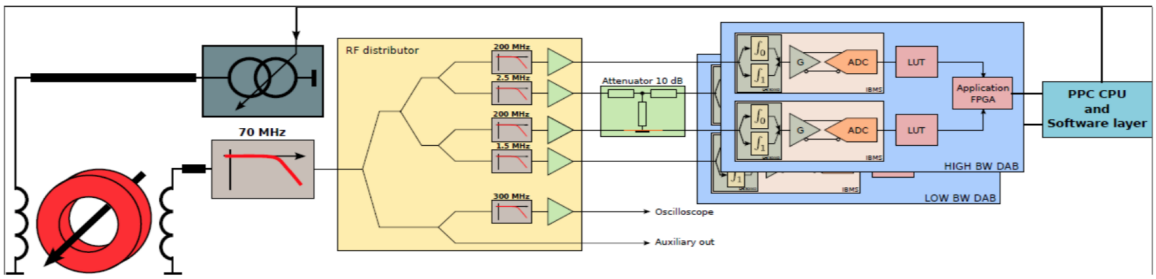

Figure 3.3: A schematic diagram of the FBCT and its DAQ [46].

3.1.3 Bunch Population Measurement

It is necessary to normalise the bunch-by-bunch measurements from the FBCT to the total current from the DCCT as the absolute values of the measurements provided by the former devices are not sufficiently accurate. Each beam is equipped with two sets of each type of bunch current transformer, which are operated independently and known as system A and system B. If all instruments are working perfectly the measurements from systems A and B should agree to within 0.1%. Each system thus serves as a precision cross-check on the other and, in practical terms, operating with two systems gives suitable redundancy in case of technical problems with one set of instruments. For the measurement of relative bunch populations an alternative device to the FBCT called the Beam Pickup Timing System, or BPTX, is also available. The BPTX is a part of the ATLAS experiment and is located at interaction point 1 of the LHC ring. It has a larger measurement noise than the FBCT but serves as a useful cross check as it does not discriminate between even and odd numbered bunches. The BPTX hardware is described in detail in Ref. [48].

The total population of charges measured by the FBCT for a given beam, $N_{tot,fbct}$, is the sum of the measured individual bunch populations, N_i, for all bunches, i, in the set of nominally filled bunches, $\mathcal{M}$, such that:

$$N_{tot,fbct} = \sum_{i \in \mathcal{M}} N_{i,fbct} \tag{3.1}$$

The bunch population fractions P_i assigned by the FBCT can then be defined as follows:

$$P_i = \frac{N_{i,fbct}}{N_{tot,fbct}} \text{ and } \sum_{i \in \mathcal{M}} P_i = 1 \tag{3.2}$$

These population fraction values, P_i, are the relevant values measured by the FBCT (and cross-checked against the BPTX) for each nominally filled bunch slot. For the purposes of an accurate luminosity measurement the value of the total beam population is then normalised to the value measured by the DCCT, $N_{tot,dcct}$. The DCCT normalisation is also adjusted slightly to take into account corrections due to ghost and satellite charges, which will be discussed later in the current chapter (Sec. 3.2). These population fractions are then combined with this corrected total beam population so that the measured values of the bunch population of a colliding bunch j, N_j, would be given by Eq. 3.3. As the luminosity is calculated per bunch crossing and in time bins, these bunch populations are also calculated in time bins as are the ghost charge corrections to the total beam current.

$$N_j = P_j N_{tot,dcct} \tag{3.3}$$

As an example, the measurement of the total beam population from a luminosity calibration

fill that took place in May 2016 can be seen in Figs. 3.4 and 3.5 while the measurement of the individual bunch populations from the FBCT can be seen in Fig. 3.6 and the difference in the total beam current as measured with each device is shown in Fig. 3.7 as a percentage of the reference value measured by the DCCT. During this calibration fill, the beam and machine conditions were well controlled and the two DCCT systems, A and B, were in agreement to within 0.03%, once stable beams were achieved.

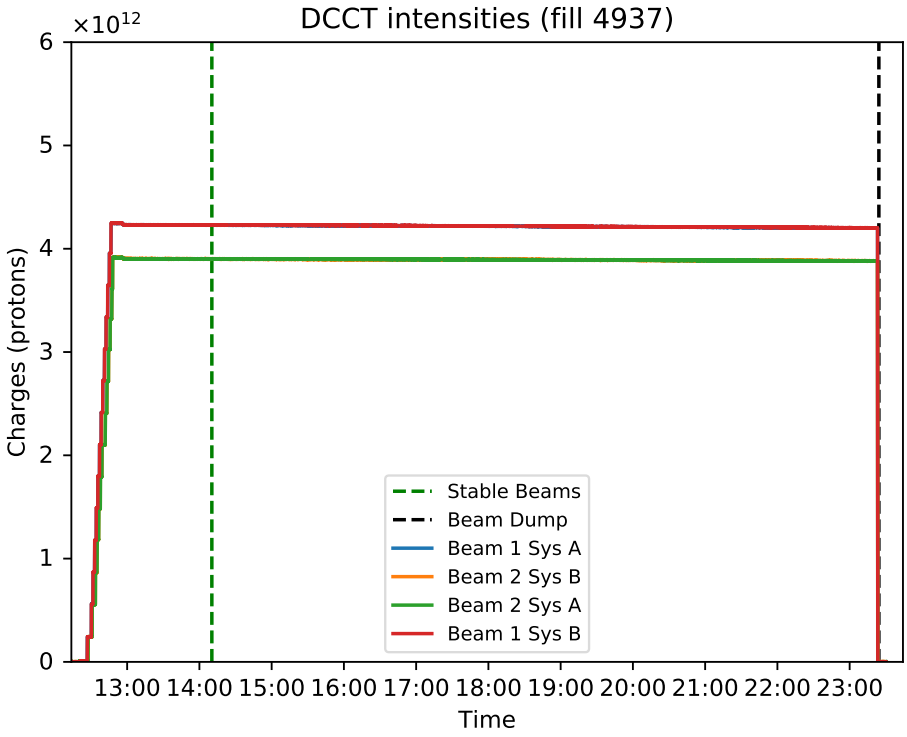

Figure 3.4: The total number of charges measured in each beam by the DCCT in LHC fill No. 4937. In this particular fill the two systems agree well enough to be indistinguishable as can be seen from Fig. 3.5.

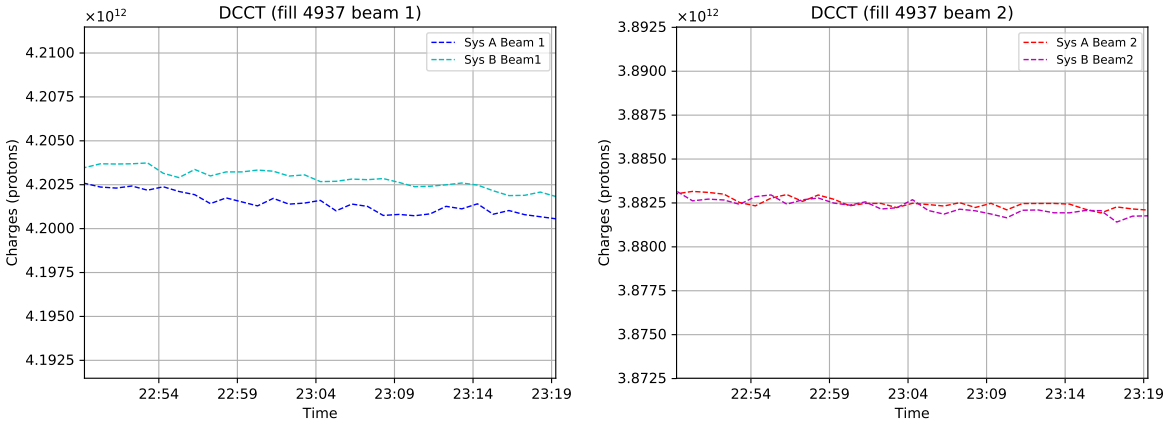

Figure 3.5: A zoomed view of the the total beam populations measured by DCCT systems A and B for each beam during 30 minutes close to the end of fill 4937.

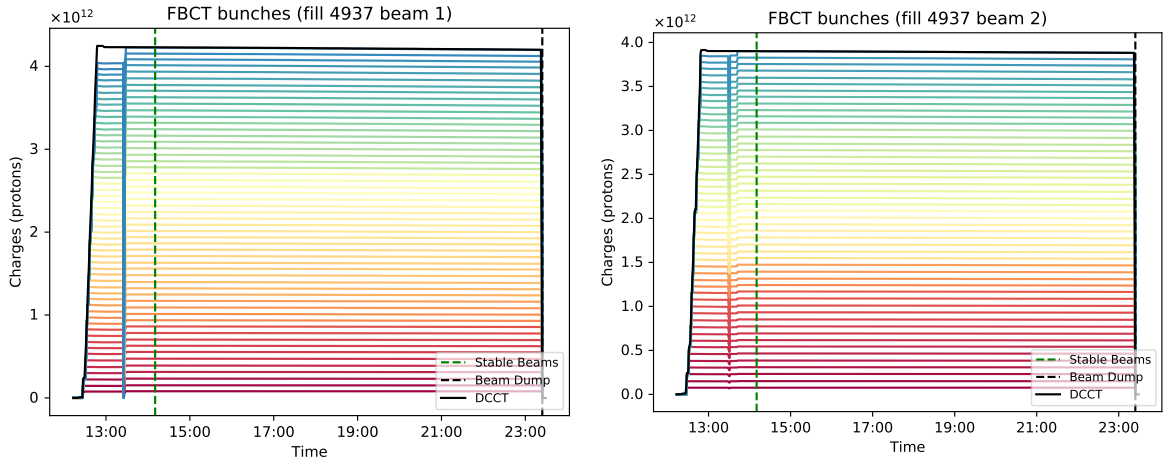

Figure 3.6: The individual bunch populations over the fill are shown here stacked so that they add up to the total beam population envelope provided by the DCCT.

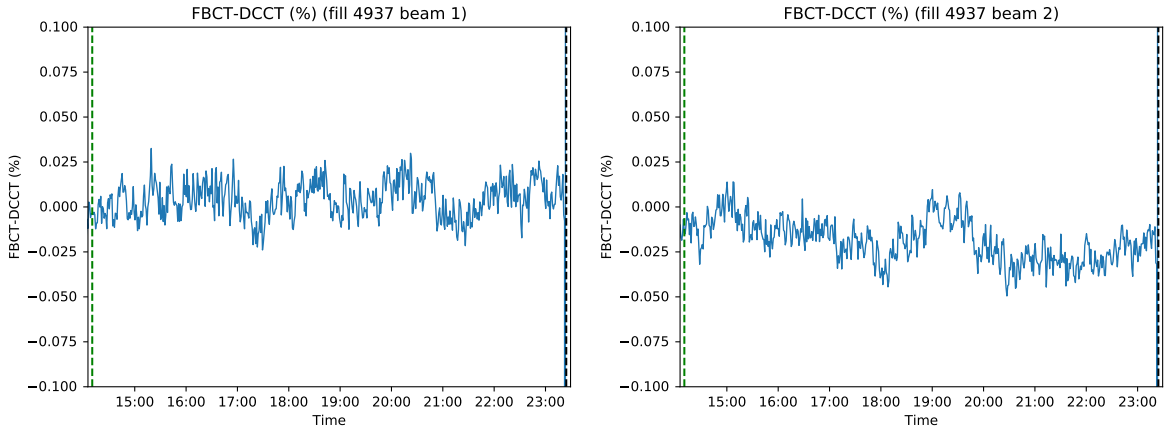

Figure 3.7: These two plots show the difference between the total beam populations measured by the DCCT and the sum of the individual bunch populations as measured by the FBCT. This value is given as a percentage of the total beam intensity measured by the DCCT.

3.1.4 DCCT Calibration and the Beam Current Uncertainty

The uncertainty on this beam current measurement was the dominant uncertainty for early luminosity calibrations at the LHC [5, 41]. A significant calibration effort was undertaken by the CERN Beam Instrumentation group and scientists from the experiments to reduce this uncertainty [41]. This calibration reduced the uncertainty for the final run 1 LHCb calibration to within $\sim$0.3% [5]. In run 2 a 16 bit ADC replaced the 12 bit model in use during run 1 and this was later further upgraded to a 24 bit model. A significant increase in performance could be expected from this new electronics, however, no detailed calibration effort has yet been completed to quantify this improvement [49]. In this thesis therefore, the value of the uncertainty is calculated as for the 12 bit ADC and this is used as a conservative estimate of

the uncertainty on the measurements made by the current equipment.

3.2 Ghost and Satellite Charges

As the DCCT measures the total circulating charge without reference to the time-structure of the beam it also picks up any charge which is outside of the nominally filled bunches. These charges, known as ghost charges, do not contribute to the luminosity seen by the LHCb detector and thus should be subtracted from the total charge value used as part of the luminosity calibration. They arise largely in the injector chain of the LHC and their value is dominated by the quality of PS to SPS bunch-to-bucket transfer [50]. This is a procedure where the longer PS bunches ($\sim$12 ns in length) are rotated in longitudinal phase space such that they fit into the shorter SPS buckets ($\sim$5 ns in length). This rotation takes place before extraction from the PS and some particles in the bunch tails are lost and can be recaptured in neighbouring buckets [51].

The intensity of charge in these nominally empty bunch slots is still very low with respect to the charge in filled slots, as can be seen in Fig. 3.8. It is thus below the threshold necessary for an observation with the FBCT. There are, however, two measurement approaches that do allow us to observe these charges. The Longitudinal Density Monitor, or BSRL, uses a synchrotron light telescope to measure the light emitted by these protons as they pass through a dedicated magnet setup. The LHCb experiment, on the other hand, can establish the proportion of these charges by comparing the number of beam-gas interactions from crossings involving filled bunch slots and those where bunch slots are nominally empty.

Conventionally, the term ghost charge refers to any charge found outside the nominally filled 25 ns bunch slots around the LHC ring. Satellite charges are those charges sitting within a filled bunch slot but outside the central 2.5 ns RF bucket of that slot. Both sets of charges are picked up by the LHC direct current current transformers (DCCTs) but do not contribute to the collisions seen by the LHC experiments. It is thus necessary to measure the fraction of these charges in order to correct the precise total charge from the DCCTs, which is used for normalisation in luminosity calibrations. In Run 2, the size of this correction varied from the percent (typical with ion beams) to the per mille level (typical during nominal proton physics).

LHCb can measure the fraction of ghost charges by counting the number of beam-gas interactions observed during empty-empty crossings, where both slots are nominally empty. Counts are normalised to absolute charge using data from beam-empty crossings, where one of the two beams contains a nominally filled bunch with a known intensity. Both satellite and ghost charges are visible to the BSRL, which makes use of the synchrotron light emitted by the circulating particles to measure the longitudinal charge distribution [50, 52].

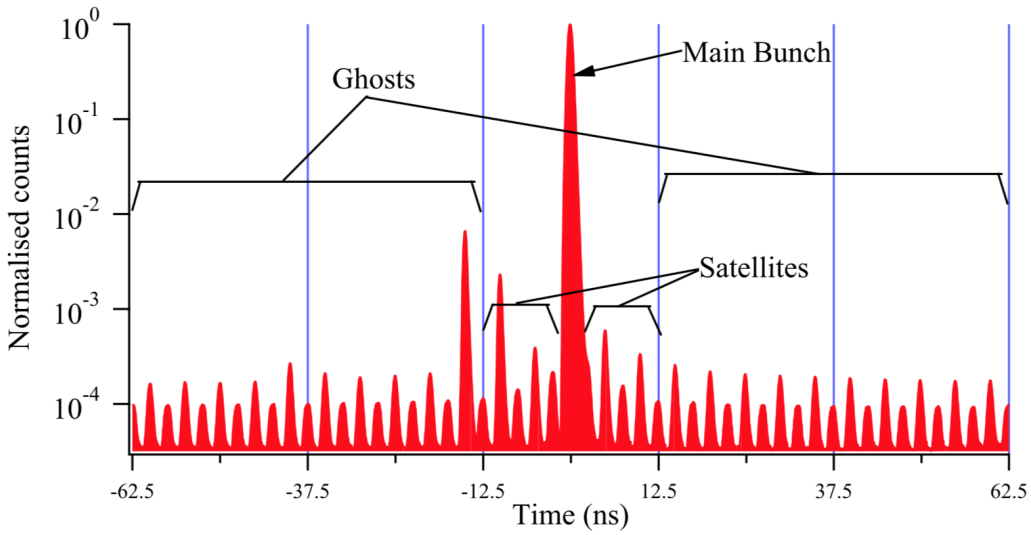

Figure 3.8: The longitudinal profile of an LHC beam in the region around one particular filled bunch slot as measured by the BSRL. The central bucket of the 25 ns slot can be seen to contain the main bunch charge and the surrounding satellite and ghost charges are seen to be orders of magnitude lower in intensity [50].

3.2.1 The Longitudinal Density Monitor

The Longitudinal Density Monitor (BSRL) is a piece of LHC instrumentation located at P4 on the LHC ring. It is made up of two Beam Synchrotron Radiation Telescopes (one per beam) based on the detection, with precise timing, of single synchrotron light photons emitted by the LHC beams. Synchrotron radiation is the electromagnetic radiation emitted when charged particles undergo a radial acceleration, as in the bending magnets of an accelerator such as the LHC. The frequency and intensity of the emitted radiation is strongly related to the energy and intensity of the accelerated beams. Moreover, the synchrotron radiation has the same time structure as the emitting beam and thus measuring the longitudinal profile of this radiation is equivalent to making a profile of the beam.

The principle of operation of this device is as shown in Figs. 3.9 and 3.10. The synchrotron radiation is emitted in the magnets shown in Fig. 3.9 and extracted 27 m downstream by a mirror to be observed by the BSRL. The emission from the dipole magnet is sufficient for a precise measurement at beam energies above 1.2 TeV, however, the presence of a purpose-built undulator is necessary for observation of beams when operating below this energy threshold (e.g. at injection). The captured photons are captured in an avalanche photo-diode (APD) and their arrival times relative to the LHC clock are then recorded by a time-to-digital converter, as shown in Fig. 3.10. A histogram can then be built up of the number of photons arriving within time bins corresponding to the RF structure of the LHC beams. After an integration time of $\sim$10 s the BSRL provides a clear longitudinal profile of

the main bunches in the circulating beams, while a precise observation of the much lower intensity ghost charges requires an integration time of closer to ∼5 minutes.

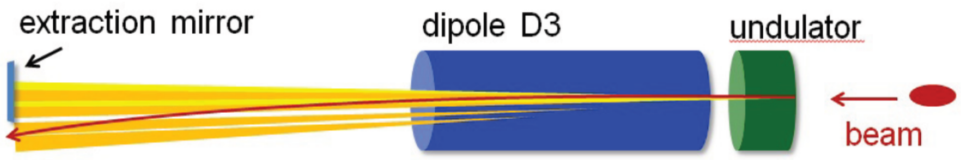

Figure 3.9: A sketch showing the emission of synchrotron radiation in the magnets close to P4 and its extraction for observation by the BSRL. The D3 dipole shown is a special class of dipole designed to increase the separation between the beams before their acceleration in the RF cavities [62].

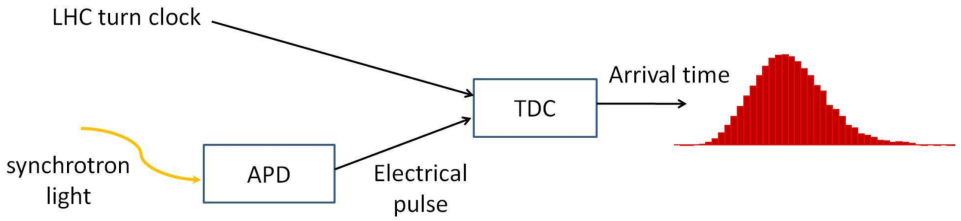

Figure 3.10: A schematic diagram showing the BSRL operating principle [50].

3.2.2 Satellite Charges

The population of all filled bunch slots of length 25 ns is nominally concentrated in one main RF bucket of length 2.5 ns. In reality, however all such bunches will contain some fraction of out of time charges that sit within the correct bunch slot but outside of the main bucket. These are the satellite charges and will be counted by the FBCT as it measures charge in bins of 25 ns but they do not contribute to the visible luminosity at LHCb. The BSRL (described in Sec. 3.2.1) is able to distinguish these charges from those in the nominal bucket and can provide a precise measurement of the fraction of satellite charges in each filled bunch slot.

While the ghost charge fraction affects the total beam intensity the satellite fraction affects the bunch intensity and has a different value for each bunch slot. The corrected bunch population, $N'_{i,j}$, for all charges in the nominally filled bucket of a nominally filled bunch slot i in beam j can be written as in Eq. 3.4 given the ghost charge fraction for the beam, $f_{ghost,j}$, and the satellite fraction for the bunch slot, $f_{sat,i,j}$:

$$N'_{i,j} = N_{i,j} \frac{N_{tot,j}(1 - f_{ghost,j})}{\sum_{i \in \mathcal{M}} N_{i,j}} (1 - f_{sat,i,j}) \tag{3.4}$$

where $\mathcal{M}$ is the set of all nominally filled bunches in beam j, the bunch population values $N_{i,j}$ are those measured by the FBCT or BPTX and $N_{tot,j}$ is the total beam population for beam j as measured by the DCCT. The proportion of satellite charges was very well controlled during the run 2 luminosity calibration sessions and this correction was generally on the order of 0.01% or less, while in run 1 they had been closer to 0.1% on average [7]. The average satellite fractions per beam as measured by the BSRL are given in Table 3.1 for a selection of fills relevant to the BGI analysis.[1]

Fill	$f_{sat,1}$	$f_{sat,2}$
4937	1.06×10^{-4}	7.41×10^{-5}
5456	2.33×10^{-3}	2.53×10^{-3}
6012	1.78×10^{-5}	8.30×10^{-5}
6864	1.59×10^{-4}	2.66×10^{-4}

Table 3.1: The average satellite charge fractions per beam circulating in the LHC as measured by the BSRL in the relevant fills. The fraction is likely higher in fill 5456 as this was part of a machine development session not a luminosity calibration session and the total charge was lower as only 10 bunches were injected per beam.

3.2.3 LHCb Ghost Charge Measurements

The BGI and BSRL measurement techniques are independent and generally in good agreement, allowing us to establish precise and accurate values for the ghost charge correction. Since the beginning of run 2 these values have generally been found to be very low and stable throughout the duration of $p-p$ calibration fills. The ghost charge fraction is generally higher during ion physics and can increase significantly throughout a fill as the total beam intensity decreases rapidly due to losses from collisions (see Sec. 3.3). The ghost charge fraction can also increase due to imperfect capture of the bunch charge within the LHC RF system, this is a problem that has been observed multiple times throughout run 2 (see Secs. 3.2.4 and 3.2.6).

To the first order the ghost charge fraction for a given beam, $f_{gc,i}$, can be calculated from the ratio between the number of beam-gas interactions observed for that beam in empty-empty crossings, n_{ee}, and the number observed in either beam-empty or empty-beam crossings, $n_{be/eb}$ (for beams 1 and 2 respectively). This ratio is then normalised with the ratio of the number of particles in beam-empty slots, N_{be}, compared to the full population of the relevant beam N_{beami}. A trigger efficiency correction factor ϵ_{tt} is also applied to take into account the fact that ghost charges can spread over the bunch slot. This calculation is shown for beam 1 in Eq. 3.5.

[1] Results based on data files extracted from: /eos/project/l/lhc-bsrl/Analysis/.

$$f_{gc,1} = \frac{n_{ee}}{n_{be}} \frac{N_{be}}{N_{beam1}} \frac{1}{\epsilon_{tt}} \tag{3.5}$$

The calculation shown in Eq. 3.5 relies on several assumptions. Firstly the target for both the beam and ghost protons must be identical, this holds as the gas is the same in either case. We also assume that at the centre of the bunch slot the efficiency is the same in both beam-empty and empty crossings and that all of the ghost charge interactions with the gas take place in empty-empty crossings. In certain cases, however, the detector dead time can lead to a difference in efficiency between crossing types and in others an accurate measurement requires beam-gas vertices from empty slots where the opposing slot is filled to be counted. Both of these situations are described in detail in Sec. 3.3.

The principal source of systematic uncertainty on the LHCb measurement of the ghost charge is the trigger efficiency correction mentioned above. The overall scale of the trigger efficiency is not important as it will be the same for vertices originating in both be and ee crossings and its value will therefore cancel when their ratio is taken as part of the ghost charge calculation in Eq. 3.5. The trigger timing dependence is due to the 25 ns timing granularity of the LHCb experiment and leads to a drop in efficiency for vertices reconstructed away from the centre of a bunch slot as well as the possibility for double counting of vertices. This is not a problem for the normal operation of the experiment as the charge in each nominally filled LHC bunch is injected such that it is trapped in the central 2.5 ns bucket of the relevant 25 ns slot. The collisions in beam-beam crossings are thus separated by the full 25 ns bunch spacing and the detector is time aligned for them. The ghost charge, however, could be distributed uniformly throughout all of the buckets that make up each bunch slot and thus if a beam-gas interaction occurs near the bunch slot edges the resulting signal in the detector may last long enough to be acquired by the trigger in the following slot. This could lead to some vertices being counted twice and thus bias the ghost charge measurement.

This effect can be corrected by identifying double-counted vertices as those which have both consecutive BCIDs and consecutive event IDs. The event ID is a value that is incremented for each accepted trigger. The relative uncertainty on the ghost charge fraction associated with this correction is usually on the order of a few percent. The trigger efficiency correction factor for each type of counting and their associated uncertainties were measured in 2013 and are given in table 3.2 [7]. These correction factors are obtained by measuring beam-gas rates after the introduction of a clock shift and comparing these rates with those measured at zero shift. This time shift is set to be equivalent to the possible longitudinal displacement of the ghost charge and subsequently leads to an equivalent decrease in efficiency [7].

Beam	ϵ_{tt} (double counting)	ϵ_{tt} (single counting)
1	1.05 ± 0.03	0.93 ± 0.02
2	0.90 ± 0.01	0.86 ± 0.01

Table 3.2: Relative beam-gas trigger efficiency correction factors for the ghost charge measurement assuming a constant charge distribution within a bunch slot [7].

The time-binned ghost charge fractions for the principal LHCb proton-proton calibration fills are shown in Figs. 3.11, 3.12 and 3.13. The full time-binned ghost charge results and their uncertainties, as determined using the LHCb BGI technique for each fill of interest during run 2 are presented in Appendix A. The measured ghost charge fractions remained stable throughout each fill and the average value per beam for each fill was used as the bunch population correction for the luminosity calibration measurement described in Chapter 4.

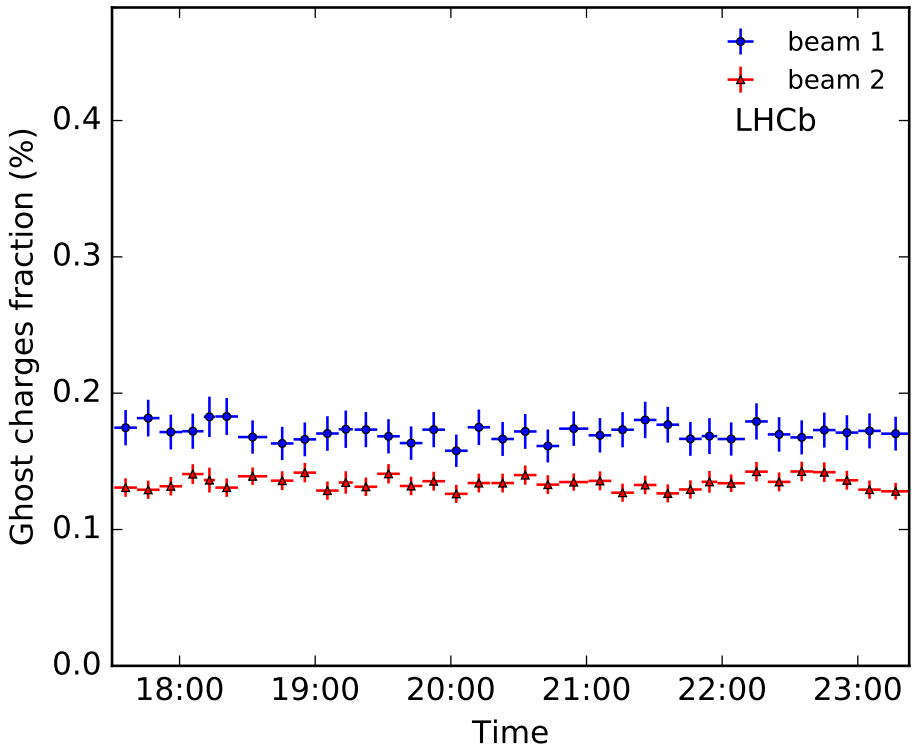

Figure 3.11: Ghost charge measured by LHCb throughout the 2016 p-p calibration fill no. 4937.

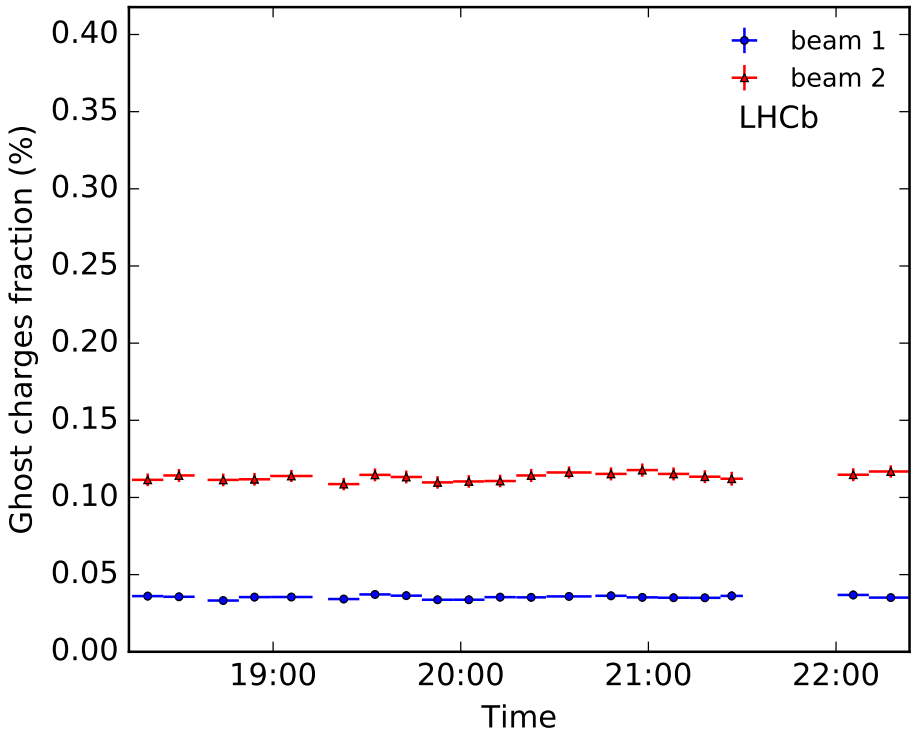

Figure 3.12: Ghost charge measured by LHCb throughout the 2017 p-p calibration fill no. 6012.

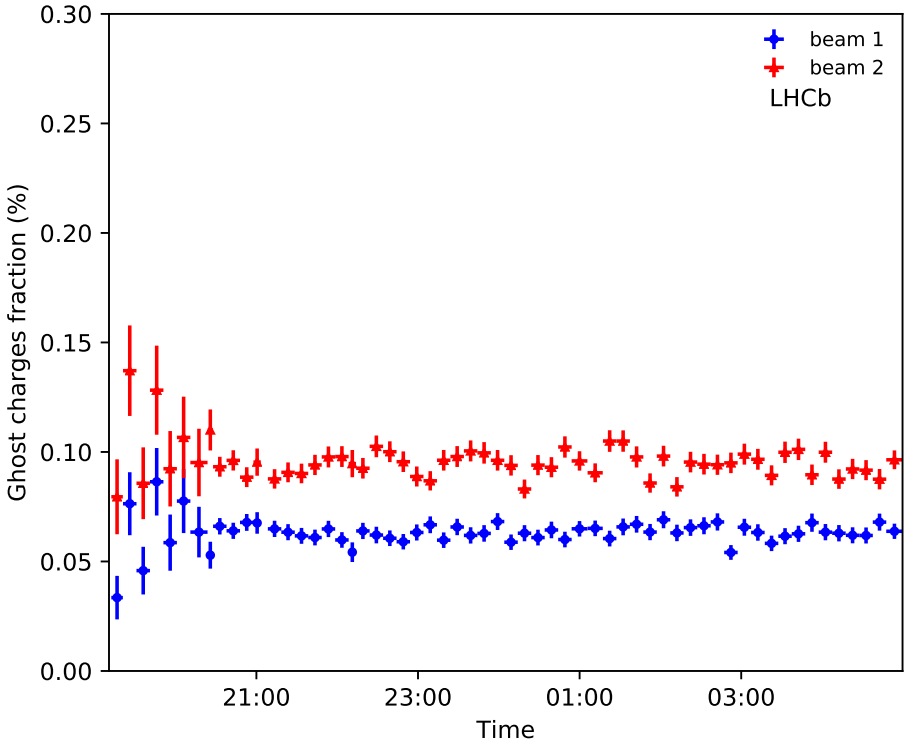

Figure 3.13: Ghost charge measured by LHCb throughout the 2018 p-p calibration fill no. 6864.

3.2.4 Measurements with the VELO Open

During late October and early November 2018 ATLAS and TOTEM participated in a short programme of collisions at low energy (E = 450 GeV) and high β^*. In these particular conditions it was not possible for LHCb to close the VELO due to the large beam sizes at IP8. However as part of the ATLAS measurement there was a vdM scan and it was requested that an LHCb ghost charge measurement be performed under these challenging conditions. Collision rates at IP8 were reduced due to the looser focusing of the beams and the observed rate was further reduced by the VELO's lower efficiency when not fully closed. Longer integration times of at least 15 minutes as well as looser cuts on the radial position and multiplicity of reconstructed vertices were therefore necessary in order to acquire a reasonable number of interaction vertices, especially in empty-empty crossings. The first fills 7299 and 7300 were affected by serious problems with the RF setup that led to very high ghost charge fractions (see Figs. 3.14 and 3.15) and poor beam quality. These problems were resolved in the early November fills 7406 and 7407 and the ghost charge fractions for these fills can be seen in Figs. 3.16 and 3.17. Alongside the challenging beam conditions there were also issues with the LHCb DAQ chain during these fills meaning that measurements for all except the last fill (7407) are based on less than 1 hour of total data per fill.

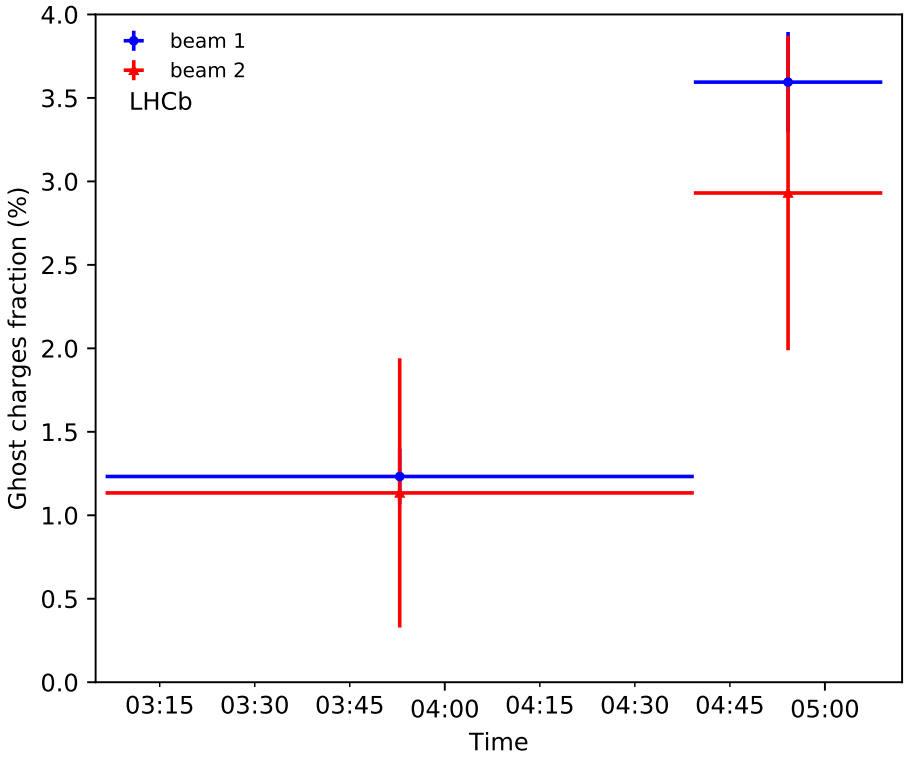

Figure 3.14: Ghost charge measured by LHCb throughout the October 2018 low-E high-β fill no. 7299.

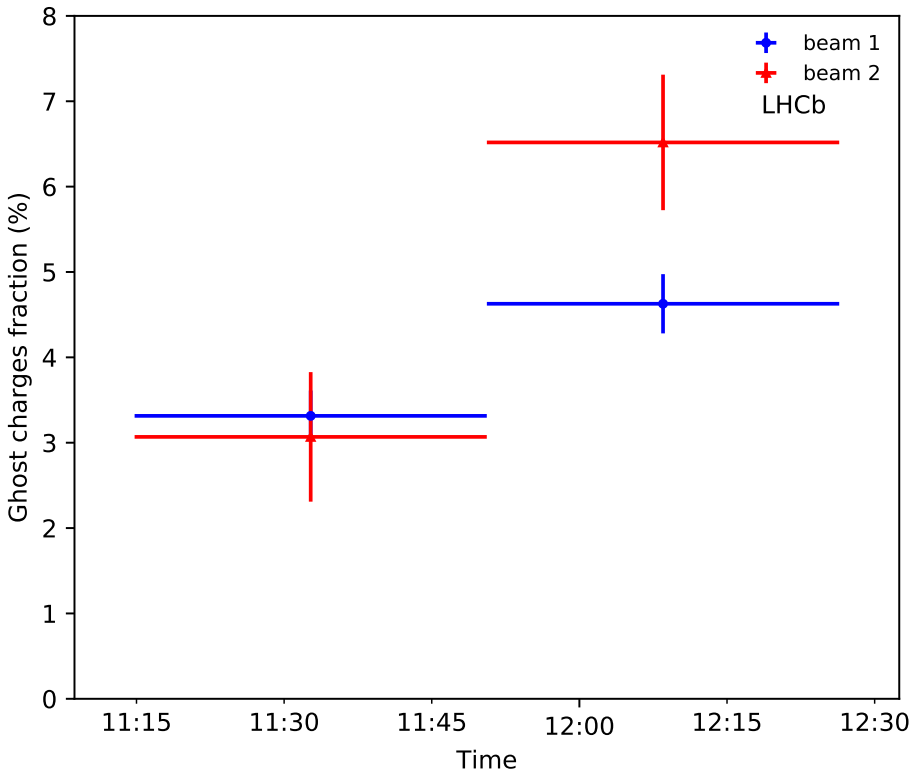

Figure 3.15: Ghost charge measured by LHCb throughout the October 2018 low-E high-β fill no. 7300.

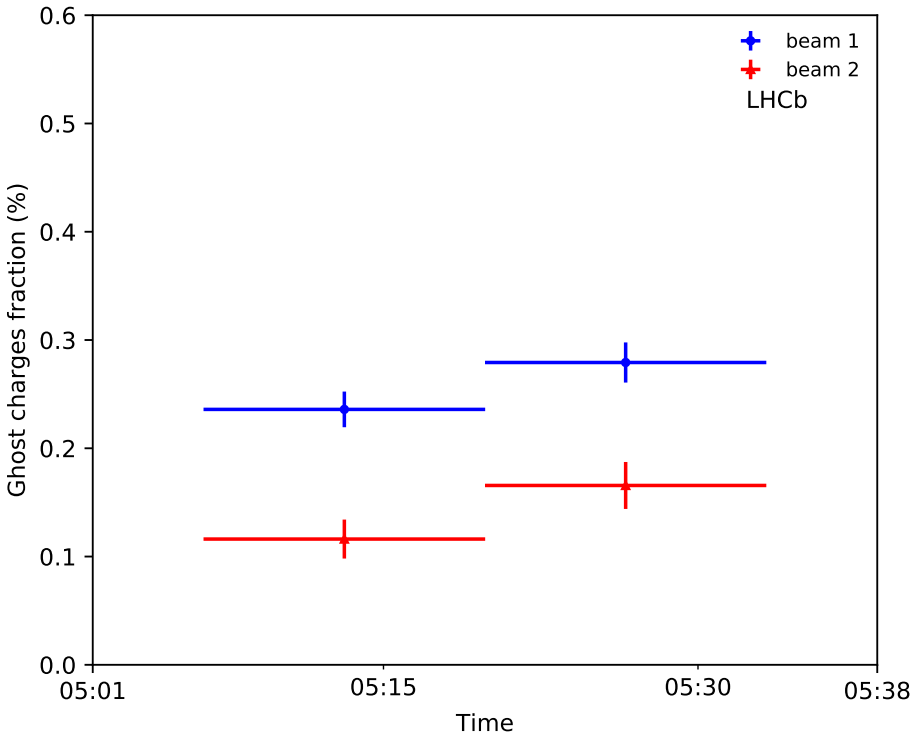

Figure 3.16: Ghost charge measured by LHCb throughout the November 2018 low-E high-β fill no. 7406.

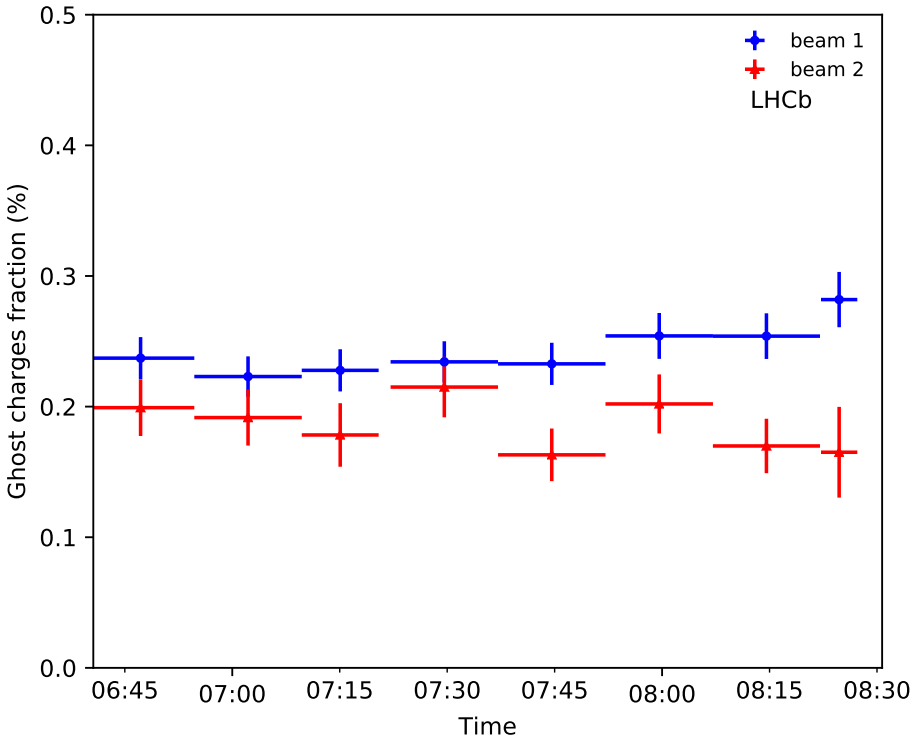

Figure 3.17: Ghost charge measured by LHCb throughout the November 2018 low-E high-β fill no. 7407.

3.2.5 LHCb DAQ Problems

During the CMS and ATLAS vdM fill of the same year unresolved problems with the LHCb data acquisition were observed indirectly via the BGI ghost charge measurement. The start of each seemingly random increase in the ghost charge fraction shown in Fig. 3.18 was found to correlate exactly with the timing of a reset of the front-end electronics of the L0 trigger (done automatically to correct periods of high dead time). After this point a certain fraction of beam-gas events from beam-empty crossings were being misidentified as originating in empty-empty crossings, greatly increasing the apparent ghost charge fraction (see Fig. 3.20). The problem was then corrected by the subsequent run change but reoccurred several times throughout the fill. The exact cause of this problem (so far observed only during this fill) has not yet been determined and is under investigation. For the purposes of the ghost-charge measurement we were able to simply remove the data from the affected time ranges. The corrected ghost-charge fractions can be seen in Fig. 3.19, and show good agreement between the BGI and BSRL approaches.

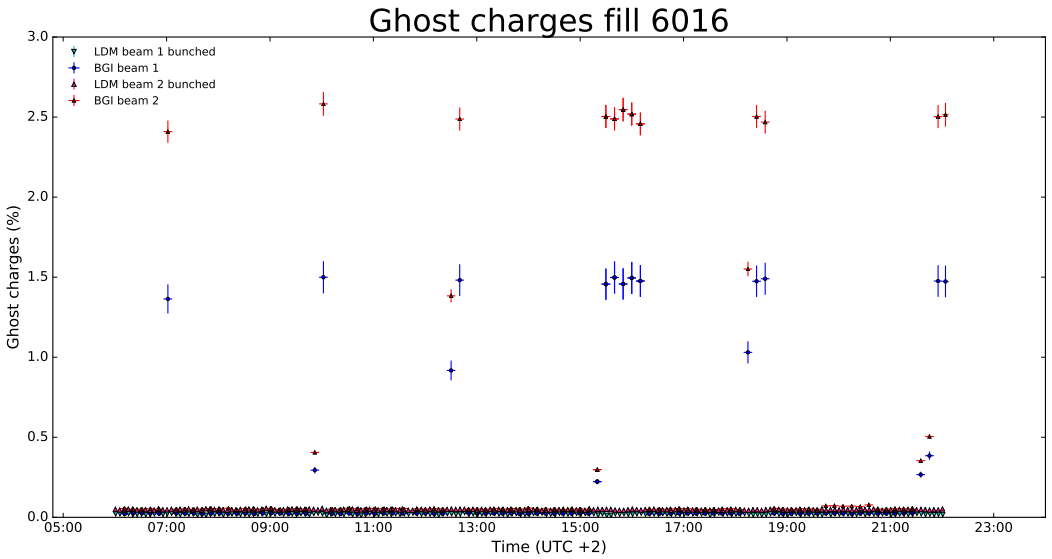

Figure 3.18: The ghost charge fraction throughout fill 6016 as seen by both LHCb and the BSRL. The LHCb measurement fluctuates throughout the fill while the BSRL values remain constant. With these larger percent level fluctuations excluded, however, the two measurement techniques agree very well, as seen in Fig. 3.19.

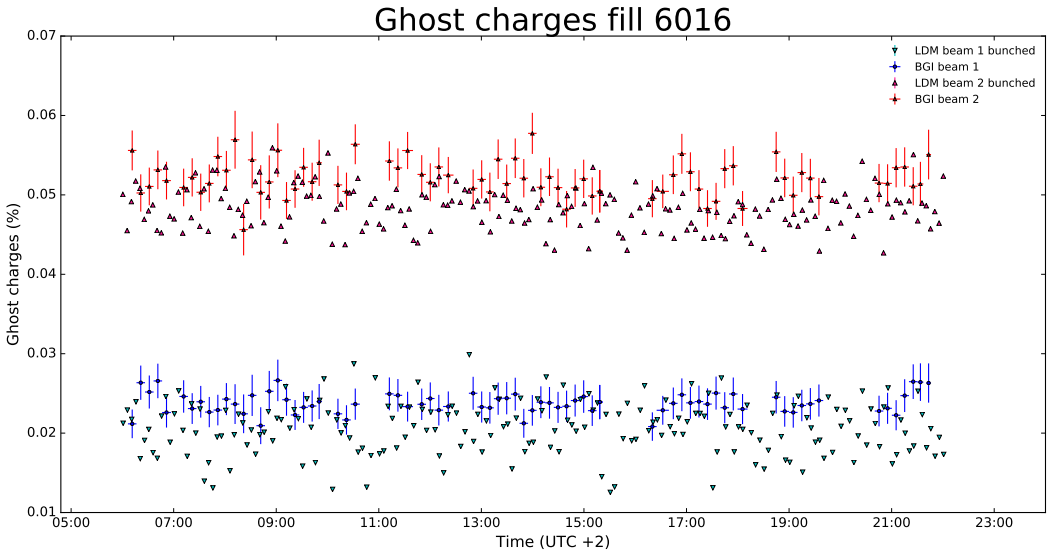

Figure 3.19: The ghost charge fraction throughout fill 6016 as seen by both LHCb and the BSRL with the LHCb data affected by problems with the DAQ removed.

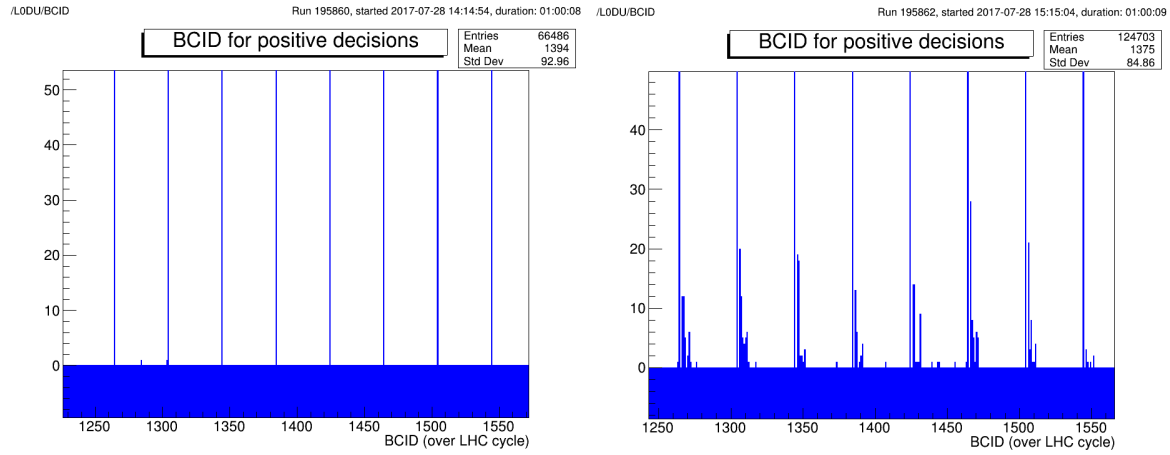

Figure 3.20: Plots from the LHCb online presenter showing the positive trigger decisions per bunch crossing ID (BCID) for two runs from fill 6016, the first unaffected by the DAQ problem and the second affected. In run 195860 nearly all positive trigger decisions occur in slots which are filled while in run 195682 a significant proportion of these events appear to "leak" into neighbouring BCIDs.

3.2.6 Beam De-Bunching at Low Energies

The importance of having an independent measurement to cross-check the BSRL results was demonstrated in November 2017 during the 2.5 TeV low-energy run of the LHC. As can be seen in Fig. 3.21 the BSRL measurement of the ghost charge fraction appears to decrease throughout the fill while the LHCb measurement increases. This is suspected to be caused by de-bunching of the LHC beam, as also seen in another low energy fill in 2015 [53]. This causes charges to be pushed outside the buckets defined by the LHC RF system. This de-bunched charge is seen as a background by the BSRL and subtracted from its measurement as part of a baseline correction. From the LHCb point of view, however, these charges still produce beam-gas interactions and thus add to the total ghost charge fraction. The difference between the DCCT and FBCT total charge values confirms the trend seen by LHCb. This provides a cross-check as any circulating de-bunched beam will be seen by the DCCT direct current measurement but not by the time-gated FBCT measurement. The uncorrected BSRL data also show an upward trend throughout the fill and their absolute offset was confirmed to be in agreement with the standby signal from the detector in the absence of beam.

3.2.7 Time Profile Measurements Using the LHCb Outer Tracker

In order to investigate this suspected de-bunching of the beam a new technique was implemented to produce the first LHCb measurement of the time profile within a 25 ns bunch slot [54]. This technique makes use of drift time measurements from LHCb's Outer Tracker

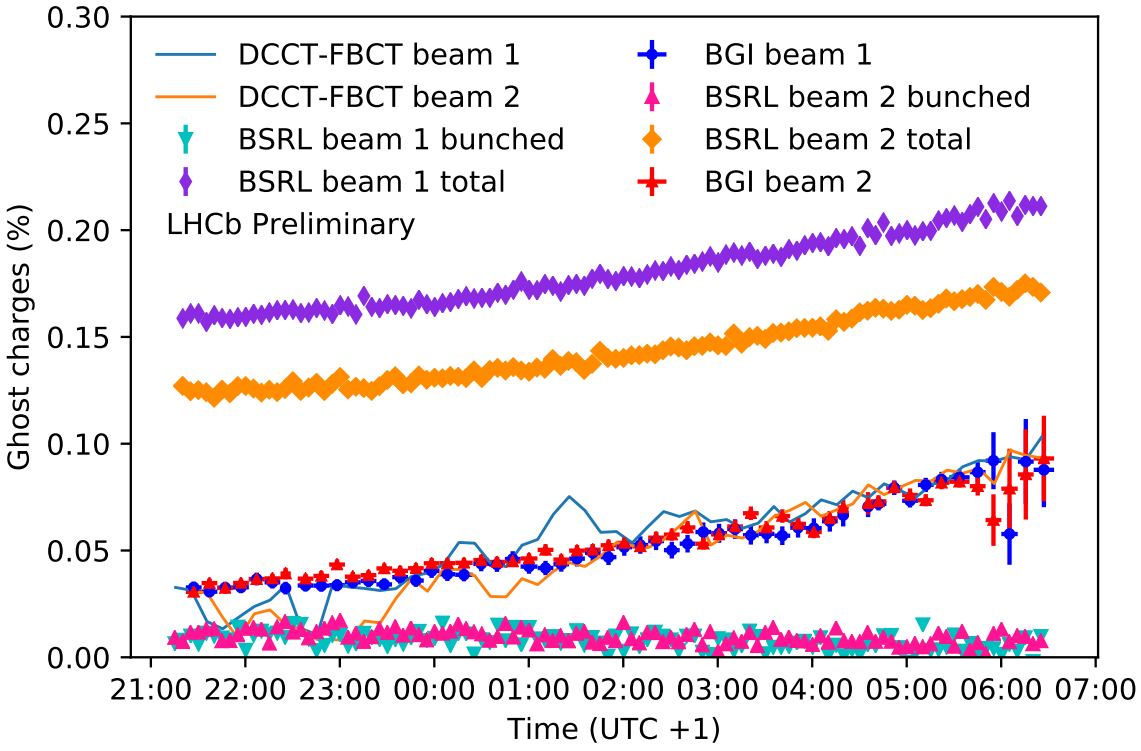

Figure 3.21: The evolution of the ghost charge fraction throughout LHC fill no. 6380 as measured with the LHCb BGI method and the LHC BSRL instrument. The BSRL values are shown with (bunched) and without (total) the background subtraction. The difference between the DCCT and FBCT total charge measurements, normalised to the earliest LHCb data points for each beam, is shown as a cross-check.

(OT) to assign time coordinates to reconstructed vertices. Due to the asymmetric geometry of the LHCb detector it is only possible to make measurements for LHC beam 1.

The OT is a gaseous detector forming the outer section of the three downstream tracking stations T1–T3. These stations contain just under 100 modules with each module made up of two staggered layers of drift tubes. The arrival times of ionization clusters produced by charged particles are measured with respect to the beam crossing time (from the LHC clock) and then digitised for each 25 ns slot. This digitised value is given in units of 0.4 ns, as the 25 ns window is encoded with 6 bits. As of Run II these time values are now calibrated in real-time as described in Ref. [55]. The improved drift-time resolution of the OT hits in Run II allows timing information to be assigned to tracks and vertices. Drift time residuals are calculated as the difference between the measured hit drift time and the prediction from the fitted track position. The time value for a single track can then be defined as the weighted average of the drift time residuals from the hits making up the track. The time value for a vertex is finally calculated as the weighted average of the track times of all tracks associated with that vertex.

The standard LHCb reconstruction expects interactions to occur within the narrow window

of the luminous region time distribution with a spread of 0.25 ns. Therefore, the observation of the larger time deviations across the 25 ns slot, associated with ghost charges, requires a modification of the reconstruction chain, where various windows related to OT hit timing are relaxed. In addition, the fitted track trajectory, and hence the drift time residuals, is biased by the assumed zero time origin of the interaction, which in turn leads to a bias in the measured track time. To overcome this, multiple reconstructions of each event are performed, each time shifting all OT hit times by a constant in steps of 2.5 ns covering the full 25 ns slot. The reconstructed event with the best global fit quality of all tracks containing OT hits is retained. The value of the applied shift is then summed with the measured residual to give the time value. Using beam-gas interactions from beam-empty crossings, which have a narrow, centred time distribution, we find a vertex time resolution on the order of 0.5 ns.

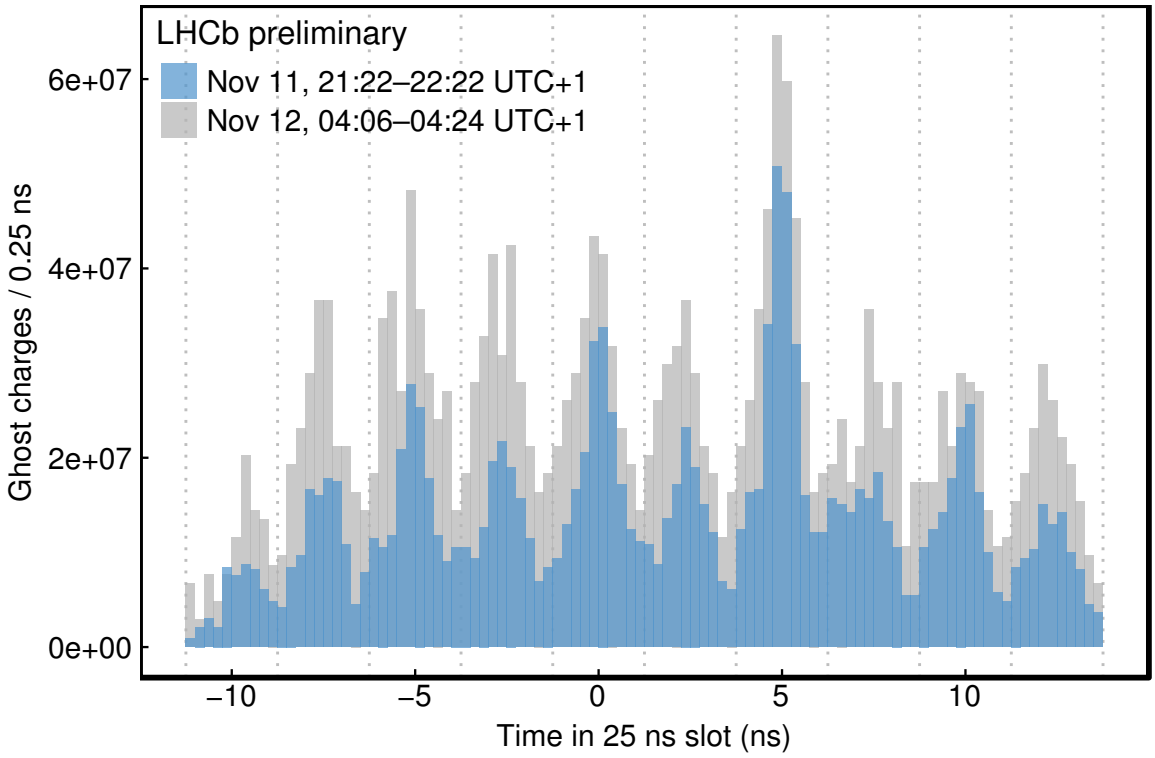

Figure 3.22: Distribution of measured vertex time for interactions of beam 1 with the gas in the range −11.25 to 13.75 ns, integrated over all empty-empty crossings, for two time periods during LHC fill no. 6380.

The first such measurement can be seen in Fig. 3.22, presenting data from two distinct time periods during the 2017 LHC 2.5 TeV calibration session. The vertex time values relative to the central bucket are shown integrated across all empty-empty crossings for the two time periods. The data from the later time period shows an increase in the ghost charge across all buckets and the 2.5 ns spacing observed between peaks in each case gives a hint of the debunching taking place during this fill. For comparison a further measurement was made in a 2018 calibration fill at a beam energy of 6.5 TeV and the results can be seen in Fig. 3.23. As

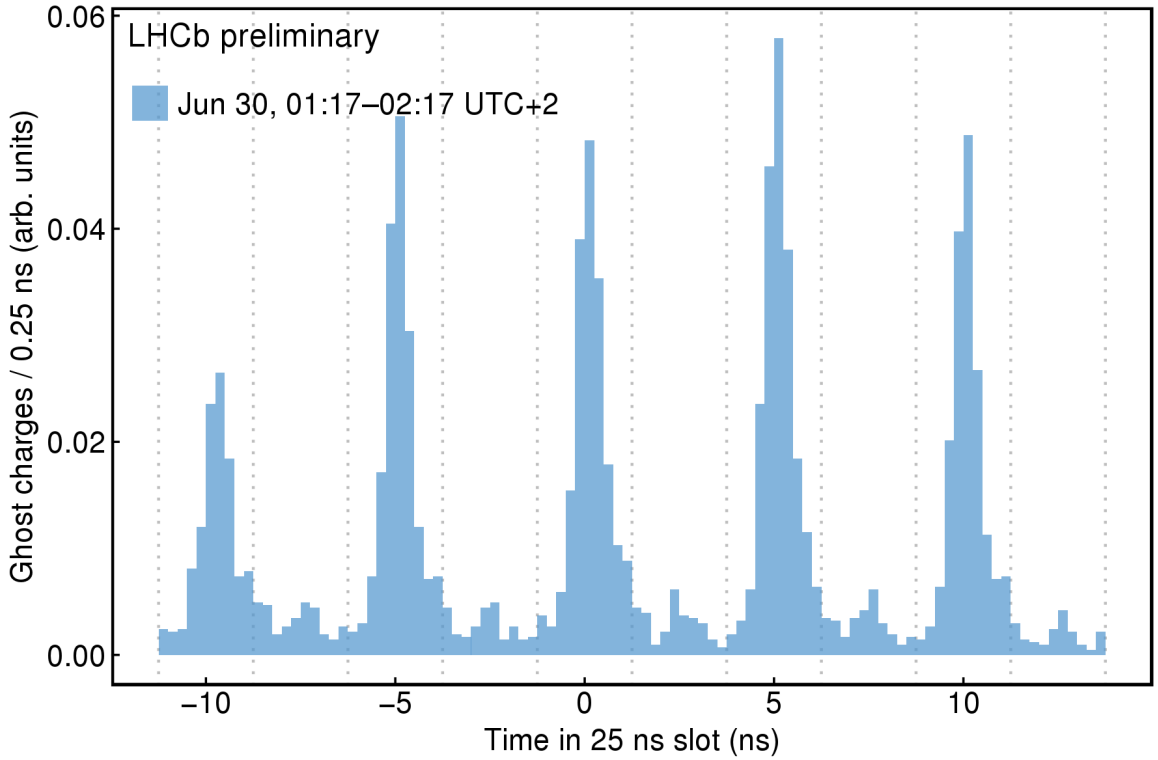

Figure 3.23: Distribution of measured vertex time for interactions of beam 1 with the gas in the range −11.25 to 13.75 ns, integrated over all empty-empty crossings during LHC fill no. 6864.

seen from this figure under nominal LHC operation, at 6.5 TeV, the 200 MHz RF structure of SPS is preserved and the bunch trains provided by the injector chain to the LHC show peaks in their longitudinal charge distribution every 5 ns [56]. However, due to suboptimal RF set up during 2.5 TeV operation, charge seems to leak out of this 5 ns structure and collect in the stable 2.5 ns buckets of the LHC's 400 MHz RF. Our present understanding of the time resolution limits our ability to distinguish potential de-bunched charge sitting between RF buckets from a simple overlap of adjacent peaks. We also need to understand to what extent the trigger and reconstruction efficiency of these measurements reduces at the trailing and leading edges of the bunch slot where the detector timing is not optimal.

3.3 Measurements with Ion Beams

As well as the normal operation of the LHC with proton beams, collisions between counter-circulating lead ion beams took place in both Autumn 2015 and 2018. In late 2016 collisions also took place between alternating lead ion and proton beams. Measurements of the ghost charge with heavy ion beams present their own particular set of challenges.

Calculating the higher ghost fraction during ion physics required the modification of the

LHCb approach to look for ghost charges not just from empty-empty bunch crossings but also ghost charges that could be present in the nominally empty bunch slot of a beam-empty crossing. This leads to a modification of the calculation presented in Eq. 3.5, with the updated form in Eq. 3.6 being used for beam 1, for example. Here the term n_{eb} has been added to the numerator and is the total number of reconstructed beam1-gas interactions in crossings where the beam 1 slot was nominally empty but the beam 2 slot was nominally filled.

$$f_{gc,1} = \frac{(n_{ee} + n_{eb})}{n_{be}} \frac{N_{be}}{N_{beam1}} \frac{1}{\epsilon_{tt}} \tag{3.6}$$

This modification was especially important as the calibration fills for ion physics do not have a dedicated filling scheme and thus contain hundreds more beam-empty crossings than a typical proton physics calibration fill. The distribution of these various vertices in the x-z plane can be seen in Fig. 3.24. Including these vertices leads to an increase in the LHCb measurement of several percent and clearly improved the agreement between the LHCb and BSRL measurements for ion physics fills. A set of examples of measurements in such fills are given in Figs. 3.25, 3.26, 3.27 and 3.28.

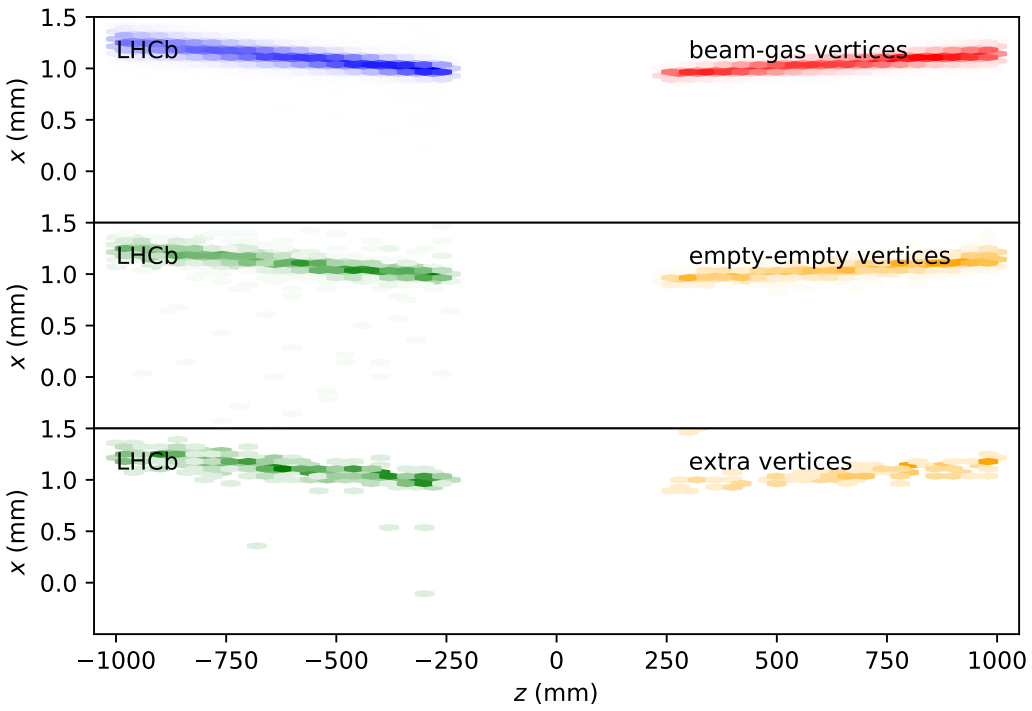

Figure 3.24: The distribution of beam-gas vertices in the $x - z$ plane as measured by LHCb in the 2016 lead ion run. The top plot shows the vertices from beam-empty crossings where the vertex is associated with the nominally filled beam. The second plot shows the beam-gas vertices present in empty-empty crossings. The third plot shows beam-gas vertices from beam-empty crossings where the vertex is associated with the beam coming from the nominally empty bunch slot.

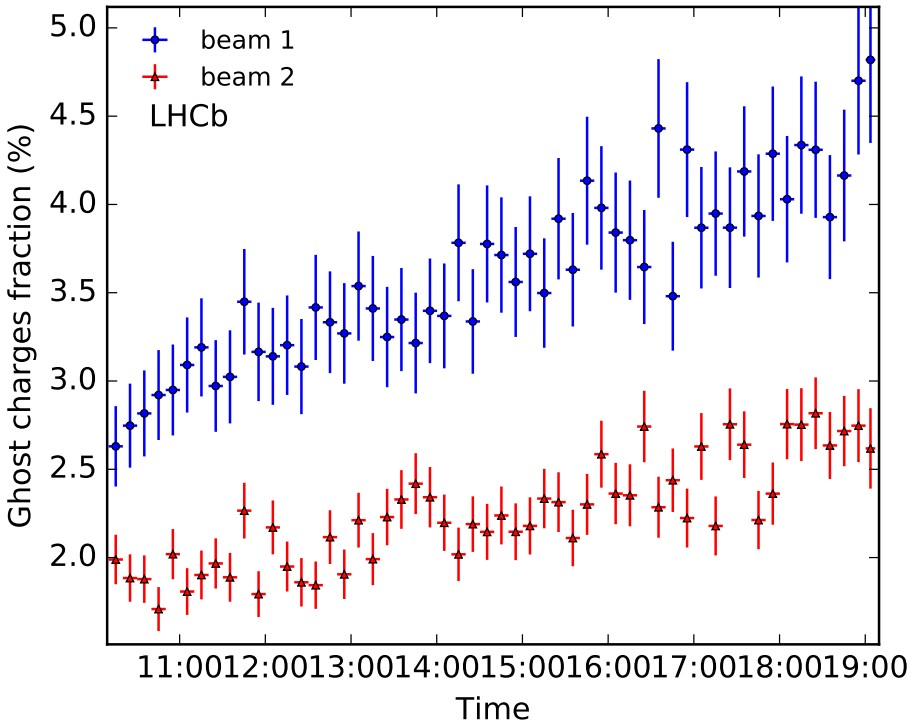

Figure 3.25: Ghost charge fractions measured by LHCb throughout the 2015 Pb-Pb calibration fill no. 4689.

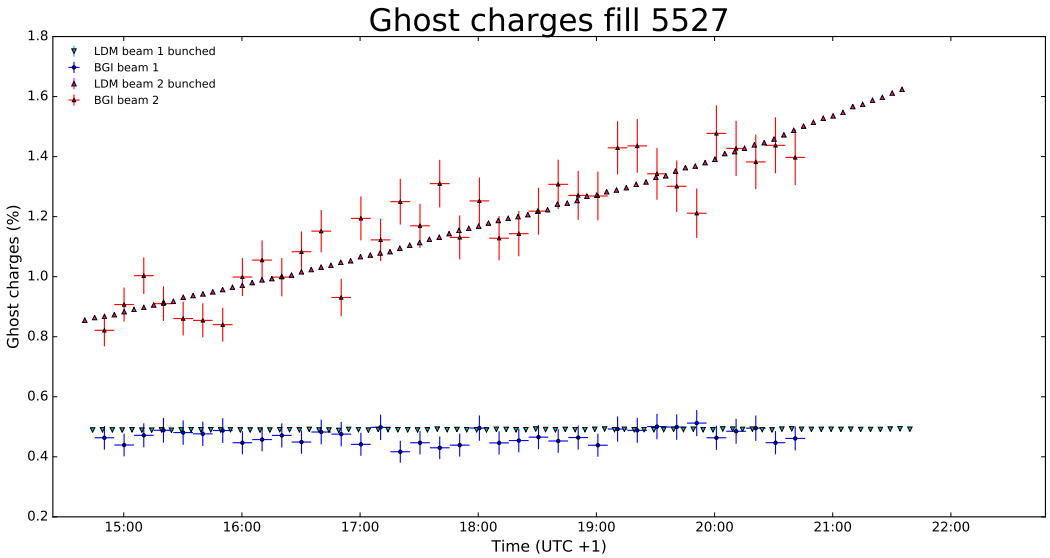

Figure 3.26: Ghost charge fractions measured by both by LHCb and the BSRL throughout the 2016 p-Pb calibration fill no. 5527. Beam 1 is the proton beam and beam 2 the lead ion beam. The two methods show good agreement throughout the fill.

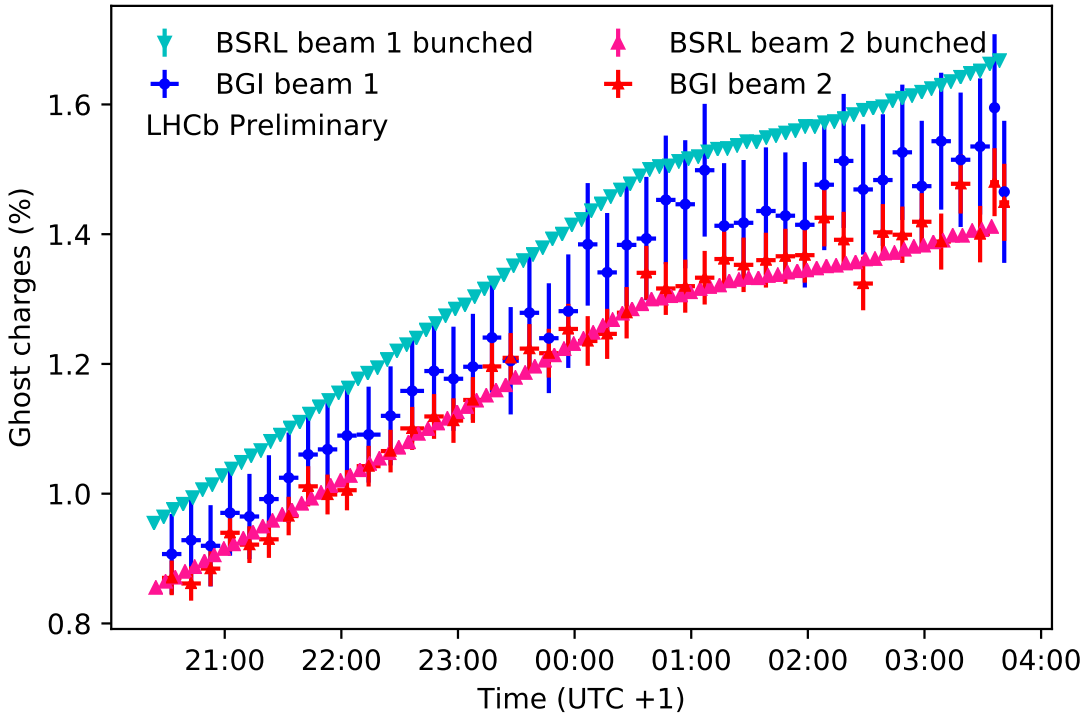

Figure 3.27: Ghost charge fractions measured by LHCb and the BSRL throughout the 2018 Pb-Pb calibration fill no. 7440. The two methods show good agreement throughout the fill.

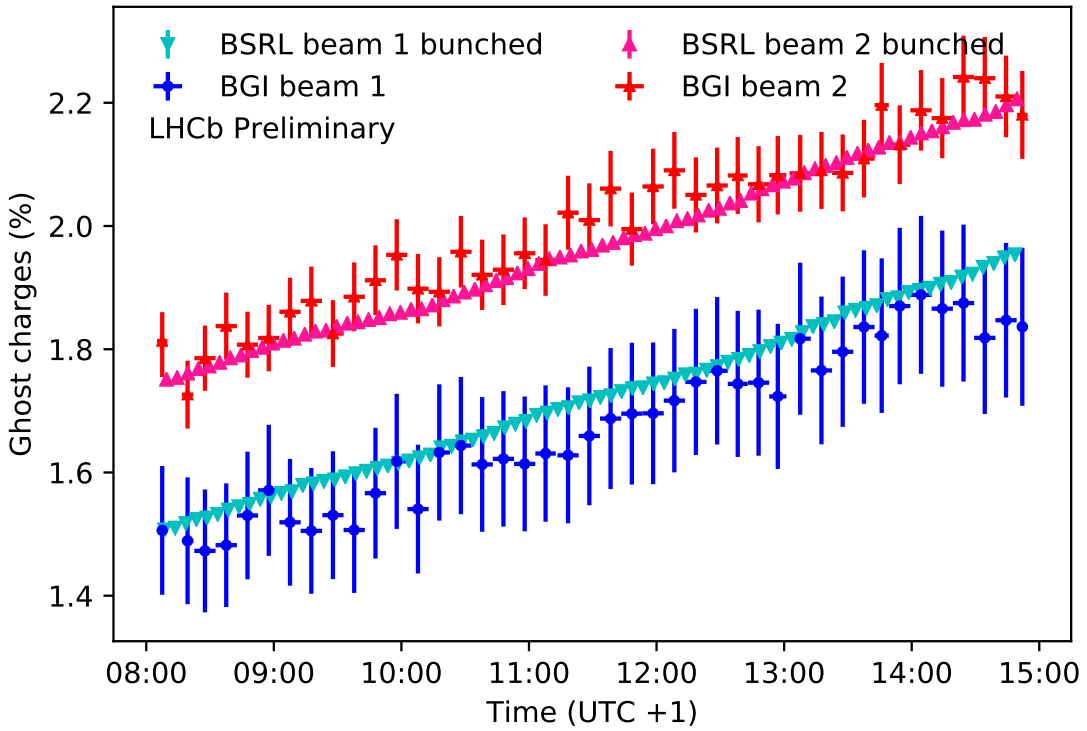

Figure 3.28: Ghost charge fractions measured by LHCb and the BSRL throughout the 2018 Pb-Pb calibration fill no. 7441. The two methods show good agreement throughout the fill.

Run 2 also saw the first injection of xenon beams into the LHC accelerator. This took place in October 2017 and was LHC fill number 6295 During this a short fill a quick vdM scan was performed and LHCb was able to make a measurement of the ghost charge that can be seen in Fig. 3.29. In this fill the duration of collisions at IP8 was short and the beam intensity was low so these measurements required a longer integration time and have a larger than usual uncertainty.

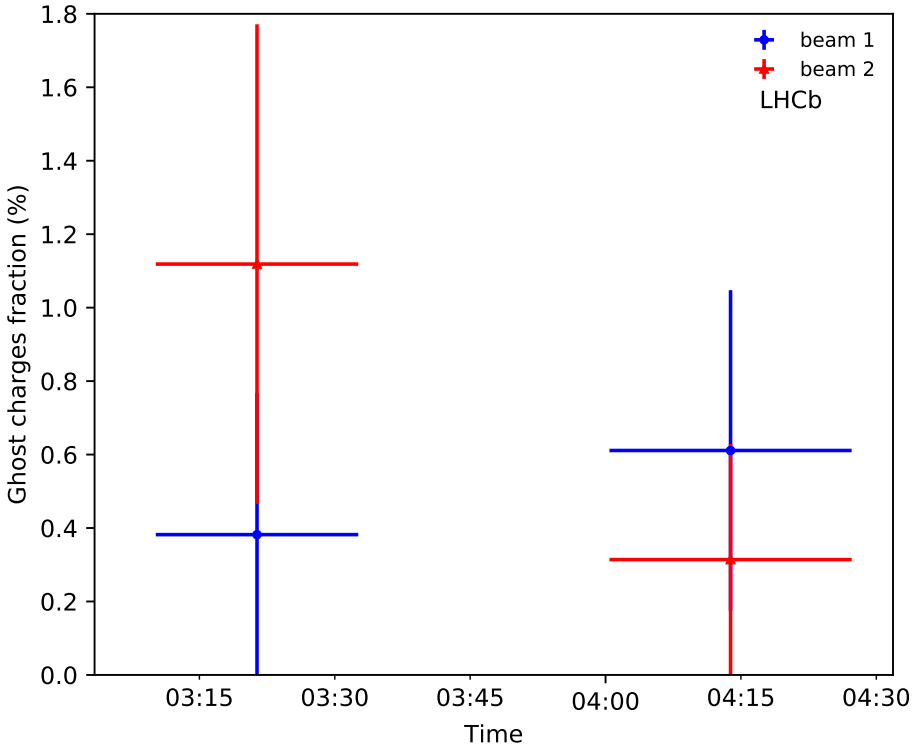

Figure 3.29: Ghost charge fractions measured by LHCb throughout the 2017 Xe-Xe fill no. 6295.

3.3.1 Dead Time Corrections

The LHCb RICH is the experiment's only subdetector to have a dead time that exceeds the 25 ns spacing between the bunch slots in the LHC accelerator. This dead time can lead to an effect where a signal in the RICH masks the presence of a beam-gas interaction in the subsequent bunch crossing. This can systematically bias the measurement of the ghost charge as if there is an asymmetry in the effect on empty-empty and beam-empty crossings the ratio between the number of beam-gas interactions observed in each will be affected. The magnitude of the effect depends on the filling scheme in use for the LHC. For example, filling schemes where a large proportion of empty-empty crossings are preceded by beam-beam crossings can give a systematically lower measurement of the ghost charge as beam-gas collisions in empty-empty crossings are likely to be lost when the RICH is triggered

by beam-beam collisions in the earlier bunch crossing. In order to mitigate this effect the RICH detector can be excluded from the LHCb DAQ chain during luminosity calibration measurements.

However, during certain luminosity calibration fills data were also taken parasitically for LHCb's fixed target physics programme and it was thus not desirable to exclude the RICH in this way. In these cases it was necessary to correct for this effect. This correction was done by comparing the observed rates in the HLT for each type of bunch crossing relative to the expected rates of 8 kHz for beam-beam crossings, 3.2 kHz for beam-empty crossing and 1.6 kHz for empty-empty crossings. The corrections for fills in the 2018 lead ion calibration session are in the range 2-5%.

3.4 Conclusions

Bunch population measurements are a field of LHC instrumentation that has seen constant development throughout the life of the accelerator. They now make use of a wide range of instrumentation to deliver both precise and accurate results. This allows cross-checks between independent measurement devices at most stages of the measurement process. The LHCb contribution during run 2 has been a complete programme of ghost charge measurements for all luminosity calibration fills. These are of use both for the calibration of luminosity at LHCb and at all other experiments that use the LHC. This ghost charge measurement effort has required a flexible approach based on changing beam and machine conditions as well as consideration of input from the equivalent BSRL measurements in each case. For the LHCb calibration measurement it has also been necessary to make use of the total beam charge and relative bunch population measurements provided by the DCCT and FBCT devices. The precision on these measurements has gone from being on the percent level (the dominant source of systematic uncertainty in early LHCb luminosity calibrations) to closer to a value of one per mille. It was, however, still necessary for this aspect of the luminosity measurement to be conducted thoroughly and a variety of second order effects were of special importance in cases where the LHC was configured for conditions other than proton-proton collisions at $\sqrt{s} = 13$ TeV.

Chapter 4

Luminosity Calibration with Beam-Gas Imaging at $\sqrt{s} = 13$ TeV

The beam parameter and geometry measurements performed via beam-gas imaging described in Chapter 2 and the bunch population measurements described in Chapter 3 provide all the necessary ingredients for a measurement of the luminosity in those calibration periods where these measurements were performed. In order for these measurements to be used to calculate the integrated luminosity at $\sqrt{s} = 13$ TeV in run 2, a procedure to calibrate the LHCb luminosity counters needs to be defined based on well-understood elements of the detector response to determine a calibration cross-section for these counters. These counters and their measurement are described in Sec. 4.1 below while the final calibration results based on data from the 2016 calibration session (LHC fill 4937) are presented in Sec 4.2.

4.1 Luminosity Counters and Interaction Rates

4.1.1 Luminosity Counters

The instantaneous luminosity recorded by a particle physics experiment will vary throughout the course of a fill (often lasting many hours) as factors such as the bunch populations and transverse emittances change over time. The luminosity must therefore be measured in a short enough period of time for these quantities to remain suitably stable. In order to make a measurement of the cross-section of any given physics process the relative luminosity during the time in which this process was measured must be determined. This relative luminosity is proportional to the interaction rate of any process that occurs as a result of the beams' interaction. Thus a set of luminosity counters, whose rate is simple to measure, are recorded simultaneously with the physics data. The luminosity measurements made during dedicated

calibration fills allow the measurement of a counter's interaction rate, R_c to be related to its cross-section, $\sigma_{ref,c}$ as in Eq. 4.1:

$$\sigma_{ref,c} = \frac{R_c}{\mathcal{L}} \tag{4.1}$$

where the rate is defined as in Eq. 4.2 if a number of events N_c are recorded in a time t:

$$R_c = \frac{dN_c}{dt} \tag{4.2}$$

and the luminosity, $\mathcal{L}$, determined from the measured bunch intensities and overlaps along with the revolution frequency, f_{rev}, of the LHC:

$$\mathcal{L} = f_{rev} N_1 N_2 \mathcal{O}. \tag{4.3}$$

A different reference cross-section can be measured for each counter and the list of available counters at LHCb is set out in Table 4.1. The counters are generally based on the response of one of LHCb's individual subdetectors as described in Sec. 1.3. The thresholds given in this table indicate the minimum detector response required for a count to be recorded for the given counter. At LHCb, luminosity counters based on the VELO detector response have been shown to exhibit the greatest stability over long periods of time [4]. The VELO tracks and vertices can be recorded at any spatial position or within a fiducial volume corresponding to a cylinder centred at the beam crossing point and satisfying $|z| < 300$ mm and $x^2 + y^2 < 4$ mm. The principal counters used for this analysis will be *Track* and *Vertex*.

Counter	Threshold	Description
Track	≥ 2 tracks	VELO tracks within the cylinder around the beam-line satisfying: $\lvert z\rvert < 300$ mm and $x^2 + y^2 < 4$ mm
Vertex	≥ 1 vertex	Reconstructed vertices within a cylinder defined by: $\lvert z\rvert < 300$ mm and $x^2 + y^2 < 4$ mm
SPD	≥ 2 hits	Hit multiplicity in the SPD subdetector
PU	≥ 2 hits	Hit multiplicity in the VELO pile-up sensors
RzVelo	≥ 2 tracks	Number of VELO tracks
$SumEt$	≥ 15 MeV	Sum of transverse energy deposited in the LHCb calorimeters
PV3D	≥ 1 vertex	Reconstructed vertices at any position
muon	≥ 1 muon	Number of detected muons

Table 4.1: The full list of luminosity counters defined at LHCb and recorded in parallel with physics data. The threshold here gives the minimum activity required for a count to be recorded.

4.1.2 Interaction Rate Calculation

In practice, at LHCb the counter rate, R_c, is determined by measuring the fraction of empty events where no visible event passes the reference counter threshold. This fraction is denoted by $P(0)$. Some sort of interaction may have taken place during these empty events but if this is not recorded by the relevant detector (for example due to a limited acceptance or dead-time) then it is not visible and therefore the event is recorded as being empty. Given a total number of bunch crossings, N_{xing}, some proportion of those crossings will pass the threshold to record a count for the reference counter, N_{ref}, and some proportion will be empty, N_0. The total number of empty crossings can be written as in Eq. 4.4:

$$N_0 = N_{xing} - N_{ref} \tag{4.4}$$

therefore the fraction of empty events across all crossings, $P_c(0)$, can be expressed as in Eq. 4.5:

$$P_c(0) = \frac{N_0}{N_{xing}} = 1 - \frac{N_{ref}}{N_{xing}} \tag{4.5}$$

Instead of counting the total number of bunch crossings, N_{xing}, triggers are created for each counter that fire randomly on bunch crossings at a fixed average frequency, f_{rnd}. The total number of crossings can then be related to the number of triggered events, N_{rnd}, with the revolution frequency, f_{rev}, by Eq. 4.6:

$$N_{xing} = N_{rnd}\frac{f_{rev}}{f_{rnd}} \tag{4.6}$$

The fraction of empty events in this sample of triggered crossings, $P(0)$, can then be written in terms of the number of visible events in a given number of triggered events as in Eq. 4.7:

$$P(0) = 1 - \frac{N_{ref}}{N_{rnd}} \tag{4.7}$$

During physics data taking the random trigger rate is distributed with a ratio 70%:15%:10%:5% for bb, be, eb and ee crossings, respectively, with the rate for bb crossings set to 1 kHz. For dedicated BGI calibration sessions the bb rate is increased to 5 kHz with the proportions changed such that the equivalent ratio is now 52.6%:21%:21%:5.4%, which gives acquisition rates of 5:2:2:0.5 kHz for the respective crossing types.

This sampling rate is shared between all bunch crossings, however, Eq. 4.7 still applies to individual bunch pairs. It is simply necessary to take the proportion of random triggers for that bunch pair as N_{rnd} and the number of visible events during crossings of those bunches as N_{ref}. The number of interactions per bunch crossing, n, follow a Poisson distribution

$P(n, \mu)$ as defined in Eq. 4.8:

$$P(n, \mu) = \frac{e^{-\mu}\mu^n}{n!} \tag{4.8}$$

where μ is the average number of interactions per crossing. As only visible interactions are seen by the detector it is necessary to use the average number of visible interactions per crossing, μ_{ref}, in the place of μ. The probability, P_{ref}, of observing a visible interaction in a given crossing is the sum of all events where $n > 0$ as in Eq. 4.9:

$$P_{ref} = \sum_{n=1}^{\infty} P(n, \mu_{ref}) = 1 - P(0, \mu_{ref}) = 1 - e^{-\mu_{ref}} = \frac{N_{ref}}{N_{rnd}} \tag{4.9}$$

The average number of visible interactions per bunch crossing μ_{ref} can thus be written as in Eq. 4.10:

$$\mu_{ref} = -\ln\left(1 - \frac{N_{ref}}{N_{rnd}}\right) = -\ln\left(\frac{N_0}{N_{rnd}}\right) \tag{4.10}$$

where $N_0 = N_{rnd} - N_{ref}$. This approach is known as the zero counting method.

The visible cross-section of a counter, σ_{ref}, can be calculated from its rate, μ_{ref} as in Eq. 4.11:

$$\sigma_{ref} = \frac{\mu_{ref} f_{rev}}{\mathcal{L}} = \frac{\mu_{ref}}{N_1 N_2 \mathcal{O}} \tag{4.11}$$

As each counter has a different sensitivity each counter will have a different value of σ_{ref} and once this value is known the integrated luminosity of any given data taking period can be determined by measuring μ_{ref} for this period and for the corresponding counter.

Background Correction

During the dedicated luminosity calibration fills the average visible interaction rate μ_{ref} is measured as shown in Eq. 4.10 in time bins of 4 minutes for each reference counter in Table 4.1. This raw measured rate will, however, include contributions from the beam-gas interaction background which is much larger when the SMOG gas injection system necessary for BGI is in use. If we account for this additional background the measured average number of visible interactions per bunch crossing can be written as in Eq. 4.12:

$$\mu_{ref} = -\ln P_{bb}(0) - [-\ln P_{bkg}(0)] \tag{4.12}$$

where the background contribution is given by the contributions from the beam-gas bunch crossing types as shown in Eq. 4.13:

$$-\ln P_{bkg}(0) = -\ln P_{be}(0) - \ln P_{eb}(0) \tag{4.13}$$

The probabilities $P_{bb,be,eb}(0)$ are the probabilities of an empty event being recorded in the bunch crossing type given by the index. The background contribution from each beam is proportional to both the gas pressure in the interaction region and the intensity of the relevant beam. The interaction rate correction per BCID must therefore be evaluated with knowledge of the colliding bunch populations. Then a background correction normalised per charged particle, μ^c_{ref}, can be established for each beam. For a total number n of non-colliding bunches i in a given beam the background contribution for that beam can be calculated with Eq. 4.14:

$$\mu^c_{ref} = \sum_{i=1}^{n} \frac{1}{n} \frac{\mu_{ref,i}}{N_i} \tag{4.14}$$

where N_i is the population of bunch i and the average rate for each bunch is given by Eq. 4.15:

$$\mu_{ref,i} = -\ln P_i(0) \tag{4.15}$$

The corrected value for the rate can then be written as in Eq. 4.16:

$$\mu_{ref} = \mu^{raw}_{ref} - \mu^c_{ref,1} N_1 - \mu^c_{ref,2} N_2 \tag{4.16}$$

where μ^{raw}_{ref} is the raw observed interaction rate for a pair of colliding bunches and N_1 and N_2 are the populations of each bunch.

4.1.3 Interaction Rate Measurements

The measured interaction rate per bunch crossing for both the *Track* and *Vertex* counters throughout fill 4937 are shown in Fig. 4.1. Both the raw and corrected values are given. The magnitude of the background correction factors for this fill is shown for each counter in Fig. 4.2 and the ratio of the two counters in this fill is shown in Fig. 4.3. The background correction for the *Track* is approximately one order of magnitude larger than for the *Vertex*. The *Vertex* counter is used for all BGI calibration measurements presented in Sec. 4.2 both due to this difference in background correction and previous studies that have shown the *Vertex* counter is more stable during periods of SMOG gas injection [7]. The luminosity propagation to the full LHCb run 2 dataset however will be done with the *Track* counter as this is the counter used in the vdM analysis. The final reference cross-section for the counter can be determined from the BGI measurement for the *Vertex* counter and the ratio of the rates of the two counters as in Eq. 4.17.

$$\sigma_{Track} = \frac{\mu_{Track}}{\mu_{Vertex}} \sigma_{Vertex} \tag{4.17}$$

The average value for the ratio between these two counters for $\sqrt{s} = 13$ TeV beams is

measured in fill 4937 as:

$$\frac{\mu_{Track}}{\mu_{Vertex}} = 1.097 \pm 0.006 \tag{4.18}$$

where the uncertainty given is statistical.

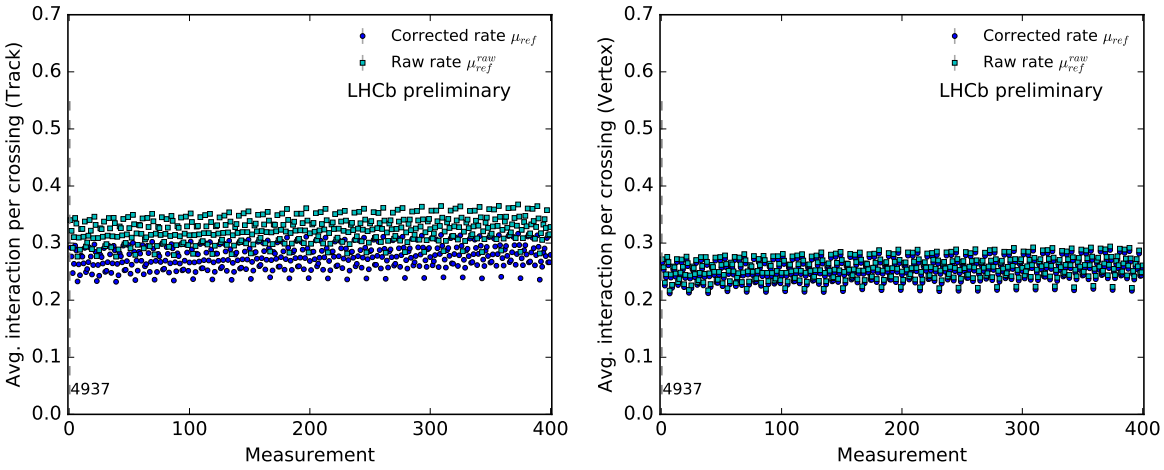

Figure 4.1: The raw and background corrected interaction rates for the *Track* (left) and *Vertex* (right) counters in fill 4937. The measurements are ordered by time.

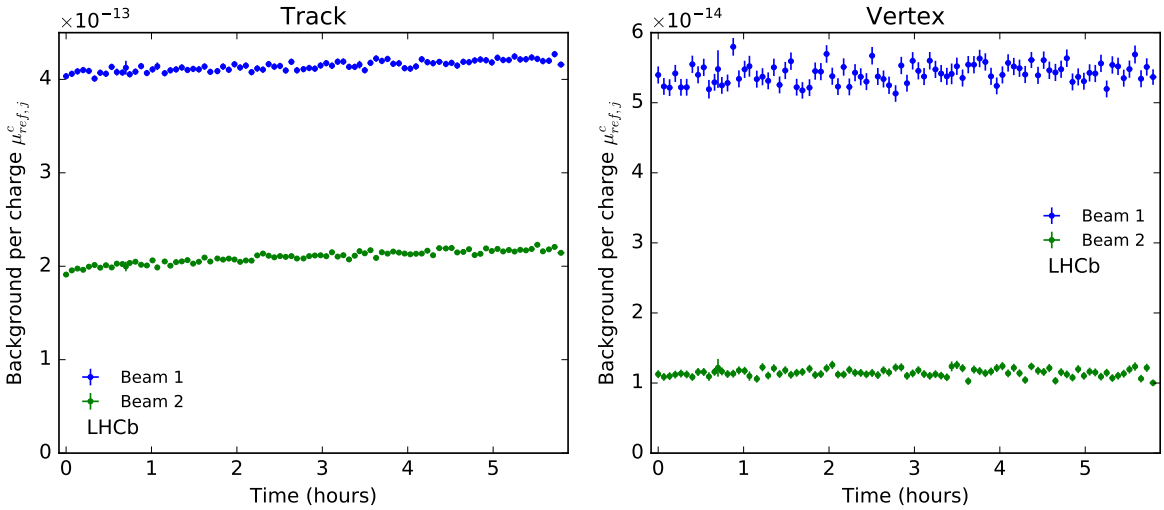

Figure 4.2: The background correction factors per charge for the *Track* (left) and *Vertex* (right) counters in fill 4937. The corrections for the *Track* counter are about one order of magnitude larger than for the *Vertex* counter.

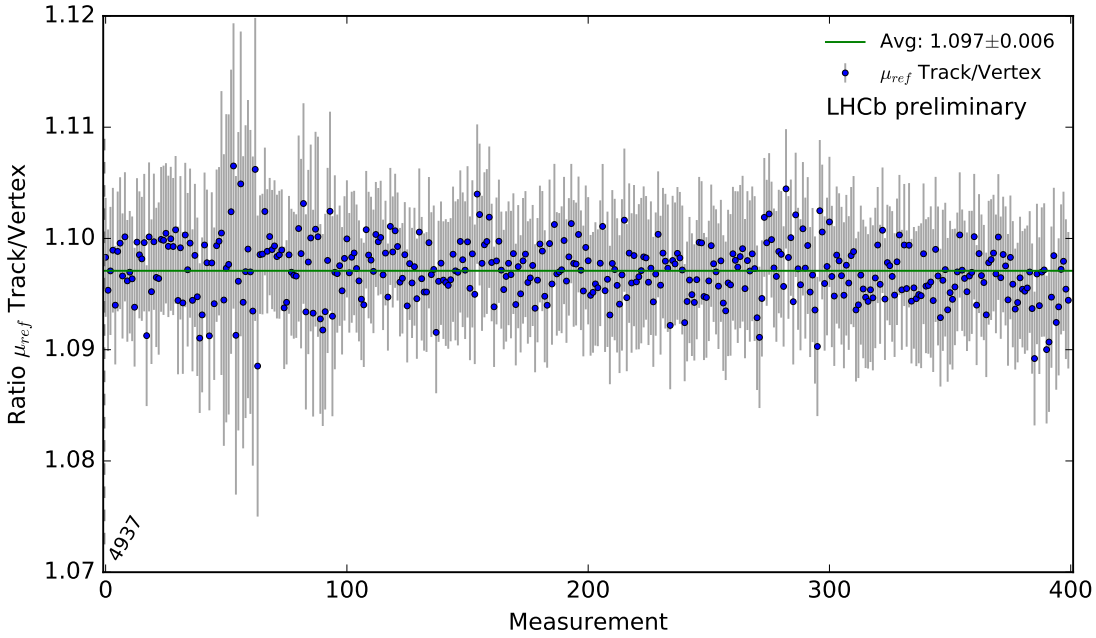

Figure 4.3: The ratio of the corrected interaction rates of the *Track* and *Vertex* counters in fill 4937. The measurements are ordered by time, the uncertainties shown are statistical and the green line shows the average value for the fill.

4.1.4 Systematic Uncertainties

The counters *Track* and *Vertex* are restricted to record only events that originate near the interaction point within the fiducial volume defined in Table 4.1. The alternative counters *RzVelo* and *PV3D* record the same detector activity but without this spatial restriction. The main effect of this difference is that the level of background correction required is larger for these unrestricted counters than for those that record events only within a specified volume. This difference can be seen in the ratio between the corrected and uncorrected interaction rates for each counter as shown in Fig. 4.4.

Despite this large background the rates of *Track* (*Vertex*) and *RzVelo* (*PV3D*) should, in principle, be equal after correction and any difference in their rates would indicate a possible systematic error in the rate measurement. The ratios of these two sets of counters in fill 4937 are shown in Fig. 4.5 and are both compatible with a ratio of one. Therefore no systematic uncertainty is assigned.

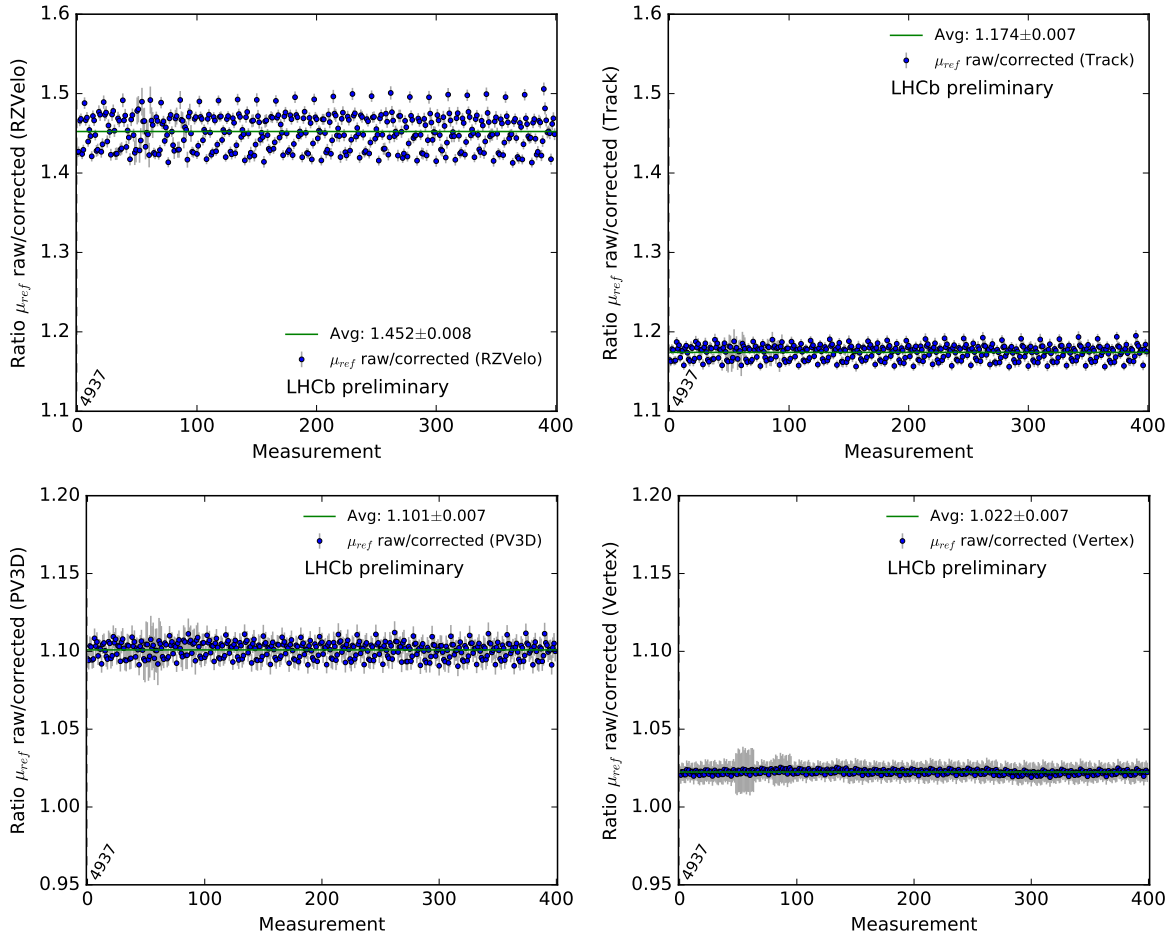

Figure 4.4: The ratios of the raw and uncorrected interaction rates for the counters: *RzVelo* (top left), *Track* (top right), *PV3D* (bottom left) and *Vertex* (bottom right). The measurements are ordered by time, the uncertainties shown are statistical and the green line shows the average value for the fill.

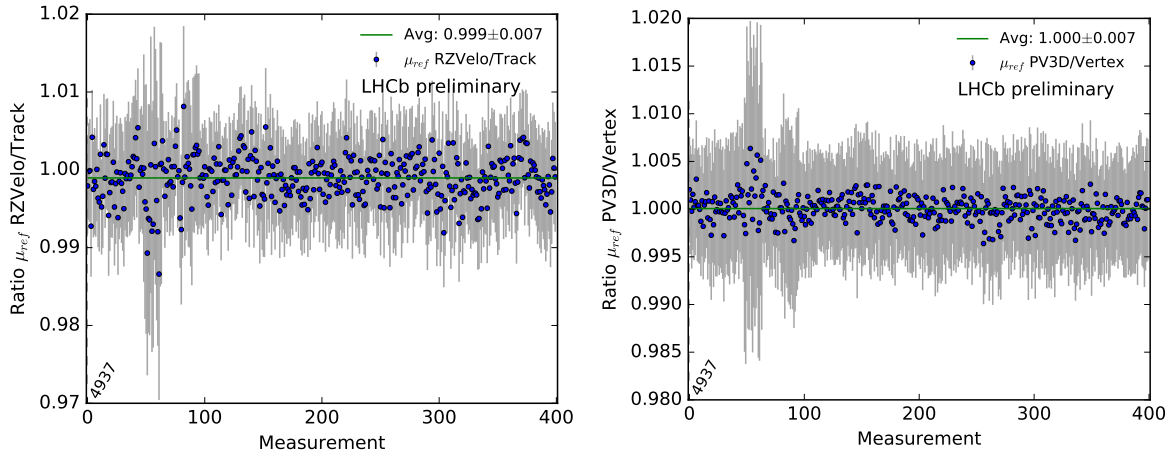

Figure 4.5: The ratios of the corrected interaction rates of the *RzVelo* and *Track* (left), *PV3D* and *Vertex* (right) counters in fill 4937. The measurements are ordered by time, the uncertainties shown are statistical and the green line shows the average value for the fill.

4.2 Beam-Gas Imaging Calibration Results

4.2.1 Per Bunch Luminosity Calibration

The instantaneous luminosity $\mathcal{L}$ for each colliding bunch pair in each 15 minute time bin is calculated using Eq. 4.19, with the LHC revolution frequency f_{rev}, the overlap integral values $\mathcal{O}$, evaluated as described in Chapter 2, and the bunch intensity product $N_1 N_2$, determined as described in Chapter 3.

$$\mathcal{L} = f_{rev} N_1 N_2 \mathcal{O} \tag{4.19}$$

The bunch populations for these measurements are calculated including the satellite and ghost charge corrections described in Sec. 3.2 with the expression given in Eq. 3.4. These luminosity measurements are then used in combination with the measured interaction rate μ_{ref} (as described in Sec. 4.1) to evaluate the visible cross-section for a reference counter σ_{ref} as in Eq. 4.20.

$$\sigma_{ref} = \frac{\mu_{ref} f_{rev}}{\mathcal{L}} = \frac{\mu_{ref}}{N_1 N_2 \mathcal{O}} \tag{4.20}$$

Measured per-bunch cross-section results for the *Vertex* counter obtained via the BGI method using a two-dimensional global fit model and based on data from fill 4937 are shown in Fig. 4.6. There is no overall trend visible in time and the individual per-bunch measurements are distributed around the central value. The evolution of the *Vertex* cross-section measurement along with the corresponding intensity product, overlap integral and interaction rate is shown for one colliding bunch pair from this fill in Fig. 4.7. Here the cross-section measurement can be seen to remain stable as expected even as the bunch populations diminish and the overlap integral grows in magnitude. A fit quality cut was implemented on these measurements removing a small number of measurements (9 out of 400) that do not pass a $\chi^2/ndof > 2$ cut. After this cut the average $\chi^2/ndof$ value for the two-dimensional fits is 1.07 and the full set of such results is shown in Fig. 2.22. The central value of the measured cross-sections is 60.00 mb and their root mean square (RMS) spread is 1.34%.

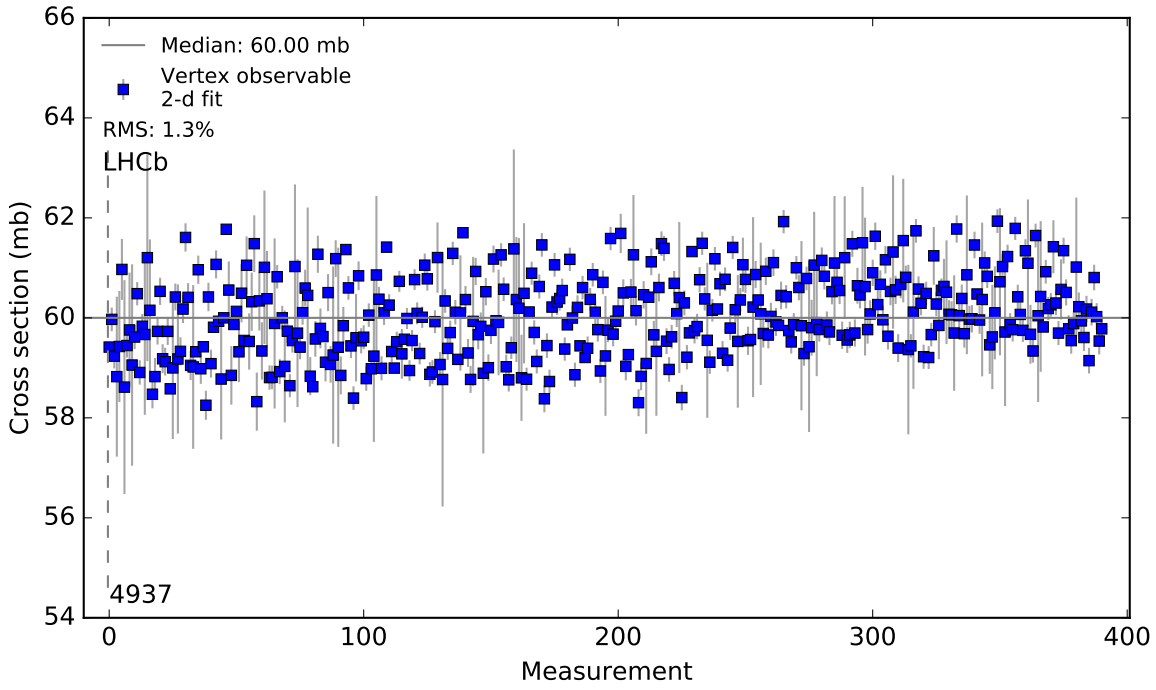

Figure 4.6: The measured calibration cross-section values at $\sqrt{s} = 13$ TeV throughout LHC fill no. 4937 for the *Vertex* counter.

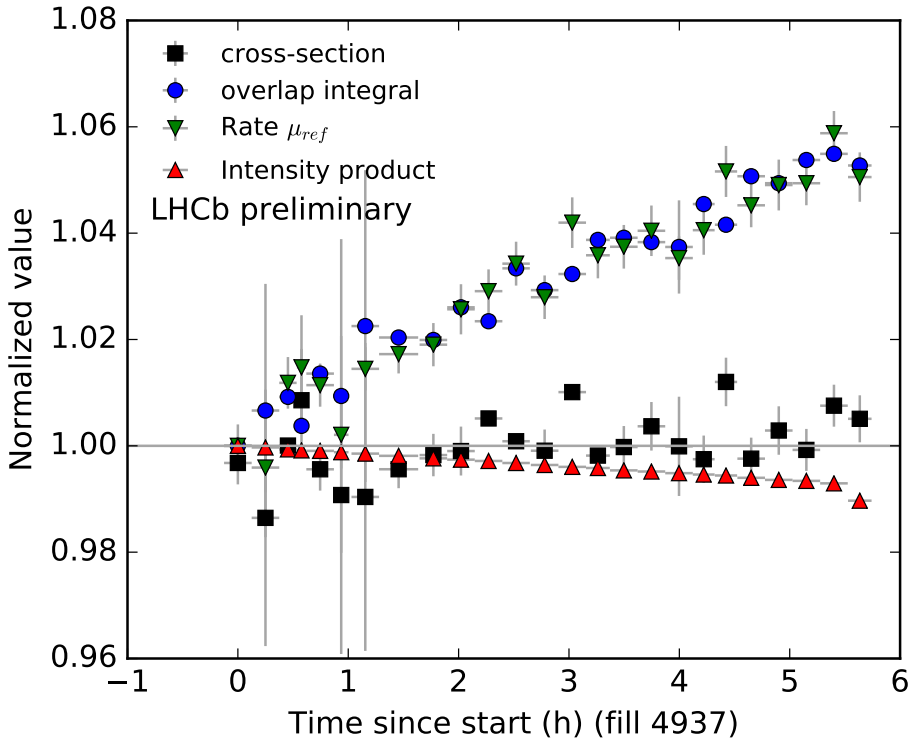

Figure 4.7: The evolution of the measured *Vertex* cross-section, overlap, bunch product and interaction rate for the bunch pair with BCID 342 throughout fill 4937. The cross-section is normalised to its average while the other values are normalised to their first data point.

4.2.2 Calibration Corrections and Systematic Uncertainties

A variety of systematic uncertainties contribute to the overall uncertainty on this reference cross-section measurement and need to be accounted for, these will be described in detail here.

Measurement Spread

Cross-section measurements for all colliding bunch pairs in fill 4937 are shown in Fig. 4.8 for the *Vertex* counter. These measurements have an RMS spread of 1.34%. This spread is due to the statistical uncertainty of the individual measurements but also due to noise in the bunch population measurements as well as any possible fit bias induced by the variation in bunch parameters between the circulating LHC bunches. This RMS spread is taken as a systematic uncertainty on the final calibration measurement.

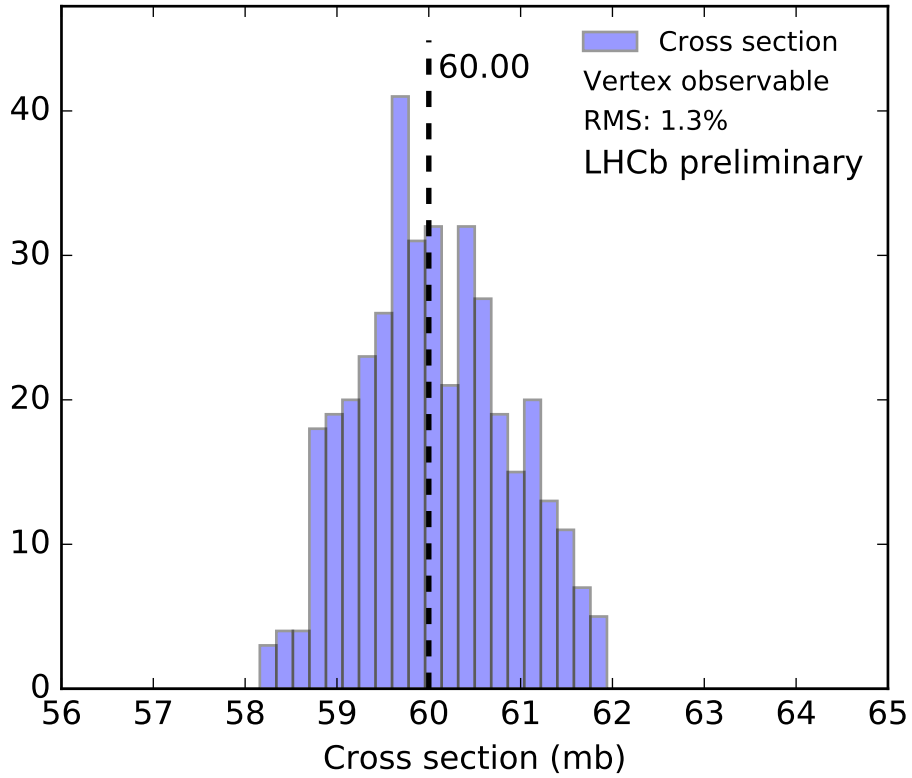

Figure 4.8: Histograms showing the measured calibration cross-section values at $\sqrt{s} = 13$ TeV for the *Vertex* counter.

Beam-Beam Resolution

A measure of the relative importance of the beam-beam resolution compared to the beam size, R, is defined in Eq. 4.21. R is defined such that a possible underestimation of the

resolution would lead to a linear dependence of the measured cross-section as a function of R. The terms in R are the widths of the beam-beam resolution function, $\sigma_{res,x(y)}$, the beam widths at collision, $\sigma_{x(y)}$, the length of the luminous region, σ_z, and the crossing angle, ϕ. This expression assumes equal beam sizes for the two colliding beams, for the full derivation see pages 96-97 of Ref. [7].

$$R = \frac{2\sigma_{res,x}^2}{4\sigma_x^2 + \sigma_z^2 \sin^2(\phi)} + \frac{\sigma_{res,y}^2}{2\sigma_y^2} \tag{4.21}$$

In order to estimate an uncertainty on the cross-section due to this resolution dependence we can plot the values of the cross-section obtained for different values of R and then extrapolate from these points a value of the cross-section as R tends to zero and the resolution importance becomes negligible. The difference between this cross-section value and the central value can be taken as a systematic uncertainty due to the beam-beam resolution. For run 2 this is achieved by measuring the cross-section twice, once including only beam-beam vertices with a track multiplicity less than 50 and again including only beam-beam vertices with a track multiplicity greater than or equal to 50. This gives a difference in R due to the multiplicity dependence of the vertex position resolution. These two measurements are shown as a function of R in Fig. 4.9 and as two overlapping histograms in Fig. 4.10. Fitting a line between these two points and projecting to a value of $R = 0$ gives a cross-section of 59.95 mb for the *Vertex* counter and the difference between this and the measured cross-section using all vertices is taken as a systematic uncertainty with a value of 0.09%.

In LHC fill 5456 a measurement of the *Vertex* cross-section was also performed as part of a machine development session with a wide range of widths for the individual colliding bunch pairs as shown in Fig. 5.8. This range of widths implies a wide range of values for the parameter R. The difference in the measured cross-section of 3.8% for the widest and narrowest bunches in this fill sets an upper bound on the possible uncertainty in the case of very different bunch sizes. However, this effect is clearly much smaller in a calibration fill with nominal BGI bunches due to their well-controlled, uniform transverse emittances and the broad bunch widths seen with a focusing strength of $\beta^* = 24$ m.

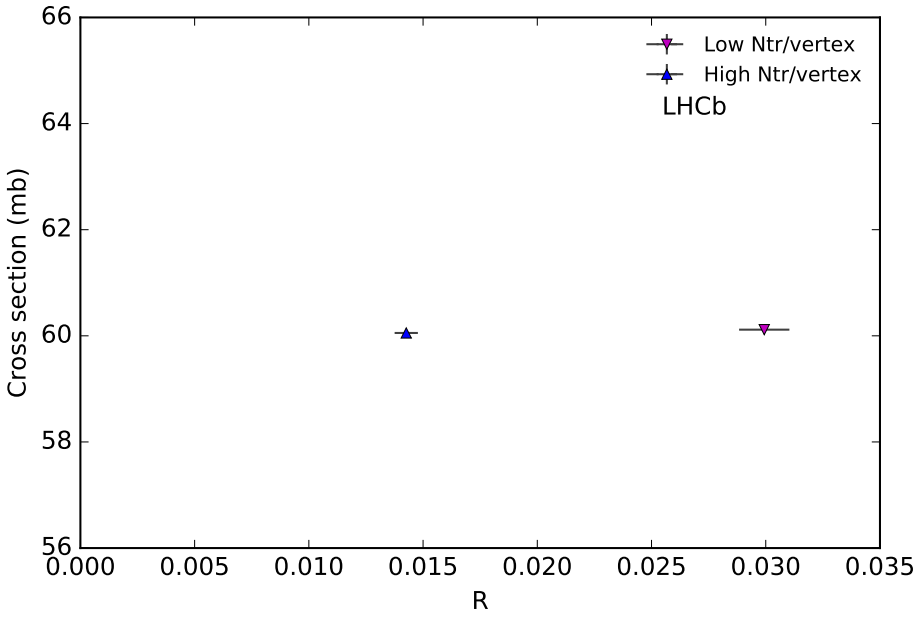

Figure 4.9: The different calibration cross-section measurements for samples of vertices with different multiplicities at a function of R.

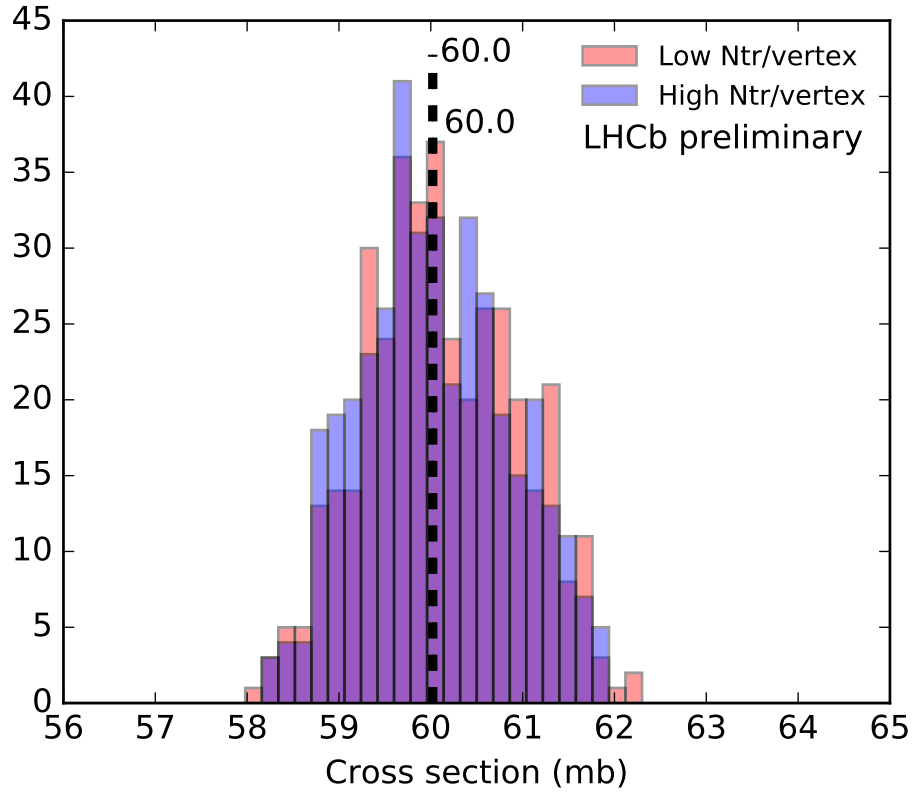

Figure 4.10: Histograms showing different calibration cross-section measurements for samples of vertices with different multiplicities.

Beam-Gas Resolution Corrections

A set of correction factors discussed in Sec. 2.5.3 are applied to the beam-gas resolution measurement. The necessity to include these correction factors for consistent beam position measurements across the longitudinal range of the VELO indicates a possible systematic uncertainty in the resolution measurement. Under the conservative assumption of a 100% error on their determination the overlap integrals are also measured without applying these correction factors. The resulting cross-section measurements for the *Vertex* counter are shown in Fig. 4.11 overlaid with the measurements including the corrections. The difference in the average measured cross-section with and without these correction factors is therefore taken as a systematic uncertainty on the final measurement of 0.12%.

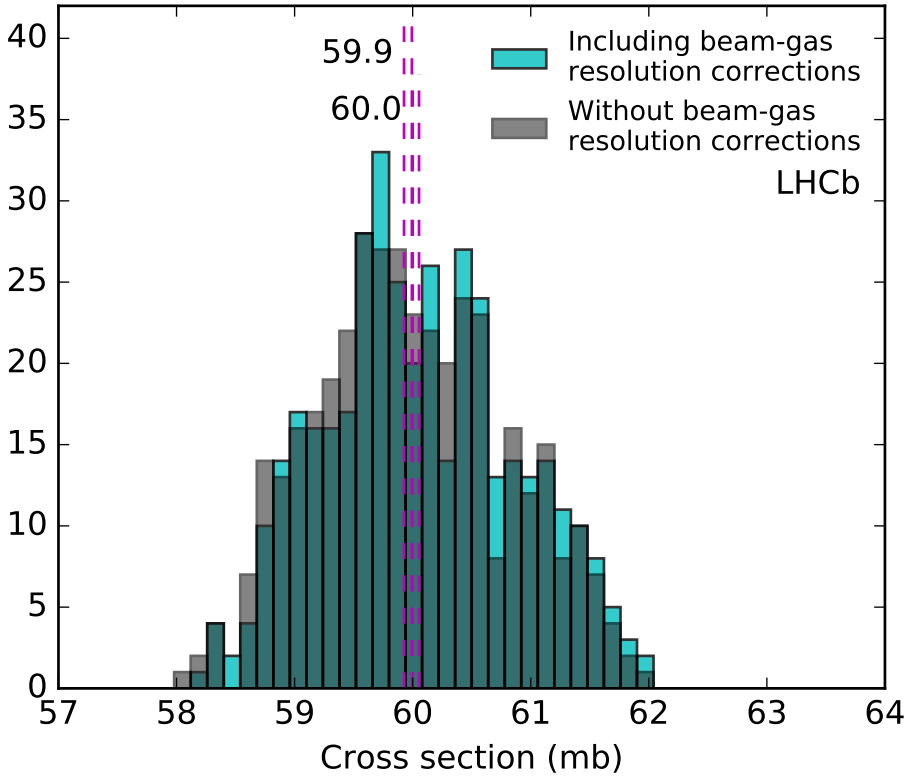

Figure 4.11: The difference in the distribution of calibration cross-section measurements for the *Vertex* counter at 13 TeV with and without beam-gas resolution corrections.

Crossing Angle and Detector Alignment

Any misalignment of the VELO subdetector could cause a degradation of the vertex position resolution and also broaden the observed beam width. The resolution uncertainty has been discussed above and the beam broadening effect is measured and corrected for as described in Sec. 2.6.4. However, another possible effect of any misalignment is on the determination of the crossing angle, which has an important effect on the evaluation of the overlap integral.

Previous studies in run 1 showed that across a set of 47 different VELO alignments for the same collision data, a spread in the crossing angle of 10 μrad is observed [7]. This variation in angle was found to induce a variation of up to 0.45% in the value of the overlap integral and this maximum value is taken as an estimate of the systematic uncertainty due to this effect.

Fit Shape

The double Gaussian fit shape used to describe the transverse bunch profiles does not allow for any further Gaussian components that could broaden or narrow the tails of the bunch distributions. If any higher order Gaussian components of the bunch profile are present the tails of the distribution would contain either a larger or smaller fraction of the bunch population with respect to the expectation from the fit.

The fraction of vertices in the tails beyond the double sided 99th percentile as predicted by the two-dimensional double Gaussian fit is shown for all fits from luminosity calibration fill 4937 in Fig. 4.12. The tail populations of the measured distributions is approximately 0.2% lower than the expectation for fits in the luminous region and up to 1% higher for the beam-gas distributions. This indicates that the true beam distributions are broader in the tails for the beam-gas vertices and narrower for the beam-beam vertices. The average deviation from the expectation is largest for the beam 1 vertices and this value of 0.5% is assigned as a systematic uncertainty due to the fit model on the final calibration result.

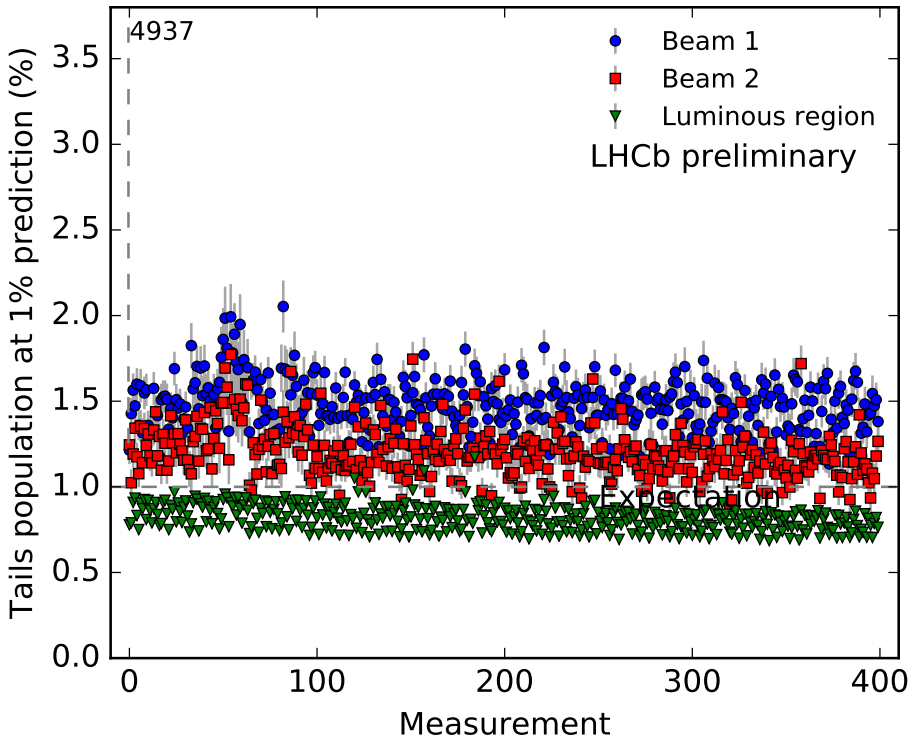

Figure 4.12: The proportion of vertices in the tails beyond the double-sided 99th percentile of the fitted bunch shapes in fill 4937. The fraction of vertices in the tails is underestimated by the fit for the beam-gas distributions and slightly overestimated for the beam-beam distributions.

Longitudinal Reconstruction Efficiency

The convolved bunch length and longitudinal crossing position are measured using a fit to the longitudinal distribution of the luminous region as described in Sec. 2.6.3. This measurement makes use of all vertices in the range $-250 < z < 250$ mm without reference to the directionality of their constituent tracks. This selection limits any distortion of the luminous region shape but does allow for the possibility of some small background from beam-gas interactions in this longitudinal range.

In order to account for this background and additional measurement of these parameters is performed by requiring at least two tracks in each direction for all selected vertices. This eliminates any beam-gas background but distorts the measured shape of the luminous region as backward tracks originating at a position of approximately $z > -95$ mm are not within the acceptance of the VELO. All cross-section measurements have been performed with both sets of track requirements and the difference in the measured cross-section of 0.05% is taken as a systematic uncertainty on the final measurement.

Pressure Gradient

The BGI method measures the colliding bunch profiles using beam-gas interaction vertices, making the implicit assumption that the pressure of the gas target is uniform in the transverse directions. The beam-gas interaction rate is proportional to the pressure of this residual gas and thus any pressure gradient running perpendicular to the beam trajectory would distort the measured transverse shape. This effect was measured in run 1 by displacing the beams along the transverse axes during collision and measuring the variation in beam-gas rates [7]. The relative error introduced by a possible pressure gradient was measured to be 0.03% and this is included as a systematic uncertainty on the final measurement.

FBCT Uncertainties

As discussed in Sec. 3.1.3, the relative bunch populations measured by the FBCT can be cross-checked with those measured by the BPTX system operated by the ATLAS experiment. This redundancy proved to be useful in fill 4937 where an offset was observed between the FBCT measurements of odd and even numbered bunches [49, 57]. These are measured by two independent devices that make up the full FBCT system. The BPTX, however, uses the same measurement device irrespective of the BCID and can be used to correct the two FBCT measurements. To account for this correction the calibration measurement is performed with the individual bunch populations given by both the FBCT and BPTX systems. The measurements of the *Vertex* cross-section using each device are found to be in good agreement (60.00 mb vs 60.26 mb) and the FBCT measurements are preferred due to their lower measurement spread (1.34% vs 1.53%). The difference in the central values of 0.43% is taken as an additional systematic uncertainty on the final calibration result.

Earlier comparisons of FBCT and BPTX measurements have shown some evidence of a possible non-linearity in both systems [46]. However, experience in run 1 showed that this effect was small at higher intensities ($\sim 10^{11}$ protons per bunch) [7, 46].

This possible small non-linearity can be described by a non-zero offset when extrapolating to zero bunch intensity. The value of this offset can be inferred from a combination of all cross-section measurements carried out during a fill as the true value of the cross-section is independent of the individual colliding bunch pairs. A fit is performed with both the offsets and cross-section values as free parameters, as described in Ref. [46]. The effect of these offsets on the individual measurements in fill 4937 is shown in Fig. 4.13 and as a histogram in Fig. 4.14. The measured value of the cross-section is seen to shift by 0.22 mb after these corrections are applied and this difference is taken as a systematic uncertainty of 0.37% on the final calibration measurement.

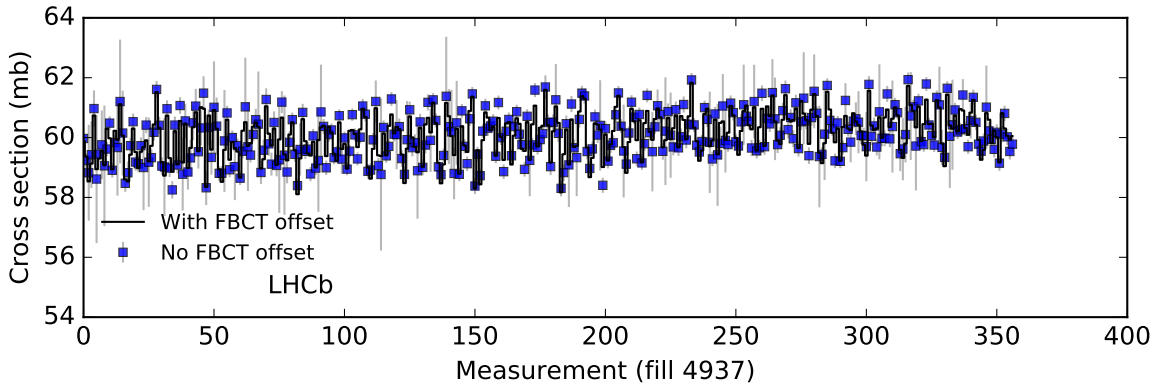

Figure 4.13: The measured cross-section values with and without an FBCT offset for the *Vertex* counter in fill 4937. The values without the offset are shown by the data points and the values with the offset are shown by the line. The measurements are sorted by time and BCID.

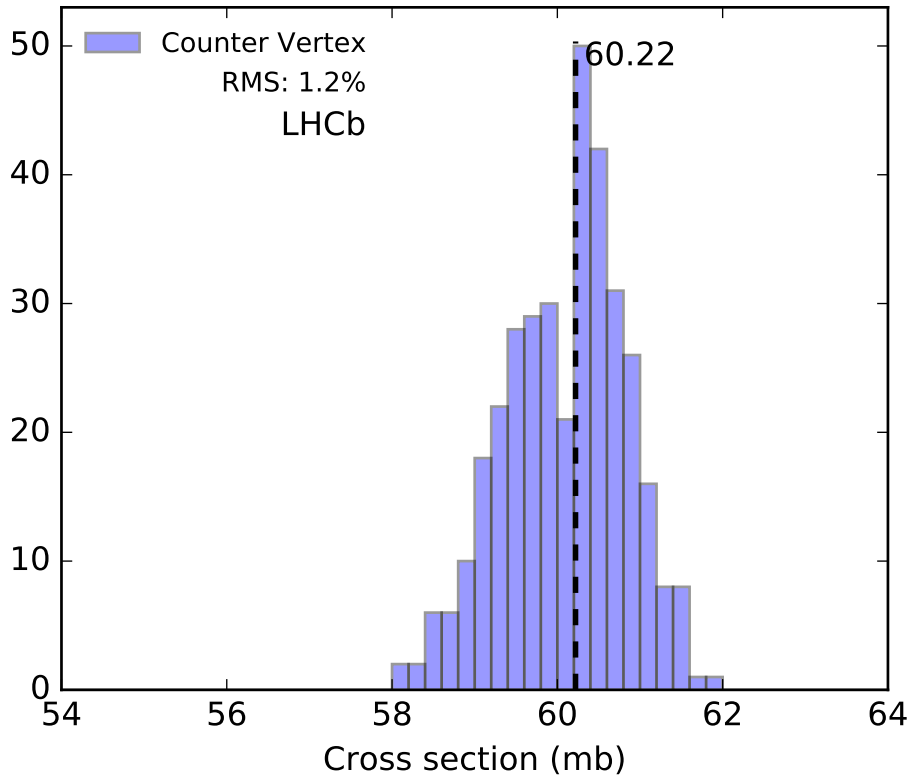

Figure 4.14: A histogram showing the measured cross-section values with an FBCT offset for the *Vertex* counter in fill 4937. The measurement spread is reduced with the corrections applied, from 1.34% to 1.22%, and the central value is shifted by 0.22 mb.

Summary

All of the systematic uncertainties considered as part of the BGI calibration analysis are summarised in Table 4.2. The total calibration uncertainty is determined from the sum in quadrature of the individual uncertainties.

An uncertainty of 0.08% is assigned to the conversion from the *Vertex* to the *Track* counter based on the largest observed difference in their ratios between physics and luminosity calibration data [58]. The 0.05% transverse scale precision of the VELO subdetector discussed in Sec. 1.3.1 is also included as a further systematic uncertainty. The bunch current normalisation error from the DCCT is discussed in Sec. 3.1.4 and the corrections for ghost and satellite charges are described in Sec. 3.2. The uncertainties due to these corrections are calculated for the ghost charge by propagating the error values given in Table A.1 and for the satellite charge by conservatively assuming a 100% uncertainty on the average satellite fraction in this fill of 0.01%, measured by the BSRL and given in Table 3.1.

Uncertainty	Value (%)
Measurement spread	1.34
Beam-beam resolution	0.09
Beam-gas resolution	0.12
Crossing angle & alignment	0.45
Fit model	0.50
Longitudinal reconstruction efficiency	0.05
Pressure gradient	0.03
Track/*Vertex* counter ratio	0.08
FBCT odd-even difference	0.43
FBCT non-linearity offset	0.37
DCCT uncertainty	0.30
Ghost charge	0.03
Satellite charge	0.01
VELO transverse scale	0.05
Total calibration uncertainty	1.64

Table 4.2: The full set of uncertainties considered for the LHCb luminosity calibration via the beam-gas imaging method. The total uncertainty is obtained from the sum of the individual uncertainties in quadrature.

4.2.3 Final Calibration Results

The reference cross-section for pp collsions at $\sqrt{s} = 13$ TeV for the *Vertex* counter is measured via the beam-gas imaging method to have the value given in Eq. 4.22:

$$\sigma_{Vertex} = 60.00 \pm 0.98 \text{ mb} \tag{4.22}$$

The list of all uncertainties considered for this measurement is given in Table 4.2 and the total relative uncertainty for this counter is found to be 1.64%. As the *Track* counter is the reference counter used during physics data-taking this measured cross-section is converted using the ratio of the two counters during the calibration period: $\mu_{Track}/\mu_{Vertex} = 1.097 \pm 0.006$. The combination of these measurements has a relative error of 1.73% and gives a final calibration result for the *Track* counter of:

$$\sigma_{Track} = 65.82 \pm 1.14 \text{ mb} \tag{4.23}$$

This calibration cross-section can then be used to determine the integrated luminosity in any given run 2 LHCb dataset at an energy of $\sqrt{s} = 13$ TeV in combination with the recorded interaction rate for the *Track* counter over the relevant data-taking period.

4.3 Conclusions

In this chapter the luminosity calibration process at LHCb is described and a new measurement of the calibration cross-sections for two different luminosity counters is reported. The luminosity counters in use at LHCb and their definitions are given in Sec. 4.1.1 while the measurement of the interaction rates for these counters is discussed in the remainder of Sec. 4.1. The Beam Gas Imaging per-bunch calibration measurements for the 2016 luminosity calibration session are reported in Sec. 4.2.1 for pp collisions at $\sqrt{s} = 13$ TeV, while the full range of systematic uncertainties affecting this measurement are described and evaluated in Sec. 4.2.2. Finally the values of the calibration cross-sections for the *Vertex* and *Track* counters are given in Sec. 4.2.3 along with the total uncertainty on each calibration measurement.

Chapter 5

Cross-Calibration of LHC Beam Profile Monitors

5.1 Introduction

At the LHC there are a number of different devices, employing a variety of techniques, capable of measuring the transverse profiles of the bunches making up the circulating proton beams in both planes and for each beam. Using the BGI method, the LHCb experiment has the unique capability (among the major LHC particle physics experiments) of providing measurements of individual bunch widths, which can be used to calculate the transverse emittance of each bunch with precise knowledge of the LHC accelerator optics.

In late 2016 a cross-calibration session was organised and the evolution of the beam profiles was monitored by all available profile monitors throughout an entire LHC fill. The LHCb beam size measurements were compared to those of the other existing LHC profile monitors in order to determine the level of agreement between the different profile measurement techniques. This took place during a dedicated cross-calibration Machine Development (MD) period in October 2016 (LHC fill no. 5456) in which the profiles of a small number of bunches with a large spread of transverse emittances were measured to help understand the compatibility of measurements from the different profile monitors. The injected bunches had normalised transverse emittances falling approximately within the range of $1 < \epsilon_{x,y} < 6$ μm [60]. This difference in transverse emittance was induced selectively as the bunches made their way through the LHC injector chain and should give a ratio of $\sim$2.4 between the widths of the smallest and largest bunches at any given point on the LHC ring.

The main pieces of instrumentation used by the LHC Beam Instrumentation group to measure transverse beam profiles, apart from the LHCb measurement, are the LHC wire scanners (WS) and the transverse Beam Synchrotron Radiation monitors (BSRT) [61, 62] (which op-

erate on a similar principle to the longitudinal monitor described in Sec. 3.2.1). The two general purpose experiments ATLAS and CMS are also able to provide a measurement of the convoluted size of both beams but cannot extract the information for individual beams with a high degree of accuracy. Here I will only present the comparison of LHCb results with the reference measurement from the WS in detail. Results from other experiments and instrumentation systems are detailed in [60, 63] and also take the WS measurement as their reference measurement.

5.2 The LHC Wire Scanners

The WS measurement is generally taken as the reference against which all other instrumentation approaches were compared and calibrated. A WS is an intercepting measurement device consisting of a thin carbon wire that is moved in a linear motion across the beam, as seen in Fig. 5.1. The resulting interaction between the beam and the wire produces a flux of secondary particles that are detected by means of a scintillator located several metres downstream from the wire. In order to measure the intensity of this secondary emission the light produced in the scintillator is captured by a coupled photomultiplier tube. The acquisition of both the wire position and emission intensity are synchronised with the revolution frequency of the particles in the beam so that one acquisition is made per turn around the machine for each bunch in the beam. The beam profile can then be determined by plotting the count rate in the scintillator against the wire position relative to the beam. This principle is illustrated in Fig. 5.2.

Similar devices are used for beam-profile measurement in all of the accelerator rings at CERN although with varying designs based on the beam conditions in each machine [61]. In the LHC the wire moves at a constant rate of 1 m/s and the device can only be used below a certain intensity threshold without risking destruction of the carbon wire through sublimation. At the LHC injection energy of 450 GeV this risk of wire damage is the limiting factor on the beam intensity. At the maximum beam energy for run 2 of 6.5 TeV a further constraint is imposed by the fact that losses from the beam produce a sufficient heat load to risk a quench in the LHC's superconducting magnets [64]. This MD session was therefore conducted with just 10 proton bunches per LHC beam and large spacing between bunches.

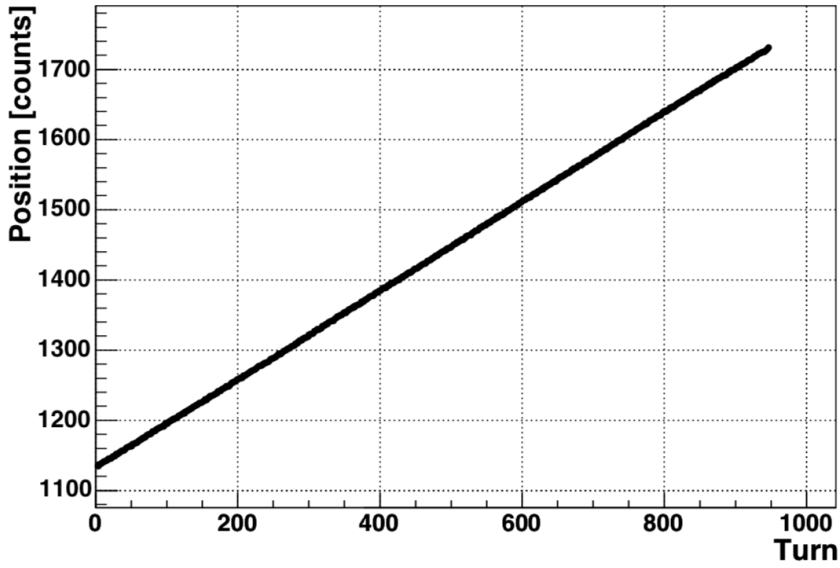

Figure 5.1: The linear movement of the wire position during a typical measurement with the WS. The position is recorded with a potentiometer and its values are given in counts, as read by the analog to digital converter connected to its output. The unit of time is one turn around the machine, which is equivalent to $1/f_{rev}$ seconds [61].

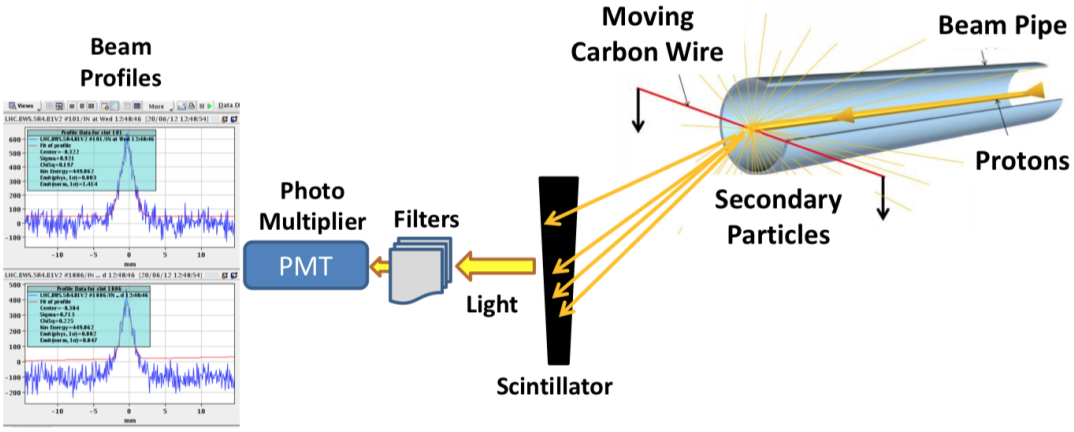

Figure 5.2: A diagram illustrating the working principle of a wire scanner system (figure taken from Ref. [62]). Secondary particles from the interaction between the beam and the wire generate light in a scintillator which is detected by a photomultiplier tube. The profile of the beam is reconstructed from the intensity recorded by the photomultiplier and the position of the wire.

5.3 LHCb Measurements

During this fill helium gas was injected into the beam pipe at LHCb using the SMOG system and the same optics were used as during a luminosity calibration fill, with $\beta^* = 24$ m at IP8. This optics configuration ensures that the beam sizes are increased relative to their sizes during normal physics operation and thus the relative effect of the VELO resolution on the measurement is reduced. The small number of bunches also allowed a large spacing between them in time, avoiding any issues with dead-time or spill-over between bunches.

5.3.1 Online and Offline Measurement Approaches

During data-taking, online monitoring of the beam properties involves the collection of suitable reconstructed beam-gas interaction vertices, and the periodic publication of the measured values once sufficient statistics have been accumulated. The beam-gas interactions can be isolated by analysing only be or eb bunch crossings, in which a filled bunch from only one of the two beams passed through the LHCb IP. Currently, due to bandwidth and computing constraints, only a fraction of bunch crossings are available to process for monitoring in real time [65].

Offline, the analysis can be repeated using the full available sample of beam-gas vertices (including those from bb crossings) and a more precise event selection. This has the effect of reducing the statistical component of the uncertainty and the offline approach also allows for a more careful treatment of any potential systematic uncertainties. In particular, the online analysis was run using a VELO vertex position resolution description determined using data from a previous fill. In the offline analysis, however, it was possible to run a new resolution analysis (see Sec. 2.5) on data from the same fill and thus to more accurately measure the position resolution of the acquired vertices during the period the cross-calibration data was recorded. The beam parameters and bunch profiles were then measured using the same techniques described in Chapter 2 of this thesis. The transverse profile fits were performed using the simple Gaussian model given in Eq. 2.11 as this is the model most directly comparable with that used by the other profile measurement devices.

From Fig. 5.3 it can be seen that the agreement between both methods is good for larger beam sizes where the resolution is much smaller in magnitude than the beam size. However, a more pronounced difference between the two measurements can be seen for smaller beam sizes where the magnitude of the resolution starts to become comparable to the size of the beams.

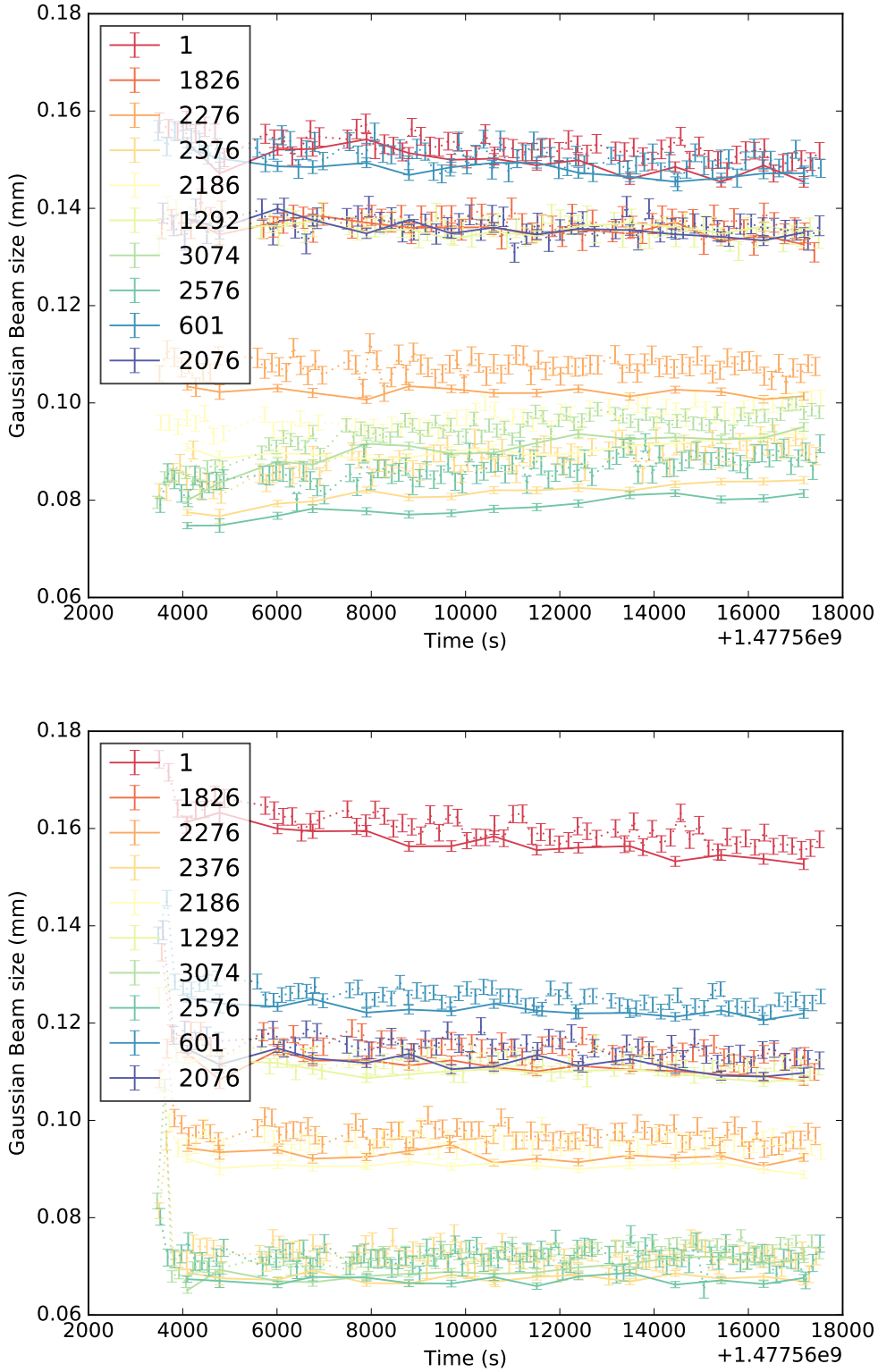

Figure 5.3: The horizontal (top) and vertical (bottom) transverse bunch widths measured by LHCb in fill 5456 for LHC beam 1. These measurements were made using both the online (dotted line) and offline (solid line) measurement approaches. The online beam profile measurement is documented in Ref. [65]. The numbers in the key correspond to the BCID for each measured bunch. Bunches with the same BCID from each beam were colliding pairs at IP8 and the beam 2 bunches have very similar transverse sizes.

5.3.2 Comparison with Wire Scanner Measurements

The LHCb experiment is located at interaction point 8 of the LHC while the WS system is located at point 4 (see Fig. 1.1). In order to make comparisons between the beam sizes measured by the two instruments it was thus necessary to measure the value of the β function at the location of each. This was done using a technique known as k-modulation, illustrated in Fig. 5.4.

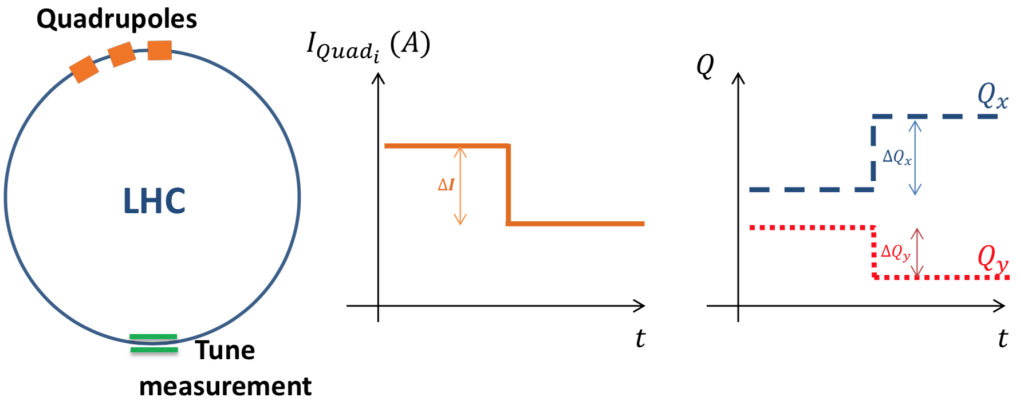

Figure 5.4: The working principle of a k-modulation measurement.

This measurement is performed at a quadrupole by varying its focusing strength, k. This is achieved by varying the current I through the electromagnet and thus the strength of the focusing field. This change in focusing strength will then induce a change in the tune of the beam, Q. The tune is defined as the number of complete betatron oscillations an individual particle in the beam will have completed during one full turn around the ring. Its mathematical definition is presented in Eq. 5.1 where s is the path around the accelerator ring.

$$Q \equiv \frac{1}{2\pi} \oint \frac{ds}{\beta(s)} \tag{5.1}$$

The tune can be measured from the beam orbit observed by the beam position monitors located around the LHC ring [66]. The change in strength, Δk can then be shown to be related to the β function and the change in tune as in Eq. 5.2, where l_q is the length of the quadrupole in question [61].

$$\beta = 4\pi \frac{\Delta Q}{l_q \Delta k} \tag{5.2}$$

This technique is thus used to measure the β function at the quadrupoles on either side of the point of interest. The value at the location of the measurement device is then determined by a polynomial extrapolation as described in [67]. This is done separately at IP8 and point 4 using the nearest quadrupoles to each measurement device.

With a measured value of β it is then possible to directly compare the beam sizes measured

by each instrument. From the values presented in Figs. 5.5 and 5.6 it can be seen that the two techniques agree to within 10% for all beams and dimensions except in the x measurement for beam 1. A discrepancy of $\sim 40\%$ is observed here, with the emittances measured by LHCb systematically larger than those measured by the WS. Checks were carried out on the LHCb measurement to eliminate potential sources of systematic error. In particular we looked for any significant longitudinal variation in the measured transverse beam size over the length of the VELO as this could indicate a problem with the resolution determination. However as shown in Fig. 5.7, the measured width is found to remain stable over a range of longitudinal positions within the VELO. Other checks on the internal consistency of the LHCb measurement were performed with the measured beam slopes and beam profile shapes remaining stable throughout the fill. The deviation could be due to a systematic problem with the WS measurement. However, given the past reliability of these instruments and the better agreement between the WS and other measurement approaches the most likely explanation is an error in the β^* measurement for LHCb. The consistency of the LHCb measurement was also checked by using these data to measure an effective cross-section with a similar approach to that described in Chapter 4. The cross-section measurement for the *Vertex* counter can be seen in Fig. 5.8. This was found to be stable to within a few percent across bunches and over the duration of the fill and its central value agrees, within uncertainties, with that given in Eq. 4.22.

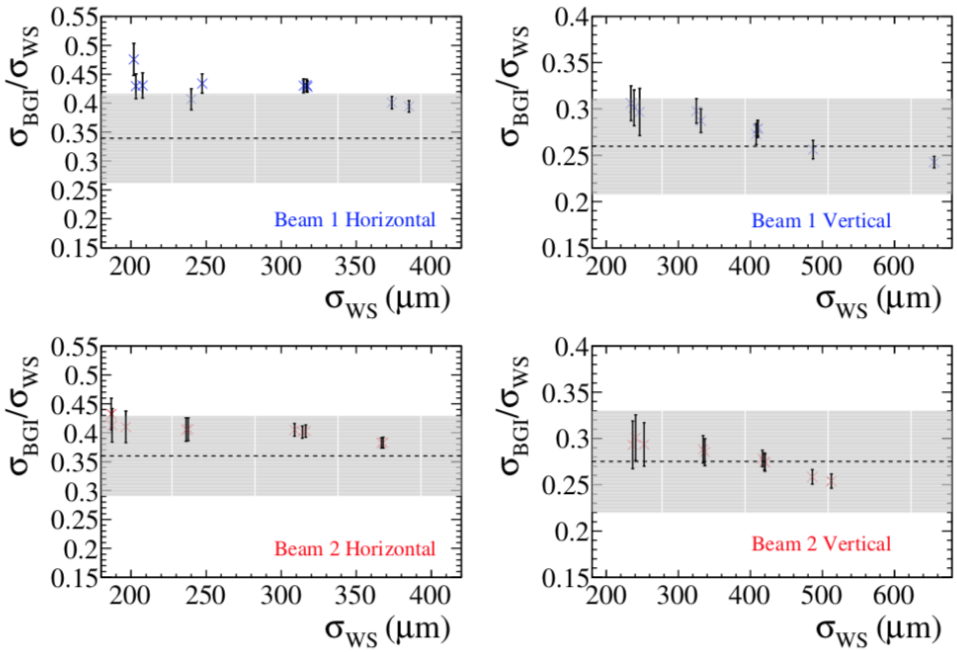

Figure 5.5: The ratio of beam sizes measured by LHCb to that measured by the WS as a function of the WS measurement. Each point represents a different bunch. The dotted line shows the ratio between the values of β measured at each point and thus the expected ratio between the beam size measurements. The grey bands show the uncertainty from the β measurements at the two points [65].

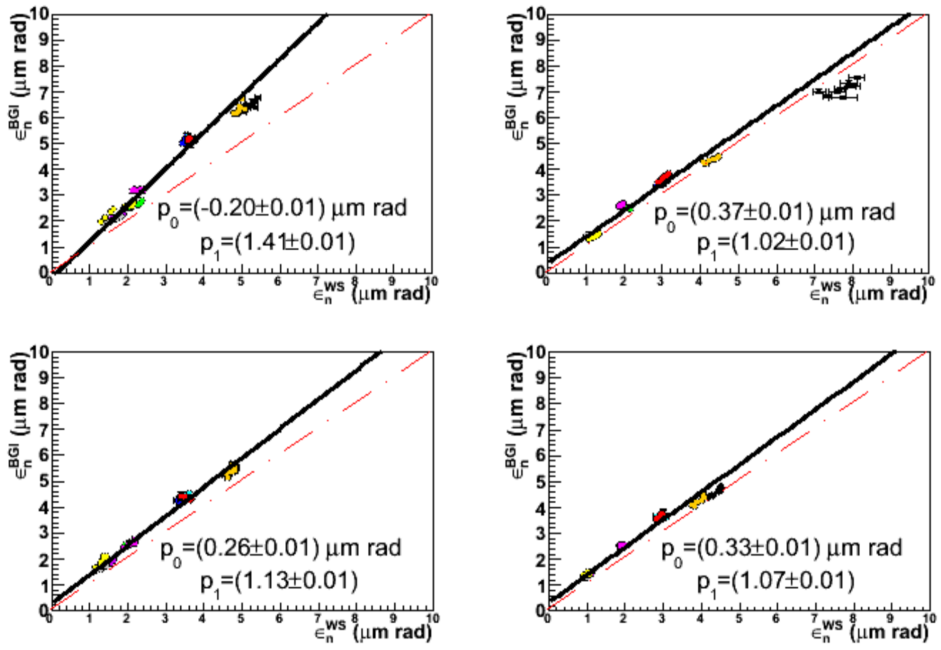

Figure 5.6: The emittance values measured by the LHCb BGI method as a function of those measured using the WS. The emittance values are calculated using the measured beam sizes and β values at each point via Eq. 1.7. Each point on the plot represents a bunch and the dashed dotted line the expected fit to those points if the two measurements were in perfect agreement [60]. The plots are arranged as in Fig. 5.5 with the horizontal (vertical) measurements in the left (right) column and the measurements for beam 1 (2) given above (below). The uncertainties shown in this figure are only those that are statistical in nature.

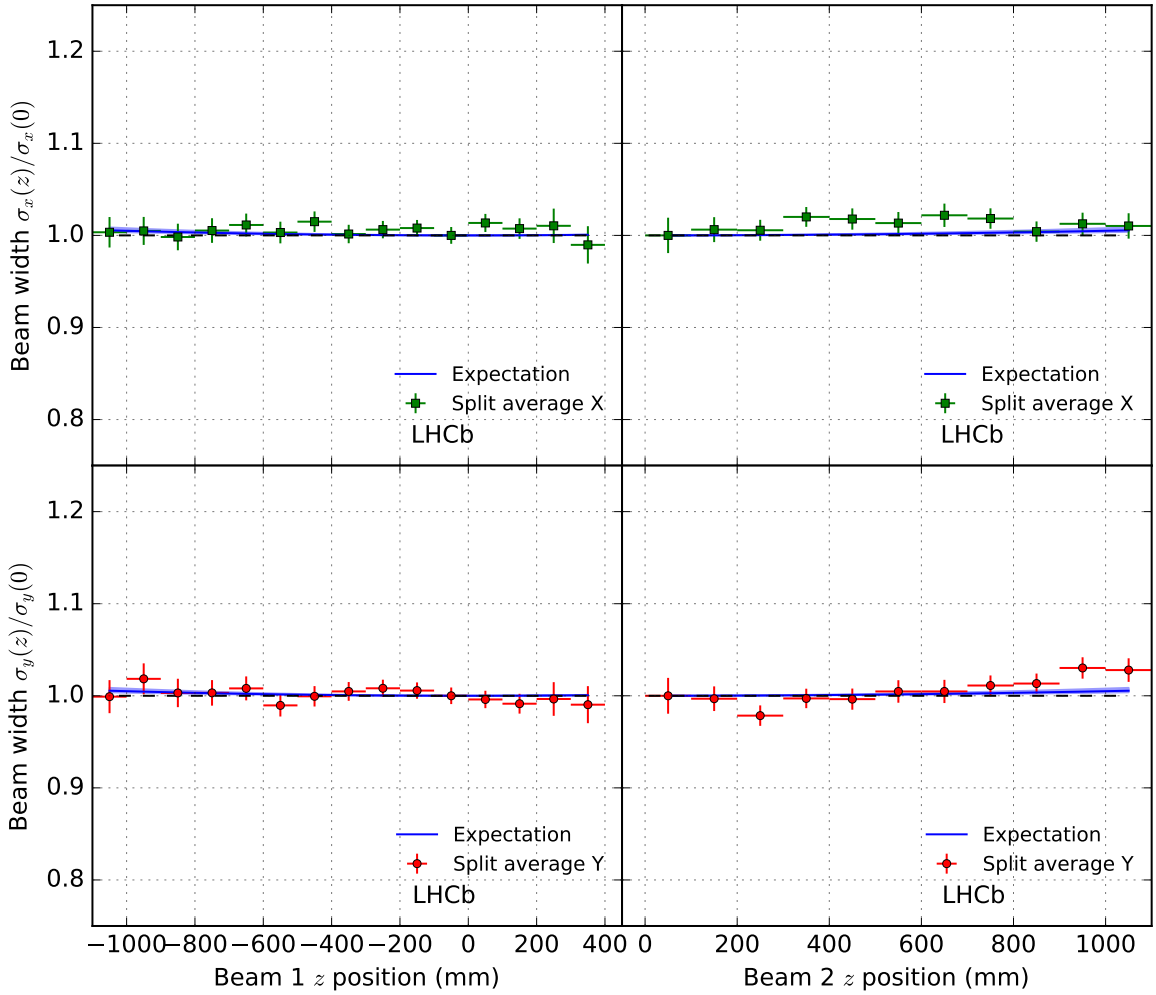

Figure 5.7: The variation of the beam width measured using the BGI method in x and y over the length of the VELO in fill 5456. The beam width measurements are normalised to their values at the centre of the IP. The expectation deviates by a small amount from a flat line towards the edges of the longitudinal range due to the hourglass effect. No systematic variation is observed.

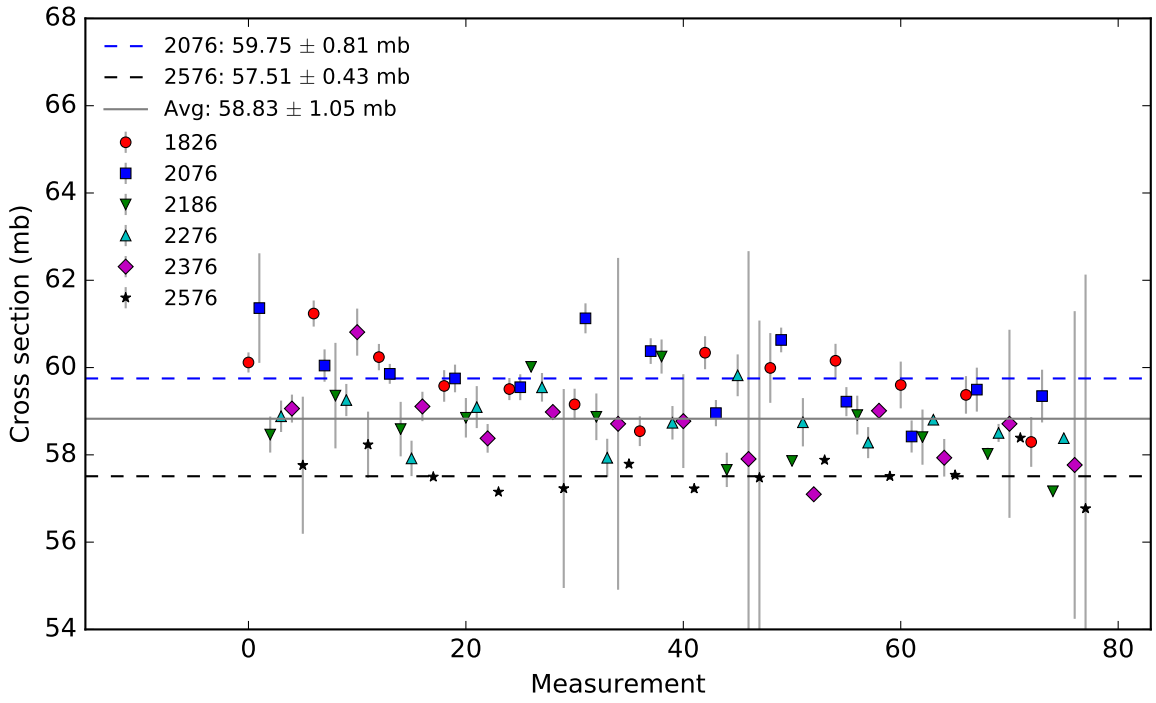

Figure 5.8: The different calibration cross-section measurements for the *Vertex* reference counter as measured in LHC fill no. 5456. Only the bunches colliding at IP8 are included. The measurements are significantly different for the largest and smallest bunch widths due to the relative importance of the vertex resolution but their average value remains stable over time. The average value for the widest bunch (2076) is shown by the blue dashed line, for the narrowest bunch (2576) by the black dashed line and for all colliding bunches by the solid grey line.

5.4 Conclusions

This machine development study was the first dedicated cross-calibration of all LHC beam profile monitors and took place under dedicated machine conditions. The measurements produced by LHCb were shown to agree to within 10% with those produced by the reference measurement device in all cases except for the measured horizontal size of LHC beam 1. The large discrepancy in this case does not seem to be due to any clear systematic effect at LHCb. One possible explanation is a large systematic error in the measurement of the β at IP 8, however, in order to confirm this hypothesis it would be necessary to undertake a new machine development session with a different configuration of the LHC optics.

Chapter 6

Dynamic Vacuum

6.1 Introduction

Beam-induced dynamic vacuum effects are well documented at the LHC with larger beam intensities leading to non-negligible increases in the vacuum pressure within the LHC beam pipe [68, 69]. One example of this is at LHCb where during run 1 of the LHC a five-fold increase in the vacuum pressure was observed at pressure gauges within the volume of its VELO subdetector under the influence of 1380 bunches of 2×10^{14} protons [15]. Throughout the duration of run 2 the LHC has regularly operated with more than 2000 bunches per fill and yet larger beam intensities are foreseen for the future running of the accelerator as part of the High Luminosity LHC project.

It has been proposed that these dynamic vacuum effects could be enhanced by the proximity of the RF foil that isolates the VELO detector modules. This foil is retracted during injection but approaches to within 5 mm of the collision point after the declaration of stable beams. If this is the case, then understanding the effect could become more important in the context of the new VELO design proposed for the LHCb upgrade. As part of the changes to the subdetector a new RF foil design will be implemented with a smaller distance of closest approach of only 3 mm [70]. In addition, as the LHC moves to High Luminosity conditions the increasing bunch intensities will also increase the magnitude of any surface bombardment effect.

In order to investigate this possible effect, the changes in the observed rate of beam-gas interactions inside and outside the volume between the two RF boxes, before and after the VELO closing were measured. To achieve this without biasing the measurement through the change in geometric acceptance due to movement of the VELO, it is necessary to make use of LHCb's downstream tracking system for the vertex reconstruction (see Fig. 1.4). These tracking stations are most commonly used in conjunction with the VELO tracks to form what

are known as long tracks to measure the momentum of long-lived particles that pass through LHCb's magnet before decaying. However, they can also be used as independent tracking detectors in their own right.

6.2 Vertexing Algorithm

As the downstream tracking is not normally used for precise primary vertex reconstruction, the capabilities of these tracking detectors needed to be assessed and an adapted vertexing algorithm implemented for the purposes of this study. The vertexing results presented here were obtained by running a modified version of the LHCb event reconstruction application *Brunel v50r1* using a *GaudiPython* script. This script runs a modified version of the track reconstruction [59] where information from the VELO is not used to seed the pattern recognition, such that the result makes use of only those tracks that can be reconstructed as "Downstream" tracks. These are seeded using only information from the TT and T stations, unlike Long tracks which also use information from the VELO. The difference can be seen graphically in Fig. 6.1. Some tracks which are normally found as Long will instead be found as Downstream, however this will not be possible in all cases due to the loss of information from the VELO.

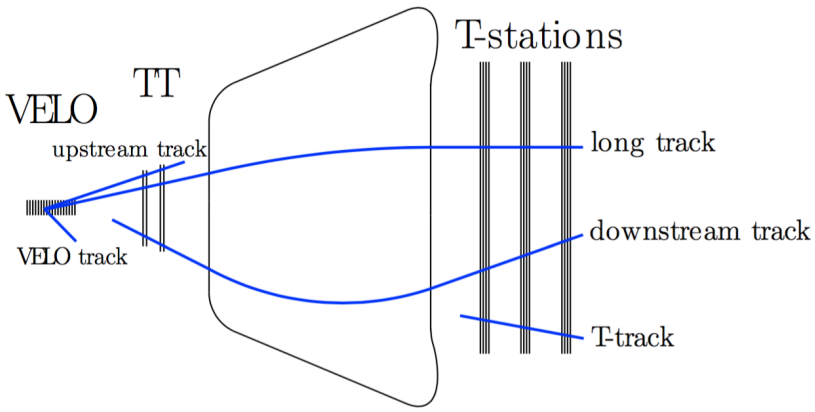

Figure 6.1: The different types of reconstructed track used at LHCb [17]. Each type of track is assigned an integer key as in Table 6.1.

Key	Track Type
1	VELO
3	Long
4	Upstream
5	Downstream
6	T

Table 6.1: The integer keys assigned to each type of track reconstructed by LHCb.

The Downstream tracks reconstructed in this way are then used to produce a vertex using an LHCb *TrackStateVertex* (TSV) fit on an event-by-event basis. This fitted vertex is then iteratively refined, if possible, by removing the track with the highest χ^2 contribution until either the track multiplicity falls to a value of 4 tracks or the χ^2 per degree of freedom for the vertex falls below a value of 10. This simple approach will only allow the reconstruction of one vertex per event so in order to conduct a like-for-like comparison for the purpose of benchmarking, we pre-select only events where the standard PV finding algorithm also reconstructed only one primary vertex. For benchmarking of the vertexing algorithm the vertex positions generated by this method are saved alongside those found by the standard PV algorithm, which are taken as the reference or "true" positions. In order to estimate the resolution of the downstream vertex the difference between these two vertex positions is calculated, again on an event-by-event basis. The ensemble of these differences is then fitted with a Gaussian distribution and its standard deviation is taken as the resolution. The relative efficiency of the downstream vertexing is determined by equation 6.1 where η is the efficiency, n_{PV} is the total number of beam-gas vertices found by the standard PV algorithm and n_d is the number of selected downstream vertices.

$$\eta = \frac{n_d}{n_{PV}} \tag{6.1}$$

6.3 Vertexing Performance

The algorithm was tested using data from LHCb run 175507 of LHC fill number 4964 which took place in May 2016 with a β^* of 3 m at IP8, bunch intensities of approximately 10^{11} protons per bunch and an average μ of 1.08. This fill was chosen as it contained 253 bunches, out of 1752, that were non-colliding at IP8 and thus a significant rate of 1.1 kHz was produced in the BEAMGAS stream of LHCb's High Level Trigger (HLT). Of this rate 63% of events were beam-gas events in a slot where beam 1 (2) is nominally filled (empty) and thus observable by the downstream tracking system. Due to the large peak at small values of $|z|$ that can be seen in Fig. 6.2, a cut was also applied on the longitudinal position of the vertices. A value of $|z| < 200$ mm was chosen in order to remove contamination from beam-beam interactions in the luminous region.

Initial checks on this vertexing approach were performed to make sure that the process of excluding VELO information was producing the desired effect. The histograms in Fig. 6.3 show the differing contents of the track container *Rec/Track/Best* before and after the exclusion of VELO information. After this modification the information from VELO tracks is lost and only Downstream tracks remain but the number of available Downstream tracks increases due to the migration of a large number of Long tracks into Downstream tracks.

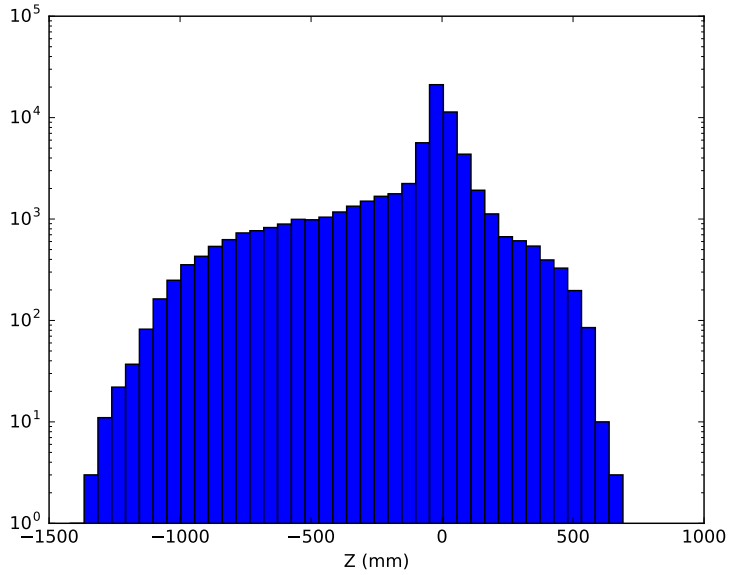

Figure 6.2: The z profile of reconstructed beam-gas vertices showing the large peak in the luminous region which indicates a contamination from beam-beam events.

There is not a one-to-one equivalence here as not all Long tracks can be reconstructed without VELO seeds as the efficiency of reconstruction is lower using only TT seeds. It can be seen, however, from Fig. 6.4 that the number of Downstream tracks after this exclusion is monotonically correlated with the sum of Long and Downstream tracks before the exclusion. Further checks were also performed to assess the Gaussian nature of the distribution of differences which can be clearly seen in Fig. 6.5.

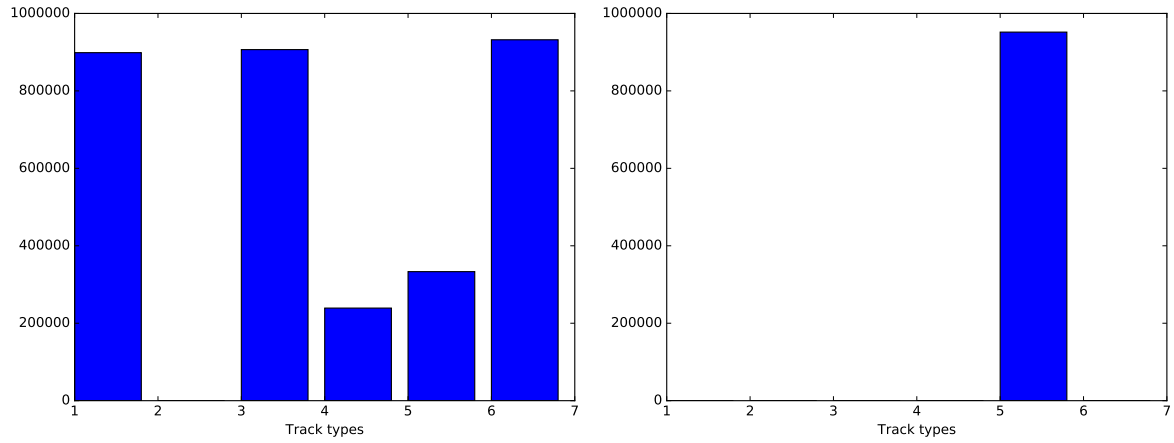

Figure 6.3: Histograms showing the different track types in the container *Rec/Track/Best* before and after the exclusion of VELO information (left and right plot respectively). The track types are as defined in Fig. 6.1 and Table 6.1.

The key performance parameters for this vertexing procedure are the efficiency and the resolution. A sufficiently small resolution is required to allow discrimination between genuine

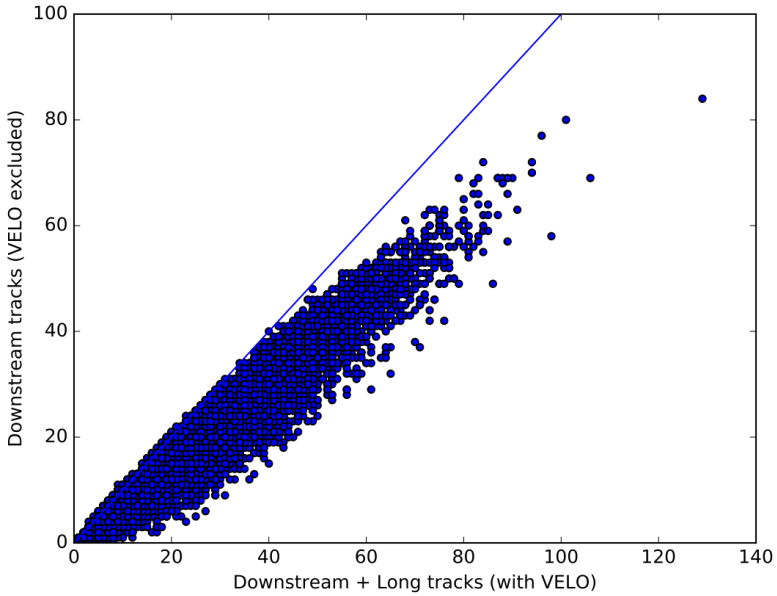

Figure 6.4: The total number of Downstream tracks after VELO exclusion as a function of Long and Downstream tracks before the exclusion of VELO information. There is a clear monotonic relation and the line shows a linear correlation with a coefficient of 1 for reference.

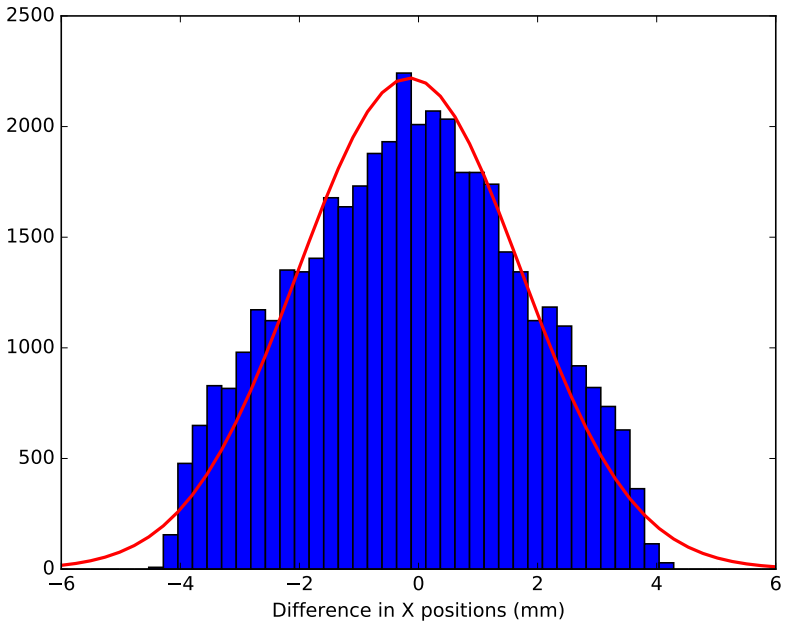

Figure 6.5: The distribution of differences in x position between standard beam-gas vertices and those reconstructed using the downstream tracking. Values obtained with a radial cut at 4 mm and no multiplicity cut. The red line shows a Gaussian fit to the data.

beam-gas interactions and interactions in the RF foil that could mimic them. These would

otherwise be indistinguishable on an event-by-event basis. In this study it was found possible to achieve resolutions of $\sigma_x = 1.87$ mm, $\sigma_y = 1.30$ mm and $\sigma_z = 101$ mm with a very loose cut on the multiplicity of nTracks ≥ 3.

With the VELO modules closed, the RF foil is positioned at 5 mm from the interaction point. Assuming a radial selection of $\rho \leq 4$ mm, these values for the transverse resolution give a clearance of more than 2σ from vertices originating in the foil with an efficiency of 64%. This should be sufficient to exclude more than 90% of material interactions which could otherwise appear indistinguishable from a beam-gas interaction. The longitudinal resolution is more than sufficient to localise vertices within the 1 m length of the VELO module. This is far from the only possible configuration and the evolution of the two transverse resolutions and the efficiency with a varying cut on the multiplicity can be seen in Figs. 6.6 - 6.7. A tighter cut on the vertex multiplicity was examined but was seen to lead to a sharp drop in the efficiency and only small gains in transverse resolution. To confirm that this resolution is sufficient to exclude any significant background effect, further studies are necessary to determine the magnitude of the background effect from material interactions. The resolution in x was generally observed to be worse than that in y. This is due to the design of the downstream tracking system, which is optimised to make momentum measurements in the horizontal bending plane of the LHCb dipole magnet.

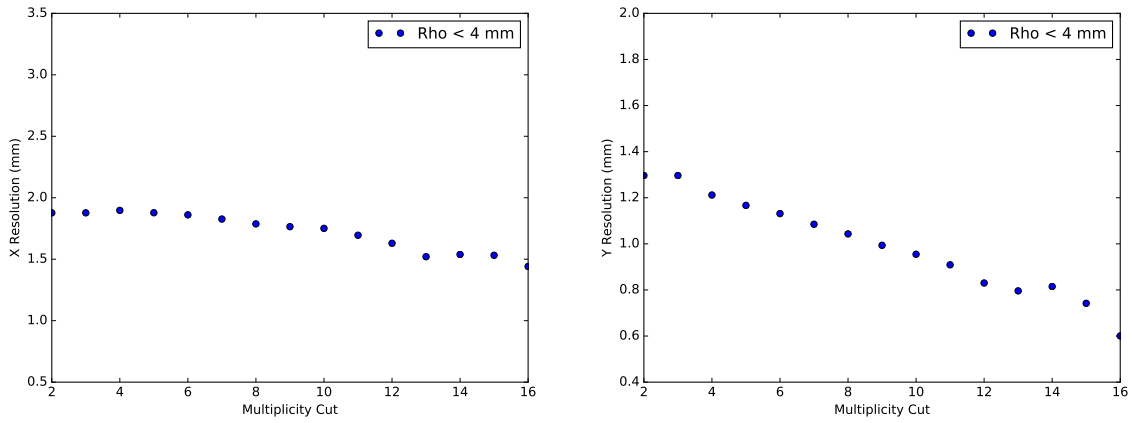

Figure 6.6: The x and y resolutions as a function of the cut on the multiplicity of the vertex.

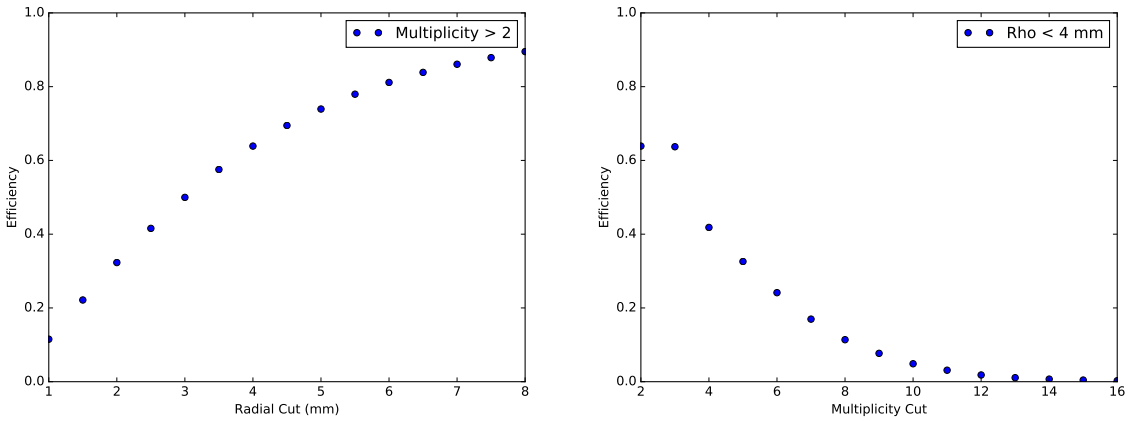

Figure 6.7: The efficiency as a function of cuts on the radial position and the multiplicity of the vertex.

6.4 Dynamic Vacuum Measurements

We would expect the proposed dynamic vacuum effects to cause a beam-intensity dependent pressure differential between the residual gas inside and outside the VELO. In order to measure this possible effect in the following measurements we reconstruct beam-gas vertices using only the downstream stations, achieving a transverse resolution of $1.9\,\mathrm{mm}$ in x, $1.3\,\mathrm{mm}$ in y and a longitudinal resolution of $\sigma_z = 11\,\mathrm{cm}$. Vertices are classified as being inside or outside the VELO based on the position of the VELO edges as measured in Ref. [72]. Margins of $\pm 2\sigma_z$ are used to avoid cross-feed between the two samples, resulting in ranges of $[-13, 53]$ cm ($[-200, -57] \cup [97, 200]$ cm) for the inside (outside) range. The longitudinal positions of the vertices reconstructed within each region can be seen in Fig. 6.8. A radial cut of $4\,\mathrm{mm}$ is applied to the reconstructed vertex position in order to limit contamination from material interactions. The longitudinal variation of the vertex reconstruction efficiency, ρ, is estimated when the VELO is open as the ratio of the rates of beam-gas vertices in the two fiducial regions, as shown in Eq. 6.2. The rates are average rates calculated by simple division of the number of reconstructed vertices by the time period of observation.

$$\rho = \frac{R_{\text{in—open}}}{R_{\text{out—open}}} \tag{6.2}$$

Finally, after the VELO is closed the beam-gas vertex rates are used to estimate the pressure inside relative to outside, calculated as in Eq. 6.3. This approach avoids the need for a precise baseline pressure measurement. Such a baseline measurement is not possible with the currently installed pressure gauges.

$$\frac{p_{\text{in}}}{p_{\text{out}}} = \frac{R_{\text{in—closed}}}{R_{\text{out—closed}}/\rho} = \frac{R_{\text{in—closed}}R_{\text{in—open}}}{R_{\text{out—closed}}R_{\text{out—open}}} \tag{6.3}$$

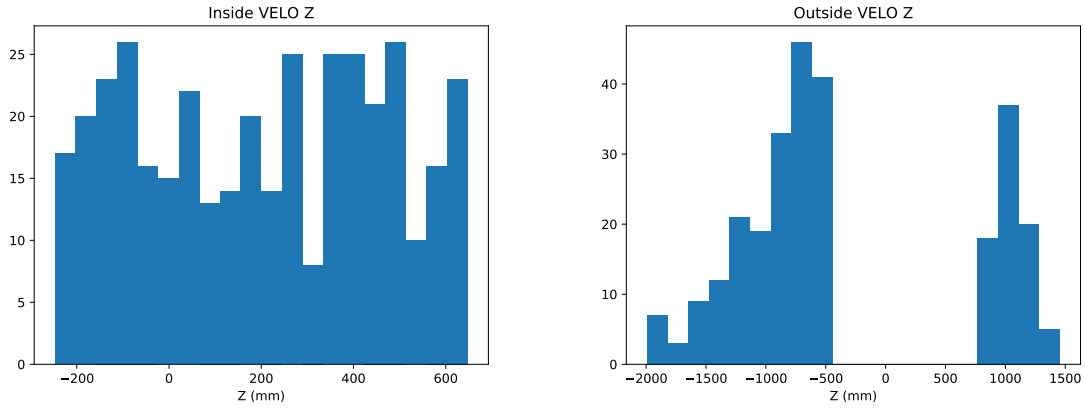

Figure 6.8: Histograms showing the longitudinal positions of vertices classified as being inside (left) and outside (right) of the VELO volume.

The outlined method is applied in two separate LHC fills of differing beam intensities. At a lower intensity, data come from LHC fill no. 6012 with 57 bunches per beam and at the higher intensity from LHC fill no. 6245 with 1916 bunches per beam. Under high intensity conditions only vertices from bunches crossing the opposing beam's abort gap are used in order to eliminate contamination from ghost charge p-p collisions. These could take place if ghost charge in the nominally empty slot were to collide with a proton in the filled slot. The abort gap is a longitudinal segment of the beam, at least 3 μs in length, that is specially monitored and cleaned in order to avoid a quench of the LHC dipoles during the beam dump process [73]. The kicker magnets used to perform the dump have a finite rise time during which their magnetic field strength varies and without this gap any passing charge would be sprayed into the surrounding superconducting dipole magnets, possibly depositing enough energy to cause a quench. Ghost charge fractions in this portion of the beam are, therefore, typically much lower than elsewhere so the contamination from ghost charge interactions should be negligible. The data recorded at low beam intensity is used as a control sample, assuming the effect under these conditions is small with respect to any potential effect at high intensity.

The longitudinal variation of the reconstruction efficiency, ρ, is measured with the data from the two fills and the difference of 8% is conservatively taken as a systematic uncertainty. Small variations ($\simeq 0.5\sigma_z$) in the boundaries of the fiducial volumes are found to have a negligible impact on the result, so no systematic uncertainty is assigned to this exclusion procedure. With all of these sources of uncertainty taken into account the relative pressure change shown in Eq. 6.4 is observed at high intensity, where the first uncertainty is statistical

and the second is systematic.

$$\frac{p_{\text{in}}}{p_{\text{out}}} = 1.21 \pm 0.02 \pm 0.08 \tag{6.4}$$

The results at low intensity are given in Eq. 6.5 with the first uncertainty again being statistical and the second systematic.

$$\frac{p_{\text{in}}}{p_{\text{out}}} = 1.04 \pm 0.04 \pm 0.08 \tag{6.5}$$

The results at low intensity are compatible with a ratio of 1 (indicating no effect due to the VELO foil position), however, those at high intensity show a statistically significant increase within the VELO volume, at 2.6 standard deviations. This indicates a measurable pressure increase with closed VELO at high beam intensity.

6.5 Conclusions

This study demonstrated a new use case for beam-gas interactions at LHCb. A new vertexing method was developed and deployed under a variety of beam conditions. The performance of this vertexing approach was evaluated and it was demonstrated to provide the necessary precision for useful measurements of beam-gas interactions. In order to evaluate any possible influence of the VELO foil position on beam-induced dynamic vacuum effects these measurements were made in two LHC fills of differing intensities. The results from the low intensity fill were taken as a reference and used to evaluate any possible effect at high intensity. A statistically significant increase in the beam-gas interaction rate was observed in the fill with higher beam intensity. This implies a real increase in pressure due to an enhancement of beam induced vacuum degradation when the VELO foil is brought into closer proximity with the LHC beams.

Chapter 7

Conclusions

This thesis presents a new absolute luminosity calibration measurement at LHCb for pp collsions at $\sqrt{s} = 13$ TeV measured via the beam-gas imaging (BGI) technique with data acquired in the 2016 luminosity calibration session. The measured reference cross-sections under these conditions for the *Track* and *Vertex* counters are $\sigma_{Track} = 65.82 \pm 1.14$ mb and $\sigma_{Vertex} = 60.00 \pm 0.98$ mb, respectively.

The principle of the BGI technique is explained in Chapter 2 of this thesis and the full set of BGI measurements from 2016 necessary for the calibration result are presented here alongside further beam imaging results from a broader set of run 2 calibration data. The experimental conditions under which this calibration data was recorded are set out here, including the process of gas injection vital for the BGI measurement, as well as the trigger configuration and offline event selection used at LHCb for these calibration fills throughout run 2 of the LHC. The procedure for determining the vertex position resolution from collision data via the split vertex method, a crucial element of a precise BGI measurement, is then described and measurements of the resolution are reported along with all necessary corrections. With a precise knowledge of the detector resolution it is possible to accurately measure the LHC beam profiles and parameters on a bunch-by-bunch level from their interactions with gas molecules in the LHCb beam pipe and with each other. This accurate description of the bunches colliding at LHCb allows for a precise evaluation of the overlap integral between them, a quantity that is directly proportional to the luminosity their collisions produce.

The measurement of the other important ingredient for a precise measurement of the luminosity, the bunch populations, is described in Chapter 3. These measurements make use of an array of different LHC instrumentation that is described at the start of the chapter along with the results relevant for the calibration measurement. A small correction to these LHC measurements is provided by the LHCb BGI measurement of the ghost charge, circulating charge not captured in a nominally filled LHC bunch slot. This topic then presented and described in detail. Ghost charge results are reported under a wide range of conditions including the

first such measurements made with the VELO subdetector in its open position and with the first xenon beams circulating in the LHC. A full set of BGI ghost charge measurements for all relevant run 2 fills is given in Appendix A. The utility of the LHCb measurement as a cross-check on measurements from LHC instrumentation is also demonstrated and a novel timing technique making use of the LHCb Outer Tracker is described. The additional timing information permits the first LHCb measurement of the longitudinal LHC beam profile with a time granularity smaller than an individual bunch slot.

In chapter 4 the work from the previous two chapters is combined to produce a luminosity calibration measurement for pp collsions at $\sqrt{s} = 13$ TeV. The luminosity counters required to propagate the calibration measurement to the full LHCb dataset are defined here and the measurement of the interaction rates for these counters is detailed. The calibration cross-section results determined for these counters are then reported and the full range of systematic uncertainties affecting this measurement are described and evaluated. The reference cross-section for the *Track* counter, used for the luminosity determination in LHCb physics data, is determined to a precision of 1.73%.

Chapters 5 and 6 set out two additional studies that make use of beam-gas interactions at LHCb. The first is a collaborative effort in which a cross-calibration of all existing bunch profile measurement techniques at the LHC was performed. The second is a study of possible dynamic vacuum effects due to the movement of the VELO subdetector and relies on a novel vertexing approach making use of the LHCb experiment's downstream tracking stations. This approach demonstrates a statistically significant pressure increase within the VELO volume due to its movement, at 2.6 standard deviations.

The BGI technique in use at LHCb has proven to be a powerful and unique measurement tool at the LHC and provides a complementary luminosity calibration to the well-established van der Meer approach that all other LHC experiments normally carry out, with a comparable level of precision [74].

Appendix A

Ghost Charge Results

This appendix presents the full set of corrected ghost charge fraction measurements carried out by LHCb for all relevant LHC run 2 fills using the BGI technique. This data serves as a reference for anyone undertaking a luminosity calibration analysis on LHC run 2 data. It is also available in electronic format at the following address: `https://twiki.cern.ch/twiki/bin/view/LHCbPhysics/GhostAndSatelliteChargeAnalysis`.

A.1 2016 $\sqrt{s}$ = 13 TeV p-p

A.1.1 Fill 4937

Table A.1: The BGI ghost charge measurement over time for fill 4937. The systematic uncertainties are correlated from one point to the next. The time is a UNIX timestamp and represents the centre of the integration interval dt.

time (s)	dt (s)	$f_{gc,1}$ (%)	syst. (%)	stat. (%)	$f_{gc,2}$ (%)	syst. (%)	stat. (%)
1463499384.0	600.0	0.175	0.012	0.006	0.131	0.004	0.006
1463499984.0	600.0	0.182	0.012	0.006	0.129	0.003	0.006
1463500584.0	600.0	0.171	0.011	0.006	0.132	0.004	0.006
1463501167.0	600.0	0.172	0.011	0.006	0.141	0.004	0.006
1463501609.0	600.0	0.183	0.012	0.009	0.136	0.004	0.008
1463502067.0	600.0	0.183	0.012	0.006	0.131	0.004	0.006
1463502754.5	600.0	0.168	0.011	0.005	0.139	0.004	0.005
1463503540.0	600.0	0.163	0.011	0.006	0.136	0.004	0.006
1463504140.0	600.0	0.166	0.011	0.006	0.142	0.004	0.006
1463504740.0	600.0	0.17	0.011	0.006	0.129	0.003	0.006
1463505227.5	600.0	0.174	0.011	0.007	0.134	0.004	0.007

Continued on next page

Table A.1 – *Continued from previous page*

time	dt	$f_{gc,1}$ (%)	syst. (%)	stat. (%)	$f_{gc,2}$ (%)	syst. (%)	stat. (%)
1463505761.0	600.0	0.173	0.011	0.006	0.131	0.004	0.006
1463506361.0	600.0	0.168	0.011	0.006	0.141	0.004	0.006
1463506961.0	600.0	0.163	0.011	0.006	0.132	0.004	0.006
1463507561.0	600.0	0.173	0.011	0.006	0.135	0.004	0.006
1463508161.0	600.0	0.158	0.01	0.006	0.126	0.003	0.006
1463508759.0	600.0	0.175	0.012	0.006	0.134	0.004	0.006
1463509390.0	600.0	0.166	0.011	0.006	0.134	0.004	0.006
1463509990.0	600.0	0.172	0.011	0.006	0.14	0.004	0.006
1463510590.0	600.0	0.161	0.011	0.006	0.133	0.004	0.006
1463511277.5	600.0	0.174	0.011	0.005	0.135	0.004	0.005
1463511973.0	600.0	0.169	0.011	0.006	0.136	0.004	0.006
1463512573.0	600.0	0.173	0.011	0.006	0.127	0.003	0.006
1463513173.0	600.0	0.18	0.012	0.006	0.133	0.004	0.006
1463513773.0	600.0	0.177	0.012	0.006	0.126	0.003	0.006
1463514373.0	600.0	0.166	0.011	0.006	0.129	0.003	0.006
1463514879.0	600.0	0.169	0.011	0.007	0.135	0.004	0.007
1463515456.0	600.0	0.166	0.011	0.005	0.134	0.004	0.005
1463516127.0	600.0	0.179	0.012	0.006	0.142	0.004	0.006
1463516727.0	600.0	0.17	0.011	0.006	0.135	0.004	0.006
1463517327.0	600.0	0.168	0.011	0.006	0.143	0.004	0.006
1463517927.0	600.0	0.173	0.011	0.006	0.142	0.004	0.006
1463518527.0	600.0	0.171	0.011	0.006	0.136	0.004	0.006
1463519127.0	600.0	0.172	0.011	0.006	0.129	0.003	0.006
1463519820.5	600.0	0.17	0.011	0.005	0.128	0.003	0.005

A.1.2 Fill 4945

Table A.2: Ghost charge measurement over time for fill 4945. The systematic uncertainties are correlated from one point to the next. The time is a UNIX timestamp and represents the centre of the integration interval dt.

time	dt	$f_{gc,1}$ (%)	syst. (%)	stat. (%)	$f_{gc,2}$ (%)	syst. (%)	stat. (%)
1463591125.0	293.5	0.046	0.003	0.009	0.042	0.001	0.009
1463591418.5	293.5	0.037	0.002	0.003	0.043	0.001	0.004

Continued on next page

Table A.2 – *Continued from previous page*

time	dt	$f_{gc,1}$ (%)	syst. (%)	stat. (%)	$f_{gc,2}$ (%)	syst. (%)	stat. (%)
1463592444.5	293.5	0.042	0.003	0.005	0.05	0.001	0.006
1463591944.0	293.5	0.04	0.003	0.003	0.043	0.001	0.003
1463593167.5	293.5	0.039	0.003	0.002	0.045	0.001	0.003
1463593694.0	293.5	0.035	0.002	0.006	0.032	0.001	0.007
1463594185.0	293.5	0.038	0.003	0.003	0.042	0.001	0.003
1463594785.0	293.5	0.039	0.003	0.003	0.04	0.001	0.003
1463595517.5	293.5	0.04	0.003	0.002	0.049	0.001	0.003
1463596159.0	293.5	0.044	0.003	0.006	0.039	0.001	0.007
1463596523.0	293.5	0.034	0.002	0.005	0.054	0.001	0.007
1463596935.0	293.5	0.042	0.003	0.003	0.042	0.001	0.003
1463597535.0	293.5	0.037	0.002	0.003	0.042	0.001	0.003
1463598090.0	293.5	0.037	0.002	0.003	0.052	0.001	0.004
1463598703.0	293.5	0.037	0.002	0.003	0.046	0.001	0.003
1463599391.0	293.5	0.042	0.003	0.002	0.046	0.001	0.003
1463600125.0	293.5	0.045	0.003	0.003	0.049	0.001	0.003
1463600806.0	293.5	0.041	0.003	0.002	0.043	0.001	0.003
1463601267.0	293.5	0.041	0.003	0.007	0.066	0.002	0.01
1463601425.5	293.5	0.04	0.003	0.005	0.041	0.001	0.005
1463601651.5	293.5	0.037	0.002	0.005	0.053	0.001	0.007
1463602077.0	293.5	0.035	0.002	0.003	0.051	0.001	0.003
1463602677.0	293.5	0.037	0.002	0.003	0.041	0.001	0.003
1463603277.0	293.5	0.038	0.002	0.003	0.047	0.001	0.003
1463603877.0	293.5	0.038	0.002	0.003	0.047	0.001	0.003
1463604477.0	293.5	0.037	0.002	0.003	0.045	0.001	0.003
1463605033.5	293.5	0.035	0.002	0.003	0.047	0.001	0.004
1463605599.0	293.5	0.042	0.003	0.003	0.044	0.001	0.003
1463606244.5	293.5	0.037	0.002	0.002	0.038	0.001	0.003
1463607005.0	293.5	0.036	0.002	0.003	0.044	0.001	0.003
1463607605.0	293.5	0.035	0.002	0.003	0.046	0.001	0.003
1463608205.0	293.5	0.04	0.003	0.003	0.041	0.001	0.003
1463608684.5	293.5	0.036	0.002	0.003	0.043	0.001	0.004
1463609302.5	293.5	0.035	0.002	0.002	0.046	0.001	0.003
1463610107.0	293.5	0.042	0.003	0.003	0.046	0.001	0.003
1463610707.0	293.5	0.034	0.002	0.003	0.052	0.001	0.003
1463611307.0	293.5	0.036	0.002	0.003	0.045	0.001	0.003

Continued on next page

Table A.2 – *Continued from previous page*

time	dt	$f_{gc,1}$ (%)	syst. (%)	stat. (%)	$f_{gc,2}$ (%)	syst. (%)	stat. (%)
1463611907.0	293.5	0.039	0.003	0.003	0.047	0.001	0.003
1463612507.0	293.5	0.037	0.002	0.003	0.048	0.001	0.003
1463613104.0	293.5	0.042	0.003	0.003	0.046	0.001	0.003
1463613709.0	293.5	0.042	0.003	0.003	0.048	0.001	0.003
1463614309.0	293.5	0.038	0.002	0.003	0.045	0.001	0.003
1463614909.0	293.5	0.04	0.003	0.003	0.041	0.001	0.003
1463615525.0	293.5	0.042	0.003	0.003	0.046	0.001	0.003

A.1.3 Fill 4954

Table A.3: Ghost charge measurement over time for fill 4954. The systematic uncertainties are correlated from one point to the next. The time is a UNIX timestamp and represents the centre of the integration interval dt.

time	dt	$f_{gc,1}$ (%)	syst. (%)	stat. (%)	$f_{gc,2}$ (%)	syst. (%)	stat. (%)
1464335857.0	459.0	0.208	0.014	0.009	0.148	0.004	0.008
1464336316.0	459.0	0.197	0.013	0.009	0.162	0.004	0.009
1464336783.0	459.0	0.203	0.013	0.006	0.152	0.004	0.006
1464337383.0	459.0	0.189	0.012	0.006	0.151	0.004	0.006
1464337983.0	459.0	0.196	0.013	0.006	0.143	0.004	0.006
1464338583.0	459.0	0.19	0.013	0.006	0.14	0.004	0.006
1464339183.0	459.0	0.187	0.012	0.006	0.146	0.004	0.006
1464339649.5	459.0	0.208	0.014	0.009	0.151	0.004	0.008
1464340125.0	459.0	0.196	0.013	0.006	0.143	0.004	0.006
1464340725.0	459.0	0.188	0.012	0.006	0.142	0.004	0.006
1464341325.0	459.0	0.185	0.012	0.006	0.157	0.004	0.006
1464341925.0	459.0	0.194	0.013	0.006	0.139	0.004	0.006
1464342525.0	459.0	0.206	0.014	0.006	0.147	0.004	0.006
1464343124.5	459.0	0.19	0.013	0.006	0.149	0.004	0.006
1464343732.0	459.0	0.194	0.013	0.006	0.148	0.004	0.006
1464344332.0	459.0	0.186	0.012	0.006	0.146	0.004	0.006
1464344932.0	459.0	0.201	0.013	0.006	0.144	0.004	0.006
1464345532.0	459.0	0.188	0.012	0.006	0.15	0.004	0.006
1464346132.0	459.0	0.195	0.013	0.006	0.148	0.004	0.006

Continued on next page

Table A.3 – *Continued from previous page*

time	dt	$f_{gc,1}$ (%)	syst. (%)	stat. (%)	$f_{gc,2}$ (%)	syst. (%)	stat. (%)
1464346733.0	459.0	0.202	0.013	0.006	0.144	0.004	0.006

A.1.4 Fill 5456

Table A.4: Ghost charge measurement over time for fill 5456. The systematic uncertainties are correlated from one point to the next. The time is a UNIX timestamp and represents the centre of the integration interval dt.

time	dt	$f_{gc,1}$ (%)	syst. (%)	stat. (%)	$f_{gc,2}$ (%)	syst. (%)	stat. (%)
1477564781.5	1080.5	0.458	0.03	0.03	0.42	0.011	0.037
1477565862.0	1080.5	0.613	0.022	0.02	0.472	0.006	0.023
1477566607.0	1080.5	0.554	0.019	0.016	0.469	0.01	0.019
1477567749.0	1080.5	0.606	0.02	0.02	0.428	0.007	0.022
1477568349.0	1080.5	0.585	0.021	0.02	0.479	0.006	0.023
1477568949.0	1080.5	0.601	0.023	0.02	0.427	0.008	0.022
1477569549.0	1080.5	0.584	0.02	0.02	0.489	0.009	0.023
1477570149.0	1080.5	0.581	0.021	0.02	0.429	0.007	0.022
1477570751.0	1080.5	0.584	0.021	0.02	0.482	0.008	0.023
1477571361.0	1080.5	0.55	0.023	0.019	0.463	0.006	0.023
1477571961.0	1080.5	0.59	0.025	0.02	0.478	0.007	0.023
1477572543.0	1080.5	0.566	0.018	0.02	0.453	0.007	0.023
1477573336.0	1080.5	0.598	0.022	0.02	0.413	0.005	0.022
1477573936.0	1080.5	0.565	0.018	0.02	0.461	0.005	0.023
1477574599.5	1080.5	0.617	0.026	0.019	0.448	0.007	0.021
1477575272.0	1080.5	0.584	0.022	0.02	0.433	0.005	0.022
1477575872.0	1080.5	0.626	0.022	0.021	0.453	0.005	0.023
1477576472.0	1080.5	0.607	0.022	0.02	0.46	0.005	0.023
1477577175.0	1080.5	0.564	0.016	0.017	0.444	0.007	0.019

A.2 2016 p-Pb

A.2.1 Fill 5527

Table A.5: Ghost charge measurement over time for fill 5527. The systematic uncertainties are correlated from one point to the next. The time is a UNIX timestamp and represents the centre of the integration interval dt.

time	dt	$f_{gc,1}$ (%)	syst. (%)	stat. (%)	$f_{gc,2}$ (%)	syst. (%)	stat. (%)
1479822626.0	600.0	0.463	0.031	0.025	0.821	0.022	0.049

Continued on next page

Table A.5 – *Continued from previous page*

time	dt	$f_{gc,1}$ (%)	syst. (%)	stat. (%)	$f_{gc,2}$ (%)	syst. (%)	stat. (%)
1479823226.0	600.0	0.439	0.029	0.024	0.907	0.024	0.051
1479823826.0	600.0	0.472	0.031	0.025	1.003	0.027	0.055
1479824426.0	600.0	0.488	0.032	0.026	0.91	0.024	0.052
1479825026.0	600.0	0.481	0.032	0.025	0.861	0.023	0.051
1479825624.0	600.0	0.477	0.031	0.026	0.854	0.023	0.052
1479826231.0	600.0	0.487	0.032	0.026	0.84	0.023	0.052
1479826831.0	600.0	0.447	0.03	0.025	0.999	0.027	0.057
1479827431.0	600.0	0.457	0.03	0.025	1.055	0.028	0.059
1479828031.0	600.0	0.471	0.031	0.026	0.998	0.027	0.058
1479828631.0	600.0	0.449	0.03	0.025	1.083	0.029	0.061
1479829232.0	600.0	0.483	0.032	0.026	1.152	0.031	0.064
1479829841.0	600.0	0.476	0.031	0.026	0.931	0.025	0.057
1479830441.0	600.0	0.442	0.029	0.025	1.194	0.032	0.066
1479831041.0	600.0	0.498	0.033	0.026	1.123	0.03	0.064
1479831641.0	600.0	0.417	0.028	0.024	1.25	0.034	0.068
1479832241.0	600.0	0.447	0.03	0.025	1.169	0.031	0.066
1479832842.0	600.0	0.43	0.028	0.025	1.31	0.035	0.071
1479833451.0	600.0	0.439	0.029	0.025	1.131	0.03	0.067
1479834051.0	600.0	0.496	0.033	0.027	1.252	0.034	0.071
1479834651.0	600.0	0.446	0.029	0.025	1.128	0.03	0.067
1479835251.0	600.0	0.454	0.03	0.025	1.143	0.031	0.069
1479835851.0	600.0	0.465	0.031	0.026	1.218	0.033	0.071
1479836452.0	600.0	0.453	0.03	0.025	1.308	0.035	0.074
1479837061.0	600.0	0.464	0.031	0.026	1.271	0.034	0.074
1479837661.0	600.0	0.439	0.029	0.025	1.269	0.034	0.074
1479838261.0	600.0	0.493	0.033	0.026	1.429	0.038	0.08
1479838861.0	600.0	0.488	0.032	0.026	1.436	0.039	0.081
1479839461.0	600.0	0.501	0.033	0.027	1.343	0.036	0.078
1479840062.0	600.0	0.499	0.033	0.027	1.301	0.035	0.078
1479840672.0	600.0	0.512	0.034	0.027	1.212	0.033	0.075
1479841272.0	600.0	0.463	0.031	0.026	1.477	0.04	0.085
1479841872.0	600.0	0.485	0.032	0.026	1.427	0.038	0.083
1479842472.0	600.0	0.495	0.033	0.027	1.382	0.037	0.083
1479843072.0	600.0	0.447	0.03	0.025	1.438	0.039	0.085
1479843673.0	600.0	0.461	0.03	0.026	1.397	0.038	0.084

A.2.2 Fill 5533

Table A.6: Ghost charge measurement over time for fill 5533. The systematic uncertainties are correlated from one point to the next. The time is a UNIX timestamp and represents the centre of the integration interval dt.

time	dt	$f_{gc,1}$ (%)	syst. (%)	stat. (%)	$f_{gc,2}$ (%)	syst. (%)	stat. (%)
1479903161.0	603.0	0.339	0.022	0.022	0.371	0.01	0.034
1479903764.0	603.0	0.346	0.023	0.022	0.419	0.011	0.036
1479915128.0	603.0	0.32	0.021	0.018	0.587	0.016	0.045
1479915728.0	603.0	0.313	0.021	0.018	0.672	0.018	0.05
1479916328.0	603.0	0.328	0.022	0.019	0.673	0.018	0.05
1479916928.0	603.0	0.331	0.022	0.019	0.659	0.018	0.051
1479917528.0	603.0	0.341	0.023	0.02	0.727	0.02	0.055
1479918127.5	603.0	0.355	0.023	0.021	0.607	0.016	0.051
1479918735.0	603.0	0.315	0.021	0.02	0.665	0.018	0.053
1479919335.0	603.0	0.33	0.022	0.02	0.528	0.014	0.048
1479919935.0	603.0	0.321	0.021	0.02	0.617	0.017	0.053
1479920535.0	603.0	0.328	0.022	0.02	0.684	0.018	0.056
1479921135.0	603.0	0.343	0.023	0.021	0.655	0.018	0.056
1479921736.0	603.0	0.343	0.023	0.021	0.764	0.021	0.06
1479922346.0	603.0	0.318	0.021	0.02	0.743	0.02	0.061
1479922946.0	603.0	0.336	0.022	0.021	0.717	0.019	0.059
1479923623.0	603.0	0.322	0.021	0.018	0.826	0.022	0.058

A.2.3 Fill 5559

Table A.7: Ghost charge measurement over time for fill 5559. The systematic uncertainties are correlated from one point to the next. The time is a UNIX timestamp and represents the centre of the integration interval dt.

time	dt	$f_{gc,1}$ (%)	syst. (%)	stat. (%)	$f_{gc,2}$ (%)	syst. (%)	stat. (%)
1480507345.0	600.0	0.463	0.031	0.03	0.251	0.007	0.018
1480507945.0	600.0	0.48	0.032	0.031	0.284	0.008	0.02

Continued on next page

Table A.7 – *Continued from previous page*

time	dt	$f_{gc,1}$ (%)	syst. (%)	stat. (%)	$f_{gc,2}$ (%)	syst. (%)	stat. (%)
1480508545.0	600.0	0.528	0.035	0.033	0.306	0.008	0.021
1480509145.0	600.0	0.53	0.035	0.034	0.311	0.008	0.022
1480509745.0	600.0	0.587	0.039	0.037	0.322	0.009	0.023
1480510345.0	600.0	0.55	0.036	0.036	0.304	0.008	0.022
1480511037.0	600.0	0.55	0.036	0.037	0.342	0.009	0.024
1480511637.0	600.0	0.581	0.038	0.038	0.289	0.008	0.022
1480512237.0	600.0	0.588	0.039	0.039	0.289	0.008	0.022
1480512837.0	600.0	0.549	0.036	0.038	0.31	0.008	0.023
1480513437.0	600.0	0.63	0.042	0.042	0.288	0.008	0.022
1480514036.0	600.0	0.624	0.041	0.042	0.316	0.008	0.024
1480514644.0	600.0	0.677	0.045	0.044	0.348	0.009	0.025
1480515179.0	600.0	0.701	0.046	0.051	0.331	0.009	0.027

A.2.4 Fill 5563

Table A.8: Ghost charge measurement over time for fill 5563. The systematic uncertainties are correlated from one point to the next. The time is a UNIX timestamp and represents the centre of the integration interval dt.

time	dt	$f_{gc,1}$ (%)	syst. (%)	stat. (%)	$f_{gc,2}$ (%)	syst. (%)	stat. (%)
1480581820.0	600.0	1.094	0.072	0.066	0.19	0.005	0.016
1480582420.0	600.0	1.053	0.07	0.066	0.193	0.005	0.017
1480583020.0	600.0	1.137	0.075	0.071	0.246	0.007	0.019
1480583620.0	600.0	1.047	0.069	0.069	0.203	0.005	0.018
1480584220.0	600.0	1.069	0.071	0.071	0.192	0.005	0.018
1480584819.0	600.0	1.083	0.072	0.072	0.199	0.005	0.018
1480585427.0	600.0	1.13	0.075	0.076	0.178	0.005	0.018
1480586027.0	600.0	1.281	0.085	0.082	0.17	0.005	0.017
1480586627.0	600.0	1.176	0.078	0.079	0.23	0.006	0.02
1480587227.0	600.0	1.246	0.082	0.082	0.211	0.006	0.02
1480587827.0	600.0	1.176	0.078	0.082	0.191	0.005	0.019
1480588428.0	600.0	1.341	0.089	0.088	0.189	0.005	0.019
1480589037.0	600.0	1.41	0.093	0.092	0.183	0.005	0.019
1480589637.0	600.0	1.422	0.094	0.093	0.216	0.006	0.02

Continued on next page

Table A.8 – *Continued from previous page*

time	dt	$f_{gc,1}$ (%)	syst. (%)	stat. (%)	$f_{gc,2}$ (%)	syst. (%)	stat. (%)
1480590237.0	600.0	1.462	0.097	0.096	0.191	0.005	0.019
1480590951.5	600.0	1.37	0.09	0.08	0.194	0.005	0.016

A.2.5 Fill 5565

Table A.9: Ghost charge measurement over time for fill 5565. The systematic uncertainties are correlated from one point to the next. The time is a UNIX timestamp and represents the centre of the integration interval dt.

time	dt	$f_{gc,1}$ (%)	syst. (%)	stat. (%)	$f_{gc,2}$ (%)	syst. (%)	stat. (%)
1480619019.0	719.0	0.679	0.045	0.036	0.236	0.006	0.019
1480619738.0	719.0	0.701	0.046	0.032	0.249	0.007	0.017
1480629399.0	719.0	1.168	0.077	0.059	0.251	0.007	0.019
1480629999.0	719.0	1.258	0.083	0.064	0.225	0.006	0.019
1480630480.0	719.0	1.18	0.078	0.081	0.248	0.007	0.026

A.2.6 Fill 5568

Table A.10: Ghost charge measurement over time for fill 5568. The systematic uncertainties are correlated from one point to the next. The time is a UNIX timestamp and represents the centre of the integration interval dt.

time	dt	$f_{gc,1}$ (%)	syst. (%)	stat. (%)	$f_{gc,2}$ (%)	syst. (%)	stat. (%)
1480692254.0	600.0	0.918	0.061	0.045	0.261	0.007	0.019
1480692854.0	600.0	0.899	0.059	0.046	0.259	0.007	0.02
1480693454.0	600.0	0.852	0.056	0.045	0.229	0.006	0.019
1480694054.0	600.0	0.963	0.064	0.049	0.243	0.007	0.02
1480694654.0	600.0	1.013	0.067	0.051	0.225	0.006	0.02
1480695254.0	600.0	1.037	0.068	0.053	0.251	0.007	0.021
1480695862.0	600.0	0.921	0.061	0.051	0.265	0.007	0.022
1480696462.0	600.0	1.114	0.074	0.057	0.242	0.007	0.021
1480697062.0	600.0	1.054	0.07	0.056	0.213	0.006	0.02

Continued on next page

Table A.10 – *Continued from previous page*

time	dt	$f_{gc,1}$ (%)	syst. (%)	stat. (%)	$f_{gc,2}$ (%)	syst. (%)	stat. (%)
1480697662.0	600.0	0.942	0.062	0.054	0.238	0.006	0.021
1480698262.0	600.0	1.01	0.067	0.056	0.266	0.007	0.022
1480698863.0	600.0	1.162	0.077	0.061	0.222	0.006	0.021
1480699537.5	600.0	1.044	0.069	0.054	0.242	0.006	0.02
1480700241.0	600.0	1.11	0.073	0.059	0.241	0.006	0.021

A.3 2017 $\sqrt{s}$ = 13 TeV p-p

A.3.1 Fill 6012

Table A.11: Ghost charge measurement over time for fill 6012. The systematic uncertainties are correlated from one point to the next. The time is a UNIX timestamp and represents the centre of the integration interval dt.

time	dt	$f_{gc,1}$ (%)	syst. (%)	stat. (%)	$f_{gc,2}$ (%)	syst. (%)	stat. (%)
1501172410.0	600.5	0.036	0.002	0.001	0.111	0.003	0.003
1501173010.5	600.5	0.036	0.002	0.001	0.114	0.003	0.003
1501173859.0	600.5	0.033	0.002	0.001	0.111	0.003	0.003
1501174459.0	600.5	0.035	0.002	0.001	0.112	0.003	0.003
1501175166.0	600.5	0.035	0.002	0.001	0.114	0.003	0.002
1501176171.0	600.5	0.034	0.002	0.001	0.109	0.003	0.003
1501176771.0	600.5	0.037	0.002	0.001	0.115	0.003	0.003
1501177371.0	600.5	0.036	0.002	0.001	0.113	0.003	0.003
1501177971.0	600.5	0.034	0.002	0.001	0.11	0.003	0.003
1501178571.0	600.5	0.034	0.002	0.001	0.11	0.003	0.003
1501179172.0	600.5	0.035	0.002	0.001	0.111	0.003	0.003
1501179767.0	600.5	0.035	0.002	0.001	0.114	0.003	0.003
1501180493.5	600.5	0.036	0.002	0.001	0.116	0.003	0.002
1501181299.0	600.5	0.036	0.002	0.001	0.115	0.003	0.003
1501181899.0	600.5	0.035	0.002	0.001	0.118	0.003	0.003
1501182499.0	600.5	0.035	0.002	0.001	0.115	0.003	0.003
1501183099.0	600.5	0.035	0.002	0.001	0.113	0.003	0.003
1501183614.0	600.5	0.036	0.002	0.002	0.112	0.003	0.003

Continued on next page

Table A.11 – *Continued from previous page*

time	dt	$f_{gc,1}$ (%)	syst. (%)	stat. (%)	$f_{gc,2}$ (%)	syst. (%)	stat. (%)
1501185946.0	600.5	0.037	0.002	0.001	0.115	0.003	0.003
1501186666.5	600.5	0.035	0.002	0.001	0.117	0.003	0.002

A.3.2 Fill 6016

Table A.12: Ghost charge measurement over time for fill 6016. The systematic uncertainties are correlated from one point to the next. The time is a UNIX timestamp and represents the centre of the integration interval dt.

time	dt	$f_{gc,1}$ (%)	syst. (%)	stat. (%)	$f_{gc,2}$ (%)	syst. (%)	stat. (%)
1501215105.0	600.0	0.021	0.001	0.001	0.056	0.001	0.002
1501215705.0	600.0	0.026	0.002	0.001	0.05	0.001	0.002
1501216305.0	600.0	0.025	0.002	0.001	0.051	0.001	0.002
1501216905.0	600.0	0.027	0.002	0.001	0.053	0.001	0.002
1501217513.0	600.0	0.023	0.001	0.001	0.052	0.001	0.002
1501218716.0	600.0	0.025	0.002	0.001	0.051	0.001	0.002
1501219316.0	600.0	0.023	0.002	0.001	0.052	0.001	0.002
1501219916.0	600.0	0.024	0.002	0.001	0.05	0.001	0.002
1501220516.0	600.0	0.023	0.001	0.001	0.051	0.001	0.002
1501221116.0	600.0	0.023	0.002	0.001	0.055	0.001	0.002
1501221717.0	600.0	0.024	0.002	0.001	0.053	0.001	0.002
1501222326.0	600.0	0.024	0.002	0.002	0.057	0.002	0.003
1501222926.0	600.0	0.022	0.001	0.002	0.046	0.001	0.003
1501223526.0	600.0	0.025	0.002	0.002	0.054	0.001	0.003
1501224126.0	600.0	0.021	0.001	0.002	0.05	0.001	0.003
1501224726.0	600.0	0.025	0.002	0.002	0.052	0.001	0.003
1501225327.0	600.0	0.027	0.002	0.002	0.056	0.001	0.003
1501225937.0	600.0	0.024	0.002	0.001	0.049	0.001	0.002
1501226537.0	600.0	0.022	0.001	0.001	0.051	0.001	0.002
1501227137.0	600.0	0.023	0.002	0.001	0.053	0.001	0.002
1501227737.0	600.0	0.023	0.002	0.001	0.052	0.001	0.002
1501228229.0	600.0	0.024	0.002	0.002	0.054	0.001	0.003
1501229547.0	600.0	0.022	0.001	0.001	0.051	0.001	0.002
1501230147.0	600.0	0.022	0.001	0.001	0.05	0.001	0.002

Continued on next page

Table A.12 – *Continued from previous page*

time	dt	$f_{gc,1}$ (%)	syst. (%)	stat. (%)	$f_{gc,2}$ (%)	syst. (%)	stat. (%)
1501230764.5	600.0	0.024	0.002	0.001	0.056	0.002	0.002
1501233157.0	600.0	0.025	0.002	0.001	0.054	0.001	0.002
1501233757.0	600.0	0.025	0.002	0.001	0.053	0.001	0.002
1501234437.5	600.0	0.023	0.002	0.001	0.056	0.001	0.002
1501235429.0	600.0	0.024	0.002	0.001	0.053	0.001	0.002
1501236029.0	600.0	0.024	0.002	0.001	0.052	0.001	0.002
1501236629.0	600.0	0.023	0.002	0.001	0.054	0.001	0.002
1501237294.0	600.0	0.023	0.002	0.001	0.052	0.001	0.002
1501239038.0	600.0	0.025	0.002	0.001	0.051	0.001	0.002
1501239638.0	600.0	0.023	0.002	0.001	0.052	0.001	0.002
1501240212.0	600.0	0.023	0.002	0.001	0.05	0.001	0.002
1501240794.0	600.0	0.024	0.002	0.001	0.076	0.002	0.002
1501241394.0	600.0	0.025	0.002	0.001	0.072	0.002	0.002
1501241994.0	600.0	0.025	0.002	0.001	0.074	0.002	0.002
1501242594.0	600.0	0.022	0.001	0.001	0.07	0.002	0.002
1501243194.0	600.0	0.023	0.002	0.001	0.078	0.002	0.002
1501243792.5	600.0	0.024	0.002	0.001	0.072	0.002	0.002
1501244398.0	600.0	0.024	0.002	0.001	0.052	0.001	0.002
1501244998.0	600.0	0.023	0.002	0.001	0.051	0.001	0.002
1501245598.0	600.0	0.023	0.002	0.001	0.048	0.001	0.002
1501246198.0	600.0	0.024	0.002	0.001	0.051	0.001	0.002
1501246798.0	600.0	0.025	0.002	0.001	0.052	0.001	0.002
1501247399.0	600.0	0.023	0.002	0.001	0.05	0.001	0.002
1501248009.0	600.0	8.757	0.578	0.029	15.126	0.407	0.043
1501248609.0	600.0	63.596	4.201	0.146	147.236	3.961	0.343
1501249209.0	600.0	63.683	4.207	0.147	146.727	3.947	0.342
1501249809.0	600.0	63.757	4.211	0.147	147.036	3.955	0.342
1501250409.0	600.0	63.735	4.21	0.147	146.613	3.944	0.341
1501251010.0	600.0	63.784	4.213	0.146	146.518	3.941	0.341
1501248009.0	600.0	8.757	0.578	0.029	15.126	0.407	0.043
1501248609.0	600.0	63.596	4.201	0.146	147.236	3.961	0.343
1501249209.0	600.0	63.683	4.207	0.147	146.727	3.947	0.342
1501249809.0	600.0	63.757	4.211	0.147	147.036	3.955	0.342
1501250409.0	600.0	63.735	4.21	0.147	146.613	3.944	0.341
1501251010.0	600.0	63.784	4.213	0.146	146.518	3.941	0.341

Continued on next page

Table A.12 – *Continued from previous page*

time	dt	$f_{gc,1}$ (%)	syst. (%)	stat. (%)	$f_{gc,2}$ (%)	syst. (%)	stat. (%)
1501251619.0	600.0	0.021	0.001	0.001	0.05	0.001	0.002
1501252350.0	600.0	0.023	0.002	0.001	0.05	0.001	0.002
1501253090.0	600.0	0.024	0.002	0.001	0.053	0.001	0.002
1501253690.0	600.0	0.025	0.002	0.001	0.055	0.001	0.002
1501254290.0	600.0	0.024	0.002	0.001	0.053	0.001	0.002
1501254890.0	600.0	0.024	0.002	0.001	0.051	0.001	0.002
1501255490.0	600.0	0.024	0.002	0.001	0.048	0.001	0.002
1501256091.0	600.0	0.025	0.002	0.001	0.049	0.001	0.002
1501256700.0	600.0	0.023	0.002	0.001	0.053	0.001	0.002
1501257300.0	600.0	0.025	0.002	0.001	0.054	0.001	0.002
1501257950.5	600.0	0.023	0.002	0.001	0.048	0.001	0.002
1501260310.0	600.0	0.025	0.002	0.001	0.055	0.001	0.002
1501260910.0	600.0	0.023	0.002	0.001	0.052	0.001	0.002
1501261510.0	600.0	0.023	0.001	0.001	0.05	0.001	0.002
1501262110.0	600.0	0.023	0.002	0.001	0.053	0.001	0.002
1501262710.0	600.0	0.024	0.002	0.001	0.052	0.001	0.002
1501263311.0	600.0	0.024	0.002	0.001	0.05	0.001	0.002
1501267531.0	600.0	0.023	0.002	0.001	0.051	0.001	0.002
1501268131.0	600.0	0.023	0.002	0.001	0.051	0.001	0.002
1501268731.0	600.0	0.022	0.001	0.001	0.053	0.001	0.002
1501269331.0	600.0	0.025	0.002	0.001	0.054	0.001	0.002
1501269931.0	600.0	0.026	0.002	0.001	0.051	0.001	0.002
1501270436.0	600.0	0.026	0.002	0.002	0.051	0.001	0.002
1501271011.0	600.0	0.026	0.002	0.002	0.055	0.001	0.003

A.4 2017 Xe-Xe

A.4.1 Fill 6295

Table A.13: Ghost charge measurement over time for fill 6295. The systematic uncertainties are correlated from one point to the next. The time is a UNIX timestamp and represents the centre of the integration interval dt.

time	dt	$f_{gc,1}$ (%)	syst. (%)	stat. (%)	$f_{gc,2}$ (%)	syst. (%)	stat. (%)
1507857699.0	3148.0	0.382	0.025	0.383	1.119	0.03	0.652
1507860847.0	3148.0	0.611	0.04	0.435	0.314	0.008	0.315

A.5 2017 $\sqrt{s}$ = 5 TeV p-p

A.5.1 Fill 6380

Table A.14: Ghost charge measurement over time for fill 6380. The systematic uncertainties are correlated from one point to the next. The time is a UNIX timestamp and represents the centre of the integration interval dt.

time	dt	$f_{gc,1}$ (%)	syst. (%)	stat. (%)	$f_{gc,2}$ (%)	syst. (%)	stat. (%)
1510432049.0	600.0	0.033	0.002	0.002	0.031	0.001	0.002
1510432649.0	600.0	0.031	0.002	0.002	0.035	0.001	0.002
1510433249.0	600.0	0.033	0.002	0.002	0.032	0.001	0.002
1510433849.0	600.0	0.033	0.002	0.002	0.035	0.001	0.002
1510434449.0	600.0	0.037	0.002	0.002	0.037	0.001	0.002
1510435047.5	600.0	0.035	0.002	0.002	0.037	0.001	0.002
1510435550.0	600.0	0.032	0.002	0.002	0.039	0.001	0.002
1510436310.0	600.0	0.034	0.002	0.002	0.037	0.001	0.002
1510436910.0	600.0	0.034	0.002	0.002	0.038	0.001	0.002
1510437510.0	600.0	0.034	0.002	0.002	0.043	0.001	0.002
1510438110.0	600.0	0.035	0.002	0.002	0.038	0.001	0.002
1510438710.0	600.0	0.036	0.002	0.002	0.038	0.001	0.002
1510439308.0	600.0	0.034	0.002	0.002	0.042	0.001	0.002
1510439914.0	600.0	0.038	0.002	0.002	0.04	0.001	0.002
1510440514.0	600.0	0.036	0.002	0.002	0.042	0.001	0.002

Continued on next page

Table A.14 – *Continued from previous page*

time	dt	$f_{gc,1}$ (%)	syst. (%)	stat. (%)	$f_{gc,2}$ (%)	syst. (%)	stat. (%)
1510441114.0	600.0	0.04	0.003	0.002	0.044	0.001	0.002
1510441714.0	600.0	0.039	0.003	0.002	0.044	0.001	0.002
1510442346.0	600.0	0.039	0.003	0.002	0.044	0.001	0.002
1510443004.0	600.0	0.044	0.003	0.002	0.046	0.001	0.002
1510443604.0	600.0	0.043	0.003	0.002	0.045	0.001	0.002
1510444204.0	600.0	0.046	0.003	0.002	0.045	0.001	0.002
1510444825.5	600.0	0.042	0.003	0.002	0.046	0.001	0.002
1510445454.0	600.0	0.042	0.003	0.002	0.05	0.001	0.002
1510446054.0	600.0	0.044	0.003	0.002	0.046	0.001	0.002
1510446654.0	600.0	0.046	0.003	0.002	0.05	0.001	0.002
1510447254.0	600.0	0.049	0.003	0.002	0.05	0.001	0.002
1510447854.0	600.0	0.047	0.003	0.002	0.052	0.001	0.002
1510448455.5	600.0	0.052	0.003	0.002	0.054	0.001	0.002
1510449066.0	600.0	0.053	0.003	0.002	0.052	0.001	0.002
1510449666.0	600.0	0.054	0.004	0.002	0.056	0.002	0.002
1510450266.0	600.0	0.05	0.003	0.002	0.057	0.002	0.002
1510450866.0	600.0	0.053	0.004	0.002	0.061	0.002	0.002
1510451466.0	600.0	0.059	0.004	0.002	0.053	0.001	0.002
1510452067.0	600.0	0.058	0.004	0.002	0.058	0.002	0.002
1510452677.0	600.0	0.06	0.004	0.002	0.061	0.002	0.003
1510453277.0	600.0	0.057	0.004	0.002	0.067	0.002	0.003
1510453877.0	600.0	0.058	0.004	0.002	0.061	0.002	0.002
1510454477.0	600.0	0.057	0.004	0.002	0.066	0.002	0.003
1510455077.0	600.0	0.061	0.004	0.002	0.062	0.002	0.003
1510455678.0	600.0	0.06	0.004	0.002	0.059	0.002	0.002
1510456287.0	600.0	0.064	0.004	0.002	0.065	0.002	0.003
1510456797.0	600.0	0.067	0.004	0.003	0.07	0.002	0.003
1510457744.0	600.0	0.071	0.002	0.005	0.072	0.002	0.005
1510458142.0	600.0	0.072	0.002	0.003	0.073	0.001	0.003
1510458742.0	600.0	0.079	0.002	0.003	0.08	0.001	0.003
1510459342.0	600.0	0.073	0.002	0.003	0.076	0.001	0.003
1510459942.0	600.0	0.081	0.002	0.003	0.074	0.001	0.003
1510460542.0	600.0	0.083	0.002	0.003	0.082	0.001	0.003
1510461227.5	600.0	0.084	0.002	0.002	0.082	0.001	0.003
1510461922.0	600.0	0.087	0.002	0.004	0.08	0.001	0.004

Continued on next page

Table A.14 – *Continued from previous page*

time	dt	$f_{gc,1}$ (%)	syst. (%)	stat. (%)	$f_{gc,2}$ (%)	syst. (%)	stat. (%)
1510462522.0	600.0	0.092	0.003	0.013	0.064	0.001	0.012
1510463134.0	600.0	0.058	0.002	0.014	0.079	0.002	0.019
1510463754.0	600.0	0.092	0.004	0.02	0.086	0.001	0.021
1510464443.5	600.0	0.088	0.003	0.017	0.093	0.003	0.02

A.6 2018 $\sqrt{s}$ = 13 TeV p-p

A.6.1 Fill 6864

Table A.15: Ghost charge measurement over time for fill 6864. The systematic uncertainties are correlated from one point to the next. The time is a UNIX timestamp and represents the centre of the integration interval dt.

time	dt	$f_{gc,1}$ (%)	syst. (%)	stat. (%)	$f_{gc,2}$ (%)	syst. (%)	stat. (%)
1530292609.5	564.5	0.033	0.001	0.01	0.08	0.002	0.017
1530293174.0	564.5	0.076	0.004	0.014	0.137	0.002	0.021
1530293774.0	564.5	0.046	0.001	0.011	0.086	0.001	0.016
1530294374.0	564.5	0.086	0.005	0.015	0.128	0.003	0.02
1530294974.0	564.5	0.059	0.004	0.012	0.092	0.003	0.017
1530295574.0	564.5	0.078	0.004	0.014	0.107	0.002	0.018
1530296257.0	564.5	0.063	0.003	0.011	0.095	0.001	0.015
1530296763.0	564.5	0.053	0.002	0.006	0.11	0.001	0.009
1530297186.0	564.5	0.066	0.002	0.003	0.093	0.001	0.004
1530297786.0	564.5	0.064	0.002	0.003	0.096	0.001	0.005
1530298386.0	564.5	0.068	0.002	0.003	0.088	0.001	0.004
1530298849.5	564.5	0.068	0.002	0.005	0.095	0.001	0.006
1530299626.0	564.5	0.065	0.002	0.003	0.088	0.001	0.004
1530300226.0	564.5	0.063	0.002	0.003	0.091	0.001	0.004
1530300826.0	564.5	0.062	0.002	0.003	0.09	0.001	0.004
1530301426.0	564.5	0.061	0.002	0.003	0.094	0.001	0.004
1530302026.0	564.5	0.065	0.002	0.003	0.098	0.001	0.005
1530302626.0	564.5	0.06	0.002	0.003	0.098	0.001	0.005
1530303089.5	564.5	0.054	0.002	0.004	0.095	0.001	0.006

Continued on next page

Table A.15 – *Continued from previous page*

time	dt	$f_{gc,1}$ (%)	syst. (%)	stat. (%)	$f_{gc,2}$ (%)	syst. (%)	stat. (%)
1530303561.0	564.5	0.064	0.002	0.003	0.093	0.002	0.004
1530304161.0	564.5	0.062	0.002	0.003	0.103	0.002	0.005
1530304761.0	564.5	0.061	0.002	0.003	0.1	0.001	0.005
1530305361.0	564.5	0.059	0.001	0.003	0.096	0.001	0.005
1530305961.0	564.5	0.063	0.002	0.003	0.089	0.001	0.004
1530306561.0	564.5	0.067	0.002	0.003	0.087	0.001	0.004
1530307161.0	564.5	0.06	0.001	0.003	0.096	0.001	0.005
1530307761.0	564.5	0.066	0.002	0.003	0.098	0.001	0.005
1530308361.0	564.5	0.062	0.002	0.003	0.1	0.001	0.005
1530308961.0	564.5	0.063	0.002	0.003	0.1	0.002	0.005
1530309561.0	564.5	0.068	0.002	0.003	0.096	0.001	0.005
1530310161.0	564.5	0.059	0.001	0.003	0.094	0.001	0.004
1530310761.0	564.5	0.063	0.002	0.003	0.083	0.001	0.004
1530311361.0	564.5	0.061	0.002	0.003	0.094	0.001	0.004
1530311961.0	564.5	0.064	0.002	0.003	0.093	0.001	0.004
1530312561.0	564.5	0.06	0.002	0.003	0.102	0.001	0.005
1530313212.5	564.5	0.065	0.002	0.003	0.096	0.001	0.004
1530313909.5	564.5	0.065	0.002	0.003	0.09	0.001	0.004
1530314555.0	564.5	0.06	0.002	0.003	0.105	0.001	0.005
1530315155.0	564.5	0.066	0.002	0.003	0.105	0.001	0.005
1530315755.0	564.5	0.067	0.002	0.003	0.098	0.001	0.005
1530316355.0	564.5	0.063	0.002	0.003	0.086	0.001	0.004
1530316955.0	564.5	0.069	0.002	0.003	0.098	0.001	0.005
1530317552.0	564.5	0.063	0.002	0.003	0.084	0.001	0.004
1530318157.0	564.5	0.065	0.002	0.003	0.095	0.001	0.005
1530318757.0	564.5	0.066	0.002	0.003	0.094	0.001	0.005
1530319357.0	564.5	0.068	0.002	0.003	0.094	0.001	0.005
1530319957.0	564.5	0.054	0.001	0.003	0.095	0.001	0.005
1530320557.0	564.5	0.066	0.002	0.003	0.099	0.001	0.005
1530321158.0	564.5	0.063	0.002	0.003	0.097	0.001	0.005
1530321768.0	564.5	0.058	0.001	0.003	0.089	0.001	0.004
1530322368.0	564.5	0.062	0.002	0.003	0.1	0.001	0.005
1530322968.0	564.5	0.063	0.002	0.003	0.101	0.001	0.005
1530323568.0	564.5	0.068	0.002	0.003	0.09	0.002	0.004
1530324168.0	564.5	0.063	0.002	0.003	0.1	0.001	0.005

Continued on next page

Table A.15 – *Continued from previous page*

time	dt	$f_{gc,1}$ (%)	syst. (%)	stat. (%)	$f_{gc,2}$ (%)	syst. (%)	stat. (%)
1530324769.0	564.5	0.063	0.002	0.003	0.088	0.001	0.004
1530325378.0	564.5	0.062	0.002	0.003	0.092	0.001	0.004
1530325978.0	564.5	0.062	0.002	0.003	0.092	0.001	0.004
1530326578.0	564.5	0.068	0.002	0.003	0.088	0.002	0.004
1530327243.5	564.5	0.064	0.002	0.003	0.096	0.001	0.004

A.6.2 Fill 6868

Table A.16: Ghost charge measurement over time for fill 6868. The systematic uncertainties are correlated from one point to the next. The time is a UNIX timestamp and represents the centre of the integration interval dt.

time	dt	$f_{gc,1}$ (%)	syst. (%)	stat. (%)	$f_{gc,2}$ (%)	syst. (%)	stat. (%)
1530353395.0	600.0	0.148	0.004	0.004	9.884	0.263	0.038
1530353995.0	600.0	0.145	0.004	0.004	9.925	0.264	0.038
1530354595.0	600.0	0.156	0.004	0.004	9.9	0.264	0.038
1530355195.0	600.0	0.148	0.004	0.004	9.853	0.262	0.038
1530355795.0	600.0	0.151	0.004	0.004	9.856	0.262	0.038
1530356394.0	600.0	0.146	0.004	0.004	9.829	0.262	0.038
1530357001.0	600.0	0.148	0.004	0.004	9.987	0.265	0.038
1530357601.0	600.0	0.145	0.004	0.004	9.881	0.263	0.038
1530358201.0	600.0	0.147	0.004	0.004	9.894	0.263	0.038
1530358801.0	600.0	0.149	0.004	0.004	9.839	0.262	0.038
1530359401.0	600.0	0.144	0.004	0.004	9.846	0.262	0.038
1530359921.0	600.0	0.149	0.004	0.004	9.922	0.264	0.044
1530360524.0	600.0	0.142	0.004	0.004	0.19	0.002	0.005
1530361124.0	600.0	0.143	0.004	0.004	0.189	0.002	0.005
1530361724.0	600.0	0.148	0.004	0.004	0.195	0.003	0.005
1530362324.0	600.0	0.147	0.004	0.004	0.187	0.003	0.005
1530362924.0	600.0	0.144	0.004	0.004	0.187	0.002	0.005
1530363523.5	600.0	0.139	0.004	0.004	0.192	0.002	0.005
1530364132.0	600.0	0.139	0.004	0.004	0.193	0.003	0.005
1530364732.0	600.0	0.149	0.004	0.004	0.196	0.002	0.005
1530365332.0	600.0	0.147	0.004	0.004	0.182	0.002	0.005

Continued on next page

Table A.16 – *Continued from previous page*

time	dt	$f_{gc,1}$ (%)	syst. (%)	stat. (%)	$f_{gc,2}$ (%)	syst. (%)	stat. (%)
1530365932.0	600.0	0.142	0.004	0.004	0.184	0.002	0.005
1530366532.0	600.0	0.145	0.004	0.004	0.183	0.003	0.005
1530367133.0	600.0	0.143	0.004	0.004	0.192	0.002	0.005
1530367742.0	600.0	0.144	0.004	0.004	0.183	0.002	0.005
1530368342.0	600.0	0.145	0.004	0.004	0.192	0.003	0.005
1530368942.0	600.0	0.139	0.004	0.004	0.192	0.003	0.005
1530369542.0	600.0	0.138	0.004	0.004	0.186	0.002	0.005
1530370142.0	600.0	0.149	0.004	0.004	0.181	0.002	0.005
1530370743.0	600.0	0.147	0.004	0.004	0.185	0.002	0.005
1530371353.0	600.0	0.146	0.004	0.004	0.193	0.003	0.005
1530371953.0	600.0	0.145	0.004	0.004	0.184	0.003	0.005
1530372553.0	600.0	0.141	0.004	0.004	0.187	0.002	0.005
1530373153.0	600.0	0.146	0.004	0.004	0.182	0.003	0.005
1530373753.0	600.0	0.144	0.004	0.004	0.181	0.002	0.005
1530374354.0	600.0	0.14	0.004	0.004	0.193	0.003	0.005
1530375059.0	600.0	0.145	0.004	0.003	0.185	0.002	0.004
1530376289.0	600.0	0.149	0.004	0.004	0.192	0.002	0.005
1530376889.0	600.0	0.149	0.004	0.004	0.181	0.003	0.005
1530377489.0	600.0	0.144	0.004	0.004	0.197	0.003	0.005
1530378089.0	600.0	0.143	0.005	0.004	0.183	0.002	0.005
1530378689.0	600.0	0.142	0.004	0.004	0.193	0.003	0.005
1530379285.0	600.0	0.147	0.004	0.004	0.188	0.003	0.005
1530380104.5	600.0	0.144	0.004	0.003	0.186	0.003	0.004
1530381234.0	600.0	0.145	0.004	0.004	0.186	0.002	0.005
1530381834.0	600.0	0.135	0.004	0.004	0.189	0.002	0.005
1530382434.0	600.0	0.143	0.004	0.004	0.187	0.002	0.005
1530383034.0	600.0	0.142	0.004	0.004	0.188	0.003	0.005
1530383634.0	600.0	0.148	0.004	0.004	0.182	0.002	0.005
1530384235.0	600.0	0.143	0.004	0.004	0.18	0.003	0.005
1530384844.0	600.0	0.143	0.004	0.004	0.188	0.002	0.005
1530385444.0	600.0	0.15	0.004	0.004	0.183	0.002	0.005
1530386044.0	600.0	0.146	0.004	0.004	0.194	0.003	0.005
1530386644.0	600.0	0.144	0.004	0.004	0.18	0.002	0.005
1530387244.0	600.0	0.139	0.004	0.004	0.19	0.002	0.005
1530387845.0	600.0	0.14	0.004	0.004	0.191	0.002	0.005

Continued on next page

Table A.16 – *Continued from previous page*

time	dt	$f_{gc,1}$ (%)	syst. (%)	stat. (%)	$f_{gc,2}$ (%)	syst. (%)	stat. (%)
1530388454.0	600.0	0.137	0.004	0.004	0.182	0.002	0.005
1530389054.0	600.0	0.143	0.004	0.004	0.184	0.002	0.005
1530389654.0	600.0	0.14	0.004	0.004	0.183	0.002	0.005
1530390254.0	600.0	0.15	0.005	0.004	0.186	0.002	0.005
1530390854.0	600.0	0.144	0.004	0.004	0.184	0.002	0.005
1530391455.0	600.0	0.14	0.004	0.004	0.187	0.002	0.005
1530392065.0	600.0	0.155	0.004	0.004	0.187	0.002	0.005
1530392665.0	600.0	0.141	0.004	0.004	0.182	0.002	0.005
1530393265.0	600.0	0.14	0.004	0.004	0.192	0.002	0.005
1530393865.0	600.0	0.143	0.004	0.004	0.183	0.002	0.005
1530394465.0	600.0	0.145	0.004	0.004	0.186	0.002	0.005
1530395066.0	600.0	0.141	0.004	0.004	0.186	0.003	0.005
1530395675.0	600.0	0.14	0.004	0.004	0.188	0.002	0.005
1530396275.0	600.0	0.143	0.004	0.004	0.182	0.002	0.005
1530396875.0	600.0	0.135	0.004	0.004	0.185	0.002	0.005
1530397475.0	600.0	0.142	0.004	0.004	0.176	0.003	0.005
1530398075.0	600.0	0.143	0.004	0.004	0.186	0.002	0.005
1530398676.0	600.0	0.14	0.004	0.004	0.185	0.002	0.005
1530399285.0	600.0	0.14	0.004	0.004	0.179	0.002	0.005
1530399885.0	600.0	0.143	0.004	0.004	0.186	0.002	0.005
1530400485.0	600.0	0.143	0.004	0.004	0.185	0.002	0.005
1530401085.0	600.0	0.147	0.004	0.004	0.186	0.002	0.005
1530401685.0	600.0	0.142	0.004	0.004	0.182	0.002	0.005
1530402286.0	600.0	0.145	0.004	0.004	0.191	0.002	0.005
1530402896.0	600.0	0.137	0.004	0.004	0.187	0.002	0.005
1530403496.0	600.0	0.14	0.004	0.004	0.193	0.002	0.005
1530404096.0	600.0	0.141	0.004	0.004	0.19	0.003	0.005
1530404696.0	600.0	0.15	0.004	0.004	0.181	0.002	0.005
1530405296.0	600.0	0.14	0.004	0.004	0.181	0.002	0.005
1530405816.5	600.0	0.138	0.004	0.004	0.191	0.003	0.006
1530407656.0	600.0	0.142	0.004	0.004	0.183	0.002	0.005
1530408391.0	600.0	0.142	0.004	0.003	0.188	0.003	0.004
1530409791.0	600.0	0.147	0.004	0.004	0.181	0.002	0.005
1530410391.0	600.0	0.143	0.004	0.004	0.181	0.003	0.005
1530410991.0	600.0	0.139	0.004	0.004	0.194	0.002	0.005

Continued on next page

Table A.16 – *Continued from previous page*

time	dt	$f_{gc,1}$ (%)	syst. (%)	stat. (%)	$f_{gc,2}$ (%)	syst. (%)	stat. (%)
1530411591.0	600.0	0.138	0.004	0.004	0.183	0.002	0.005
1530412191.0	600.0	0.147	0.004	0.004	0.184	0.002	0.005
1530412790.0	600.0	0.138	0.004	0.004	0.179	0.002	0.005
1530413397.0	600.0	0.145	0.004	0.004	0.179	0.002	0.005
1530413997.0	600.0	0.133	0.004	0.004	0.18	0.002	0.005
1530414597.0	600.0	0.14	0.004	0.004	0.179	0.003	0.005
1530415197.0	600.0	0.137	0.003	0.004	0.187	0.002	0.005
1530415797.0	600.0	0.14	0.004	0.004	0.189	0.002	0.005
1530416398.0	600.0	0.136	0.004	0.004	0.19	0.002	0.005
1530417007.0	600.0	0.137	0.004	0.004	0.188	0.002	0.005
1530417607.0	600.0	0.139	0.004	0.004	0.181	0.003	0.005
1530418207.0	600.0	0.138	0.004	0.004	0.187	0.002	0.005
1530418807.0	600.0	0.142	0.004	0.004	0.18	0.002	0.005
1530419407.0	600.0	0.146	0.004	0.004	0.18	0.003	0.005
1530420008.0	600.0	0.148	0.004	0.004	0.175	0.002	0.005
1530420618.0	600.0	0.14	0.004	0.004	0.169	0.002	0.005
1530421218.0	600.0	0.142	0.004	0.004	0.18	0.002	0.005
1530421818.0	600.0	0.143	0.004	0.004	0.185	0.002	0.005
1530422418.0	600.0	0.145	0.004	0.004	0.188	0.002	0.005
1530423018.0	600.0	0.137	0.004	0.004	0.189	0.003	0.005
1530423619.0	600.0	0.14	0.004	0.004	0.178	0.002	0.005
1530424228.0	600.0	0.142	0.004	0.004	0.183	0.002	0.005
1530424678.0	600.0	0.14	0.004	0.005	0.177	0.002	0.007
1530426181.0	600.0	0.138	0.004	0.004	0.194	0.003	0.005
1530426781.0	600.0	0.135	0.004	0.004	0.188	0.003	0.005
1530427381.0	600.0	0.144	0.004	0.004	0.187	0.003	0.005
1530427834.5	600.0	0.131	0.004	0.005	0.187	0.003	0.007
1530428791.0	600.0	0.142	0.004	0.004	0.183	0.002	0.005
1530429391.0	600.0	0.135	0.004	0.004	0.186	0.003	0.005
1530429991.0	600.0	0.14	0.004	0.004	0.187	0.002	0.005
1530430737.0	600.0	0.143	0.004	0.003	0.19	0.003	0.004

A.7 2018 900 GeV high β^*

A.7.1 Fill 7406

Table A.17: Ghost charge measurement over time for fill 7406. The systematic uncertainties are correlated from one point to the next. The time is a UNIX timestamp and represents the centre of the integration interval dt.

time	dt	$f_{gc,1}$ (%)	syst. (%)	stat. (%)	$f_{gc,2}$ (%)	syst. (%)	stat. (%)
1541387604.0	805.5	0.236	0.015	0.007	0.116	0.003	0.018
1541388409.5	805.5	0.279	0.017	0.007	0.166	0.004	0.021

A.7.2 Fill 7407

Table A.18: Ghost charge measurement over time for fill 7407. The systematic uncertainties are correlated from one point to the next. The time is a UNIX timestamp and represents the centre of the integration interval dt.

time	dt	$f_{gc,1}$ (%)	syst. (%)	stat. (%)	$f_{gc,2}$ (%)	syst. (%)	stat. (%)
1541393248.0	900.0	0.237	0.015	0.006	0.199	0.005	0.021
1541394148.0	900.0	0.223	0.014	0.006	0.192	0.005	0.021
1541394920.0	900.0	0.228	0.015	0.007	0.178	0.005	0.024
1541395792.0	900.0	0.234	0.015	0.006	0.215	0.006	0.022
1541396692.0	900.0	0.233	0.015	0.006	0.163	0.004	0.02
1541397592.0	900.0	0.254	0.016	0.006	0.202	0.005	0.022
1541398490.5	900.0	0.254	0.016	0.006	0.17	0.005	0.02
1541399099.0	900.0	0.282	0.018	0.012	0.165	0.004	0.034

A.8 2018 Pb-Pb

A.8.1 Fill 7440

Table A.19: Ghost charge measurement over time for fill 7440. The systematic uncertainties are correlated from one point to the next. The time is a UNIX timestamp and represents the centre of the integration interval dt.

time	dt	$f_{gc,1}$ (%)	syst. (%)	stat. (%)	$f_{gc,2}$ (%)	syst. (%)	stat. (%)
1542051179.0	600.0	0.907	0.06	0.015	0.87	0.023	0.013
1542051779.0	600.0	0.928	0.061	0.015	0.862	0.023	0.013
1542052379.0	600.0	0.92	0.061	0.015	0.884	0.024	0.013
1542052979.0	600.0	0.97	0.064	0.016	0.94	0.025	0.014
1542053579.0	600.0	0.965	0.064	0.016	0.921	0.025	0.014
1542054180.5	600.0	0.992	0.066	0.017	0.93	0.025	0.014
1542054790.0	600.0	1.025	0.068	0.017	0.966	0.026	0.014
1542055390.0	600.0	1.06	0.07	0.018	1.011	0.027	0.015
1542055990.0	600.0	1.068	0.071	0.018	0.999	0.027	0.015
1542056590.0	600.0	1.09	0.072	0.018	1.005	0.027	0.015
1542057258.5	600.0	1.091	0.072	0.017	1.042	0.028	0.014
1542057935.0	600.0	1.12	0.074	0.019	1.066	0.029	0.016
1542058602.0	600.0	1.158	0.077	0.017	1.101	0.03	0.015
1542059277.0	600.0	1.189	0.079	0.02	1.119	0.03	0.017
1542059877.0	600.0	1.177	0.078	0.02	1.113	0.03	0.017
1542060477.0	600.0	1.196	0.079	0.021	1.144	0.031	0.017
1542061065.0	600.0	1.241	0.082	0.021	1.196	0.032	0.018
1542061643.5	600.0	1.205	0.08	0.023	1.209	0.033	0.02
1542062221.0	600.0	1.279	0.084	0.022	1.224	0.033	0.019
1542062821.0	600.0	1.24	0.082	0.022	1.217	0.033	0.019
1542063421.0	600.0	1.281	0.085	0.022	1.254	0.034	0.019
1542064021.0	600.0	1.384	0.091	0.024	1.235	0.033	0.019
1542064621.0	600.0	1.341	0.089	0.023	1.246	0.034	0.019
1542065222.0	600.0	1.383	0.091	0.024	1.279	0.034	0.02
1542065831.0	600.0	1.393	0.092	0.024	1.34	0.036	0.021
1542066431.0	600.0	1.453	0.096	0.025	1.316	0.035	0.02
1542067031.0	600.0	1.446	0.096	0.025	1.32	0.036	0.02
1542067631.0	600.0	1.499	0.099	0.026	1.333	0.036	0.021
1542068231.0	600.0	1.413	0.093	0.025	1.362	0.037	0.021
1542068832.0	600.0	1.418	0.094	0.025	1.353	0.036	0.021

Continued on next page

Table A.19 – *Continued from previous page*

time	dt	$f_{gc,1}$ (%)	syst. (%)	stat. (%)	$f_{gc,2}$ (%)	syst. (%)	stat. (%)
1542069522.0	600.0	1.436	0.095	0.025	1.36	0.037	0.021
1542070122.0	600.0	1.428	0.094	0.025	1.366	0.037	0.021
1542070722.0	600.0	1.415	0.093	0.025	1.368	0.037	0.021
1542071322.0	600.0	1.476	0.098	0.026	1.425	0.038	0.022
1542071922.0	600.0	1.513	0.1	0.026	1.391	0.037	0.021
1542072523.0	600.0	1.469	0.097	0.026	1.324	0.036	0.021
1542073132.0	600.0	1.483	0.098	0.026	1.403	0.038	0.022
1542073732.0	600.0	1.526	0.101	0.027	1.399	0.038	0.022
1542074332.0	600.0	1.474	0.097	0.026	1.419	0.038	0.022
1542074932.0	600.0	1.543	0.102	0.027	1.389	0.037	0.022
1542075532.0	600.0	1.515	0.1	0.027	1.478	0.04	0.023
1542076133.0	600.0	1.535	0.101	0.027	1.4	0.038	0.022
1542076579.0	600.0	1.595	0.105	0.042	1.48	0.04	0.034
1542076878.0	600.0	1.465	0.097	0.051	1.449	0.039	0.045

A.8.2 Fill 7441

Table A.20: Ghost charge measurement over time for fill 7441. The systematic uncertainties are correlated from one point to the next. The time is a UNIX timestamp and represents the centre of the integration interval dt.

time	dt	$f_{gc,1}$ (%)	syst. (%)	stat. (%)	$f_{gc,2}$ (%)	syst. (%)	stat. (%)
1542092866.5	715.5	1.506	0.099	0.032	1.813	0.049	0.032
1542093582.0	715.5	1.489	0.098	0.03	1.726	0.046	0.029
1542094073.0	715.5	1.473	0.097	0.022	1.785	0.048	0.022
1542094673.0	715.5	1.482	0.098	0.022	1.838	0.049	0.023
1542095273.0	715.5	1.53	0.101	0.023	1.807	0.049	0.022
1542095873.0	715.5	1.571	0.104	0.023	1.818	0.049	0.023
1542096473.0	715.5	1.519	0.1	0.023	1.861	0.05	0.023
1542097074.5	715.5	1.505	0.099	0.023	1.879	0.051	0.023
1542097684.0	715.5	1.531	0.101	0.023	1.825	0.049	0.023
1542098284.0	715.5	1.507	0.1	0.023	1.885	0.051	0.023
1542098884.0	715.5	1.566	0.103	0.024	1.912	0.051	0.024
1542099484.0	715.5	1.618	0.107	0.024	1.953	0.053	0.024

Continued on next page

Table A.20 – *Continued from previous page*

time	dt	$f_{gc,1}$ (%)	syst. (%)	stat. (%)	$f_{gc,2}$ (%)	syst. (%)	stat. (%)
1542100084.0	715.5	1.541	0.102	0.023	1.898	0.051	0.024
1542100685.0	715.5	1.632	0.108	0.025	1.893	0.051	0.024
1542101295.0	715.5	1.644	0.109	0.025	1.958	0.053	0.024
1542101895.0	715.5	1.613	0.107	0.025	1.921	0.052	0.024
1542102495.0	715.5	1.622	0.107	0.025	1.929	0.052	0.024
1542103095.0	715.5	1.614	0.107	0.025	1.956	0.053	0.025
1542103684.0	715.5	1.631	0.108	0.025	1.945	0.052	0.025
1542104319.0	715.5	1.628	0.108	0.025	2.022	0.054	0.025
1542104919.0	715.5	1.659	0.11	0.026	2.01	0.054	0.025
1542105519.0	715.5	1.688	0.111	0.026	2.061	0.055	0.026
1542106119.0	715.5	1.695	0.112	0.026	1.995	0.054	0.025
1542106719.0	715.5	1.696	0.112	0.026	2.064	0.056	0.026
1542107318.0	715.5	1.717	0.113	0.026	2.09	0.056	0.027
1542107926.0	715.5	1.747	0.115	0.027	2.05	0.055	0.026
1542108526.0	715.5	1.765	0.117	0.027	2.066	0.056	0.026
1542109107.0	715.5	1.744	0.115	0.028	2.082	0.056	0.027
1542109695.0	715.5	1.746	0.115	0.027	2.068	0.056	0.027
1542110237.5	715.5	1.723	0.114	0.03	2.082	0.056	0.03
1542110869.0	715.5	1.817	0.12	0.028	2.086	0.056	0.027
1542111469.0	715.5	1.766	0.117	0.028	2.09	0.056	0.027
1542112069.0	715.5	1.796	0.119	0.028	2.086	0.056	0.027
1542112669.0	715.5	1.836	0.121	0.029	2.109	0.057	0.027
1542113169.5	715.5	1.822	0.12	0.035	2.196	0.059	0.035
1542113678.0	715.5	1.87	0.124	0.029	2.132	0.057	0.028
1542114278.0	715.5	1.888	0.125	0.03	2.188	0.059	0.028
1542114878.0	715.5	1.866	0.123	0.029	2.175	0.059	0.028
1542115478.0	715.5	1.875	0.124	0.03	2.242	0.06	0.029
1542116078.0	715.5	1.818	0.12	0.029	2.24	0.06	0.029
1542116678.5	715.5	1.847	0.122	0.029	2.21	0.059	0.029
1542117137.5	715.5	1.836	0.121	0.041	2.18	0.059	0.041

A.8.3 Fill 7442

Table A.21: Ghost charge measurement over time for fill 7442. The systematic uncertainties are correlated from one point to the next. The time is a UNIX timestamp and represents the centre of the integration interval dt.

time	dt	$f_{gc,1}$ (%)	syst. (%)	stat. (%)	$f_{gc,2}$ (%)	syst. (%)	stat. (%)
1542141014.0	625.0	0.643	0.042	0.051	0.833	0.022	0.062
1542141639.0	625.0	0.665	0.044	0.036	0.791	0.021	0.041
1542142156.5	625.0	0.721	0.048	0.026	0.972	0.026	0.028
1542142551.0	625.0	0.778	0.051	0.015	0.995	0.027	0.015
1542143151.0	625.0	0.756	0.05	0.014	0.991	0.027	0.015
1542143751.0	625.0	0.763	0.05	0.014	0.968	0.026	0.015
1542144351.0	625.0	0.766	0.051	0.014	1.025	0.028	0.015
1542144951.0	625.0	0.742	0.049	0.014	1.04	0.028	0.016
1542145551.5	625.0	0.775	0.051	0.015	1.026	0.028	0.015
1542146160.0	625.0	0.791	0.052	0.015	1.011	0.027	0.015
1542146760.0	625.0	0.806	0.053	0.015	1.07	0.029	0.016
1542147360.0	625.0	0.777	0.051	0.015	1.03	0.028	0.016
1542147960.0	625.0	0.789	0.052	0.015	1.024	0.028	0.016
1542148560.0	625.0	0.836	0.055	0.016	1.047	0.028	0.016

A.8.4 Fill 7443

Table A.22: Ghost charge measurement over time for fill 7443. The systematic uncertainties are correlated from one point to the next. The time is a UNIX timestamp and represents the centre of the integration interval dt.

time	dt	$f_{gc,1}$ (%)	syst. (%)	stat. (%)	$f_{gc,2}$ (%)	syst. (%)	stat. (%)
1542213310.0	600.0	1.179	0.078	0.019	1.58	0.043	0.02
1542213910.0	600.0	1.202	0.079	0.019	1.536	0.041	0.02
1542214510.0	600.0	1.236	0.082	0.019	1.568	0.042	0.02
1542215110.0	600.0	1.229	0.081	0.019	1.587	0.043	0.02
1542215710.0	600.0	1.213	0.08	0.019	1.556	0.042	0.02
1542216310.0	600.0	1.231	0.081	0.019	1.632	0.044	0.021
1542216917.0	600.0	1.257	0.083	0.02	1.67	0.045	0.021
1542217517.0	600.0	1.267	0.084	0.02	1.63	0.044	0.021

Continued on next page

Table A.22 – *Continued from previous page*

time	dt	$f_{gc,1}$ (%)	syst. (%)	stat. (%)	$f_{gc,2}$ (%)	syst. (%)	stat. (%)
1542218117.0	600.0	1.261	0.083	0.02	1.605	0.043	0.021
1542218717.0	600.0	1.256	0.083	0.02	1.654	0.044	0.021
1542219241.0	600.0	1.236	0.082	0.023	1.686	0.045	0.025
1542228676.0	600.0	1.491	0.098	0.024	1.799	0.048	0.024
1542229276.0	600.0	1.418	0.094	0.023	1.85	0.05	0.024
1542229876.0	600.0	1.451	0.096	0.023	1.772	0.048	0.024
1542230476.0	600.0	1.466	0.097	0.024	1.819	0.049	0.024
1542231076.0	600.0	1.422	0.094	0.023	1.824	0.049	0.024
1542231557.0	600.0	1.403	0.093	0.03	1.859	0.05	0.032
1542232078.0	600.0	1.439	0.095	0.024	1.918	0.052	0.025
1542232678.0	600.0	1.518	0.1	0.024	1.876	0.05	0.025
1542233363.5	600.0	1.465	0.097	0.021	1.905	0.051	0.022

A.8.5 Fill 7483

Table A.23: Ghost charge measurement over time for fill 7483. The systematic uncertainties are correlated from one point to the next. The time is a UNIX timestamp and represents the centre of the integration interval dt.

time	dt	$f_{gc,1}$ (%)	syst. (%)	stat. (%)	$f_{gc,2}$ (%)	syst. (%)	stat. (%)
1543457646.0	600.0	1.177	0.078	0.022	2.327	0.063	0.029
1543458246.0	600.0	1.187	0.078	0.022	2.355	0.063	0.03
1543458846.0	600.0	1.207	0.08	0.022	2.379	0.064	0.03
1543459446.0	600.0	1.276	0.084	0.025	2.422	0.065	0.032
1543460046.0	600.0	1.234	0.082	0.023	2.421	0.065	0.031
1543460645.5	600.0	1.287	0.085	0.024	2.539	0.068	0.033
1543461254.0	600.0	1.281	0.085	0.024	2.58	0.069	0.033
1543461854.0	600.0	1.308	0.086	0.025	2.66	0.072	0.034
1543462454.0	600.0	1.39	0.092	0.026	2.666	0.072	0.034
1543463054.0	600.0	1.304	0.086	0.025	2.785	0.075	0.036
1543463654.0	600.0	1.408	0.093	0.026	2.809	0.076	0.036
1543464255.0	600.0	1.418	0.094	0.027	2.834	0.076	0.037
1543464864.0	600.0	1.434	0.095	0.027	2.981	0.08	0.039
1543465464.0	600.0	1.469	0.097	0.028	2.877	0.077	0.038

Continued on next page

Table A.23 – *Continued from previous page*

time	dt	$f_{gc,1}$ (%)	syst. (%)	stat. (%)	$f_{gc,2}$ (%)	syst. (%)	stat. (%)
1543466064.0	600.0	1.466	0.097	0.028	2.941	0.079	0.039
1543466664.0	600.0	1.557	0.103	0.03	3.087	0.083	0.041
1543467264.0	600.0	1.603	0.106	0.031	3.111	0.084	0.041
1543467865.0	600.0	1.595	0.105	0.031	3.211	0.086	0.043
1543468474.0	600.0	1.536	0.101	0.03	3.277	0.088	0.043
1543469074.0	600.0	1.624	0.107	0.031	3.267	0.088	0.044
1543469674.0	600.0	1.659	0.11	0.032	3.344	0.09	0.045
1543470274.0	600.0	1.689	0.112	0.033	3.357	0.09	0.045
1543470874.0	600.0	1.72	0.114	0.034	3.531	0.095	0.048
1543471475.0	600.0	1.708	0.113	0.034	3.51	0.094	0.048
1543472085.0	600.0	1.757	0.116	0.035	3.656	0.098	0.05
1543472685.0	600.0	1.816	0.12	0.036	3.619	0.097	0.05
1543473285.0	600.0	1.879	0.124	0.037	3.847	0.103	0.053
1543473885.0	600.0	1.951	0.129	0.039	3.752	0.101	0.052
1543474485.0	600.0	1.929	0.127	0.038	3.825	0.103	0.053
1543475086.0	600.0	1.877	0.124	0.038	3.895	0.105	0.054
1543475695.0	600.0	1.887	0.125	0.038	3.938	0.106	0.055
1543476295.0	600.0	2.008	0.133	0.04	4.034	0.109	0.057
1543476895.0	600.0	2.006	0.132	0.041	4.059	0.109	0.057
1543477495.0	600.0	2.072	0.137	0.042	4.052	0.109	0.057
1543478095.0	600.0	2.065	0.136	0.042	4.31	0.116	0.062
1543478644.0	600.0	2.075	0.137	0.046	4.166	0.112	0.065
1543481379.0	600.0	2.177	0.144	0.045	4.377	0.118	0.063
1543481979.0	600.0	2.172	0.143	0.045	4.308	0.116	0.061
1543482579.0	600.0	2.378	0.157	0.049	4.477	0.12	0.065
1543483179.0	600.0	2.216	0.146	0.046	4.564	0.123	0.066
1543483779.0	600.0	2.299	0.152	0.047	4.569	0.123	0.066
1543484378.5	600.0	2.261	0.149	0.047	4.48	0.121	0.065
1543484986.0	600.0	2.342	0.155	0.048	4.591	0.123	0.066
1543485586.0	600.0	2.278	0.15	0.047	4.547	0.122	0.066
1543486186.0	600.0	2.377	0.157	0.049	4.552	0.122	0.066
1543486786.0	600.0	2.397	0.158	0.05	4.663	0.125	0.069
1543487386.0	600.0	2.367	0.156	0.05	4.712	0.127	0.07
1543487987.0	600.0	2.38	0.157	0.05	4.667	0.126	0.069
1543488597.0	600.0	2.407	0.159	0.05	4.753	0.128	0.07

Continued on next page

Table A.23 – *Continued from previous page*

time	dt	$f_{gc,1}$ (%)	syst. (%)	stat. (%)	$f_{gc,2}$ (%)	syst. (%)	stat. (%)
1543489197.0	600.0	2.404	0.159	0.051	4.795	0.129	0.071
1543489797.0	600.0	2.422	0.16	0.051	4.787	0.129	0.071
1543490397.0	600.0	2.428	0.16	0.051	4.841	0.13	0.072
1543490997.0	600.0	2.352	0.155	0.05	4.814	0.129	0.072
1543491598.0	600.0	2.428	0.16	0.051	5.023	0.135	0.074
1543495673.0	600.0	2.619	0.173	0.055	5.074	0.136	0.076
1543496273.0	600.0	2.567	0.17	0.054	4.99	0.134	0.075
1543496873.0	600.0	2.596	0.171	0.055	5.196	0.14	0.078
1543497473.0	600.0	2.701	0.178	0.057	5.095	0.137	0.076
1543498073.0	600.0	2.674	0.177	0.057	5.295	0.142	0.08
1543498671.5	600.0	2.616	0.173	0.056	5.253	0.141	0.079
1543499278.0	600.0	2.65	0.175	0.057	5.399	0.145	0.082
1543499878.0	600.0	2.708	0.179	0.058	5.376	0.145	0.082
1543500478.0	600.0	2.735	0.181	0.058	5.221	0.14	0.08
1543501078.0	600.0	2.675	0.177	0.057	5.279	0.142	0.081
1543501723.0	600.0	2.717	0.179	0.055	5.302	0.143	0.075

List of Tables

List of Figures

Bibliography

[1] LHCb Collaboration (R. Aaij et al.), *Measurement of the forward Z boson production cross-section in pp collisions at* $\sqrt{s} = 13$ *TeV*, JHEP 09 (2016) 136

[2] G. Montagna, O. Nicrosini, F. Piccinini, *Precision Physics at LEP*, Riv. Nuovo Cim. 21N9 (1998) 1-162, arXiv:hep-ph/9802302

[3] S. Van der Meer, *Calibration of the Effective Beam Height in the ISR*, CERN-ISR-PO-68-31, 1968

[4] LHCb Collaboration (R. Aaij et al.), *Absolute Luminosity Measurements with the LHCb Detector at the LHC*, JINST 7 (2012) P01010, LHCB-PAPER-2011-015

[5] LHCb Collaboration (R. Aaij et al.), *Precision Luminosity Measurements at LHCb*, JINST 9 (2014) no.12, P12005, LHCB-PAPER-2014-047

[6] P. Hopchev, *Absolute Luminosity Measurements at LHCb*, CERN-THESIS-2011-210

[7] C. Barschel, *Precision Luminosity Measurement at LHCb with Beam-Gas Imaging*, CERN-THESIS-2013-301

[8] C. Barschel et al., *Preliminary luminosity calibration at* $\sqrt{s} = 13$ *TeV (p-p)*, CERN-LHCb-ANA-2015-036

[9] L. Evans and P. Bryant, *LHC Machine*, JINST 3 S08001, 2008

[10] M. A. Hone, *The duoplasmatron ion source for the new CERN Linac preinjector*, CERN-PS-LR-79-37, 1979

[11] C. De Melis, *The CERN Accelerator Complex*, OPEN-PHO-ACCEL-2016-001

[12] R. Steerenberg, *LHC Report: Protons: mission accomplished*, 29 October, 2018, https://home.cern/news/news/physics/lhc-report-protons-mission-accomplished

[13] LHCb Collaboration (A. Augusto Alves et al.), *The LHCb Detector at the LHC*, 2008 JINST 3 S08005

[14] J. Jowett and M. Lamont, *LHC Report: far beyond expectations*, 13 December, 2016, https://home.cern/news/news/accelerators/lhc-report-far-beyond-expectations

[15] R. Aaij et al., *Performance of the LHCb Vertex Locator*, 2014 JINST 9 P09007

[16] R. Antunes-Nobrega et al., *LHCb reoptimized detector design and performance: Technical Design Report*, CERN-LHCC-2003-030, LHCb-TDR-9

[17] R. Aaij et al., *Performance of the LHCb trigger and full real-time reconstruction in Run 2 of the LHC*, JINST 14 (2019) P04013 (arXiv:1812.10790), CERN-LHCb-DP-2019-001

[18] The LHCb RICH group, *Performance of the LHCb RICH detector at the LHC*, arXiv:1211.6759, Eur. Phys. J. C 73 (2013) 2431, CERN-LHCb-DP-2012-003

[19] A. Papanestis, C. D'Ambrosio on behalf of the LHCb RICH Collaboration, *Performance of the LHCb RICH detectors during the LHC Run II*, Nucl. Instr. and Meth. A876 (2017), 221-224, arXiv:1703.08152, LHCb-PUB-2017-012

[20] E. P. Olloqui and the LHCb Collaboration, *LHCb Preshower (PS) and Scintillating Pad Detector (SPD): Commissioning, calibration, and monitoring*, 2009, J. Phys. Conf. Ser. 160 012046

[21] Yu. Guz, *The LHCb Calorimeter system: design, performance and upgrade*, 2017 JINST 12 C07024

[22] A. A. Alves Jr. et al., *Performance of the LHCb muon system*, JINST 8 P02022, 2013

[23] O. Gröbner, *LHC vacuum system*, CERN-OPEN-2000-288, 1999

[24] C. Benvenuti et al., *Vacuum properties of TiZrV non-evaporable getter films*, Vacuum 60 (2001) 57.

[25] M. Ferro-Luzzi, *Considerations about luminosity determination in LHCb gaseous fixed target experiments*, LHCb-INT-2015-031, 2015

[26] G. Graziani, *Production studies for Cosmic Ray Physics*, Workshop on LHCb Ion and Fixed Target Physics, CERN, 2017, `https://indico.cern.ch/event/570774/contributions/2393004/attachments/1392561/2122036/graziani_lhcbCR_public.pdf`

[27] G. Graziani on behalf of the LHCb Collaboration, *Results on heavy ion physics at LHCb*, J. Phys.: Conf. Ser. 1271 012008, arXiv:1904.04130, 2019

[28] W. Herr and B. Muratori, *The Concept of Luminosity*, Cern Accelerator School Intermediate Accelerator Physics, DESY Zeuthen, Germany, 2003, CERN-2006-002 (2016) 361

[29] S. White, *Determination of the Absolute Luminosity at the LHC*, CERN-THESIS-2010-139

[30] C. Moller, *General Properties of the Characteristic Matrix in the Theory of Elementary Particles*, K. Danske, Vidensk. Selk. Mat.-Fys.Medd. 23, 1, 1945

[31] M. Ferro-Luzzi, *Luminosity and luminous region shape for pure Gaussian bunches*, LHCb-PUB-2012-016

[32] G. Coombs, *Luminosity and Luminous Region Calculations for Different LHC Levelling Scenarios*, Masters' thesis, Imperial College London, July 2014

[33] G. W. Hill, *On the part of the motion of the lunar perigee which is a function of the mean motions of the sun and moon*, Acta mathematica, vol. 8, no. 1, pp. 1-36, 1886

[34] H. Wiedemann, *Particle accelerator physics*, vol. 1. Springer, 2003

[35] M. Conte and W. MacKay, *An Introduction to the Physics of Particle Accelerators*, pp. 35-39, World Scientific, 2008

[36] M. Kuhn, *Emittance Preservation at the LHC*, CERN-THESIS-2013-031, Mar 12, 2013

[37] C. Rubbia, *Measurement of the luminosity of $p\overline{p}$ collider with a (generalized) Van der Meer method*, CERN-$p\overline{p}$-Note-38, 1977

[38] C. Gaspar et al., *The LHCb Experiment Control System: On the path to full automation*, 13th International Conference on Accelerator and Large Experimental Physics Control Systems, Grenoble, France, 10 - 14 Oct 2011, https://accelconf.web.cern.ch/icalepcs2011/papers/mobaust06.pdf

[39] LHCb Collaboration (R. Aaij et al.), *Measurement of Antiproton Production in pHe Collisions at $\sqrt{s_{NN}} = 110$ GeV*, Phys. Rev. Lett. 121 (2018) 222001, LHCb-PAPER-2018-031

[40] Pfeiffer Vacuum, *Operating Manual: Compact Cold Cathode Gauge IKR 270*, Appendix B: Gas Type Dependence, Page 22, `https://mmrc.caltech.edu/Kratos%20XPS/accessories/Pfeiffer%20Cold%20Cath%20Gage%20IKR%20270.pdf`

[41] C. Barschel et al., *Results of the DCCT calibration studies*, CERN-ATS-Note-2012-026 PERF, May 2012

[42] P. Odier et al., *The DCCT for the LHC Beam Intensity Measurement*, CERN-BE-2009-019, 2009

[43] P. Odier et al., *DCCT Technology Review*, DC Current Transformers and Beam-Lifetime Evaluations Workshop, Lyon, 2004

[44] S. Aguilera, *Study and Characterization of Magnetic Materials for Beam Intensity Monitors at CERN*, Ph.D Thesis, Ecole Polytechnique, Lausanne, 2017, CERN-THESIS-2017-312

[45] G. Gelato, *Beam current and charge measurement*, Beam instrumentation, ed. J.Bosser, Geneva, 1994, CERN-PE-ED-001-92

[46] G. Anders et al., *Study of the Relative Bunch Populations for Luminosity Calibration*, CERN-ATS-Note-2012-028 PERF, BCNWG Note 3, 2012

[47] D. Belohrad et al., *The LHC Fast BCT system: A comparison of Design Parameters with Initial Performance*, CERN-BE-2010-010, Presented at 14th Beam Instrumentation Workshop, Santa Fe, New Mexico, United States Of America, 2 - 6 May 2010

[48] C. Ohm, T. Pauly, *The ATLAS beam pick-up based timing system*, Nucl.Instrum.Meth. A623 (2010) 558-560, arXiv:0905.3648, May 2009

[49] M. Palm, *LHC Beam Current Measurement: Performance and Issues in Run 2, Prospects for Run 3*, LHC Lumi Days 2019, Tuesday, 4 June, Geneva, Switzerland, `https://indico.cern.ch/event/813285/contributions/3406074/attachments/1855657/3047803/LumiDays_2019_MPalm_LHC_beam_current_measurement_performance_and_issues.pdf`

[50] A. Alici et al., *Study of the LHC ghost charge and satellite bunches for luminosity calibration*, CERN-ATS-Note-2012-029 PERF, BCNWG Note 4, 2012

[51] H. Timko et al., *Longitudinal transfer of rotated bunches in the CERN injectors*, Physical Review Special Topics - Accelerators and Beams 16, 051004 (2013)

[52] M. Palm et al., *Near-Saturation Single-Photon Avalanche Diode Afterpulse and Sensitivity Correction Scheme for the LHC Longitudinal Density Monitor*, 3rd International Beam Instrumentation Conference, Monterey, California, 2014, CERN-BE-2014-005

[53] M. Rihl, *Development of a non-destructive beam-profile monitor based on scintillating fibre planes and SIPMs*, Ph.D. thesis, Vienna Technical University, 2018, CERN-THESIS-2018-049

[54] G. Coombs et al., *Beam-Gas Imaging Measurements at LHCb*, Proceedings of IBIC2018, Shanghai, China, 2018, doi:10.18429/JACoW-IBIC2018-WEPB13, http://accelconf.web.cern.ch/ibic2018/papers/wepb13.pdf

[55] P. d'Argent et al., *Improved performance of the LHCb Outer Tracker in LHC Run 2*, JINST 12, P11016, 2018

[56] A. Boccardi et al., *LHC Luminosity calibration using the Longitudinal Density Monitor*, CERN-ATS-Note-2013-034 TECH, 2013

[57] V. Balagura, *Difference between even/odd bunch currents measured by FBCT*, LHCb Luminosity working group, 20 Mar 2017, `https://indico.cern.ch/event/624409/contributions/2520509/attachments/1429953/2196179/currents_fill_4937_balagura.pdf`

[58] V. Balagura, *Final Luminosity Values in Run 2 and Great Perspectives Beyond*, LHCb Week, 10 Sep 2020, `https://indico.cern.ch/event/941777/contributions/3998517/attachments/2099537/3535817/lumi_balagura.pdf`

[59] M. Kucharczyk, P. Morawski, and M. Witek, *Primary Vertex Reconstruction at LHCb*, LHCb-PUB-2014-044.

[60] R. Alemany-Fernández et al., *Cross-Calibration of the LHC Transverse Beam-Profile Monitors*, Proceedings of IPAC2017, Copenhagen, Denmark, MOPAB130, https://accelconf.web.cern.ch/ipac2017/papers/mopab130.pdf

[61] F. Roncarolo, *Accuracy of the Transverse Emittance Measurements of the CERN Large Hadron Collider*, Ph.D. thesis, LPHE, Lausanne, 2005, CERN-THESIS-2005-082

[62] G. Trad, *Development and Optimisation of the SPS and LHC beam diagnostics based on Synchrotron Radiation Monitors*, Ph.D. thesis, Subatomic and Astrophysics Dept., Universit*é* de Grenoble-Alpes, Grenoble, France, 2015, CERN-THESIS-2014-390

[63] M. Hostettler et al., *Comparison of Transverse Emittance Measurements in the LHC*, Proceedings of IPAC2017, Copenhagen, Denmark, MOPAB110, https://accelconf.web.cern.ch/ipac2017/papers/mopab110.pdf

[64] F. Roncarolo, *LHC wire scanner system: Run 1&2 experience, Plans for Run 3*, LHC Beam Size Measurement Review, 1-2 October 2019, CERN, Geneva, Switzerland, `https://indico.cern.ch/event/837340/contributions/3510873/attachments/1917780/3171296/LHC_BWS_RUN1-2_beamsizereview_Oct2019_final.pdf`

[65] T. Hadavizadeh et al., *Transverse Emittance Measurements Using LHCb's Beam-Gas Interactions*, Proceedings of IPAC2017, Copenhagen, Denmark, MOPAB131, https://accelconf.web.cern.ch/ipac2017/papers/mopab131.pdf

[66] R.J. Steinhagen, *Tune and chromaticity diagnostics*, CERN Accelerator School: Course on Beam Diagnostics, Dourdan, France, 28 May - 6 Jun 2008, pp.317 (CERN-2009-005)

[67] R. Calaga et al., β^* *Measurement in the LHC Based on K-modulation*, Conf.Proc. C110904 (2011) 1864-1866, IPAC-2011-TUPZ027, https://accelconf.web.cern.ch/IPAC2011/papers/TUPZ027.PDF

[68] C. Yin Vallgren et al., *LHC Beam Vacuum Evolution During 2015 Machine Operation*, Proceedings of IPAC2016, Busan, Korea, THPMY010, https://accelconf.web.cern.ch/ipac2016/papers/thpmy010.pdf

[69] G. Bregliozzi et al., *Vacuum pressure observations during 2011 proton run*, 3rd Evian Workshop on LHC beam operation, Evian-les-bains, France, 12 - 14 Dec 2011, https://cds.cern.ch/record/1975506/files/177p.pdf

[70] LHCb Collaboration, *LHCb VELO Upgrade Technical Design Report*, CERN-LHCC-2013-021, 2013

[71] G. Coombs et al., *Downstream vertexing performance for dynamic vacuum studies*, LHCb-INT-2016-043, Aug 2017

[72] M. Alexander et al., *Mapping the material in the LHCb vertex locator using secondary hadronic interactions*, JINST 13, P06008, 2018, CERN-LHCb-DP-2018-002

[73] J. Uythoven et al., *Abort Gap Cleaning for LHC Run 2*, Proceedings of IPAC2014, Dresden, Germany, MOPRO031, `https://cds.cern.ch/record/2003159/files/mopro031.pdf`

[74] ATLAS Collaboration, *Luminosity determination for low-pileup datasets at* $\sqrt{s} = 5$ *and 13 TeV using the ATLAS detector at the LHC*, 25th July 2020, ATLAS-CONF-2020-023